IN VIVO FLOW VELOCITY MEASUREMENT USING NUCLEAR MAGNETIC RESONANCE IMAGING.

John P. Ridgway, BSc. (Edinburgh), MSc. (Aberdeen).

PhD.

University of Edinburgh.

1989

UNIV. EDINBURGH

Declaration

This report is my own composition, and the work described has been performed by myself, unless otherwise stated in the text. All verbatim remarks have been distinguished by quotation marks, and the sources of my information have been specifically acknowledged.

John P. Ridgway

5th October, 1989.

Abstract

A new technique has been devised to measure the velocity of fluid motion within the human body by using Nuclear Magnetic Resonance (NMR) Imaging. The phase of the NMR signal is modulated in the presence of motion by the time-varying magnetic field gradients used in the imaging process. The magnetic field gradient pulse waveforms can be tailored to produce phase modulations which are linearly dependent on the components of flow velocity in a particular direction. However, phase modulations are also caused by inhomogeneities in the main magnetic field, and chemical shift and magnetic susceptibility effects, as well as by flow velocity components in other directions. In order to exclude these unwanted phase modulations, a novel technique has been developed in which two phase images are acquired, each having a different velocity dependence. Subtraction of these two images eliminates the phase modulations common to both images and leaves only the velocity-dependent phase modulations corresponding to the direction of flow being measured. The velocity dependence in each image is controlled by varying the temporal separation between two of the gradient pulses. The phase images are acquired using a field echo pulse sequence in order to maximise the signal from fast flowing blood. The two acquisitions are interleaved to avoid the possibility of mis-registration when the two phase images are subtracted. This flow imaging technique has been implemented on a 0.08 Tesla NMR imaging system (M&D Technology Ltd). It is possible to measure flow velocity components both within the imaged slice and perpendicular to the slice. The slice orientation can be angled by up to 30 degrees to allow imaging of vessels which run obliquely through the body. Measurement of velocity components perpendicular to the imaged slice gives the most accurate results, whilst imaging of velocity components within the imaged slice are of use for visualisation of flow and positioning of subsequent acquisitions. An electro-cardiographic gating system has been developed to synchronise the NMR imaging system with the subject's cardiac cycle. It is thus possible for multiple images to be acquired throughout the cardiac cycle at the same spatial position, enabling the study of pulsatile flow. Further development of the magnetic field gradient pulse waveforms has been carried out to reduce signal losses caused by accidental phase modulations in the presence of high velocity gradients. The NMR flow measurement technique has been calibrated for both low velocity (30cm/s maximum) and high velocity (100cm/s maximum) ranges. There is a good agreement between the calibrated velocity/phase relationships and those predicted by theory. The NMR technique has been compared with Doppler ultrasound in the measurement of velocity waveforms in the common carotid arteries of healthy volunteers. The maximum velocities obtained from the NMR technique were compared, and correlated well with those obtained from Doppler ultrasound. The NMR technique has also been used to investigate the low-velocity pulsatile motion of cerebrospinal-fluid, related to the cardiac cycle, in healthy volunteers and in one patient with syringomyelia.

Acknowledgments

I am very grateful to a number of people for their help and encouragement during the course of this project. Firstly, I would like to thank my supervisors, Professor Mike Smith and Professor Norman McDicken, for their continued support and advice throughout this project. I have also received valuable help and advice from Drs Lindsay Turnbull and David Kean. I am grateful to Professor Jonathan Best for the use of the equipment and resources within his department, to Dr Paul Allan for performing the Doppler ultrasound measurements in the carotid arteries, and to Mr Peter Hoskins for performing the Doppler waveform analysis.

I am particularly thankful to those people who regularly acted as volunteers during the development of the flow imaging technique, and for the volunteer studies. They include Dr Lindsay Turnbull, Dr Hamish McRitchie, Dr David Pye, Dr Mike Smith, Mr Mike Glabus, Dr John Amoore, Mr Nick Nicholson, Miss Heather Engelman and Dr Uday Gaitonde.

I was generously funded by the Scottish Home and Health Department for most of the duration of this project.

Finally, I am most thankful to my family for their continued encouragement and support, and to Jenny, for her friendship and encouragement, and for performing the unenviable task of proof-reading this thesis.

Introduction to Flow Measurement Techniques and Magnetic Resonance Imaging (MRI).

1.0. Introduction

Magnetic resonance imaging (MRI) is now established as an imaging technique for routine clinical use (Bydder, 1988). Its strength lies in its ability to image in any plane and in the soft tissue contrast obtainable by the technique. Whilst MRI has so far been used for the detection of abnormal anatomy and pathology, the image pixel intensity is also affected by the presence of flowing blood. Early studies have shown that it may be possible to quantify blood flow, first using nuclear magnetic resonance (Singer, 1959) and later using magnetic resonance imaging (Singer and Crooks, 1983; Moran, 1982). The aim of this project is to develop a non-invasive technique to measure blood flow, in vivo, using an MRI system and to compare it with an existing Doppler ultrasound flow measurement technique. The following sections of this chapter contain a summary of the existing techniques used for in vivo blood flow measurement and a brief historical introduction to MRI.

1.1. Blood Flow Measurement

The two main applications of in vivo blood flow measurement are in the assessment of cardiac function and in the detection and measurement of blood flow to organs and limbs (Terry, 1986; Lorimer et al, 1986). Recently, with the advent of Doppler ultrasound and high resolution digital subtraction angiography, it has also been possible to detect disease within the vascular system itself (Wells, 1986; Moores, 1986). A full description of the existing techniques used to measure blood flow is given in appendix III.

The two most common non-invasive measurements performed to assess cardiac function are those of ejection fraction and cardiac output (see appendix III). The ejection fraction is measured using radioisotope tracer studies (Martin, 1986). The Cardiac output can be measured using radioisotope tracer studies, ultrasound or thermodilution techniques (Lorimer et al, 1986).

There are several approaches to the measurement of the blood flow to organs and limbs (Terry, 1986). Firstly, the volume flow along the major artery supplying the organ or limb can be measured directly. The patency of most vessels can be established using x-ray contrast angiography, but, if accurate flow measurements are required, either Doppler ultrasound or electromagnetic

induction must be used. The use of electromagnetic flowmeters is highly invasive and is only usually performed during surgery. Doppler ultrasound, however, is non-invasive, although access to some vessels is restricted. Secondly, the blood flow to a particular organ can be inferred by observing the uptake (or drainage) of a suitable tracer in that organ. Finally, venous occlusion plethysmography can be used to measure blood flow to limbs by detecting changes in the volume of the limb.

The ability of Doppler ultrasound to obtain pulsatile velocity waveforms has enabled analysis of the flow dynamics within vessels (Wells, 1986). Abnormalities in these waveforms can be an indication of disease within the vessel such as stenosis. Stenosis is also detectable within vessels using a catheter-tip pressure transducer to measure the pressure gradient either side of the site of suspected stenosis (Cunningham, 1986; Simpson et al, 1985).

1.2. Limitations of Existing Techniques

Whilst most of the above techniques have been in use for many years and are capable of producing accurate results, each technique has its own limitations.

The use of plethysmography to measure blood flow in limbs is cumbersome and can suffer from inaccuracy unless performed with care (Terry, 1986). Thermodilution is often used for the determination of cardiac output, (Lorimer et al, 1986), but requires cardiac catheterisation and must also be performed carefully in order to avoid inaccuracy. The use of radioisotopes in the assessment of cardiac function is also quite common, (Martin et al, 1986), and gives reasonable accuracy, however a small radiation dose is involved which limits the frequency with which these studies can be performed in individual subjects.

Electromagnetic flowmeters produce the most accurate true flow measurements within vessels, however this technique is invasive and can only be used during surgery. Doppler ultrasound has provided an excellent, totally non-invasive technique to measure the true flow velocities in vessels and produces pulsatile waveforms in real time (Wells, 1986). Some important vessel sites, however, are not accessible to ultrasound due to the presence of bone or air between the vessel and the Doppler probe, and the technique can be subject to inaccuracy if it is not carefully performed (Burns et al, 1985).

Whilst the techniques of echocardiography (Lorimer et al, 1986), and angiography (Cunningham et al, 1986), and the

measurement of pressure gradients (Simpson et al, 1985) all produce useful functional information, they do not provide quantitative information on blood flow dynamics. There is therefore a need for a non-invasive technique which can provide accurate quantitative information on flow dynamics within the cardiovascular system.

1.3. Nuclear Magnetic Resonance

1.3.1. Historical Development

The phenomenon of nuclear magnetic resonance (NMR) was first reported simultaneously in 1946 by two independent research groups, headed by Bloch working at Stanford and Purcell working at Harvard (Bloch et al, 1946; Purcell et al, 1946). Initially, NMR was observed as the absorption of energy in the form of electromagnetic radiofrequency (rf) radiation by hydrogen nuclei in water, at a characteristic frequency, in the presence of a strong static magnetic field. It was later observed that, immediately following the removal of the energy source, a small NMR signal could be detected from the water sample, as the nuclei returned to their equilibrium state by emitting energy in the form of rf radiation. A brief description of the basic principles of the NMR phenomenon can be found in Appendix I.

During the next decade, it was found that the characteristic absorption frequency could vary slightly depending on the chemical environment of the hydrogen nuclei (Beall et al, 1984). NMR was applied to a number of different nuclei, including the hydrogen nucleus, in order to deduce the identity and structure of organic molecules from their characteristic absorption spectra. NMR very quickly became a standard analytical tool for the physical and organic chemist. Initial results using proton magnetic resonance in biological samples (Odeblad and Lindstrom, 1955) indicated the potential of NMR in biomedical applications and by 1968 NMR measurements had been obtained from small, living animals and the human arm (Ligon, 1967; Jackson, 1968). The most exciting finding in the biomedical applications of NMR was that of Damadian, who showed that it was possible to distinguish normal from cancerous tissue (Damadian, 1971). This finding was to be the main incentive for the development of whole body NMR imaging techniques in the 1970's.

In 1959, long before the possibility of NMR imaging was conceived, Singer observed that the NMR signal amplitude could be related to the presence of blood flow in the tail of a live mouse (Singer, 1959; Singer, 1981). A more exact method of flow velocity measurement was developed by Singer, using a separate transmitter coil positioned upstream from the standard transmitter/receiver coil. The standard transmit/receive system was used to obtain the

normal absorption spectrum from the enclosed flowing blood and surrounding tissue. The transmitter coil, positioned upstream, was pulsed to produce a pre-excited bolus of blood, which induced a change in the absorption spectrum on reaching the receiver coil. The time taken between excitation of the bolus and its detection was measured and allowed the average blood flow velocity to be calculated. This technique was used to produce accurate measurements of blood flow in human forearms (Morse and Singer, 1970; Singer, 1981), and was later adapted to be used in conjunction with NMR imaging techniques (Singer and Crooks, 1983).

In order to achieve in vivo NMR measurements it was necessary to develop methods of spatial localisation. The earliest of these was a technique known as Zeugmatography developed by Lauterbur in 1973 (Lauterbur, 1973). This technique used a magnetic field gradient to spatially encode the signal in one dimension. An image of two test tubes was produced by back-projection reconstruction of several one-dimensional projections obtained by this method. By 1977, various techniques for spatial localisation had been devloped and the first in vivo images were obtained. Damadian produced an image of the human thorax by moving the body through a saddle point in a static magnetic field (Damadian et al, 1977). Mansfield's group working at Nottingham, England, produced a cross section of a human finger using a

selective, irradiative, line-scanning technique (Mansfield and Maudsley, 1977), and Hinshaw's group, also working at Nottingham, produced a cross section of a human wrist, using a multiple sensitive point method (Hinshaw et al, 1978).

Initially, the spatial resolution of these images was quite poor, however, over the next five years, technical advances, particularly in the manufacturing of wide-bore high-specification magnets for whole body imaging, saw significant increases in image quality. The scanning technique adopted by most manufacturers was based on the so called 'Spin Warp' imaging technique, developed by Edelstein and Hutchison's group working at Aberdeen University (Edelstein et al, 1980). This technique is the basis of the flow imaging technique described in this thesis, and a description of its basic principles is included in Appendix II.

1.3.2. Potential Advantages of MRI for Flow Measurement

There are a number of potential advantages in using MRI as a flow measurement technique. It is completely non-invasive, requiring no surgical intervention, no catheter insertion and no injection of contrast media into the blood stream. The absence of ionising radiation allows the technique to be repeated, without limit, in

follow-up studies and allows studies to be performed safely during pregnancy. MRI can image vessels situated deep within the body, at any orientation and there is no problem of obstruction by bone or air. The use of magnetic field gradients in the MRI process causes the NMR signal to be intrinsically dependent upon motion, and consequently the technique is potentially adaptable to flow measurement.

1.3.3. Interpretation of the NMR image

The interpretation of NMR images obtained in vivo is a complex process, as the observed image pixel intensity is dependent on a number of factors (Bydder, 1988). These factors can be divided into two groups and are summarised in table 1.1 below.

Intrinsic NMR Properties	Imaging Parameters
ρ proton density	B_o magnetic field strength
T1 relaxation time	ΔB_o inhomogeneity of B_o
T2 relaxation time	TR repetition time
σ chemical shift	TE time to echo
χ_m magnetic susceptibility	TI time from inversion
$\mathcal{D}$ diffusion coefficient	G(t) gradient Waveform
f(x,t) motion, flow	B1(t) rf pulse sequence

Table 1.1

There are those factors which are based on the intrinsic NMR properties of the tissue and there are those which are based on imaging parameters. Definitions and

explanations of many of these properties and parameters can be found in Appendices I and II. The image pixel intensity is derived from the combined effect of these properties and parameters. It is therefore possible to manipulate the contrast observed on an image by varying the imaging parameters. For example, in a routine clinical situation, contrast between tissues possessing different T1 and T2 relaxation times can be maximised by optimising the TR and TE of a particular pulse sequence (Young et al, 1986a). If moving fluid is present, the pixel intensity is modulated in a way which depends not only on the TR and TE, but also on the gradient and rf pulse sequences, (G(t) and B(t)), and on the flow dynamics (Axel, 1984). In chapter 2, the precise nature of this dependence is discussed for pulse sequences which are commonly found in routine clinical use.

The Appearance of Flow on the NMR image

2.0. Introduction

As discussed in chapter 1, the NMR image pixel intensity is dependent upon many factors. In the presence of flow, the NMR signal is dependent both upon the flow dynamics and upon the radiofrequency (rf) and gradient pulse sequences. The rf pulse sequence is dictated by the type of NMR measurement pulse sequence being performed (see section A2.6). The gradient pulse sequence is dictated by both the type of NMR measurement pulse sequence and by the method of spatial localisation and spatial encoding that is being employed (see sections A2.1 and A2.3).

The magnetic field gradients are superimposed on to the main magnetic field in order to introduce spatial localisation and encoding of the NMR signal. The use of these gradients affects the signal from moving protons in two ways (Axel, 1984). Firstly, magnetic field gradients which are used in combination with rf pulses for selective excitation of an image slice give rise to 'Time of Flight' effects in vessels which carry flow at an angle to the plane of the slice (Axel, 1984; Wedeen et al, 1987). The movement of excited protons out of the slice and of non-excited protons into the slice gives rise to variations in the NMR signal intensity. These

variations are known as 'Time of Flight' phenomena. Secondly, movement of excited protons along the direction of an applied gradient gives rise to modulation of the phase of the protons (Axel, 1984; Moran and Moran, 1984; Wedeen et al, 1987).

These effects not only allow identification of flow by qualitative evaluation of the images, but they can also allow quantitation of flow velocity by measuring either the magnitude or the phase of the NMR signal.

2.1. Selective Excitation and Time of Flight Effects

The precise nature of the appearance of blood flow on an image is dependent on the pulse sequence used. Only those sequences which are based on the spin warp imaging technique described in Appendix II, and which use selective excitation of the image slice, shall be considered here. Two main types of pulse sequence shall be discussed (see section A2.2. et seq). These are the Field Echo pulse sequence, which uses a selective 90° rf pulse only, and the Spin Echo pulse sequence which uses a selective 90° rf pulse, followed by a selective 180° pulse. These two pulse types of sequence shall be treated separately as they give rise to different time of flight effects in the presence of flow through the slice.

2.1.1. The Time of Flight Effect in Field Echo Sequences

In field echo imaging, the time of flight effect is observed as an increase in signal from blood flowing through the slice, relative to stationary tissue (Figure 2.1). The effect is particularly obvious when the repetition rate, TR, of the pulse sequence is comparable with, or less than, the T1 relaxation rate of the stationary lumen (Crooks et al, 1985). The observed increase of signal within blood vessels was originally given the name 'Paradoxical Enhancement' but is now more commonly named 'flow related enhancement' (Bradley et al, 1984).

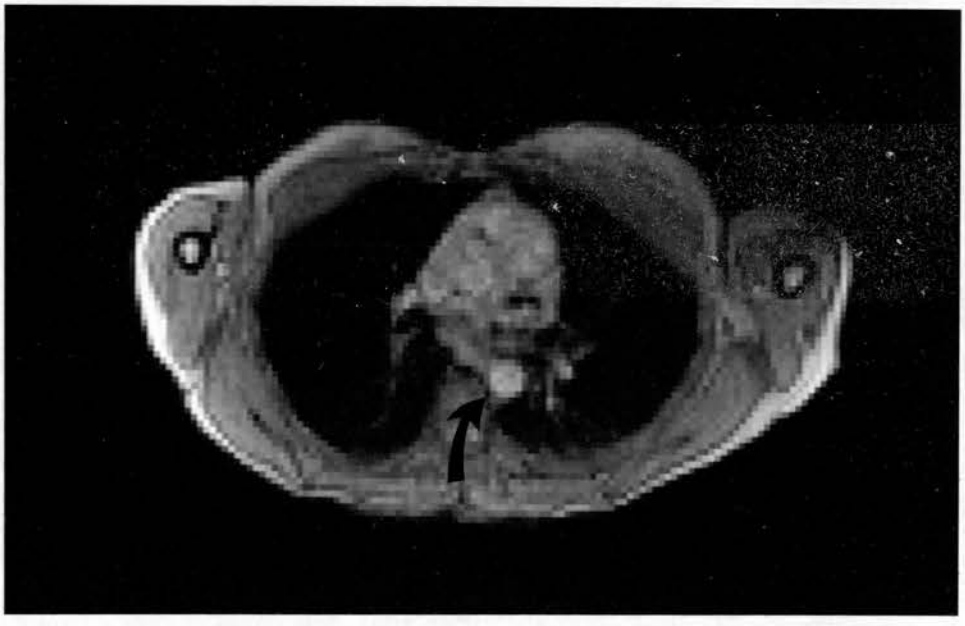

Figure 2.1.

Field echo image in the transverse plane through the thorax, showing flow related enhancement in the ascending aorta (arrow).

As a 90^{o} rf pulse is applied to a volume of protons, an NMR signal is produced resulting from their transverse magnetisation. Immediately following the 90^{o} pulse, the proton population is saturated and any further application of a 90^{o} pulse fails to produce a signal, unless some time is allowed for longitudinal relaxation to take place. Even as the protons undergo longitudinal relaxation, they are still unable to return their maximum possible signal following any subsequent 90^{o} pulse, unless they have had sufficient time to fully return to their equlibrium position. The shorter the repetition time of the 90^{o} pulses, therefore, the more saturated the proton population becomes, resulting in a reduced signal magnitude. Proton populations in the intermediate state between saturation and equilibrium are said to be partially saturated.

Partial saturation only occurs for protons within the excited region, since those outside are unaffected by the selective excitation process. If there is substantial flow of unsaturated protons into the excited region, they will be able to yield a comparatively greater signal, causing an apparent increase in signal within the vessel relative to that of the stationary lumen.

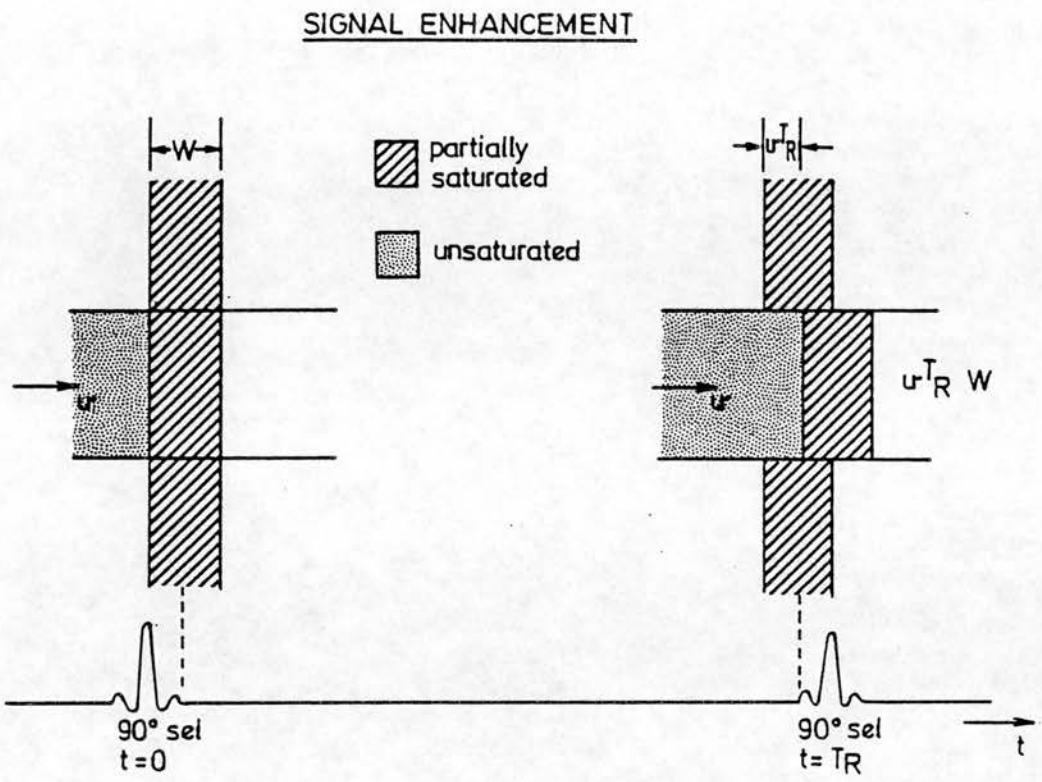

Figure 2.2.

Flow related signal enhancement caused by 'wash in' of unsaturated protons with constant velocity, v, into a slice of width, W, during the time interval, TR, between successive 90° excitation pulses.

For a steady flow velocity v, slice width W, and repetition time TR, (figure 2.2) the ratio of signal from within the vessel to that from outside can be derived. It is assumed that the proton density and T1 relaxation time is the same for material both inside and outside of the vessel, and that the flow profile is uniform across the vessel.

Neglecting the effect of T2 on the signal, the signal magnitude from partially saturated protons has a dependence on T1 given by (from section A1.8.1)

$$S_{ps} \propto M_o[1-\exp(-TR/T1)] \qquad (2.1)$$

and so the ratio of the signal from partially saturated protons, S_{ps}, to that from unsaturated protons, S_{us}, is

$$S_{ps}/S_{us} = [1-\exp(-TR/T1)] \qquad (2.2)$$

Referring to figure 2.2 we see that for the case vTR < W the signal magnitude will have two partial volume contributions; one from protons partially saturated from a previous excitation, and one from unsaturated protons entering the selected region. Hence the ratio of the observed signal intensity within the vessel, I_v, to that outside, I_o, is given by

$$I_v/I_o = \frac{(W-vTR)S_{ps} + vTRS_{us}}{WS_{ps}}$$

Using equation 2.2 this becomes,

$$I_v/I_o = \frac{p(W-vTR)[1-\exp(-TR/T1)] + pvTR}{pW[1-\exp(-TR/T1)]}$$

$$= 1 + \frac{vTR}{W}\left[\frac{1}{1-\exp(-TR/T1)} - 1\right]$$

$$= 1 + \frac{vTR}{W}\left[\frac{1}{\exp(TR/T1) - 1}\right] \qquad (2.3)$$

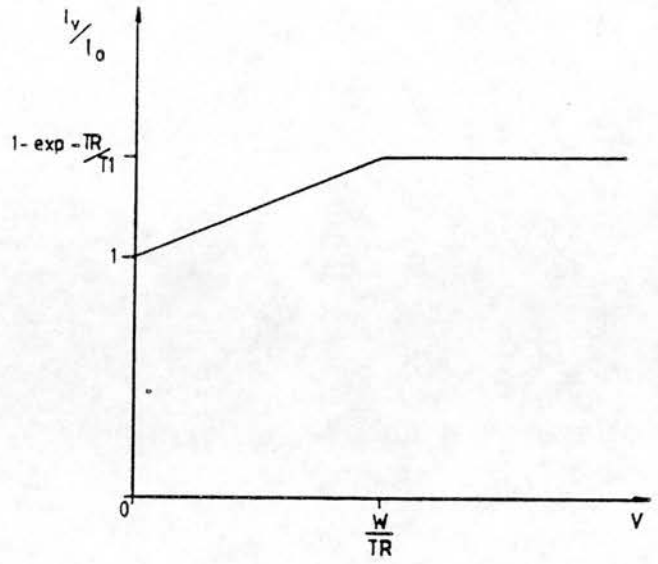

Figure 2.3

Flow related signal enhancement: Velocity dependence of the ratio of the signal intensity from flowing protons within the vessel, I_v, to that from the stationary lumen, I_o. (see equations 2.3 and 2.4).

The velocity dependence of equation 2.3 is shown in figure 2.3. For a slice thickness of 10mm, and a TR of 500ms, the signal in the vessel will be seen to increase with velocity over the range 0-2 cm/s. For flow velocities faster than this, (i.e. for the case vTR > W), the signal ceases to increase and the ratio of equation 2.3 becomes

$$I_v/I_o = \frac{1}{1 - \exp(-TR/T1)} \qquad (2.4)$$

In practice, the signal intensity observed is somewhat lower than predicted by equations 2.3 and 2.4, due to the

presence of laminar (parabolic) flow and turbulence (Axel, 1984; Bradley et al, 1984; George et al, 1985). For laminar flow the signal intensity will be related to the velocity profile across the vessel at lower velocities. In the case of turbulence, the signal intensity pattern is more complex. These effects can be largely attributed to a phenomenon known as 'Phase Dispersion' which is discussed in section 2.2.

In the case of simultaneous multiple slice imaging (see section A2.6.7), the result of equation 2.3 is only applicable for the slice which is located 'upstream' of the other slices. The flow-related signal enhancement on the downstream slices is reduced, as the blood entering these slices is pre-saturated by the upstream slices.

For very fast flow, there may be some loss of signal if velocity is great enough for the excited spins to move out of range of the receiver coil, before the signal is detected. Similarly, there would be signal loss if the velocity of flow was great enough for protons from outside the main magnetic field to arrive at the imaged region, before they had become fully magnetised. This is only likely to be a problem when using small bore magnets such as those used for spectroscopy and the imaging of limbs.

2.1.2. The Time of Flight Effect in Spin Echo Sequences

The second time-of-flight effect occurs when both the 90° and the 180° RF pulses are applied with a slice selection gradient in a spin echo pulse sequence (See sections A1.8.3, A2.2.1 and A2.5.3). Whilst the signal intensity within the vessel is enhanced at low velocities by the same mechanism as described in Section 2.1.1, at higher velocities signal void is usually observed within the vessel (figure 2.4).

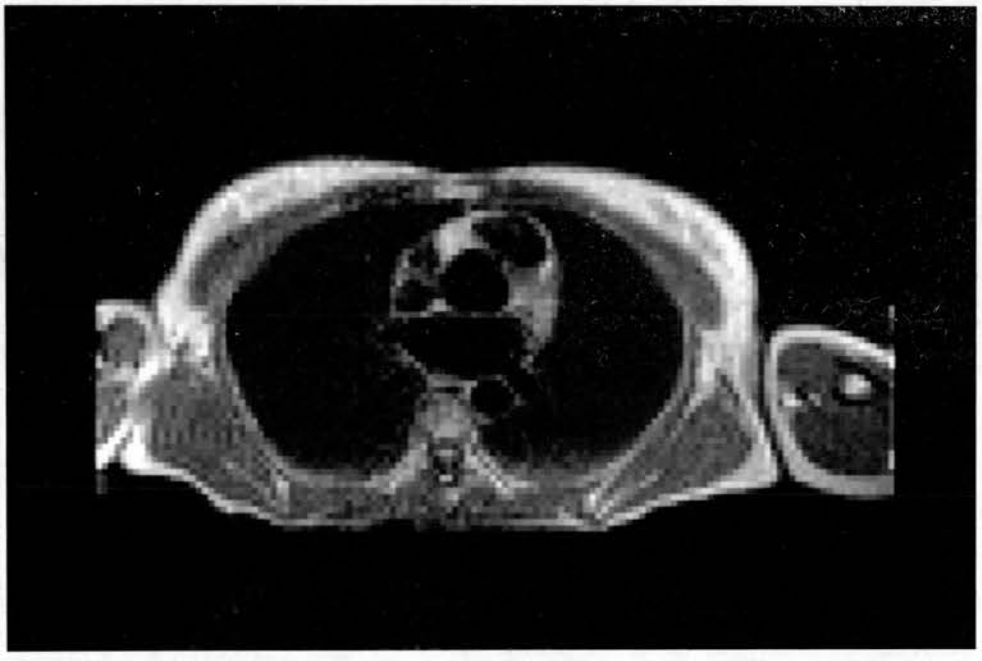

Figure 2.4.

Spin echo image in the transverse plane through the upper thorax, showing signal void within the major vessels due to the spin washout effect.

The major cause of this signal void is the washout of excited protons from the imaging slice which occurs during the period between the 90^{o} and 180^{o} pulses (figure 2.5). This time of flight phenomenon is therefore often referred to as Spin Washout. This signal void accounts for the natural contrast observed between blood and heart and vessel walls in spin echo imaging of the cardiovascular system (Herfkens et al, 1983).

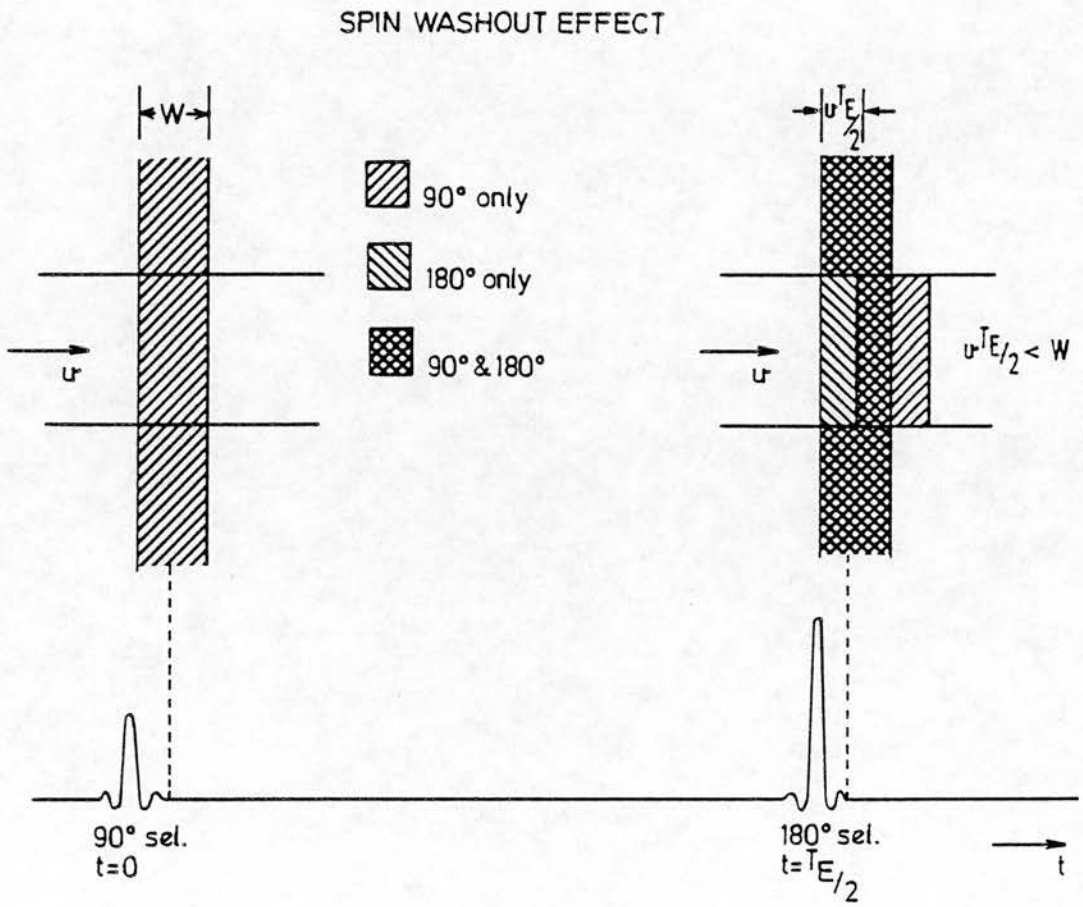

Figure 2.5.

Signal loss occurs when excited protons moving with velocity v 'wash out' of the image slice during the period TE/2 before the 180^{o} refocussing pulse is applied.

An expression can be derived to describe the ratio of the signal intensity within the vessel, to that from the stationary lumen, using figure 2.5. Initially, the effect of signal enhancement shall be neglected, although it is still applicable here for low velocities where vTE << W.

In a spin echo sequence, the NMR signal is only obtained from protons which experience both the selective 90^{o} pulse and the selective 180^{o} pulse. In the case of a uniform flow profile, by referring to figure 2.5 it can be seen that the volume of protons contributing to the signal within the vessel is decreased, because a percentage of protons excited by the 90^{o} pulse have moved out of the slice before the 180^{o} pulse is applied. The ratio of signal intensity from flowing protons, I_v, to that from stationary protons, I_o, is therefore given by

$$I_v/I_o = \frac{W - vTE/2}{W} \qquad \text{for } vTE/2 < W \qquad (2.5)$$

As the velocity increases therefore, the signal within the vessel decreases (figure 2.6). When the expression vTE/2 is greater than or equal to zero, the bolus of blood excited by the 90^{o} pulse leaves the selected slice completely, and does not experience the selective 180^{o} refocussing pulse. A complete signal void is therefore observed at these higher velocities.

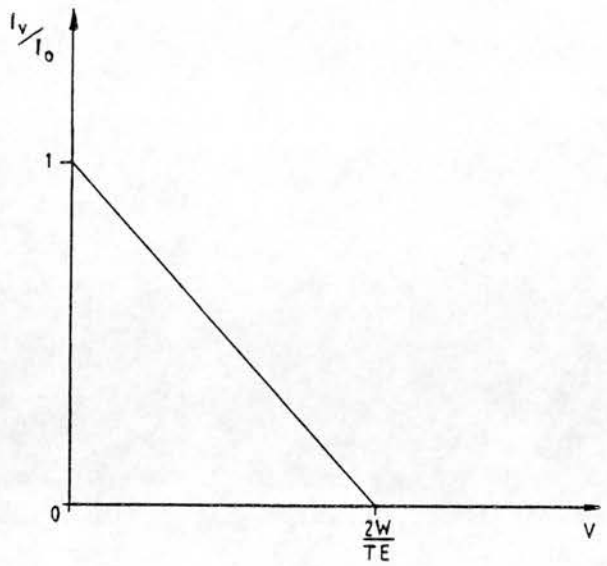

Figure 2.6

The spin washout effect: Velocity dependence of the ratio of the signal intensity from flowing protons within the vessel, I_v, to that from the stationary lumen, I_o, neglecting flow related enhancement effects. (see equation 2.5).

At low velocities, signal enhancement is also observed and it is necessary to include an additional expression to account for this. The signal magnitude for a spin echo sequence is given by

$$S_{se} \propto M_o \exp(-TE/T2)[1-\exp(-TR/T1)(2\exp(TE/2T1)-1)] \quad (2.6)$$

Including the signal enhancement effect for velocities such that vTR<W, (vTE/2 << vTR) the ratio I_v/I_o becomes

$$(W-vTE/2)\left\{1 + \frac{vTR}{W}\left[\frac{1}{1 - \exp(-TR/T1)[2\exp(TE/2T1)-1]} - 1\right]\right\} \quad (2.7)$$

Note that for TE << T1 the expression {...} of equation 2.7 reduces to equation 2.3. For the intermediate velocity range vTE/2 < W and vTR > W, the ratio becomes

$$\frac{(W-vTE/2)}{W[1 - \exp(-TR/T1)(2\exp(TE/2T1) - 1)]} \qquad (2.8)$$

As shown previously for vTE/2 > W, the ratio = 0. The behaviour of expressions 2.7 and 2.8 with increasing velocity is shown in figure 2.7 for both a T1-weighted (short TR and short TE) and a T2-weighted (long TR and long TE) spin echo pulse sequence.

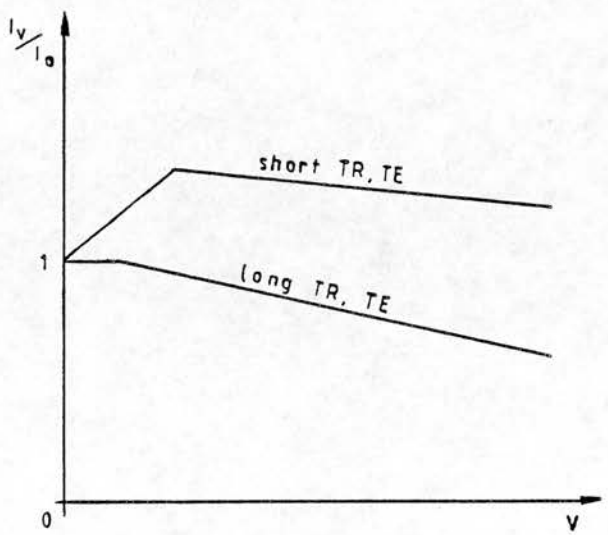

Figure 2.7

Velocity dependence of the ratio I_v/I_o for spin echo pulse sequences including both flow related enhancement and spin washout effects (see equations 2.7 and 2.8).

For the T1 weighted sequence, there is paradoxical enhancement at lower velocities, but the signal decreases to zero at higher velocities. For the T2-weighted sequence there is little paradoxical enhancement even for very slow flow and the signal quickly decreases with increasing velocity.

Whilst this treatment is for plug flow only, it serves as a simple illustration of the spin washout effect. In the presence of parabolic flow and turbulance, the signal intensity profile depends on the velocity profile and involves the effect of phase dispersion which is discussed in section 2.2. A full discussion of the observed effects for rapid flow can be found in Bradley et al (1984), where the effects observed in multiple slice imaging are also discussed.

Spin echoes are sometimes applied using non-selective 180° pulses (i.e. 180° pulses applied without a slice selection gradient (Axel, 1984)). In this case protons which leave the slice during the period TE/2 following the 90° pulse are still refocussed by the 180° pulse and so there is no spin washout effect. However, the protons which enter the slice between repetitions are no longer unsaturated, having experienced complete inversion by the 180° pulse. The signal from these protons is therefore reduced and flow related enhancement is not observed. In practice, spin echo pulse sequences using a non-selective

180^{o} pulse are rarely used because of the requirements of simultaneous multiple slice imaging.

2.1.3. Flow Measurement Using The Time of Flight Effect

All of the previously mentioned effects in this chapter are a result of motion of protons into or out of the selected imaging slice. These time of flight effects have been evaluated in the case of pulsatile flow (George et al, 1984), making it possible to interpret signal intensity patterns, found when imaging the cardiovascular system in-vivo (George et al, 1984; Herfkens et al, 1983). It was suggested by Singer as early as 1959 (Singer, 1959; Singer, 1981) that flow velocity could be quantified by measuring the time of flight of excited protons between two points along their path (See section 1.3.1). Since then, the time of flight technique has been developed and adapted for use with imaging techniques.

Singer and Crooks proposed a technique in which the signal from protons in stationary tissue was removed by pre-saturating the image slice with a selective 90^{o} pulse and then depolarising the resultant transverse magnetisation with a magnetic gradient pulse (Singer and Crooks, 1983). A selective 90^{o} excitation pulse was subsequently applied at a time, t, after the first pulse and a spin echo was formed using a selective 180^{o} pulse

(see section A2.2.1). The signal observed on the resultant images was largely due to unsaturated protons within the blood which entered the image slice during the period t. The signal intensity within the vessel was proportional to the volume of blood entering the slice.

Quantitative measurement of flow velocity was achieved by repeating the measurement for a number of different values of t. The signal intensity within the vessels for each image was dependent on the volume of unsaturated blood entering the slice, incresing as t is increased. At some value of t the signal intensity reaches a limiting value. This value of t is taken as the time taken to completely replace saturated blood with unsaturated blood and can be used to calculate the flow velocity and flow rate provided that the slice thickness and cross sectional area of the vessel are known. The overall accuracy of flow measurement by this technique was found to be around 10%.

A more detailed treatment of this technique can be found in Wehrli et al, (1985). They use the same pulse sequence which they call the Selective Saturation Recovery Spin Echo sequence (SSRSE), but whereas Singer and Crooks measured only venous flow, Wehrli et al synchronised the pulse sequence with the cardiac cycle to measure diastolic arterial flow. The expected signal intensity was derived theoretically, allowing for both signal

enhancement at low velocities and spin washout at higher velocities.

In practice, the authors found greater reduction in signal within the vessel than their theoretical model had predicted, particularly at high velocities and long TE values. This additional loss of signal can largely be attributed to phase dispersion which is caused by the slice-selection gradient in the presence of parabolic flow (see section 2.2).

Wehrli and his co-workers also derived the signal intensity relationship for a similar pulse sequence called the Non-Selective Saturation Recovery Spin Echo sequence (NSSRSE), in which the pre-saturation pulse was non-selective. In this case there is no enhancement of signal from flowing blood, whereas the signal from stationary protons is the same as for the SSRSE sequence. Visualisation of the vessels could be further improved by subtracting the SSRSE and NSSRSE image data, and thus completely removing signal from stationary tissue.

Both Singer and Crooks and Wehrli et al found that the acquisition of number of images with different recovery times was necessary to obtain reasonable accuracy, requiring a relatively long imaging time. In addition, the technique is only appropriate for relatively steady flow, although when combined with

cardiac gating the technique was able to measure diastolic flow rates in arteries. The technique becomes inaccurate for fast laminar flow, when the effects of spin washout and phase dispersion become significant.

The time of flight effect has also been exploited by Feinberg et al (1984), using a double spin echo pulse sequence to measure flow perpendicular to the image slice. Both the selective 180° refocussing pulses are applied at positions displaced downstream from the position of the selective 90° excitation pulse. The selected region of the first 180° pulse overlaps that of the excitation pulse so that some of the signal from stationary tissue is retained to provide anatomical information. The second 180° pulse is applied at a position further downstream. The signal intensity within the vessel for both the first and second echo images is dependent on the velocity distribution within the vessel, and upon the slice thickness. The signal from flowing blood at the second echo is much less susceptible to signal loss from phase dispersion because of the even echo rephasing effect (see section 2.2). The sensitivity of this technique to the mean velocity and velocity range can be controlled by altering the slice thickness and the echo time, TE. This technique was able to image both venous flow and diastolic arterial flow by synchronising the pulse sequence with the cardiac cylce, but fast systolic flow could not be imaged.

2.2. Phase Modulation and the Gradient Pulse Sequence

Time of flight effects are observed when slice-selective radiofrequency pulses are used. These radiofrequency pulses are applied in combination with magnetic field gradients to selectively excite protons within a desired plane. The magnetic field gradients have an additional effect on the signal magnitude in the presence of flow, by modulating the phase of the protons. The contributions from individual protons to the NMR signal interfere with one another, causing a reduction in signal magnitude (Axel, 1984; George et al, 1984). Phase modulation is normally observed as a dispersive effect, causing a reduction in signal magnitude. However, it can also be exploited to recover this lost signal and to provide a technique for the measurement of flow dynamics. In the following sections both the mechanism and the effects of this phase modulation are described.

2.2.1. Dependence of Phase on Magnetic Field Gradients

The magnetic field gradients cause a linear change in field strength in the direction in which they are applied (Section A2.1). For the purposes of imaging, magnetic field gradients are applied in a pulsed form for relatively short periods. (Typically, gradient pulses are just a few milliseconds in duration).

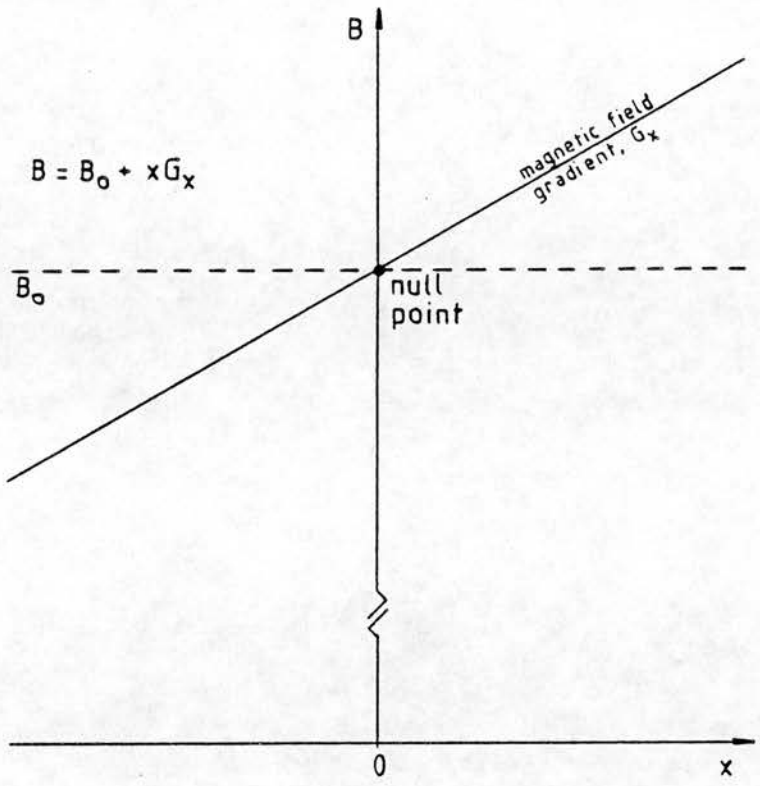

Figure 2.8.

Diagram showing a magnetic field gradient of magnitude, G_x, superimposed on a uniform magnetic field, B_o.

The angular frequency of precession of a proton (the Larmor frequency), ω_L, is dependent on the local magnetic strength that it experiences, B_o, such that

$$\omega_L = \gamma B_o \qquad 2.9$$

Consequently, when a gradient G_x is applied, the Larmor frequency of the protons, $\omega_L(x)$, depends on their spatial position along the gradient, and is given by

$$\omega_L(x) = \gamma(B_o + xG_x) \qquad 2.10$$

where x is the distance along the gradient from its null point (figure 2.8) and B_o is the field strength of the uniform magnetic field when no gradient is present. In the rotating frame of reference, with an angular frequency of $\omega_o = \gamma B_o$, the frequency of protons at the null point of the gradient will be zero, and the frequency $\omega(x)'$ of protons at position x relative to those at the origin is given by

$$\omega(x)' = \gamma x G_x \qquad 2.11$$

Since the frequency of protons varies with position along the magnetic field gradient, those at different positions will have a time-varying phase relative to one another. In the rotating frame, protons at the null point of the magnetic field gradient have zero phase. If it is assumed that, prior to the application of the magnetic field gradient, all the protons are in phase and precessing coherently, then the phase, ϕ, of the protons at position x can be predicted by integrating equation 2.11 (since $\omega = d\phi/dt$) over the period of time for which the gradient pulse is applied (Axel, 1984), as follows

$$\phi = \gamma \int x G_x \, dt \qquad 2.12a$$

Equation 2.12a can be generalised for a time-varying gradient waveform, $G_x(t)$,

$$\phi = \gamma \int x G_x(t) \, dt \qquad 2.12b$$

2.2.2. The Rephasing Condition

When forming signal echoes, the signal magnitude should reach its maximum possible value at the centre of the echo. For this to be so, all the protons have to be instantaneously moving in phase with one another (Hutchison et al, 1978). This imposes a constraint on the gradient pulse sequence, such that, for all the gradient pulses applied during the evolutionary period (figure 2.9) between the centre of the excitation pulse (t=0), and the centre of the signal echo (t=T), the sum of the phase shifts for stationary protons must be equal to zero, independent of their position along the gradient.

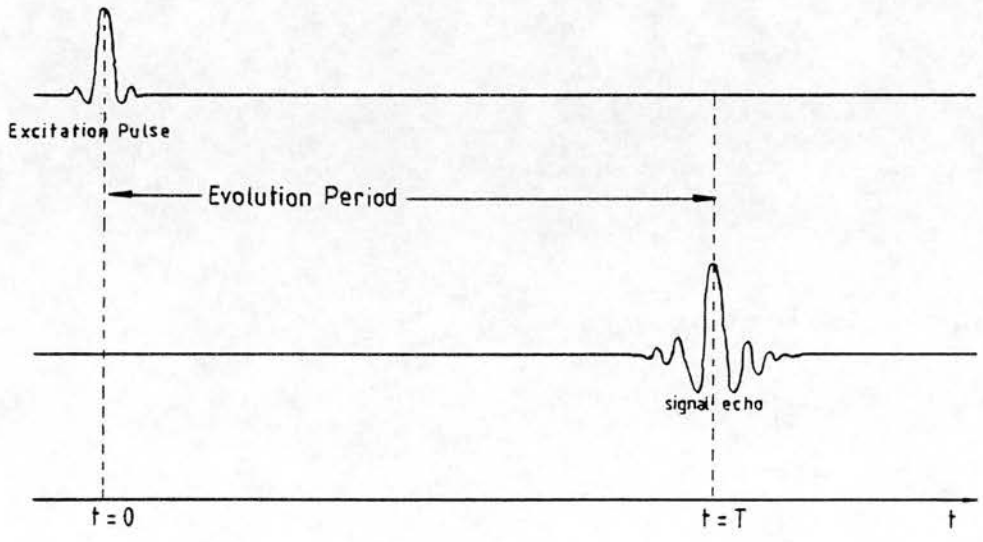

Figure 2.9.

The period between the centre of the excitation pulse (t=0), and the centre of the signal echo (t=T) is known as the evolutionary period.

This constraint, known as the rephasing condition, requires the integral of equation 2.12b to be zero for all values of x, over the period t=0 to t=T, i.e.,

$$0 = \gamma \int x G_x(t)\, dt \qquad 2.13$$

Equation 2.13 can be generalised to the three dimensional case. If the origin of the coordinate system is assumed to be coincident with the null points of the three orthogonal gradient directions, equation 2.13 can be written

$$0 = \gamma \int \underline{x}.\underline{G}(t)\, dt \qquad 2.14$$

where x is the position vector and G(t) is the time dependent gradient vector. Since the three gradient directions are mutually orthogonal, this integral can be split into three linearly independent expressions, each of which is equal to zero:

$$0 = \gamma \int x G_x(t)\, dt \qquad 2.15a$$

$$0 = \gamma \int y G_y(t)\, dt \qquad 2.15b$$

$$0 = \gamma \int z G_z(t)\, dt \qquad 2.15c$$

In practice, it is not possible to achieve complete rephasing of protons over the whole of the image slice

because of the inhomogeniety of the main magnetic field, B_o. However, it is possible to use equations 2.15a-c to optimise the gradient pulse sequences in order to obtain the maximum possible signal magnitude. For both slice selection and frequency encoding, two gradient pulses are applied; a rephasing pulse follows the slice selection gradient pulse (section A2.1.3), and a dephasing pulse precedes the frequency encoding gradient pulse (see sections A2.2.1 and A2.2.2). In order for the rephasing condition to hold, the time integrals of the two pulses must be equal in magnitude but opposite in sign. For two rectangular pulses of durations t_a and t_b and magnitudes G_a and G_b (figure 2.10) the rephasing condition of equations 2.15 gives

$$0 = \gamma \int x G_x(t)\, dt$$

$$= \gamma [G_a t_a + G_b t_b] \qquad 2.16$$

Thus the two shaded areas shown on figure 2.10 should be equal. The two gradient pulses, G_a and G_b, combine to form a composite gradient pulse waveform known as a Bipolar Gradient Pulse (Moran and Moran, 1984; Wedeen et al, 1987).

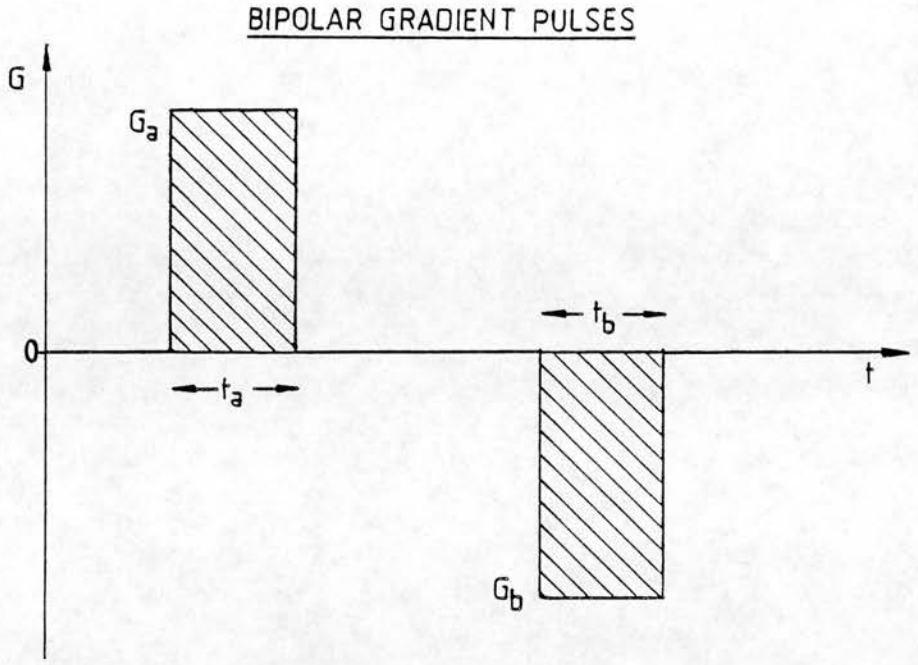

Figure 2.10.

Bipolar gradient pulses, such as those found in slice selection or frequency encoding gradient waveforms. The rephasing condition of equation 2.13 requires the shaded areas to be equal.

2.2.3. The Effect of a 180° Refocussing Pulse

In spin echo pulse sequences a 180° rf pulse is applied following the excitation pulse in order to produce a signal echo. This pulse is known as a refocussing pulse and it has the effect of bringing protons which have moved out of phase with one another back into phase, provided that the magnetic field distribution stays the same. (see section A1.8.3).

MONOPOLAR GRADIENT PULSES

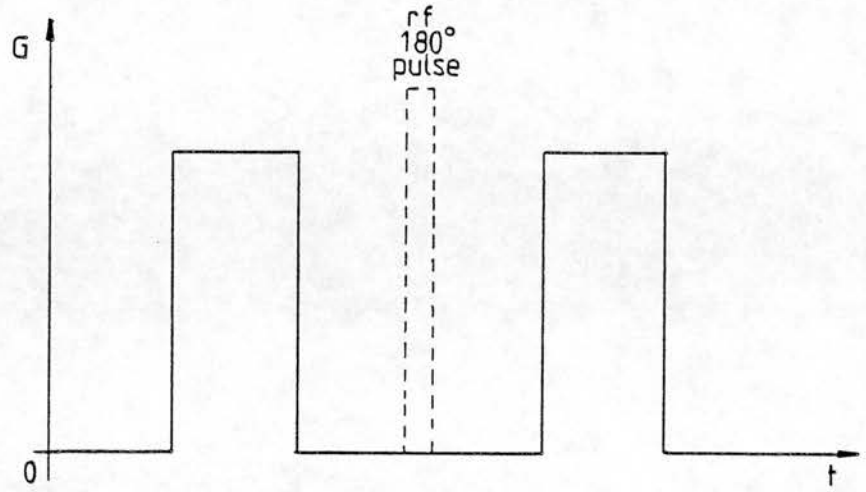

Figure 2.11.

Monopolar gradient pulses: Two gradient pulses of the same magnitude, sign and direction, applied on either side of a 180° refocussing rf pulse.

The effect of the 180° refocussing rf pulse is to change the sign of the phase shift gained up to that time. As a consequence, if a gradient pulse of the same magnitude and sign is applied before and after a 180° refocussing pulse (figure 2.11), the net phase shift imposed by these monopolar gradient pulses is zero. In a perfectly uniform magnetic field, the effect on the phase of excited protons of two such monopolar gradient pulses is equivalent to that of a bipolar pair of gradient pulses, provided that they occur on opposite sides of a 180° rf pulse (figure 2.12).

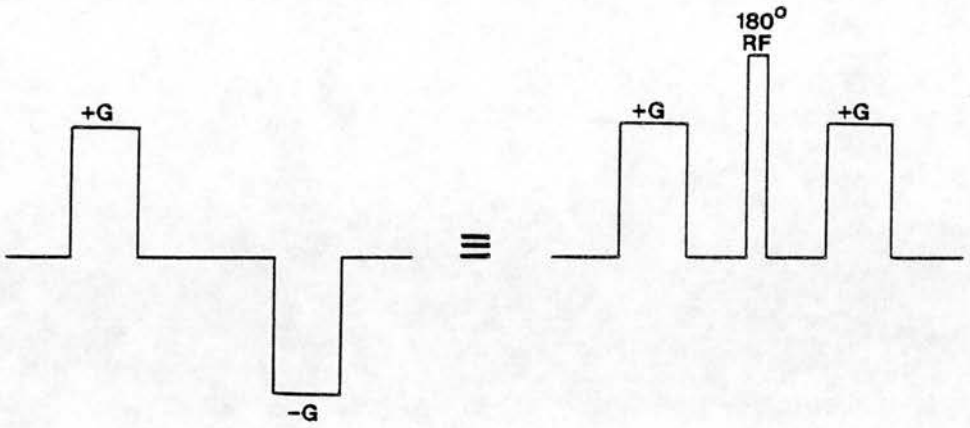

Figure 2.12.

In a perfectly uniform magnetic field, the phase shift imposed by two monopolar gradient pulses is equivalent to that imposed by a bipolar pulse pair.

2.2.4. Standard Gradient Pulse Sequences

Two of the most common pulse sequences used in clinical imaging are the field echo and spin echo pulse sequences. Whilst the exact form of the gradient pulse waveforms used used with these pulse sequences varies between different manufacturers, two examples are given to illustrate the way in which standard pulse sequences are intrinsically sensitive to flow and motion.

The Field Echo pulse sequence (sometimes known as a gradient echo sequence), is shown in figure 2.13 and is described in section A2.5.5. The slice selection gradient pulse is followed by a second gradient of opposite sign

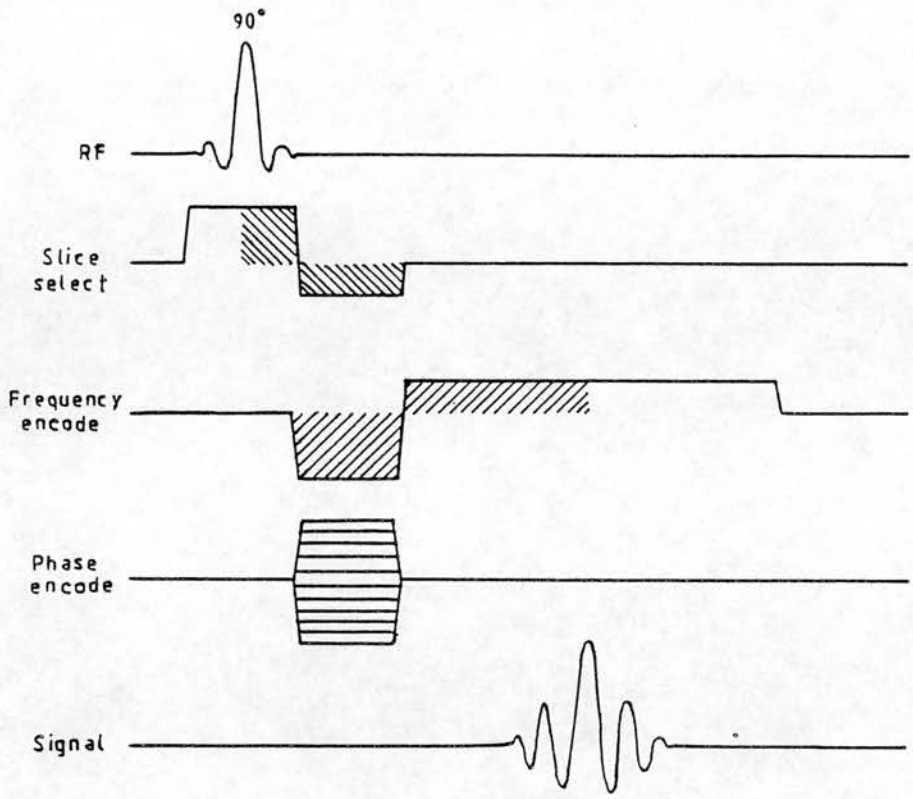

Figure 2.13.

The field echo pulse sequence. The rephasing condition requires the two shaded areas on the slice-selection gradient waveform to be equal, and the two shaded areas on the frequency-encoding gradient waveform to be equal.

in order to satisfy the rephasing condition (section A2.1.3). The magnitude of the slice-selection gradient pulse is dictated by the bandwidth of the RF pulse which is normally fixed, and by the slice thickness required (sections A2.6.4. and A2.1.1). The rephasing condition requires the two shaded areas of the slice-selection gradient waveform to be equal (figure 2.13).

The frequency-encoding gradient is preceded by a dephasing pulse so that rephasing occurs at the centre of the data collection period. The magnitude of the readout pulse is dictated by the imaging bandwidth (section A2.6.3), which is normally fixed, and the field of view (section A2.6.2). The rephasing condition requires the two shaded areas shown on the frequency-encoding gradient waveform to be equal (figure 2.13).

The Spin Echo sequence (section A2.5.3) has slice-selection and frequency-encoding gradient waveforms which can be of either monopolar or biplor form. The form of these gradient pulse waveforms depends on where the gradient pulses occur relative to the 180^{o} refocussing rf pulse. Figure 2.14 shows a spin echo sequence in which the slice-selection gradient waveform is of a bipolar form, and the frequency-encoding gradient waveform is of a monopolar form.

As with the field echo sequence, the shaded areas of the two gradient pulses should be equal for each of the gradient waveforms in order to satisfy the rephasing condition (figure 2.14). The 180^{o} pulse may also have a slice-selection gradient pulse applied at the same time (shown by the dotted line). If this gradient pulse is symmetrical about the centre of the 180^{o} pulse, the rephasing condition is satisfied.

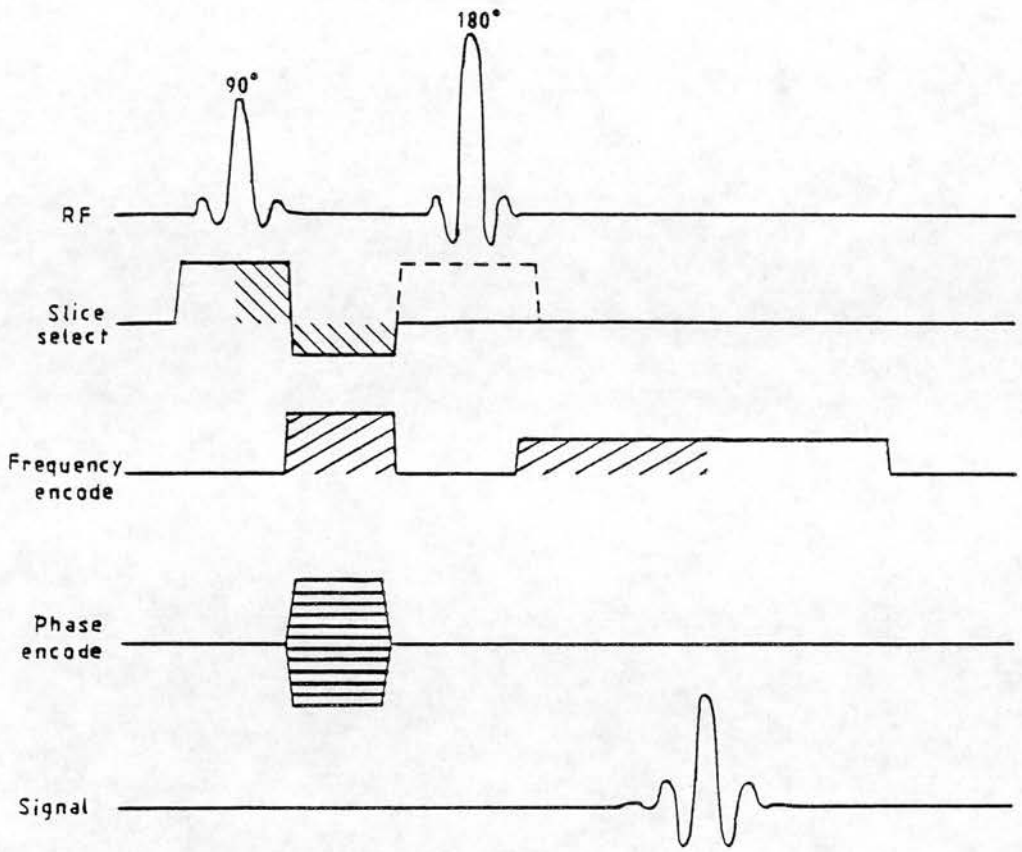

Figure 2.14.

Spin echo pulse sequence. The rephasing condition requires the two shaded areas on the bipolar slice-selection gradient waveform to be equal, and the two shaded areas on the monopolar frequency-encoding gradient waveform to be equal.

2.2.5. Magnetic Field Gradients in the Presence of Motion

If protons are not stationary but are moving along the direction of a magnetic field gradient during the evolution period of the pulse sequence, the integral of

equation 2.12b still describes the proton phase shift, but the position, x, along the gradient direction becomes time dependent and is subject to the integration with respect to time:

$$\phi = \gamma \int x(t) G_x(t)\, dt \qquad 2.17$$

As before, this integral must be zero over the signal evolution period for all values of x in order to satisfy the rephasing condition and maximise the signal from moving protons. The term x(t) can be substituted by an expression including velocity, acceleration, and higher-order terms of linear motion. The presence of motion introduces an additional phase modulation of the signal from moving protons.

2.2.6. Constant Velocity with a Bipolar Gradient Pulse

This motion related phase modulation shall first be considered for the simplest case of constant velocity (1st order) motion, in the presence of a bipolar gradient pulse pair of magnitude, G, pulse width t_w, and pulse separation T (figure 2.15). The integral of equation 2.17 which describes the phase shift can be split into two separate integrals, corresponding to the two periods when the bipolar gradient is non-zero.

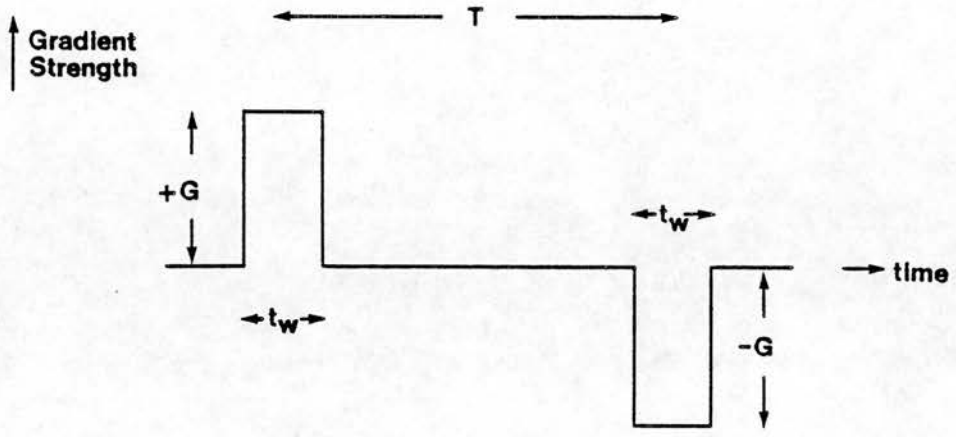

Figure 2.15.

Bipolar gradient pulse pair of magnitude G, pulse width t_w and pulse separation T.

As the shape of the gradient pulses is rectangular, the phase shift ϕ can be calculated as follows:

$$\phi = \gamma\int x(t)G_x(t)\,dt = \gamma\int_0^{t_w} x(t)G\,dt - \gamma\int_{t_w+T}^{2t_w+T} x(t)G\,dt \qquad 2.18$$

For a constant velocity $x(t) = x(0) + vt$, and the integral is evaluated thus:

$$\phi = \gamma G x t_w + \tfrac{1}{2}\gamma G v t_w^2 - \gamma G x t_w - \tfrac{1}{2}\gamma G v[2Tt_w + t_w^2]$$

$$= -\gamma G v T t_w \qquad 2.19$$

The result of equation 2.19 shows that the phase shift is proportional to the magnitude, G, and width, t_w, of the two gradient pulses, their separation in time, T, and the velocity of the moving protons, v. The phase shift for stationary protons will be zero.

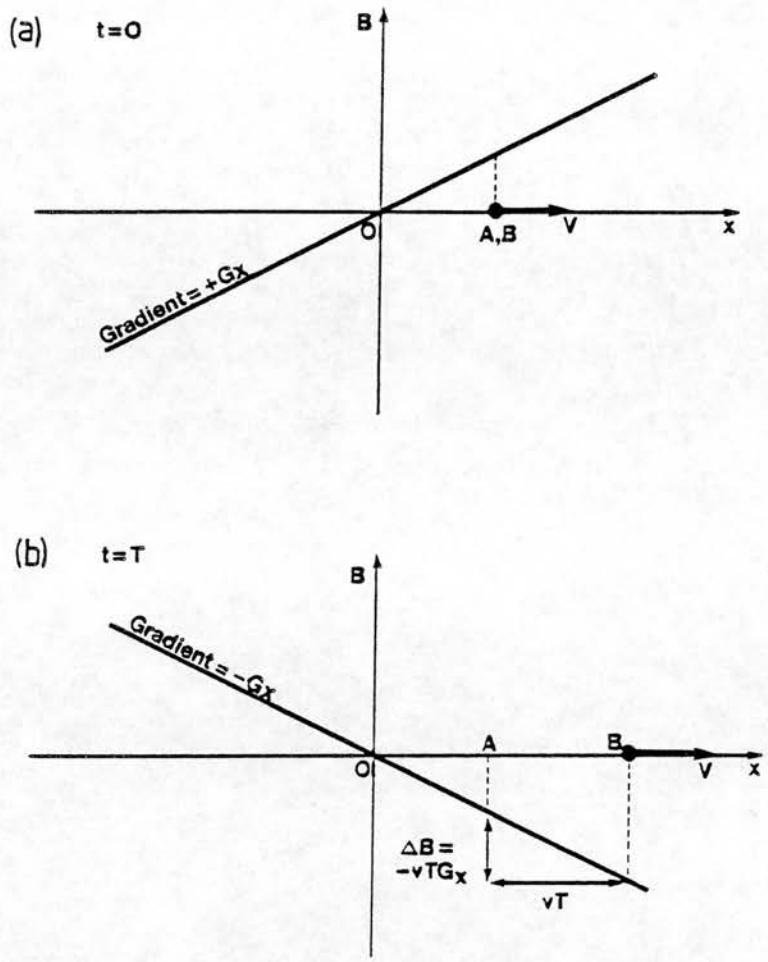

Figure 2.16.

Diagram showing magnetic field gradient applied along the x direction, with (a) magnitude $+G_x$ at time t=0, and (b) magnitude $-G_x$ at time t=T. O and A denote stationary protons, whilst B denotes protons moving with velocity, v.

This result can be illustrated further by considering figure 2.16. Figure 2.16a shows a gradient $+G_x$ applied at a time t=0. O, A, and B denote protons with O positioned at the null point of the gradient and A and B at some distance from the null point. A is stationary and B is

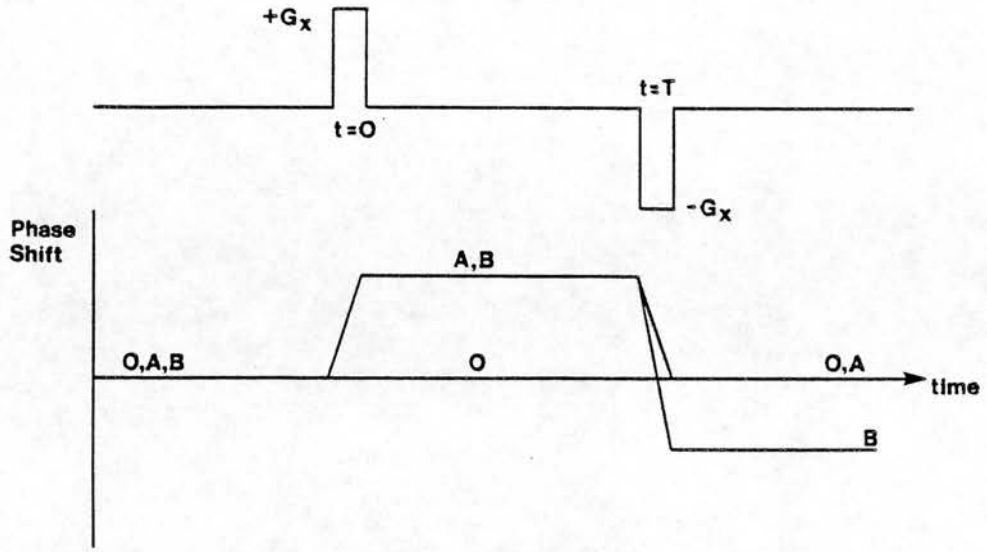

Figure 2.17.

Diagram showing the gradient magnitude and the phase of protons A and B, relative to those at the null point, O, as a function of time.

moving along the direction of the gradient at a constant velocity v. Figure 2.17 shows both the gradient magnitude and the phase shift, relative to that of protons at O, as a function of time.

When the first gradient is applied, the phase of O is unaffected, whilst both A and B gain similar phase shifts relative to O. Following the first gradient pulse, these phase shifts remain constant until the second gradient pulse of magnitude $-G_x$ is applied at a time t=T (figure 2.16b). At this point A has remained in the same position so that its phase shift is cancelled by the second gradient pulse, whilst B has moved a distance given by

vT. B will therefore experience a different change in field strength due to the presence of the gradient than before. In this case the difference is $\Delta B=-vTG_x$, giving a residual phase shift of B relative to O of $\phi = -\gamma vTG_x t_w$. (cf equation 2.19).

2.2.7. Phase Dispersion

Motion related phase modulation can be measured and used to quantify velocity (Moran, 1982; Bryant et al, 1984; Van Dijk, 1984), however it can also lead to a loss of signal in the presence of fast laminar flow or turbulent flow (Axel, 1984; Bradley et al, 1984; George et al, 1984). This signal loss is due to a loss of coherence between protons within the same imaging voxel, and is known as phase dispersion. (Le Roux and Floch, 1985; Pattany and Naylor, 1985; Wedeen, 1987). The transverse magnetisation vectors of each of the protons within the voxel are summed to form the total magnetisation vector for that voxel (figure 2.18). Maximum signal magnitude is achieved if all the individual magnetisation vectors are in phase (figure 2.18a). If they are not all in phase, then the signal magnitude is reduced (figure 2.18b). If there is an even distribution of phase angles through 360^{o}, then the signal magnitude will be zero (figure 2.18c).

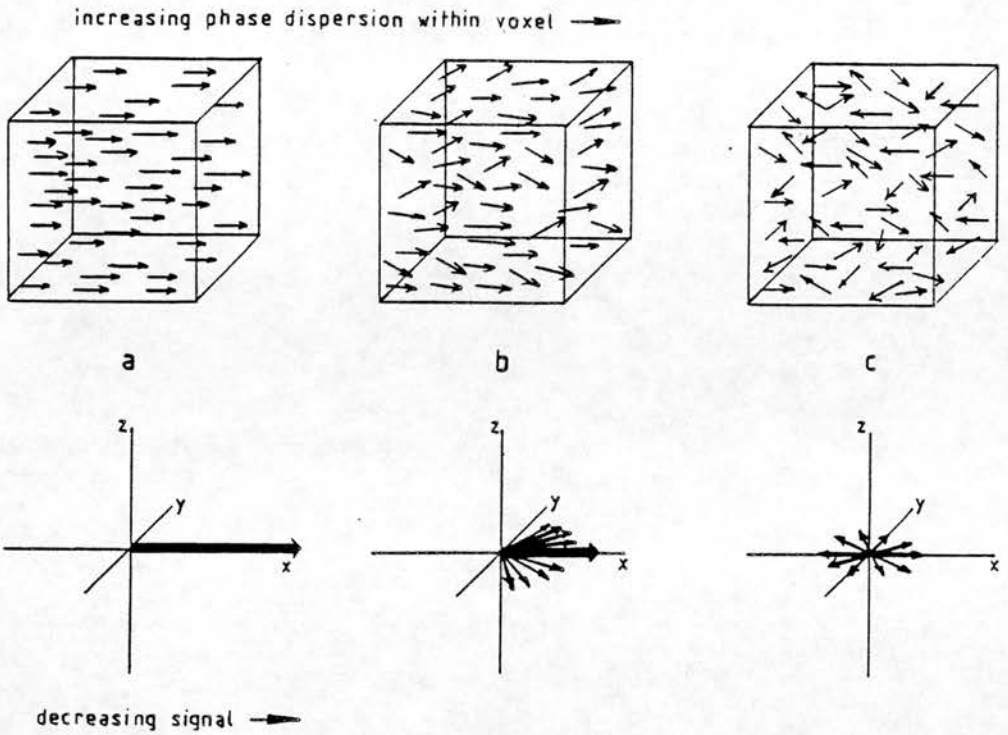

Figure 2.18.

Diagram showing the effect of increasing phase dispersion within a voxel on the signal from that voxel.

Since constant velocity motion, in the presence of a bipolar gradient pulse, generates a phase shift which is proportional to the velocity, (section 2.2.6), the presence of a range of velocities within a voxel results in a range of phase dispersion within that voxel, which reduces the signal magnitude. In practice, velocity-related phase dispersion is caused by both the readout and the slice-selection gradients of most pulse sequences.

In a physiological situation signal losses caused by phase dispersion are found wherever there are high

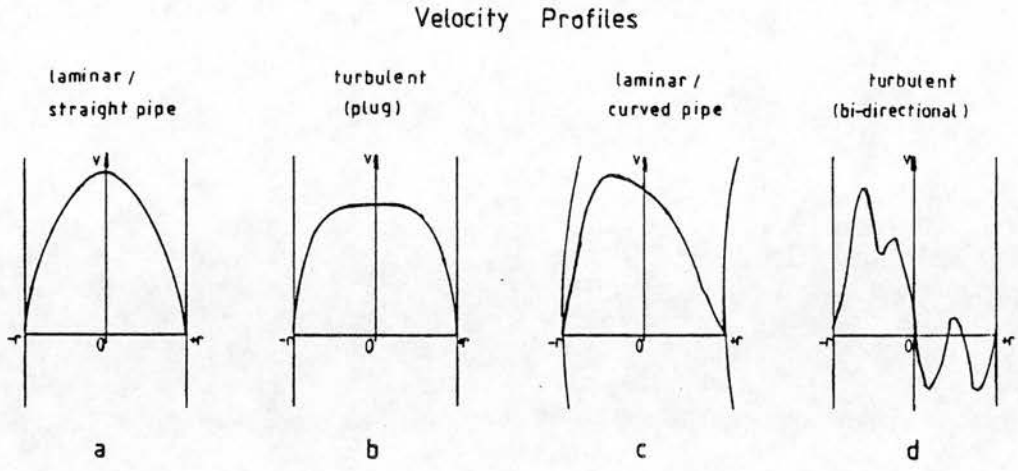

Figure 2.19.

Velocity profiles across a vessel diameter in the case of (a) laminar flow in a straight vessel, (b) turbulent (plug) flow, (c) laminar flow in a curved vessel, and (d) bi-directional turbulent flow.

velocity gradients or turbulence (Axel, 1984). The velocity gradient depends on the velocity profile across the vessel cross-section as shown in figure 2.19 (Bradley, 1984). In the case of laminar (parabolic) flow, the velocity gradient extends over much of the vessel but is greatest near the vessel wall (figure 2.19a). Even when the velocity ditribution is uniform, as in the case of plug flow (figure 2.19b), voxels at the edge of the vessel which contain both flowing blood and stationary tissue have a reduced signal magnitude. The precise nature of the velocity profile depends on the vessel geometry. For example, the maximum velocity in curved

vessels (figure 2.22c) will occur away from the centre of the vessel towards the outside wall of the curve (George et al, 1984). In the presence of turbulent flow (figure 2.22d), the velocity profiles are less predictable.

In the case of laminar or plug flow for vessels lying parallel to the plane of the image slice, phase dispersion can be observed in field echo images as dark lines adjacent to the vessel walls (Figure 2.20a). For vessels oriented perpendicular to the image slice, phase dispersion is often observed as a dark ring around the inside wall of the vessel (figure 2.20b). In the case of turbulence, phase dispersion can be observed as a complete signal void within the vessel or heart chamber (figures 2.20c and 2.20d). Phase dispersion has also been observed on images with voxels which contain the interface between two moving structures. This was observed on a spin echo image of the heart at the interface between the pericardial sac and the myocardium, as they moved in opposite directions (Moran and Moran, 1984).

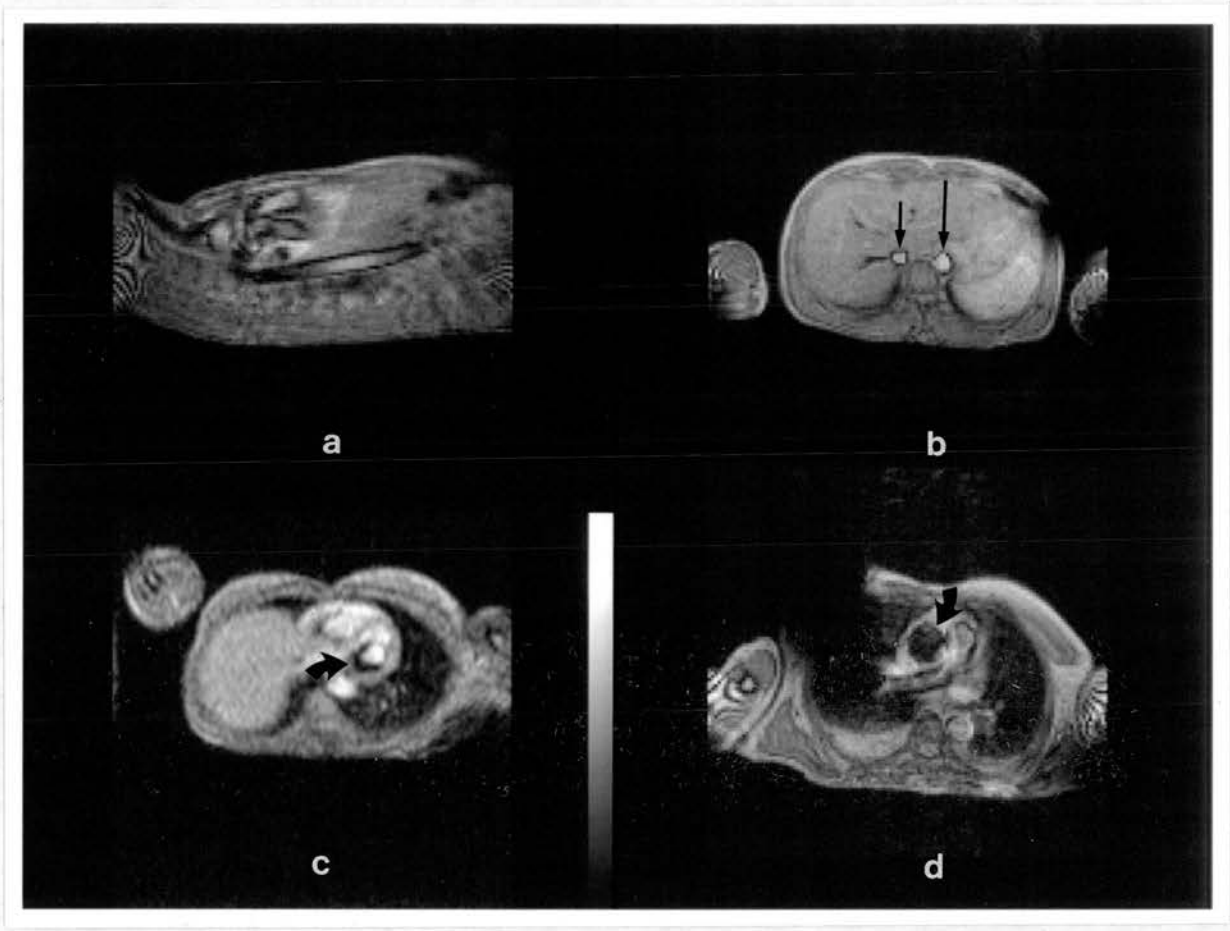

Figure 2.20.

Phase Dispersion in Field echo images (a) for in-plane flow observed as dark lines along the descending aorta and ventricular outflow tracts, (b) for through-plane flow observed as dark rings around the abdominal aorta (long arrow), and inferior vena cava (short arrow), (c) for turbulent flow observed as a signal void in the left ventricle (arrow) during early diastole, and (d) for turbulent flow observed as a signal void in the ascending aorta (arrow) as in a subject with aortic stenosis.

2.2.8. Even Echo Rephasing

Initially, phase dispersion was most commonly observed in the first-echo image generated by a multiple spin echo pulse sequence (A2.5.4). Whilst the spin washout effect accounts for much of the signal loss observed in this image in the case of arterial flow through the imaging slice, phase dispersion accounts for the signal losses observed in slow venous flow (Waluch and Bradley, 1984). Whilst the signal from slowly flowing blood is reduced in the first echo image, the image from the second echo exhibits an increased signal within the vessel relative to that of the first echo. Indeed, the signal observed on each even-numbered echo is increased relative to that observed on the preceding odd-numbered echo (figure 2.21). This effect is known as Even Echo Rephasing. (Axel, 1984; Bradley and Waluch, 1984; Waluch and Bradley, 1984.)

Even echo rephasing can be explained by considering what happens to the phase shifts of moving protons for each spin echo which is formed. Each time a 180° refocussing pulse is applied, the sign of any phase shift which has been acquired is reversed (section 2.2.3). Provided that the velocity of the protons is constant throughout the pulse sequence, and the same gradient pulses are applied to obtain each signal echo, the magnitude of the velocity-dependent phase modulation, corresponding to each echo,

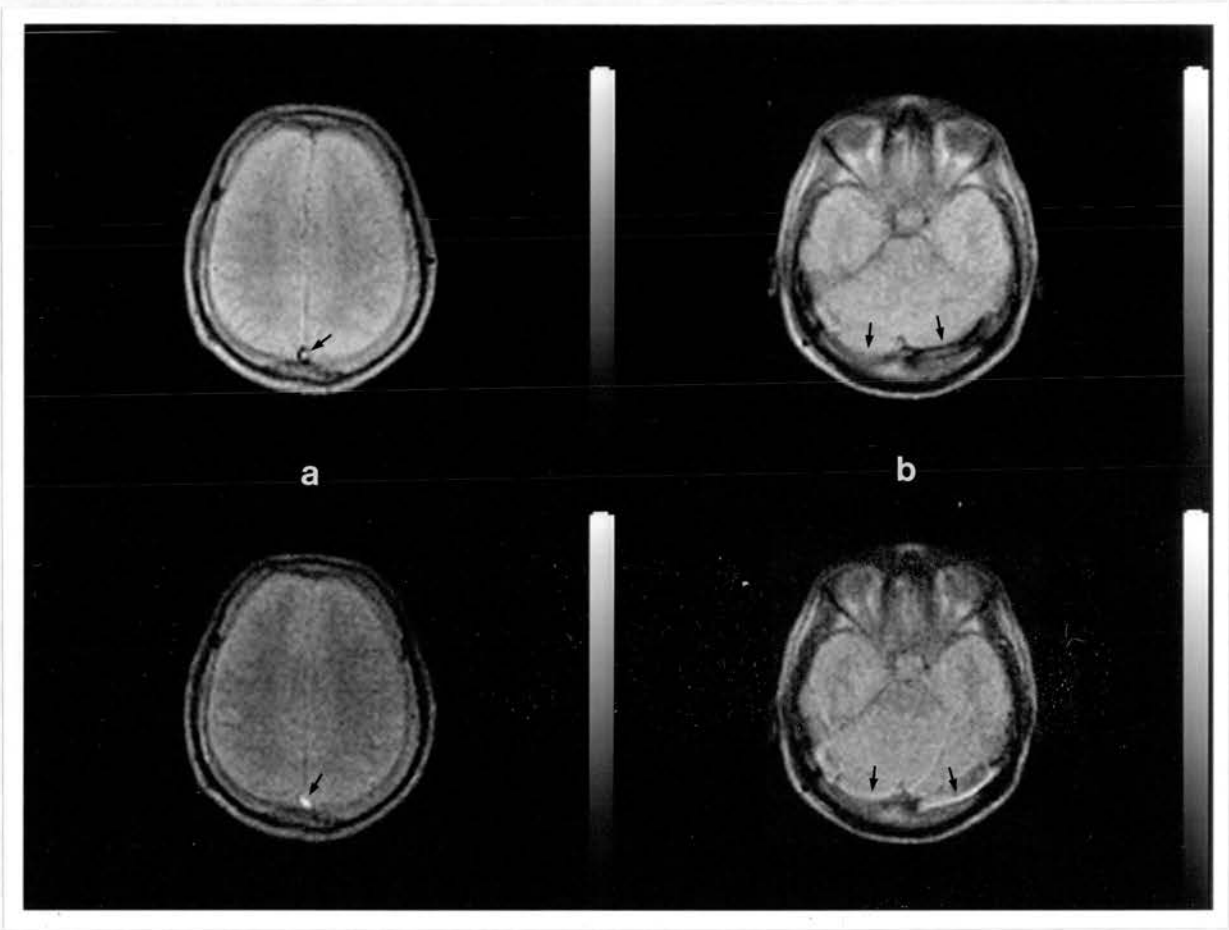

Figure 2.21.

Even echo rephasing observed on the 1st (upper) and 2nd (lower) echo images of a multiple spin echo pulse sequence in the case of slow venous flow. (a) Images showing rephasing for flow through the slice in the superior sagittal sinus (arrows). (b) Images showing rephasing for flow in-the-slice in the transverse sinuses (arrows).

will be the same. Since the 180° pulse alternates the sign of these phase shifts, the phase shift acquired for each odd-numbered echo will be cancelled at each

EDINBURGH

subsequent even-numbered echo. Therefore, the phase coherence lost at each odd-numbered echo is restored at each even-numbered echo to produce a relative increase in signal.

Even echo rephasing is observed for both flow through the slice (figure 2.21a) and flow within the slice (figure 2.21b), although it is often more apparent in the latter case (Waluch and Bradley, 1984). Dephasing and rephasing of protons flowing within the selected slice is primarily caused by the frequency-encoding gradient. Since the same pulses are applied for each echo, the phase shifts acquired at each odd-numbered echo are recovered at each even-numbered echo.

For protons flowing perpendicular to the selected slice, however, phase shifts are induced by the slice-selection gradients applied with both the initial excitation pulse and the 180^{o} refocussing pulses. Since the slice-selection gradient accompanying the excitation pulse is applied only once, phase shifts caused by this bipolar pulse are never recovered and complete rephasing is therefore never achieved.

2.2.9. Phase Modulation in the General Case

The time dependent spatial coordinate, x(t), in equation 2.13 can be expanded as a Taylor Series (Naylor et al, 1986; Pattany et al, 1987), up to the n^{th} order as follows

$$x(t) = \sum_i \frac{x^{(i)} t^i}{i!} \qquad i = 0,1,2,..,n. \qquad 2.20$$

where $x^{(i)}$ is the i^{th} differential of the positional coordinate, x. Writing out the first few terms of equation 2.20 gives:

$$x(t) = x + vt + \frac{at^2}{2} + \frac{pt^3}{6} + ... + \frac{x^{(n)} t^n}{n!} \qquad 2.21$$

where x, v, a, and p are the position, velocity, acceleration and rate-of-change of acceleration respectively at the time t=0. In general these quantities are unknown. For the gradient pulse sequences described in the previous sections the presence of such motion will mean that the rephasing condition will not be satisfied for even echoes and signal losses will occur. Although, for the simplest case of constant velocity motion, the velocity-related phase modulation can be used to quantify flow velocity, the signal losses caused by phase dispersion in the presence of higher order terms of motion prevent this measurement unless some of the signal losses are recovered.

Flow Measurement Using Phase Mapping

3.0. Introduction

In the previous chapter it has been shown that for certain gradient pulse sequences, the change in phase of moving protons, relative to that of stationary protons, is proportional to the velocity of motion. It is therefore possible to measure velocity by measuring this phase difference. One way of measuring phase is to produce a phase map from the NMR image data. In the following sections, the technique of phase mapping is described and its use and limitations in the measurement of flow is discussed. In the final section of this chapter, a phase mapping technique for flow measurement is proposed which attempts to overcome these limitations.

3.1. Phase Mapping

In most MRI systems it is possible to determine the phase of the NMR signal, relative to the system reference frequency, by using quadrature detection (Morris, 1985; Leach, 1988). This form of detection allows both the orthogonal components of the transverse magnetisation vector to be determined (section A2.4.2). Both these components of the NMR signal are recorded and the data is

digitised and stored in a data array. An image is reconstructed by applying a two dimensional Fourier transform to this data (section A2.3.2). Each element of the resultant image array also has two components, known as the 'real' and 'imaginary' components. It is possible to construct a 'real' or an 'imaginary' image using this data (figure 3.1). Whilst both these images contain information on the NMR signal magnitude, M, they are also sensitive to the phase, ϕ, of the signal and the magnitude values are modulated by either the cosine or the sine of the phase angle. The pixel intensities of the real image, r, and the imaginary image, i, are therefore given by

$$r \propto M\cos\phi \qquad 3.1a$$

$$i \propto M\sin\phi \qquad 3.1b$$

For routine NMR imaging, a magnitude image is calculated by combining the real and imaginary components, (section A2.4.2), as follows:

$$m = \sqrt{r^2 + i^2} \qquad 3.2$$

where m is the pixel intensity value for the magnitude image (figure 3.1). This image is dependent on the signal mangnitude only and is not phase-sensitive. The pixel intensity value, m, is scaled to a suitable range of values and is displayed using a linear grey-scale.

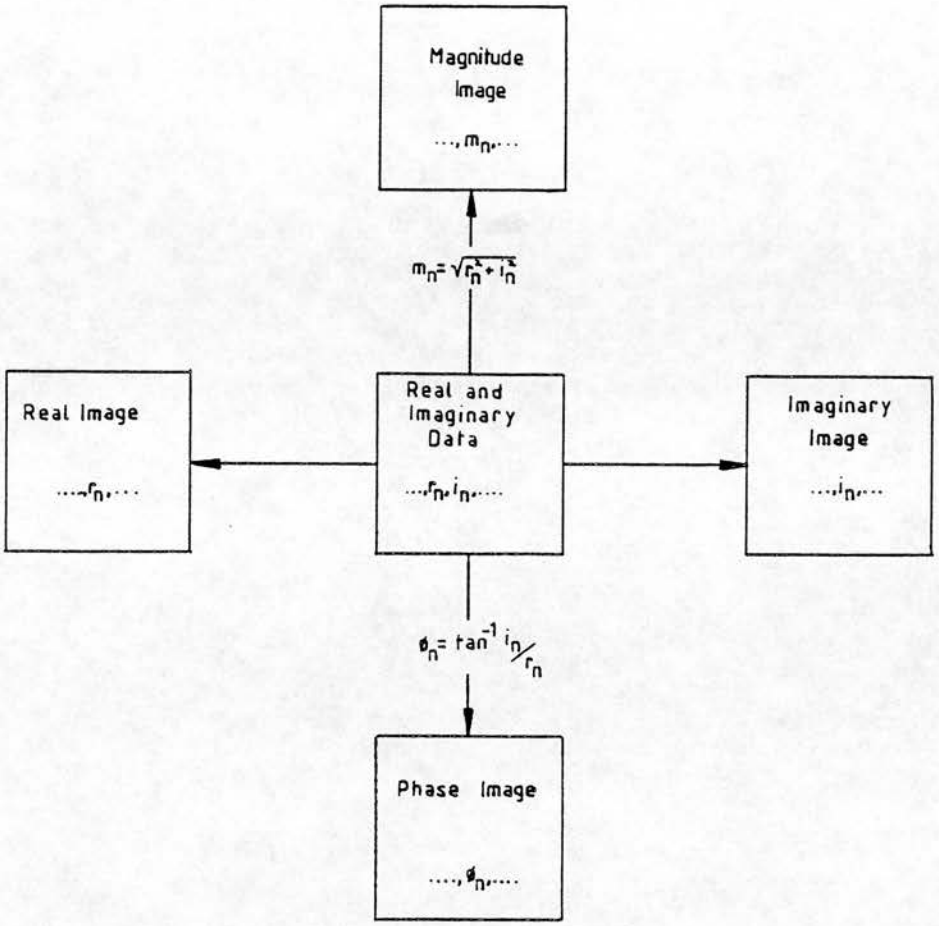

Figure 3.1.

The 'real' and 'imaginary' data can be used to produce 'real', 'imaginary' and 'phase' images, in addition to the conventional 'magnitude' (or 'modulus') image.

Whilst the magnitude image is normally the only image calculated and displayed, it is also possible to calculate the phase of the signal for each image array element (figure 3.1), by using the relation

$$\phi = \arctan(i/r) \qquad 3.3$$

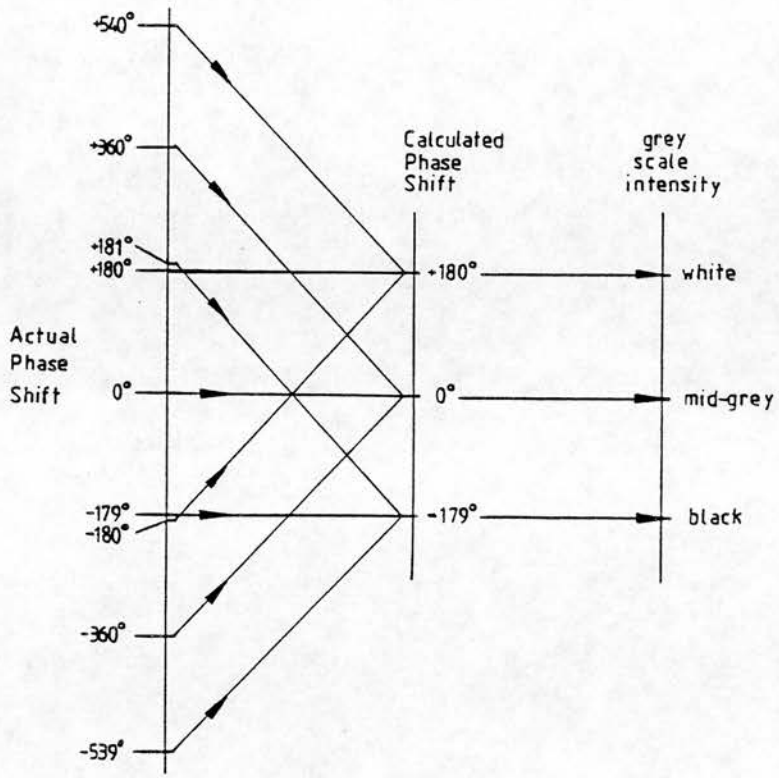

Figure 3.2.

Diagram showing the mapping of true phase shift values on to the range +/-180° and the linear grey scale used to display the phase maps.

The image generated in this fashion is often referred to as a phase map, as it maps the spatial distribution of signal phase within the image slice (Bryant et al, 1984; Van Dijk, 1984). Because of the properties of the arctan function, only phase shifts in the range +/-180° can be represented unambiguously. Phase shifts outwith this range are subject to a wrap-around effect (figure 3.2), whereby they are mapped onto the +/-180° range (Bryant et al, 1984; Van Dijk, 1984). The phase values can also be

suitably scaled and represented on a grey scale by setting the mid-grey level to represent zero phase, white to represent a phase of $+180^{o}$ and black to represent a phase of -180^{o} (figure 3.2).

Figure 3.3 shows a set of four images generated from data acquired using a field echo sequence. Both the real and imaginary images clearly show both signal magnitude and phase dependence. It should be noted that the phase is by no means uniform across the image, which suggests that its spatial distribution is also dependent on factors other than flow.

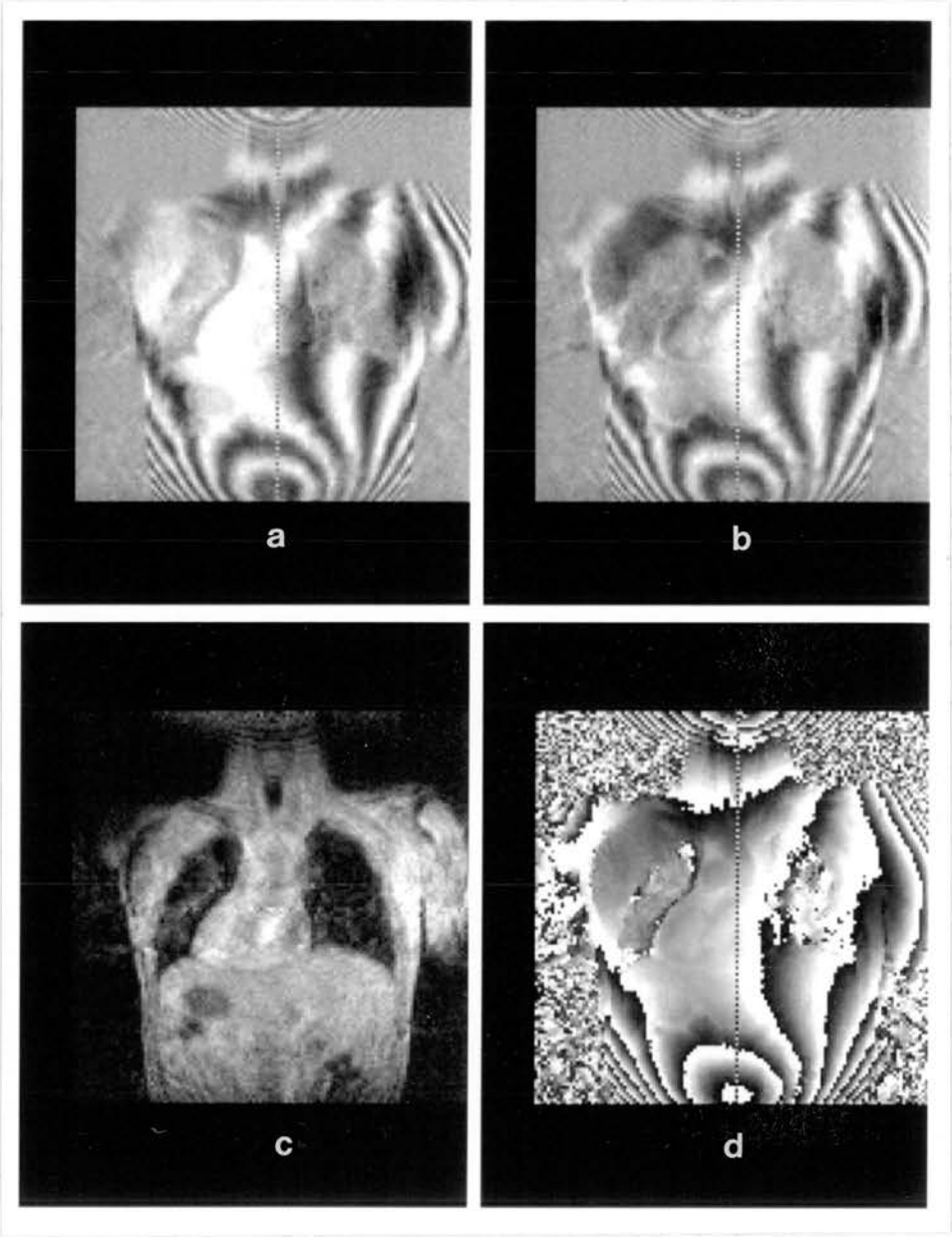

Figure 3.3.

Set of four images generated from data acquired using a field echo pulse sequence showing (a) the 'real' image, (b) the 'imaginary' image, (c) the 'magnitude' image, and (d) the 'phase' image.

3.2. Early Phase Mapping Techniques

The use of phase shifts to demonstrate flow and motion in NMR imaging was first demonstrated by a number of workers. In 1982, Moran described a method of encoding flow and motion, by inserting additional bipolar gradient pulses in any one of the three orthogonal gradient directions (Moran, 1982). This method was subsequently used to demonstrate flow by reconstructing the phase-sensitive real and imaginary images from a spin echo pulse sequence (Moran and Moran, 1984). Flow within the image plane was demonstrated in phantom studies and velocity profiles were obtained across the diameter of a tube. In the same publication, in vivo images showed velocity-related phase shifts from the moving heart wall. The pulse sequence was synchronised with the subject's ECG to obtain an image at a fixed point in the cardiac cycle. The heart chambers and vessels exhibited signal voids due to the combined effects of spin washout and phase dispersion, and therefore phase modulation related to blood flow was not demonstrated. Since only real and imaginary images were displayed, the pixel intensity was not a linear function of velocity, but was dependent on both the signal magnitude and either the sine or the cosine of the signal phase (equations 3.1a and 3.1b).

This technique was extended by Van Dijk (1984) to include the calculation of a phase image (or phase map). In this

image there is no dependence on the signal magnitude and the signal intensity is a linear function of velocity. Van Dijk exploited the phase modulation caused by the existing gradient waveforms in the spin echo sequence and did not include additional bipolar gradient pulses into the pulse sequence.

Bryant et al, (1984), devised a spin echo sequence similar to that described by Moran (Moran, 1982). A monopolar pulse pair was added to the slice selection gradient waveform at either side of the 180° refocussing pulse. This produced phase modulations for flow velocities through the slice. A phase map was calculated and was successfully calibrated for mean flow velocities of up to 40cm/s and an accuracy of within 10%. Flow velocities and flow rates were measured in the carotid and femoral arteries, although the measurement of rapid systolic flow was not reported.

The major drawback of the above techniques was that the observed phase shifts could have arisen from the interaction of more than one gradient waveform and the corresponding component of motion. The use of spin echo pulse sequences also reduced the available signal from flowing blood due to the effects of spin washout (section 2.1.2), and phase dispersion (section 2.2.7). In the work of Bryant et al, (1984) the spin washout effect was avoided by using a non-selective 180° rf pulse.

3.3. Advantages and Limitations of Phase Mapping

The techniques described in the previous section show that phase mapping has potential for the accurate measurement of flow dynamics. In comparison with the time-of-flight methods described in section 2.1.3, velocity measurement by phase mapping is more flexible and can provide greater accuracy using shorter acquisition times.

The time-of-flight methods require a number of scans to obtain a reasonable accuracy of around 10% (Singer and Crooks, 1983; Wehrli et al, 1985). Phase mapping can obtain better accuracy from just a single acquisition (Bryant et al, 1984). The measurement of signal magnitude in time- of-flight techniques leads to inaccuracy because of the effects of phase dispersion (Wehrli et al, 1985). In phase mapping techniques, the phase is measured directly, giving a linear measurement of velocity which is intrinsically more accurate (Moran and Moran, 1984). The early time-of-flight flow measurement techniques were limited to the measurement of steady or diastolic flow in a direction perpendicular to the slice. Phase mapping techniques are able to measure systolic flow (Bryant et al, 1984), and show potential for measuring flow in any direction (Moran, 1982).

Whilst phase mapping shows great potential for the

measurement of flow, the early techniques have also exhibited a number of limitations which must be overcome before they can be clinically useful. Firstly, the effects of spin washout and phase dispersion can often cause a reduction in signal magnitude, so that it is not possible to calculate the phase of protons within flowing blood. Furthermore, the presence of accidental motion-related phase modulation can lead to inaccuracies in the measurement of single velocity components. Secondly, the presence of phase modulations which are unrelated to motion can be caused by a range of effects, depending on the imaging field strength and the pulse sequence being used. These effects are most generally caused by magnetic field inhomogeneity, chemical shift, and changes in magnetic susceptibility.

In order for flow measurement using phase mapping to become a useful clinical tool, the technique must be further developed so that accidental phase modulations are reduced, and the signal losses due to the effects of spin washout and phase dispersion are avoided. The presence of phase modulations which are unrelated to flow and motion must be somehow eliminated. The pulse sequence must be flexible, so that the NMR signal can be encoded to produce velocity encoded phase shifts for any desired direction of flow, relative to both the patient and the selected image plane. The pulse sequence must be able to measure both slow venous flow and rapid pulsatile flow,

and should be able to measure both time-dependent velocity waveforms and allow time-averaged velocities to be measured or calculated. In the following sections, ways of reducing accidental phase modulation and signal losses are considered, and a practical pulse sequence, which is suitable for clinical use, is suggested.

3.4. The Spin Washout Effect

The spin washout effect occurs only in spin-echo sequences which use both a slice-selective 90° and a slice-selective 180° rf pulse (section 2.1.2). Whilst the spin washout effect is of an advantage when imaging cardiac wall motion (Van Dijk, 1984), it severely hinders the imaging and measurement of blood flow by phase mapping. This makes the conventional spin echo pulse sequence unsuitable for the measurement of high velocities for blood flowing through the image slice. For a slice thickness of 10mm, and a short echo time of 28 milliseconds, velocities of greater than 35cm/s flowing through the image slice would be immeasurable due to the total absence of signal. In practice, velocities even lower than this may not give a sufficient signal-to-noise ratio for the signal phase to be reliably calculated.

The effect can be avoided by using a non-selective 180° refocussing pulse in the spin echo pulse sequence (Bryant et al, 1984). However, this approach has two significant disadvantages. Firstly, the sequence can no longer be used for a multiple-slice acquisition, and secondly, the protons entering the image slice will be partially saturated from previous excitations and so their signal magnitude is reduced, particularly if short repetition times are used. Since it is desirable to use fast repetition times to acquire multiple images of pulsatile

flow throughout the cardiac cycle, (section 3.8.2), the spin echo pulse sequence cannot be considered suitable for the measurement of flow through the image slice using phase mapping.

Field echo pulse sequences use only a single slice-selective 90^{o} rf pulse (section 2.1.1), and therefore do not exhibit the spin washout effect. The signal observed from flowing blood is generally greater than that from surrounding tissue (section 2.1.1). This pulse sequence is therefore far more suitable for imaging rapid blood flow travelling through the image slice. The Field echo pulse sequence has the additional advantage that the magnitude of the rf excitation pulse, (i.e. the flip angle - section A2.5.5), can be reduced which in turn reduces the partial saturation effect within stationary tissue or slowly flowing blood. This allows the contrast between the flowing blood and the surrounding stationary tissue to be controlled when using short repetition times.

3.5. Phase Dispersion

Phase dispersion occurs in both spin-echo and field-echo sequences, due to the accidental modulation of the phase of moving protons by the gradient waveforms (section 2.2.7), and accounts for much of the signal loss observed

within vessels. Accidental phase modulation can also lead to inaccuracy when measuring velocity by using phase mapping techniques. It is therefore desirable to reduce this accidental phase modulation. This can be achieved by careful design of the gradient waveforms so that the phase of the signal is less sensitive to motion.

3.5.1. Pulse Sequence Desensitisation - Constant Velocity

It has been shown that phase modulation which is caused by constant-velocity motion, is corrected in the effect of even echo rephasing (section 2.2.8). Whilst this effect was originally observed in the second-echo image of a multi-spin-echo pulse sequence, the same degree of rephasing can be achieved for the first echo of either a spin echo or a field echo pulse sequence by introducing additional gradient pulses to the gradient waveform (Le Roux and Floch, 1984; Pattany and Nayler, 1985). This is illustrated in figure 3.4. Since a single bipolar pulse pair causes the same phase modulation as two monopolar pulses separated by a 180^{o} refocussing pulse, (section 2.2.3), two consecutive bipolar pulse pairs can be used to produce the same degree of rephasing, in the presence of constant velocity flow, as is observed in the even echo rephasing effect.

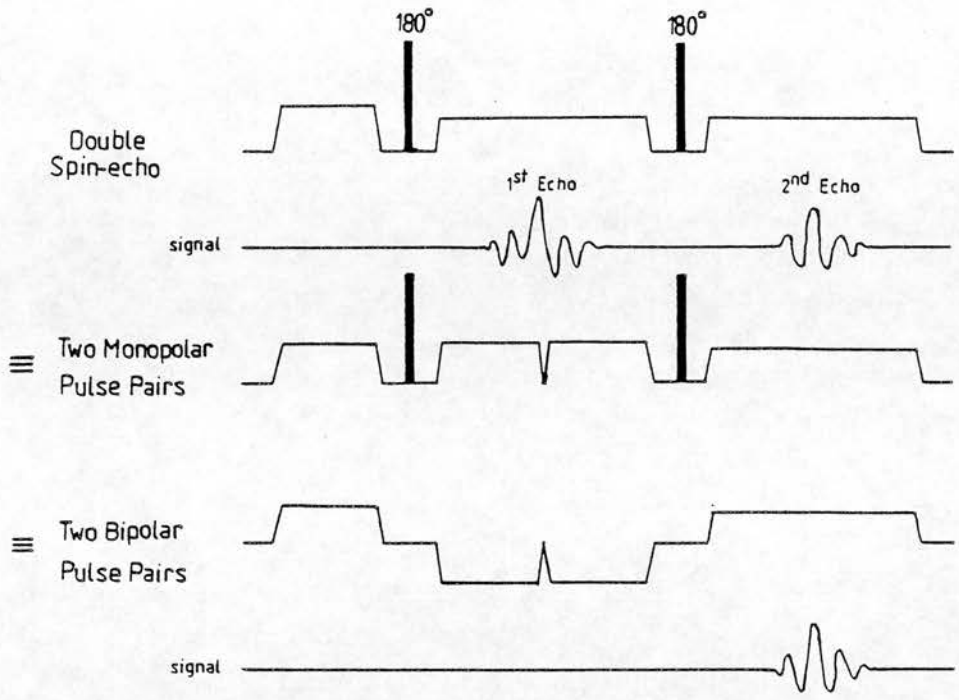

Figure 3.4.

The gradient waveform used in a double spin echo pulse sequence is equivalent to two consecutive monopolar pulse pairs, or two consecutive bipolar pulse pairs. The signal echo following the two bipolar pairs therefore exhibits the same degree of rephasing as the second echo in the double spin echo pulse sequence in the presence of constant velocity flow.

The accidental phase modulation caused by a bipolar waveform in the presence of constant velocity flow is removed by adding a second bipolar pulse of opposite polarity. The velocity dependent phase modulation that results from the first bipolar pulse, ϕ_1, is equal and opposite to that from the second bipolar pulse, ϕ_2.

Thus, from section 2.2.6, and equation 2.19,

$$\phi_1 = -\gamma G v T t_w \qquad 3.4a$$

$$\phi_2 = +\gamma G v T t_w \qquad 3.4b$$

Therefore the total phase modulation for protons of constant velocity is

$$\phi = \phi_1 + \phi_2 = 0.$$

The rephasing condition for stationary protons is automatically satisfied beacause of the use of bipolar pulse pairs. Both spin-echo (Le Roux and Floch, 1985; Pattany and Naylor, 1985) and field-echo sequences (Ridgway and Smith, 1986; Naylor et al, 1986) have been compensated by adding gradient pulses in this way.

Whilst the use of two consecutive bipolar pulse pairs can reduce accidental phase modulation which is related to constant-velocity motion, this modified gradient waveform is more sensitive to acceleration than before (Moran and Moran, 1984). As the time separation of the two bipolar pulse pairs is increased, the phase modulation due to the presence of acceleration increases. However, by combining the two middle pulses into a single pulse, this time separation is minimised and the sensitivity to acceleration is reduced.

3.5.2. Motion Desensitisation in the General Case

In order to ensure optimum design of the gradient waveform, which takes account of higher orders of motion, a more rigorous formulation is required. In section 2.2.5 a general theoretical description of accidental phase modulation was developed in which the phase modulation of moving protons, ϕ, could be described by the integral,

$$\phi = \gamma \int x(t)\, G_x(t)\, dt \qquad 3.5$$

(from equation 2.17) where $G_x(t)$ defines the time-varying gradient waveform, and $x(t)$ defines the postion of the proton at time t. For the rephasing condition to apply for all orders of motion, there must be no motion-dependent phase modulation and this integral must be equal to zero. As shown previously in section 2.2.9, $x(t)$ can be expressed as a Taylor Series (equation 2.21);

$$x(t) = x + vt + \frac{at^2}{2} + \frac{pt^3}{6} + ... + \frac{x^{(n)}t^n}{n!} \qquad 3.6$$

where the constants x, v, a, and p are the position, velocity, acceleration and pulsatility, at a time t = 0, respectively. Although the integral of equation 3.5 is required to be zero for all orders of motion, each order of motion must be treated separately†. Thus, up to the nth order of motion, setting the left hand side of equation 3.5 to zero yields a set of n+1 simultaneous equations:

† Since the values of x, v, a, p, etc, are unknown, the only way to ensure that the integral of equation 3.5 is zero, is to apply the rephasing condition separately for each order of motion.

$$0 = \gamma x \int G_x(t)\, dt \qquad 3.7a$$

$$0 = \gamma v \int G_x(t)\, t\, dt \qquad 3.7b$$

$$0 = \gamma a \int G_x(t)\, t^2\, dt \qquad 3.7c$$

$$\vdots$$

$$0 = \gamma x^{(n)} \int G_x(t)\, t^n\, dt \qquad 3.7d$$

For simplicity, the gradient waveform, $G_x(t)$ is considered as a series of m rectangular pulses with 2m edges, at times t_1, t_2, t_3, ..., t_{2m}, and magnitudes G_1, G_2, G_3, ..., G_m. Equations 3.7a-d can then be re-written as follows:

$$0 = \int_{t_1}^{t_2} G_1\, dt + \int_{t_3}^{t_4} G_2\, dt + \int_{t_5}^{t_6} G_3\, dt + \ldots. + \int_{t_{2m-1}}^{t_{2m}} G_m\, dt$$

$$0 = \int_{t_1}^{t_2} G_1 t\, dt + \int_{t_3}^{t_4} G_2 t\, dt + \int_{t_5}^{t_6} G_3 t\, dt + \ldots. + \int_{t_{2m-1}}^{t_{2m}} G_m t\, dt$$

$$0 = \int_{t_1}^{t_2} G_1 t^2\, dt + \int_{t_3}^{t_4} G_2 t^2\, dt + \int_{t_5}^{t_6} G_3 t^2\, dt + \ldots. + \int_{t_{2m-1}}^{t_{2m}} G_m t^2\, dt$$

$$\vdots$$

$$0 = \int_{t_1}^{t_2} G_1 t^n\, dt + \int_{t_3}^{t_4} G_2 t^n\, dt + \int_{t_5}^{t_6} G_3 t^n\, dt + \ldots. + \int_{t_{2m-1}}^{t_{2m}} G_m t^n\, dt$$

(equations 3.8a-d)

The trivial solution to equations 3.8a-d (i.e. $0 = G_1 = G_2 = G_3 = ... = G_m$), is only applicable in the case of the phase encoding gradient waveform. The slice-selection and frequency-encoding gradient waveforms require a non-trivial solution.

In the case of the slice-selection gradient, the value of one of the gradient pulses is determined by the slice thickness required and the bandwith of the excitation pulse (section A2.6.4). In the case of the frequency-encoding gradient, the magnitude of one of the m gradients is determined by the field of view and sampling rate of the data acquisition (section A2.6.2). If the duration of each of the m gradient pulses is fixed, then the remaining gradient magnitudes will constitute m-1 unknowns which are common to each equation.

The number of gradient pulses required depends on the highest order of motion for which the pulse sequence is to be made insensitive. For stationary tissue, (zeroth order motion), two gradient pulses are required for the rephasing condition to hold. For constant velocity motion (first order motion), three gradient pulses are required for the rephasing condition to hold. (This is equivalent to the two consecutive bipolar pulse pairs but with the centre two pulses being combined as one pulse). For nth order motion, a total of n+2 gradient pulses are required of which the magnitude of one is known. Thus for nth

order motion n+1 non-homogeneous simultaneous equations must be solved for n+1 unknown gradient pulse magnitudes. These simultaneous equations can be solved using standard mathematical techniques such as matrix inversion (Pattany et al, 1987).

This method of gradient pulse sequence desensitisation has been used successfully to reduce accidental, motion-related phase modulation and to suppress the resulting motion artefacts in both spin echo pulse sequences (Pattany et al, 1987), and field echo pulse sequences (Naylor et al, 1986). As more higher order terms of motion are corrected for, however, the gradient waveforms required become considerably more complex, making them technically difficult to implement, and causing the signal echo time to be extended unacceptably.

3.6. Phase Modulation Unrelated to Motion

In addition to phase modulation related to motion, phase modulation is also observed due to a number of other effects which are not motion-related. In spin echo imaging, many of these effects are compensated for by the 180° refocussing rf pulse used in spin echo pulse sequences. In field echo imaging, however, this is not the case and such phase modulation can be clearly observed in the phase-sensitive images (figure 3.5).

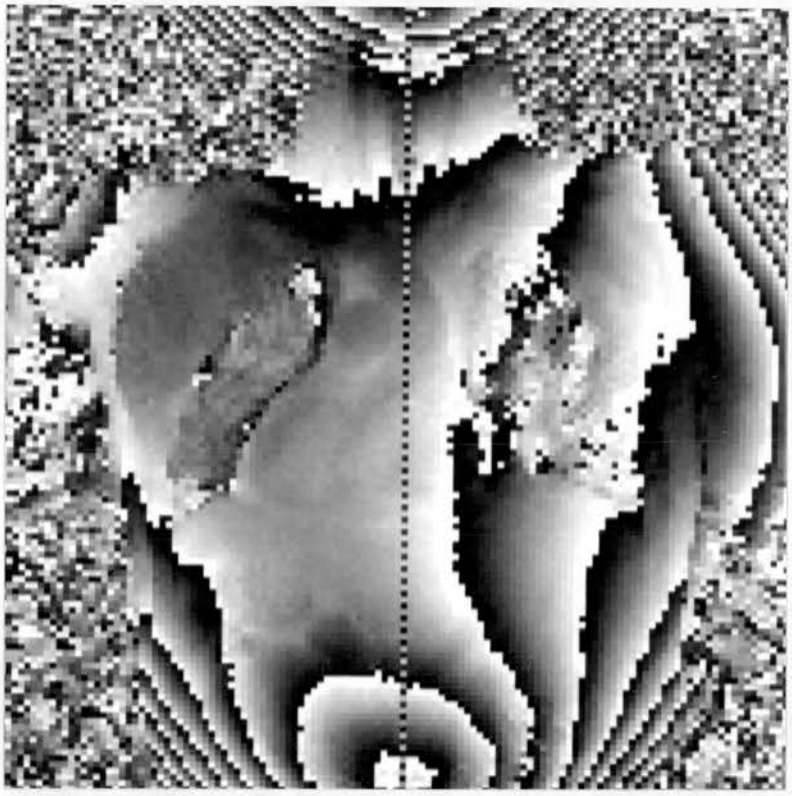

Figure 3.5.

A phase image constructed from data acquired in the coronal plane using a field echo pulse sequence. Phase modulation due to the magnetic field inhomogeneity is clearly seen, particularly near the edge of the field of view. At the centre of the field of view the heart chambers and major vessels can be distinguished. Whilst this may be due to motion-related phase modulation, in this case it is more likely to be due to differences in magnetic susceptibility.

Non-uniformities of the main magnetic field, the magnetic field gradients and the radiofrequency field can cause phase modulation which is spatially dependent. The

different NMR properties of tissues can also lead to changes in the Larmor frequency caused by the chemical shift effect, or by changes in magnetic susceptibility. Finally, an intensity gradient can often be observed on phase images because of a poorly designed imaging pulse sequence, in which the centre of the data collection period does not coincide with the centre of the signal echo.

3.6.1. Inhomogeneity of the Main Magnetic Field

The phase of the NMR signal, for a three dimensional distribution of protons, in the presence of a static magnetic field, $B(x,y,z)$, is given by

$$\phi(x,y,z) = \gamma \int B(x,y,z)\, dt \qquad 3.9$$

Equation 3.9 assumes that all protons have zero phase at time $t=0$, and neglects all other causes of phase modulation. The main field is expressed here as a spatially dependent function, $B(x,y,z)$ which can be considered as a spatially uniform main field B_o, on which is superimposed an error field, $\Delta B(x,y,z)$, such that

$$B(x,y,z) = B_o + \Delta B(x,y,z)$$

Spin echo pulse sequences in which the 180^{o} refocussing pulse occurs at half the time to echo, TE/2, compensate for this error in the main field and any resultant phase shift is cancelled (section A1.8.3). This is not the case with field echo sequences and the phase shift due to the main field inhomogeneity is given by

$$\phi(x,y,z) = \gamma TE\Delta B(x,y,z) \qquad 3.10$$

The exact form of B(x,y,z) depends on the magnet configuration, and on the quality of the magnet shim (Section A2.6.1).

3.6.2. Unwanted Components of Magnetic Field Gradients

As a direct consequence of Maxwell's equations the presence of the linear gradient magnetic fields also dictates the presence of unwanted gradient fields (Norris, 1985a). With the axes as defined in section A2.0, the three orthogonal magnetic field gradients which are desirable for imaging are G_x, G_y, and G_z, where

$$G_x = \frac{\partial B}{\partial x}z \; ; \quad G_y = \frac{\partial B}{\partial y}z \; ; \quad G_z = \frac{\partial B}{\partial z}z \; ; \qquad 3.11$$

From Maxwell's Equations we have:

$$\text{curl}B = 0 \qquad 3.12a$$

$$\text{div}B = 0 \qquad 3.12b$$

The fundamental constraints imposed by Maxwell's equations have the consequence that for each magnetic field gradient created, a second magnetic field gradient also exists which is not required. For example, for the gradient, G_x, the condition curlB=0 requires

$$\frac{\partial B}{\partial z}x - \frac{\partial B}{\partial x}z = 0 \qquad 3.13$$

The extra gradient, $\partial B_x/\partial z$, will add to the vector sum of the desired gradient and main field, causing an error in the local field strength given by

$$B_e = (G_x z)^2/2B_o \qquad 3.14$$

Similar errors can be derived for G_y and G_z, however only the gradient waveforms corresponding to the frequency-encoding and phase-encoding directions will give rise to variations in phase shift across the image. This source of error is relatively small compared to that due to the main field inhomogeneity but may still be significant when attempting to measure small phase modulations at the edge of the field of view. Modifications to spin echo pulse sequences have been suggested which eliminate this effect (Norris, 1985a).

3.6.3. Chemical Shift and Magnetic Susceptibility

The NMR phenomena related to chemical shift and magnetic susceptibility are described in appendix II (sections A2.7.1 and A2.7.2). At low magnetic field strengths, these effects have a mostly neglible effect on the signal magnitude, but they can give rise to significant phase modulation which can be observed on phase images obtained using field echo pulse sequences. For a chemical shift σ, and a field echo time, TE, the phase modulation has a dependence on σ given by (section A2.7.1),

$$\phi \propto \gamma\sigma TEB_o \qquad 3.15$$

Similarly, a difference in the magnetic susceptibility, X_m, of different tissues will give rise to a local change in magnetic field strength, and therefore a change in the Larmor frequency, resulting in a phase modulation, ϕ, given by (section A2.7.2),

$$\phi \propto \gamma\mu_o X_m TEH_o \qquad 3.16$$

where H_o is the magnetising field, and μ_o is the permeability of free space. The phase modulation observed on the phase image will appear in the same way as for the chemical shift effect. For this reason the two effects can not be distinguished. The susceptibility effect has been studied in the human brain using phase mapping

(Young et al, 1987). In this case the effect was mainly attributed to the paramagnetic contribution made by iron compounds from the breakdown products of blood. To eliminate phase modulation due to magnetic field inhomogeneities, a flood field phantom was imaged using an identical pulse sequence and the resultant phase map was subtracted from the phase map of the brain.

3.6.4. Mis-timing of the Data Collection Period

Ideally, the centre of the signal echo should occur at the centre of the data collection period. For this to be so, the frequency-encoding gradient waveform must satisfy the rephasing condition given by equation 2.12. Whilst this can be achieved theoretically, in practice it is subject to a number of possible errors. For example, there may be a constant-voltage offset on the output from the power supply to the frequency encoding gradient, or alternatively, the data collection period may not be positioned symmetrically about the centre of the signal echo.

For field echo sequences, if there is such an error, then the rephasing condition is not satisfied and complete rephasing is not achieved at the centre of data collection. This imposes a phase modulation which is linearly dependent on the distance from the null point of

the gradient. This will appear on the phase image as a linear intensity gradient across the image. If this gradient is large, the phase may 'wrap around' several times, appearing as a series of bands, each representing 360^{o} phase shift, in an orientation orthogonal to the frequency encoding direction.

There is a similar effect if there is a dc offset on the power supply to the phase encoding gradient. In this case the phase is modulated in the phase encoding direction. Such permanent magnetic field gradients could of course be due to the main field inhomogeneity, if the magnet has been poorly shimmed (section A2.6.1). This form of phase modulation can be avoided by careful design of pulse sequence waveforms and pulse sequence timing, and careful adjustment of the magnetic field homogeneity and the magnetic field gradient power supplies.

3.7. Methods of Flow Encoding

As shown in section 2.2 et seq, the existing imaging gradients of standard pulse sequences can introduce phase modulation of the NMR signal from moving protons. In sections 3.1 and 3.2 it was shown that if a phase-sensitive image is reconstructed, this phase modulation can be observed, providing a direct method of imaging flow (Section 3.2 and Moran, 1983; Moran and Moran, 1984; Bryant et al, 1984; Van Dijk, 1984).

Some of the early phase mapping techniques (Moran & Moran, 1984; Van Dijk, 1984), exploited the motion-related phase modulation caused by the existing gradient waveforms found in standard pulse sequences. This approach has a number of limitations which were discussed in section 3.3. In particular, the gradient pulse sequence is sensitive to motion in more than one direction. The combined effect of the slice-selection and the frequency-encoding gradient waveforms makes it difficult to deduce the direction of the motion which is causing the phase modulation in some instances.

A further limitation arises because the existing gradient waveforms are determined by imaging parameters such as the slice thickness and the field of view, so that the gradient magnitudes cannot be varied to control the velocity-related phase modulation. As a result a gradient

waveform which is suitable for imaging fast flow will not be suitable for imaging slow flow and vice versa.

If a more flexible flow imaging and measurement technique is to be developed, it is therefore necessary to design a gradient pulse sequence which will allow full control of the direction and the velocity of motion to be measured, independent of the selection of other imaging parameters. This has been achieved by a number of workers by inserting additional gradient pulses into the pulse sequence as suggested by Moran (Moran, 1982), although the precise method of motion-related phase encoding has varied between different research groups.

3.7.1. Adding a Bipolar Gradient

The basis of this method is to add a bipolar gradient pulse pair to one of the three orthogonal gradient waveforms (figure 3.6). This was first implemented in a spin echo pulse sequence (Moran, 1982; Moran and Moran, 1984). From section 2.2.6, for a velocity component, v, in the direction corresponding to that of the bipolar gradient, this will result in an additional phase modulation, ϕ, given by

$$\phi = -\gamma G v T t_w \qquad 3.17$$

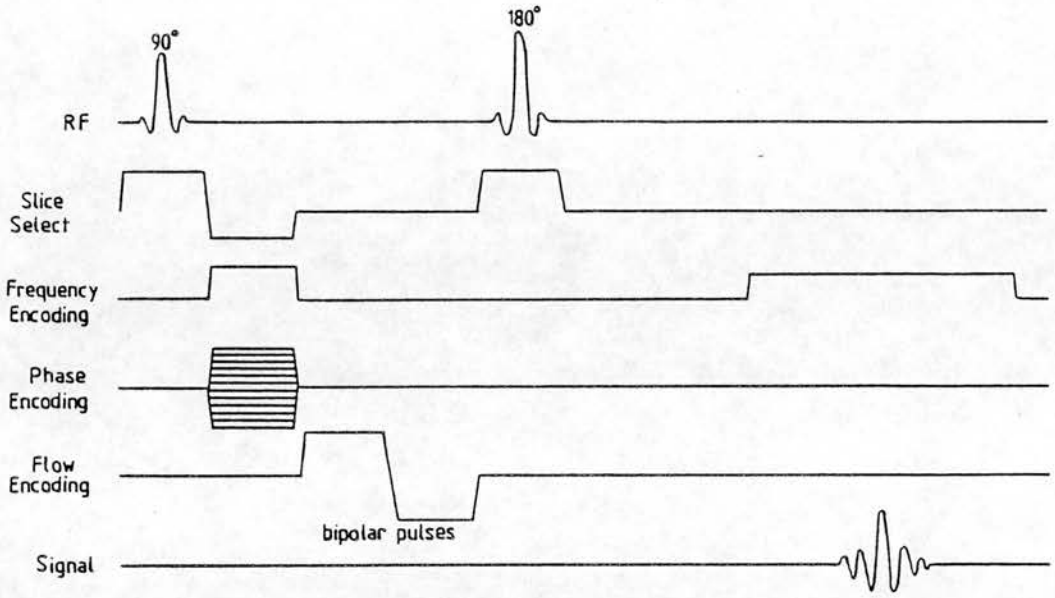

Figure 3.6.

A spin echo pulse sequence into which an additional bipolar flow-encoding gradient pulse pair has been inserted.

Accidental phase modulation due to the slice selection and frequency encoding gradients will still exist and may lead to inaccuracies in velocity measurement by phase mapping, and may cause signal losses due to phase dispersion (section 3.3).

A second pair of bipolar pulses of opposite polarity to the first pair can be added to form a quadrapolar gradient waveform (figure 3.7). In the presence of constant velocity motion, this waveform satisfies the rephasing condition and is equivalent to the gradient waveforms which produce the even echo rephasing effect

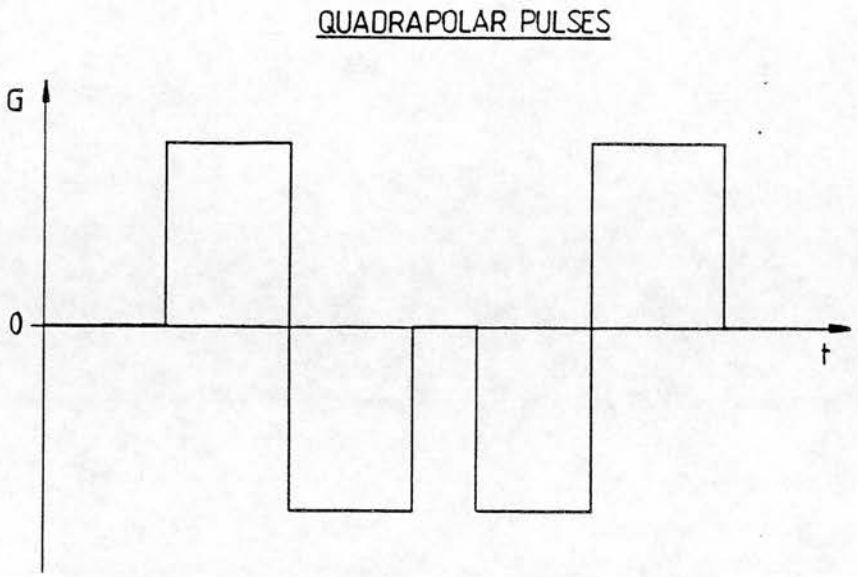

Figure 3.7.

A quadrapolar gradient pulse waveform in which the centre two pulses are of opposite polarity to the outer two pulses, but are of equal width and magnitude.

(sections 2.2.8 and 3.5.1). In the presence of higher orders of motion, however, the rephasing condition is not satisfied. For example, in the presence of constant acceleration, the signal phase is modulated in proportion to the magnitude of the acceleration (Moran and Moran, 1984). If each of the pulses has an equal duration, T, and magnitude, G, the phase modulation in the presence of flow with constant acceleration, a, is given by

$$\phi \propto aGT^3 \qquad 3.18$$

Imaging has been performed using a field echo pulse sequence with quadrapolar pulses added to the frequency encoding waveform, in order to encode acceleration in that direction (Norris, 1985b). In order to eliminate phase shifts unrelated to motion, a second acquisition was performed in which the polarity of the quadrapolar pulses were reversed and the two resultant phase maps were subtracted.

3.7.2. Adding two Monopolar Gradient Pulses

The bipolar gradient is equivalent to two monopolar gradient pulses either side of the 180^{o} refocussing pulse, in terms of the resultant velocity dependent phase modulation it causes (section 2.2.3 and Moran and Moran, 1984). Flow-related phase modulation for a particular direction can therefore be achieved in spin echo sequences by adding two such monopolar gradient pulses onto the appropriate gradient waveform (figure 3.8). This technique was employed by Bryant and his co-workers, (Bryant et al, 1984), using a calculated phase map to display and measure the phase modulation. The velocity-encoding gradient was added to the slice selection waveform and all velocities were measured assuming that motion was flowing perpendicular to the slice (section 3.2).

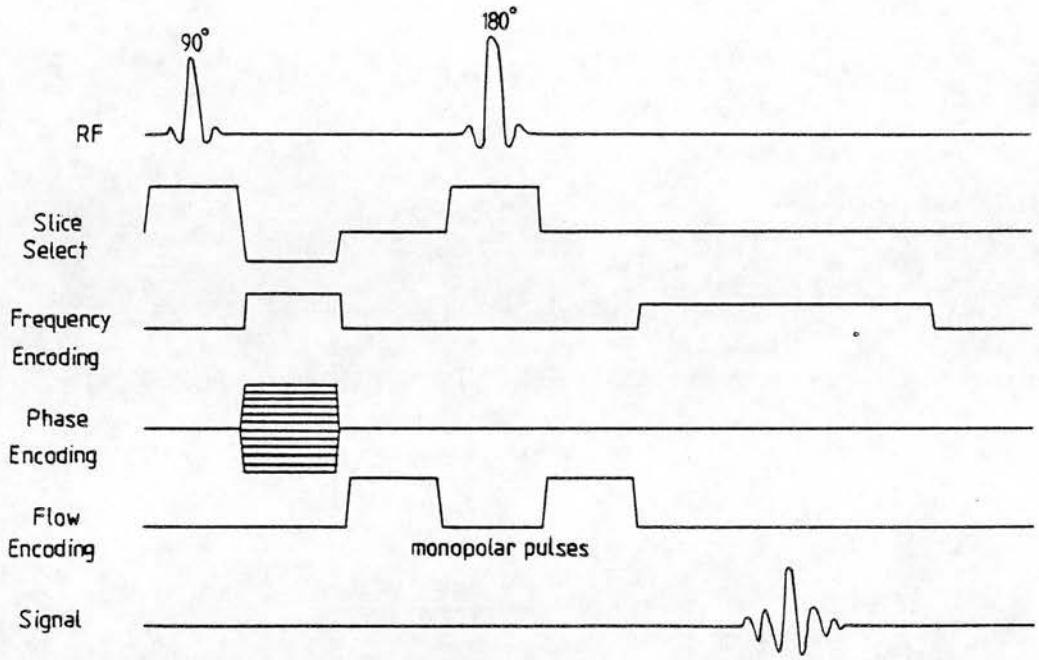

Figure 3.8.

A spin echo pulse sequence into which an additional monopolar flow-encoding gradient pulse pair has been inserted.

3.7.3. 'Zebra Stripe' Phase Display Flow Imaging

Measurement of flow velocity in the plane of the image slice can be achieved by exploiting the phase modulation caused by the frequency encoding gradient waveform (Moran and Moran, 1984; Van Dijk, 1984). Wedeen and co-workers also used the frequency encoding gradient waveform to produce motion related phase modulation, (Wedeen et al, 1985), however their method was modified to enhance the appearance of this phase modulation by deliberately mis-centering the data collection period with respect to the centre of the spin echo (figure 3.9).

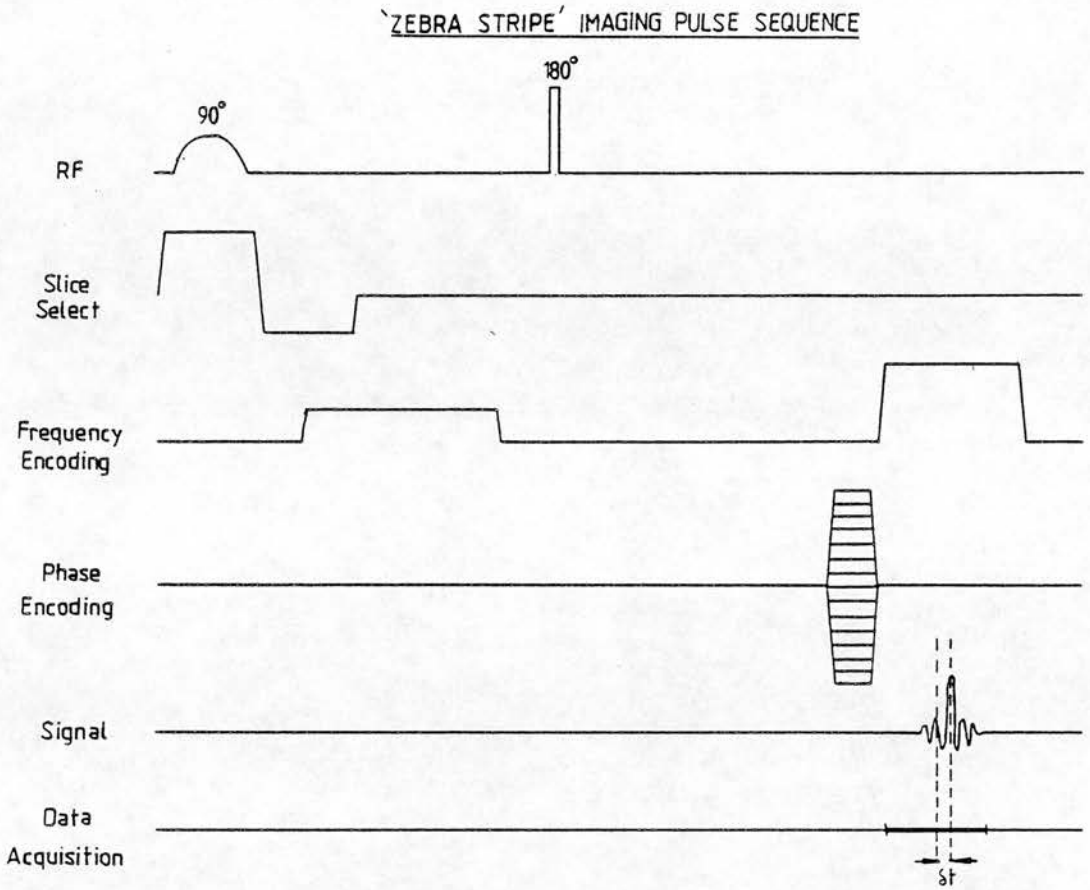

Figure 3.9.

The spin echo pulse sequence used for 'Zebra Stripe' imaging. The centre of the data collection period is offset from the centre of the signal echo by a time δt. The value of δt controls the spacing of the stripes and the amount of displacement achieved for a given velocity.

This has the effect of re-introducing the artefact discussed in section 3.6.4. The 'real' image data was used to display the resultant phase modulation which, for stationary tissue, appeared as a series of stripes perpendicular to the frequency encoding direction (figure 3.10).

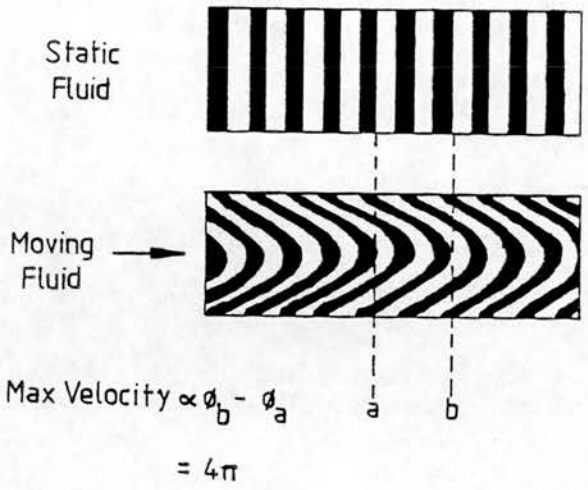

Figure 3.10.

In 'Zebra Stripe' imaging, stationary tissue appears as a series of parallel stripes. In the presence of flow the stripes are displaced along the direction of motion by an amount proportional to the flow velocity.

This technique is known as 'Zebra Stripe' flow imaging. The presence of phase modulation related to motion in the frequency encoding direction appears as a lateral displacement of the stripes (figure 3.10). Whilst recalling that the signal intensity of the real image is dependent on the cosine of the phase (section 3.1), the displacement of the stripes is proportional to the velocity of motion. Measurement of the phase shift is obtained by noting that the width of each stripe represents a phase change of 180^{o} (figure 3.10).

There are two advantages of this form of phase display. Firstly, provided that the in-plane resolution is good

enough, it gives a visual indication of the velocity profile across the vessel. Secondly, it enables phase shifts of greater than 180° to be imaged without the ambiguity caused by phase 'wrap around', and therefore increases the potential dynamic range and precision of the velocity measurement. The second advantage is offset slightly because as the dynamic range increases, so does the amount of phase dispersion when high velocity gradients are present. This problem is acknowledged by the authors and as a solution they suggest that the dynamic range should be reduced by using pulse sequences in which both the echo time (TE) and the magnitude of the frequency encoding gradient are reduced (Wedeen et al, 1985). Unfortunately, this solution also results in a loss of precision.

3.7.4. Multiple Acquisition Phase Encoding Techniques

The methods of flow imaging that have so far been discussed are limited both by accidental phase modulation due to motion and by other causes of phase modulation which are unrelated to motion (section 3.3). Two possible solutions to remove the accidental motion-related phase modulation have been suggested (Van Dijk, 1984).

The first solution was to include additional gradient pulses in the gradient waveforms to reduce the

motion-related phase modulation in unwanted directions. (section 3.5). This also reduces signal losses in the presence of high velocity gradients (section 2.2.7). However, it does not compensate for phase errors due to the magnetic field inhomogeneity and the chemical shift and magnetic susceptibility effects which are present in phase maps obtained with field echo sequences (section 3.6.3).

The second solution was to acquire a second phase map, using a bipolar slice selection gradient of opposite polarity to that in the first (Van Dijk, 1984). Whilst for stationary protons the two pulse sequences have an identical effect, the motion-dependent phase modulation induced by constant velocity components, perpendicular to the imaging slice in the first sequence, is equal, but of opposite sign to that in the second sequence. Adding the two phase maps causes the phase modulations due to motion perpendicular to the slice to cancel. This leaves only phase modulation caused by the frequency-encoding gradient waveform which represents velocity components in that direction.

3.7.5. Fourier Transform Method

This method of flow velocity imaging was developed by Redpath and co-workers (Redpath et al, 1984). It is not strictly speaking a phase mapping technique but it uses the signal phase to encode velocity in the same way that the spin warp imaging technique uses the phase to encode spatial position (Edelstein et al, 1980).

A bipolar gradient pulse is used to phase encode velocity in the direction required. A series of N acquisitions are obtained in which the bipolar pulse magnitude is varied in N equal steps from +M to -M (figure 3.11). A two-dimensional Fourier transform is applied to each of the N data sets and yields N images, each having different velocity encoding. Treating these N images as a three-dimensional data set, a further N point fourier transform with respect to the acquisition (or image) number yields N images, each of which represents a discrete part of the velocity range. The central image (image number = N/2 + 1), represents stationary material, (zero velocity), so that any pixels which contain protons which have an unchanged phase value in all acquisitions will have maximum intensity on this image. A pixel which contains protons with a non-zero velocity, v, will have a maximum intensity on image number n such that $(n-(N/2+1)) \propto v$.

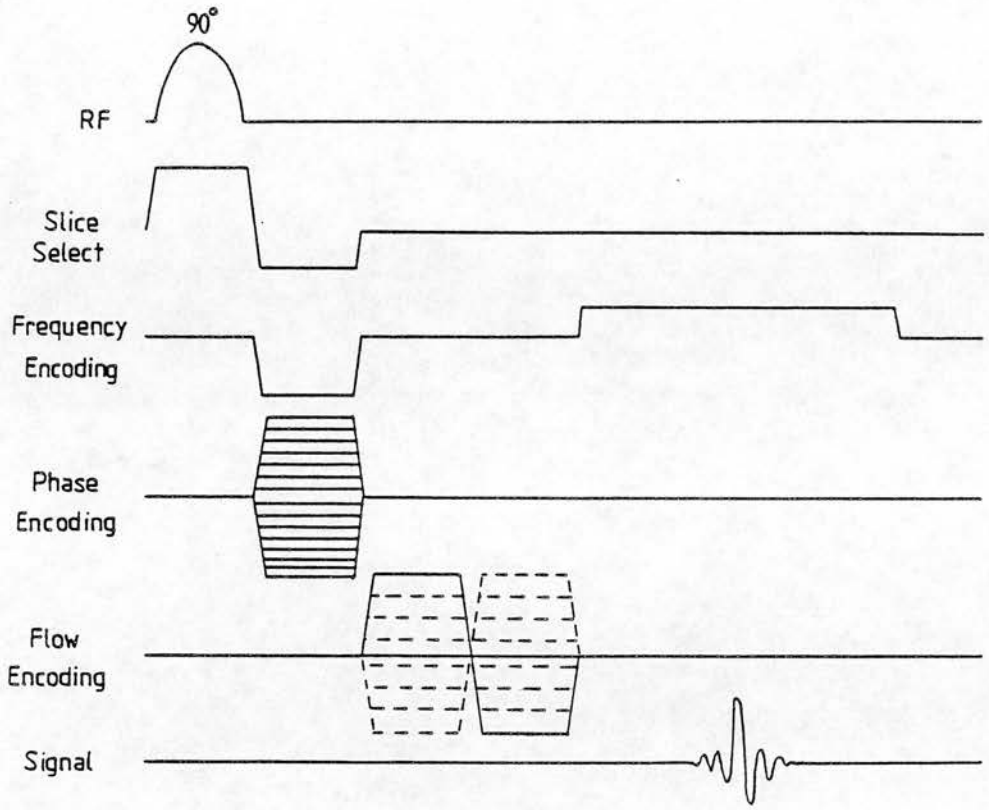

Figure 3.11.

The field echo pulse sequence used for Fourier velocity imaging. N acquisitions are performed and the magnitude of the bipolar flow encoding pulse is different for each acquisition.

Any phase shifts which are constant between acquisitions, such as those due to magnetic field inhomogeneity and chemical shift, do not affect the final image appearance. Pixels containing high velocity gradients, or flow in opposite directions, do not suffer from signal loss, but instead, non-zero signal intensity at the same position is seen in a number of images according to the range of velocities present. The main drawback of this method of

velocity encoding is that the imaging time increases in proportion to the number of additional phase encoding steps. Therefore, in order to increase the velocity resolution the imaging time must also be increased.

3.8. Imaging Pulsatile Flow and Cardiac Related Motion

Most types of motion encountered in in-vivo imaging are cyclic and are related to either the respiratory or cardiac cycles. When performing NMR imaging using the spin warp imaging technique (appendix II), the presence of such motion causes artefacts which are most commonly observed on the images as a random distribution of signal in the phase encoding direction (figure 3.12). The most obvious cause of these artefacts is the change in position along the spatial encoding gradients of a structure from one signal acquisition to the next. In addition, the degree of accidental, motion-related phase modulation may also vary between different signal acquisitions as the velocity of pulsatile blood flow varies.

Pulse sequence desensitisation (section 3.5 et seq) can considerably improve the image quality by preventing accidental phase modulation caused by flowing blood (Pattany et al, 1987). However it does not suppress artefacts due to the motion of structures between

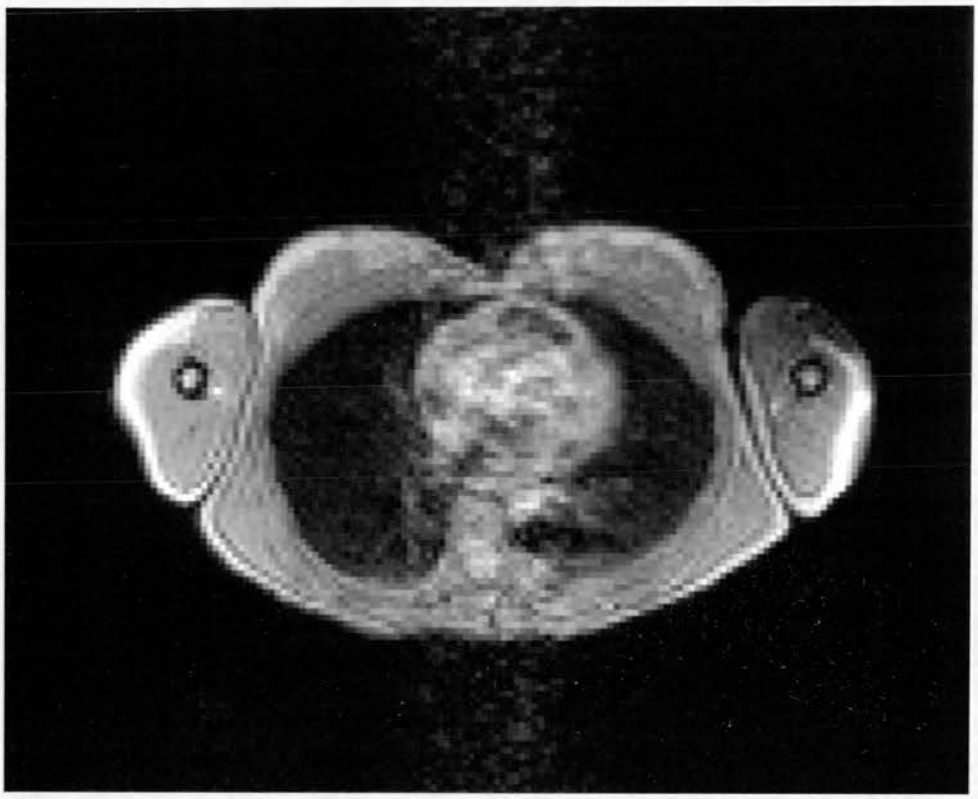

Figure 3.12.

A field echo image of the heart, acquired without synchronisation with the cardiac cycle. A random distribution of signal can be seen in the phase encoding direction as a result of cardiac motion.

different signal acquisitions. In order to image the cardiovascular system therefore, a method is required which allows each data acquisition to be synchronised with the cardiac cycle. This would allow cardiac anatomy to be imaged and blood flow velocity to be measured at specific points in the cardiac cycle.

3.8.1. Synchronisation with the Cardiac Cycle

The improvement in the quality of images of the heart obtained by cardiac synchronisation was demonstrated as early as 1982 (Pykett, 1982; Alfidi et al, 1982). The majority of methods employed synchronise the NMR data acquisition with either the R-wave of the ECG signal, or the peripheral pulse (Steiner et al, 1983; Lanzer et al, 1984).

Synchronisation with the peripheral pulse is achieved using the technique of plethysmography (Hyman and Winsor, 1961), in which a blood pressure cuff fitted with a piezo-electric pressure transducer is placed on the arm or finger. The main drawback of this method is the significant delay between the ECG R-wave and the detection of the peripheral pulse. Steiner and his co-workers found that this delay was 180-200 milliseconds on the arm and 280-300 milliseconds on the finger. It was therefore not possible to acquire data at early systole and the delay could vary significantly, making accurate synchronisation difficult. A further drawback found with plethysmography was that movements of the arms or fingers, or the flexing of muscles, resulted in artefacts being superimposed on the pulse waveform which caused artificial synchronisation signals.

Synchronisation with the electrocardiographic (ECG)

signal was more successful. Triggering the NMR sequence from the R-wave allows imaging to be performed during early systole and since the ECG waveform is more closely related to cardiac motion than the peripheral pulse, the synchronisation is more accurate. There are however problems associated with this technique. Steiner et al (1983), found that currents induced in the ECG leads resulted in artefacts appearing on the ECG waveform. Furthermore, the ECG leads could introduce external radiofrequency noise into the imaging system causing a reduction in signal to noise ratio. Electronic filtering of the ECG leads was used to reduce this interference. Similar problems were reported by Lanzer et al (Lanzer et al, 1984; Lanzer et al 1985). In the later of these publications they describe their hardware in some detail: An optical fibre link was used to isolate the patient from power line leakage currents coming from the ECG detection system. This link also served to prevent external noise from being transmitted into the NMR system.

With all the above techniques, a time delay can be added to choose a particular point in the cardiac cycle at which imaging is performed. The main drawback of cardiac-synchronised imaging is that the pulse sequence repetition time is dictated by the heart rate, which can lead to long scan times.

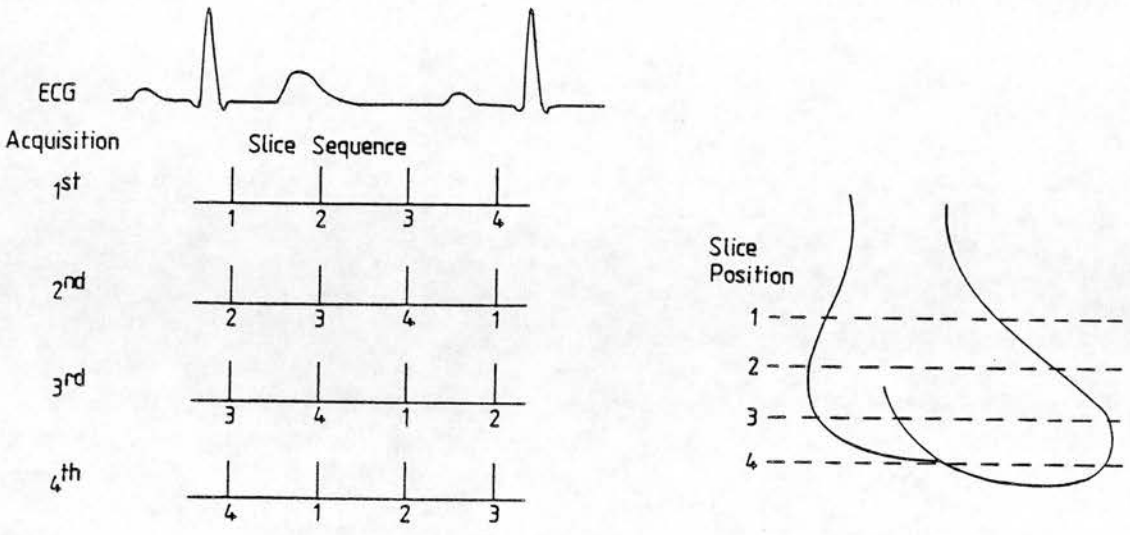

Figure 3.13.

In order to acquire images at four anatomical levels and at four different points in the cardiac cycle, four separate multiple-slice acquisitions are performed and the slice sequence is rotated for each acquisition.

3.8.2. Multiple Frame Acquisition

When imaging the heart, images are often required at more than one point in the cardiac cycle. For example, it may be necessary to obtain images both at end systole and at end diastole. If just one anatomical section is required, then the whole acquisition must be repeated for each point in the cycle. If multiple anatomical sections are required, then they can all be acquired in the same acquisition, although each section will correspond to different points in the cardiac cycle (figure 3.13).

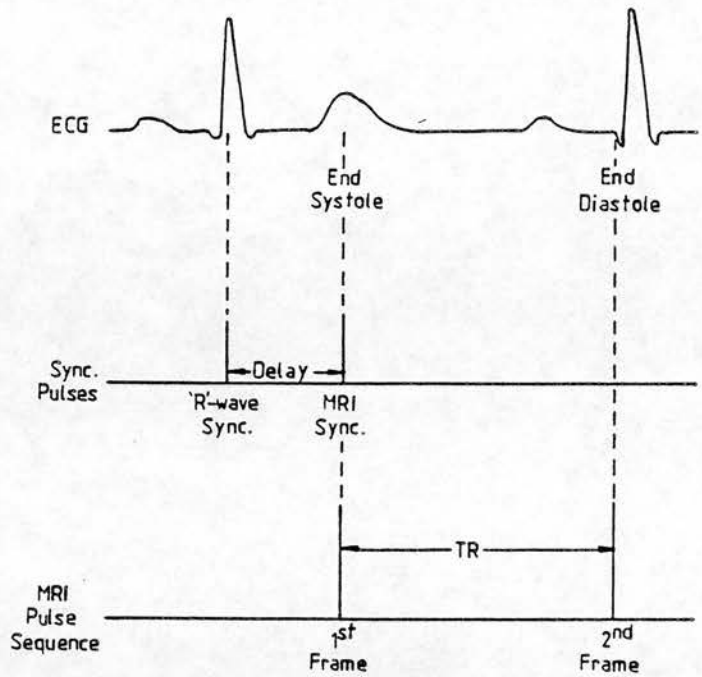

Figure 3.14.

Cardiac synchronised images can be acquired at end systole and end diastole in a single acquisition by setting a suitable delay to the first frame and a suitable repetition time value, TR to the second frame.

In order to obtain all the images required, the acquisition must then be repeated, each time rotating the temporal order of the sections until each section has been imaged at each point in the cycle (Crooks et al, 1984; Fisher et al, 1985).

Whilst a cardiac-synchronised, multiple slice acquisition is an efficient way of acquiring multiple images at multiple levels at multiple points in the cardiac cycle, if only one anatomical level is required, it becomes

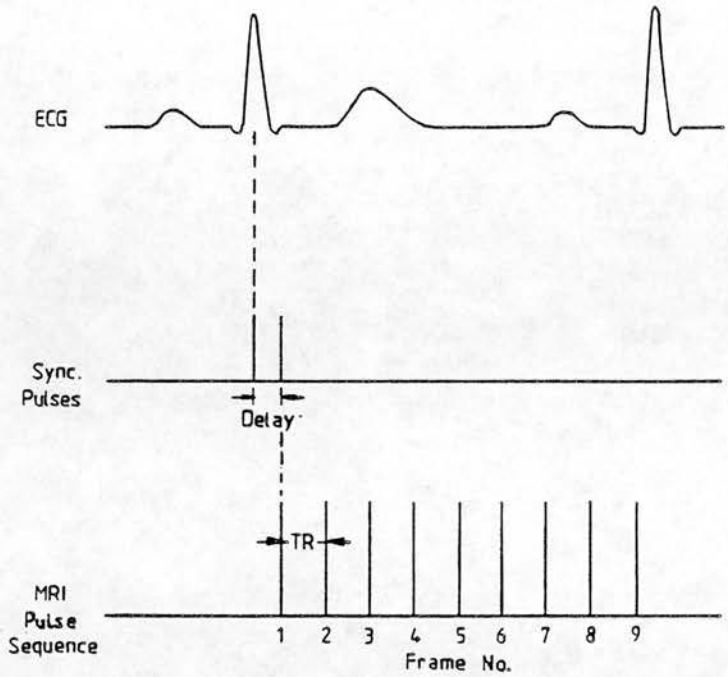

Figure 3.15.

Multiple Frame Imaging: Cardiac synchronised images can be acquired throughout the cardiac cycle by using a short delay and a short repetition time TR.

more efficient to acquire images at multiple points in the cardiac cycle during the same acquisition. For example, if end systolic and end diastolic images are required, two data acquisitions can be triggered from the same R-wave; one with a short delay and one with a long delay (figure 3.14). If images are required at more points in the cardiac cycle the pulse sequence is repeated several times during each cardiac cycle (figure 3.15). This is known as multiple frame imaging and each image is referred to as a frame. A set of images obtained at the level of the ventricles using multiple frame acquisition is shown in figure 3.16.

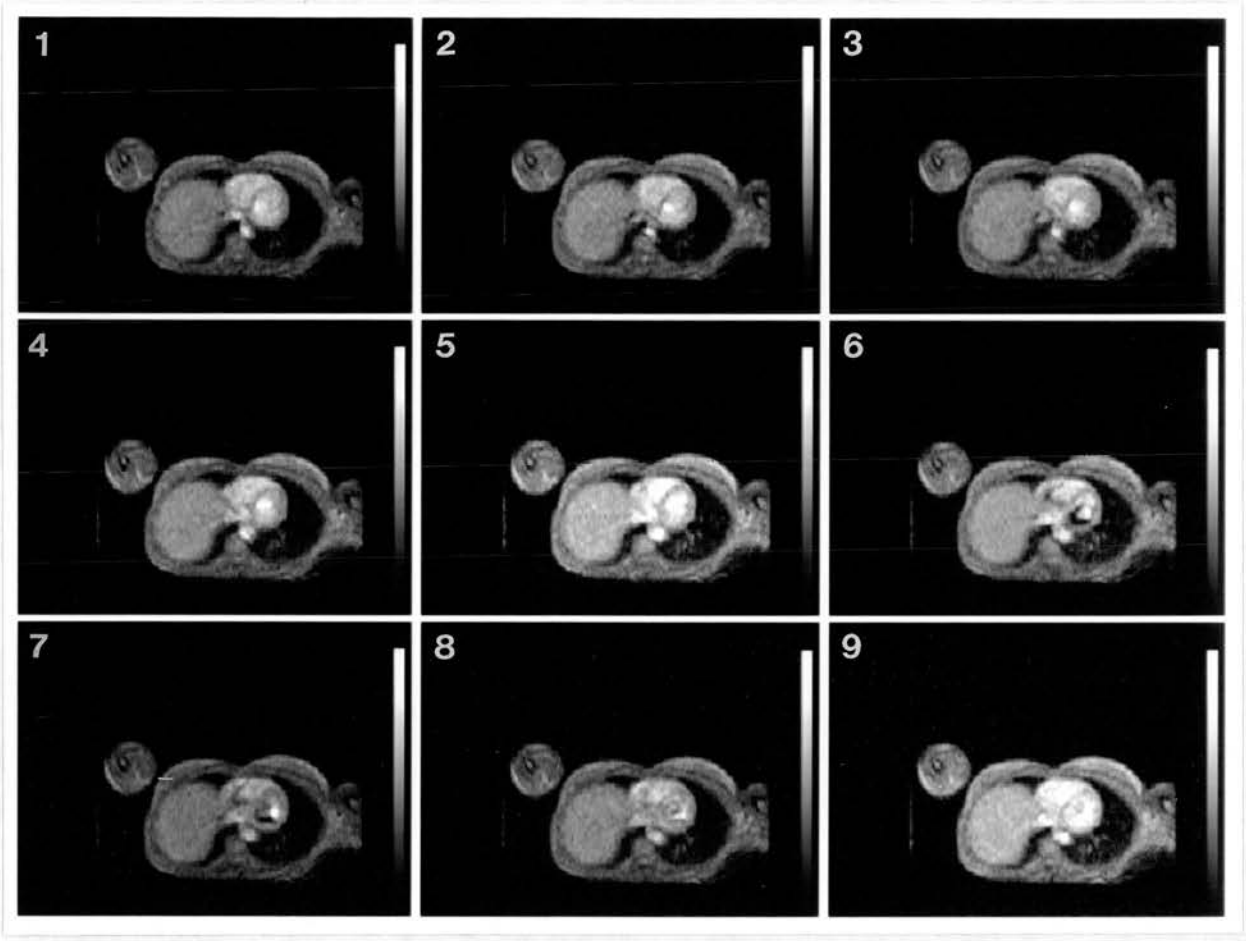

Figure 3.16.

Set of field echo images acquired in the transverse plane through the left and right ventricles of the heart using multiple frame imaging. The frame numbers are shown. These images were acquired using a reduced excitation angle of 60° and a repetition time of 100 milliseconds.

Multiple frame imaging requires rapid repetition of the pulse sequence following each R-wave trigger pulse. The signal from stationary material is therefore often reduced by the partial sauration effect. This effect is usually less marked for the first frame following the

R-wave synchronisation pulse, since it tends to have a greater recovery time than the later frames. If a field echo pulse sequence is being used, reduction of the excitation angle reduces this partial saturation effect.

If a spin echo pulse sequence is being used to acquire multiple frames, a method proposed by Waterton et al (1985), can be used to equalise the pixel intensities in each frame. This is achieved by gradually increasing the excitation angle for each successive frame. The minimum temporal resolution that can be achieved using this method, within the limits of acceptable signal to noise ratio, is five, is fairly coarse (of the order of 200ms).

For all multiple frame acquisition techniques, the temporal resolution can be improved by repeating the acquisition and adding a time delay to the start of the first frame. This process can be repeated until the desired temporal resolution is obtained.

Images which have been acquired throughout the cardiac cycle using a multiple frame acquisition, such as those shown in figure 3.16, can be displayed rapidly one after the other in order to give the impression of motion. This form of display, known as a cine loop, can help to identify moving structures and the phases of the cardiac cycle more easily.

3.9. A Practical Phase Mapping Technique

In this section a practical phase mapping technique for flow velocity measurement is proposed, which is suitable for clinical use. The limitations of early phase mapping techniques are discussed in section 3.3, and some of the requirements for a clinically useful phase mapping technique are outlined. In sections 3.4 to 3.8, a number of ways in which the limitations of phase mapping techniques can be overcome are discussed. The phase mapping technique proposed in this section was suggested in 1986 (Ridgway and Smith, 1986; see Appendix IV). It combines many of the features described in the previous sections, and also introduces a new approach to velocity encoding. The main features of the proposed phase mapping technique are as follows:

a) The technique is based on a field echo pulse sequence.

b) The technique can be synchronised with the cardiac cycle using the subjects ECG signal and multiple frame acquisitions can be performed.

c) The slice selection and frequency encoding gradient waveforms are modified to remove accidental velocity-related phase modulation.

d) Controlled, velocity-related phase modulation is achieved by increasing the separation between one pair of bipolar gradient pulses.

e) Two interleaved acquisitions are performed and the phase maps subtracted in order to remove unwanted phase modulations.

These features are discussed in more detail in the following sections.

3.9.1. The Use of a Field Echo Pulse Sequence

In order to avoid signal losses due to the spin washout effect, (section 2.1.2), a field echo pulse sequence is used as the basis for this phase mapping technique (section 3.4). This allows a strong signal to be obtained from blood flowing through the slice in the absence of phase dispersion (section 2.1.1). In addition, at fast repetition rates, the partial saturation effect can be reduced in field echo pulse sequences, by reducing the excitation angle. Therefore the field echo pulse sequence is more suitable for use in a multiple frame imaging technique (sections 3.4 and 3.8.2). The basic field echo pulse sequence is shown in figure 3.17.

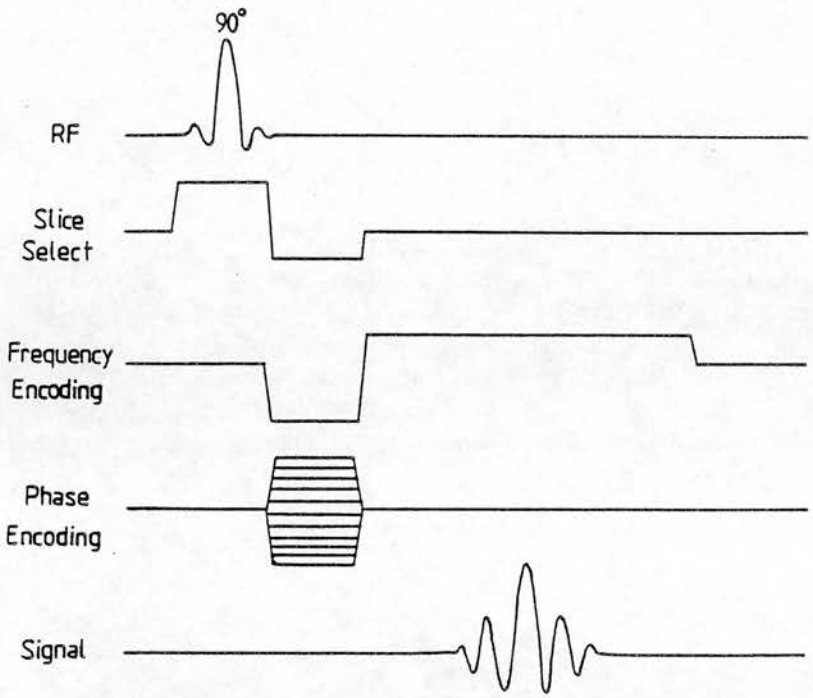

Figure 3.17.

The field echo pulse sequence which is to be used as the basis for the proposed phase mapping technique.

3.9.2. Cardiac Synchronisation

In order to measure flow velocities at a particular point in the cardiac cycle, it is necessary to synchronise the data acquisition with the subjects ECG signal (section 3.8.1). The use of the ECG signal is considered to be more precise than use of the peripheral pulse detection (Steiner et al, 1983; Lanzer et al, 1984). In order to obtain velocity waveforms in the case of pulsatile flow, multiple frame acquisition should also be possible.

3.9.3. Constant Velocity Desensitisation

Accidental motion-related phase modulation both leads to inaccuracies in velocity-related phase measurements and causes signal losses as a result of phase dispersion (sections 3.3 and 3.5). In the field pulse sequence shown in figure 3.17, the main causes of accidental phase modulation are the bipolar forms of the slice-selection gradient waveform in the presence of flow through the slice, and the frequency-encoding gradient waveform in the presence of flow in the slice (section 2.2.7). In the proposed tecnique, velocity-related accidental phase modulation is compensated for by inserting an additional bipolar pulse pair after the slice-selection gradient pulse pair, and before the frequency-encoding gradient pulse pair, as shown in figure 3.18 (section 3.5.1). The polarities of the additional pulse pairs are opposite to those of the existing pairs. The magnitudes of the new gradient pulses are calculated by applying the rephasing condition to the gradient waveform in the case of constant velocity motion.

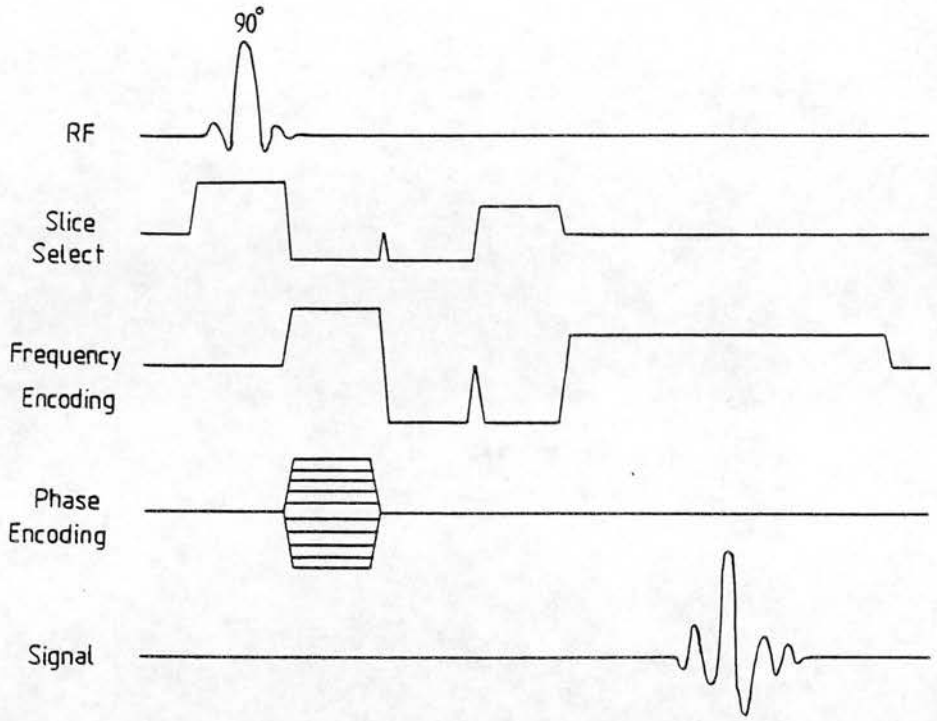

Figure 3.18.

The field echo pulse sequence shown in figure 3.17 is here modified to avoid velocity-related phase modulation, by inserting additional bipolar pulse pairs in to the slice-selection and frequency-encoding gradient waveforms.

3.9.4. Controlled Velocity Related Phase Modulation

The field echo pulse sequence shown in figure 3.18 has been modified to avoid velocity-related accidental phase modulation, by inserting additional bipolar pulses in to both the slice-selection and frequency-encoding gradient waveforms. In order to produce velocity dependent phase modulations in a controlled way, one of the gradient

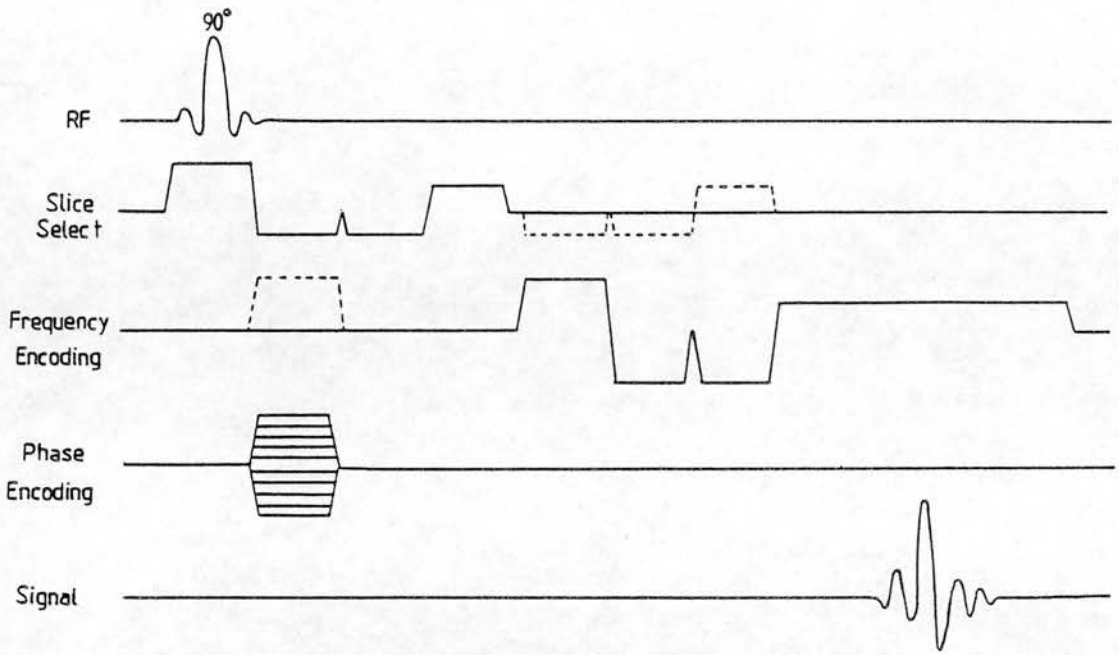

Figure 3.19.

The velocity-compensated field echo pulse sequence of figure 3.18 is further modified to produce velocity dependent phase modulations in a controlled way. To measure velocity components through-the-slice, the last three pulses of the slice-selection gradient waveform are applied later in the sequence (dotted line); To measure velocity components in-the-slice, the first pulse in the frequency-encoding gradient waveform is applied earlier in the pulse sequence.

waveforms is further modified by increasing the time separation between one of the bipolar pulse pairs, whilst keeping the pulse magnitude constant (figure 3.19). This new technique for velocity encoding was first suggested in 1986 (Ridgway and Smith, 1986; see appendix IV). For the measurement of flow velocity components perpendicular

to the image plane, the last three pulses in the slice-selection gradient waveform are applied later in the signal evolution period. For flow velocity components in the frequency-encoding direction, the first pulse in the frequency-encoding gradient is applied earlier in the evolution period.

This method of velocity encoding has the advantage over other methods in that the gradient magnitude does not have to be altered in order to produce the required velocity sensitivity. The same gradient pulses are applied, irrespective of the degree or direction of velocity encoding which is required. The velocity encoding process is therefore independent of the other imaging parameters, such as the slice thickness or the field of view. This method is also less susceptible to the errors introduced by the unwanted magnetic field gradients discussed in section 3.6.2. Any phase modulation caused by these errors is independent of the temporal position of the gradient pulses, and can therefore be removed by the subtraction of two phase maps as discussed in the next section.

One drawback of this method of velocity encoding is that it extends the echo time of the pulse sequence. This reduces the signal-to-noise ratio of the imaging technique, and increases the sensitivity of the pulse sequence to accidental phase modulation in the presence

of higher orders of motion. However, in order to encode most velocities encountered in-vivo, the increase in echo time required is estimated to be in the range of 1 to 5 milliseconds, which is not excessive.

3.9.5. Interleaved Acquisitions and Phase Map Subtraction

In section 3.7.4, a method of removing accidental phase modulations was described, in which two acquisitions were performed and the resultant phase maps were added together (Van Dijk, 1984). Whilst this technique removes unwanted phase modulations related to motion, phase modulations unrelated to motion remain. Since a field echo pulse sequence is proposed as the basic pulse sequence for this technique, the effects of magnetic field inhomogeneity and magnetic susceptibility have a marked influence on the phase values within stationary tissue (sections 3.6.1 and 3.6.3). It is therefore proposed to perform two acquisitions and to subtract the resultant phase maps.

In the proposed technique, one acquisition is performed using the velocity-compensated pulse sequence shown in figure 3.18, while the other acquisition is performed using the velocity encoding method described in the previous section (figure 3.19). Provided that the rephasing condition is satisfied, no velocity-related

phase modulation is produced by the velocity-compensated pulse sequence (section 3.5.1). However, the velocity-encoded pulse sequence produces a phase modulation, ϕ, in the presence of motion of constant velocity, v, which has a dependence given by (section 2.2.6),

$$\phi = \gamma G v t_w T \qquad 3.19$$

where G is the magnitude of the gradient pulses, t_w is their duration and T is the increase in separation of the bipolar flow-encoding gradient pulses.

The field echo time is adjusted to be the same for both acquisitions (figure 3.19). Therefore, the phase modulations caused by magnetic field inhomogeneity, chemical shifts, and changes in magnetic susceptibility will be the same for both acquisitions and will cancel out when the phase maps are subtracted. In order to avoid the problems of subject movement or magnetic field drift between the two acquisitions, the two pulse sequences are interleaved. This avoids the possibility of mis-registration when subtracting the two phase maps. This subtraction technique has the added advantage that any accidental phase modulation specific to motion, which has not been removed by pulse sequence desensitisation, will be removed on subtraction of the phase maps. The only remaining observable phase modulation should be that due to motion in the direction corresponding to the

altered gradient waveform.

3.9.6. Summary of the Proposed Pulse Sequence

An interleaved pulse sequence is proposed which allows one direction of flow to be imaged at a time and which removes the unwanted phase modulations due to other causes. Two almost identical acquisitions are performed using a field echo pulse sequence, which has been modified to reduce accidental velocity-related phase modulation, by inserting additional bipolar pulse pairs in to the slice-selection and frequency-encoding gradient waveforms. The only difference between the two acquisitions is in the the interpulse separation between one of the bipolar pulse pairs. The phase modulation, ϕ, observed for a velocity, v, following subtraction of the phase maps, is given by

$$\phi = \gamma G v t_w T$$

where G is the magnitude of the gradient pulse, t_w is the temporal duration of the gradient pulse, and T is the magnitude of the temporal shift of the pulse between the two acquisitions. There is therefore a simple linear relationship between the observed phase modulation and the velocity, and the velocity sensitivity can be easily controlled by varying the value of T.

Implementation of the Flow Imaging Technique

4.0. General Description of the MRI System

The phase mapping technique for flow measurement, described in section 3.9, was implemented on the MRI system at the Royal Infirmary, Edinburgh (figure 4.1). The system has a nominal operating field strength of 0.08 Tesla, (a nominal operating frequency of 3.4 MHz) and is based on a vertical field, resitive magnet which is water cooled (Hutchison et al, 1980; Redpath et al, 1987).

Figure 4.1.

The MRI system at the Royal Infirmary, Edinburgh.

The system was manufactured by M&D Technology Ltd, and was installed at the Royal Infirmary in March 1983 (Smith et al, 1984). Initially, only single-slice acquisitions using field echos were available. However, in 1986 the MRI system was upgraded to allow electronic slice positioning, simultaneous multiple slice acquisition, and true spin echo imaging.

This system upgrade required major changes to be made to both the computer hardware and to the system software. Although the flow imaging technique was implemented both before and after the upgrade, the following sections describe the developments carried out on the upgraded system. The technique was implemented almost entirely through software development, with only a minimum of hardware development. However, it is important to describe the computer hardware in some detail, as it determined how the flow imaging technique was implemented, and imposed some constraints on the design of the pulse sequence.

4.1. Computer Hardware

The upgraded MRI system uses two 16-bit PDP 11 computers (Digital Equipment Corporation, (DEC), Ltd); one for data processing and one for pulse sequence control and data acquisition (figure 4.2).

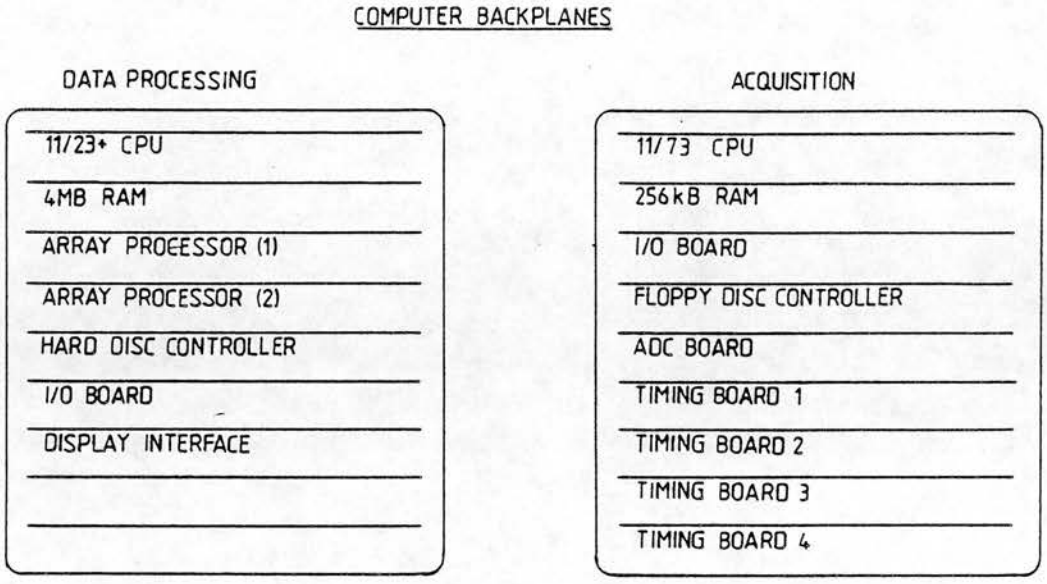

Figure 4.2.

Diagram showing the backplane configuration of the MRI system Acquisition and Data Processing computers.

The operating system used by both computers (RT11FB; DEC Ltd), is of the single user type, capable of supporting both foreground and background tasks. The MRI system software source codes are written in either FORTRAN IV or MACRO-11 assembly language.

A PDP 11/23+ with 4 Megabytes of random access memory performs most of the data processing and also serves as the operator's console. An additional array processor (SKYMNK; Sky Computers Inc., Massachusetts), increases the data processing speed. Two removable hard discs, each having a capacity of 10 Megabytes, store the operating system and the MRI system software, and are

used for the temporary storage of reconstructed images, before they are archived. The 11/23+ computer is interfaced to a 10 bit image display (Supervisor 214, Gresham Lion PPL Ltd.), which has a resolution of 384x296 pixels and can therefore accommodate up to six 128x128 images. Data input and output is achieved through a multi-channel I/O board which has both serial and parallel data ports. This I/O board provides communication between the operator's console and the patient couch, the acquisition computer, and an independent viewing console.

The acquisition computer is a PDP 11/73 with 256 Kbytes of memory. The timing of the pulse sequence and data acquisition is controlled by electronic timing boards which occupy slots in the PDP 11/73 computer backplane (figure 4.2). In the upgraded system, there are four timing boards. An additional board houses the analogue-to-digital converters (ADCs) which digitise the NMR signal. The operation of the timing boards is discussed in more detail in section 4.2.4. The acquisition computer also has an I/O board installed, which provides parallel and serial links for communication with the data processing computer and system electronics, and for the transmission of acquired data to the 11/23+ for data processing. The I/O board is also used to accept the ECG and respiratory gating signals. The operating system and acquisition software are loaded from floppy disc.

4.2. Design and Implementation of the Pulse Sequence

The basic field echo pulse sequence which was already available on the MRI system is shown in figure 3.17. (page 104). Initially, the flow imaging technique, described in section 3.9, was implemented without velocity-compensation by a simple modification of this field echo sequence (Ridgway and Smith, 1986; Appendix IV). An interleaved pulse sequence was developed which exploited the velocity-related phase modulation produced by the existing bipolar gradient waveforms of the slice-selection and frequency-encoding gradient waveforms (figure 4.3). The two field echo pulse sequences used in this interleaved sequence were almost identical, the only difference between them being the inter-pulse separation of the bipolar gradient pulse pair of one of these waveforms. (section 3.9.4). On subtracting the two phase maps obtained using this pulse sequence, the velocity-related phase modulation, present on the subtracted image (section 3.9.5), is given by

$$\phi = \gamma G v t_w T_{diff} \qquad 4.1$$

where G and t_w are the magnitude and duration of the shifted gradient pulse, T_{diff} is the difference between the two interpulse separations, and v is the velocity component in the encoded direction.

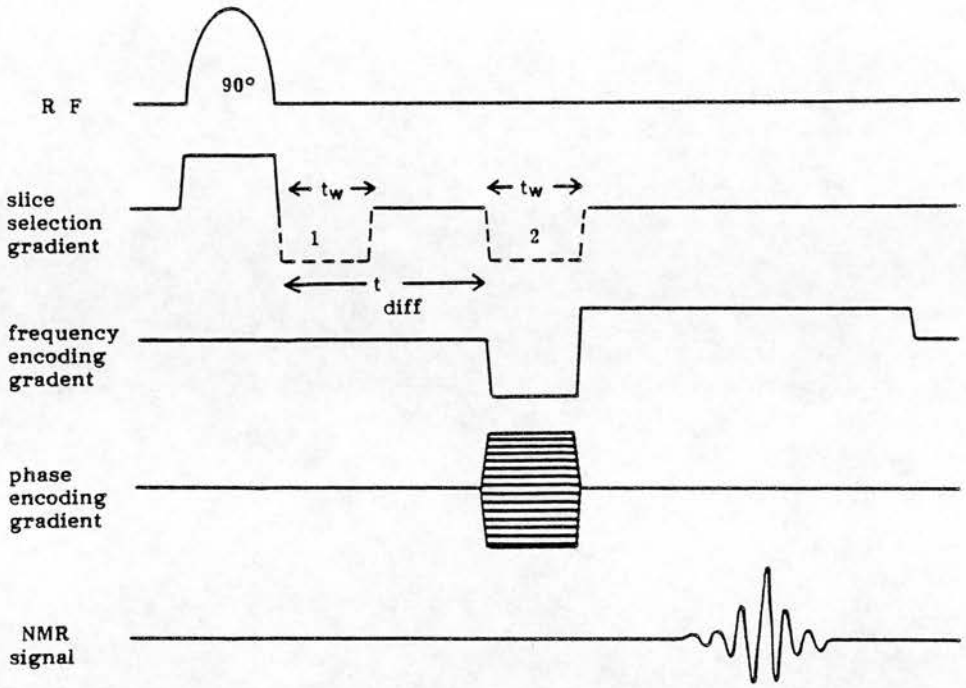

Figure 4.3.

The flow imaging technique was initially implemented without velocity compensation. In this case the position of the rephase pulse, (dotted lines), of the slice-selection gradient is altered to produce additional phase modulation for flow through the slice. A separate acquisition is performed with the rephase pulse in each position (1 & 2).

Phase modulation caused by motion in other directions is removed by the phase map subtraction, as is any phase modulation unrelated to motion. The early results obtained using this pulse sequence have been published (Ridgway and Smith, 1986; Appendix IV).

4.2.1. Desensitisation of the Pulse Sequence

In order to fully implement the flow imaging technique and to reduce phase dispersion caused by accidental phase modulations, the field echo pulse sequence was further modified by desensitising the slice-selection and frequency-encoding gradient waveforms, with respect to constant velocity motion (section 3.9.3). This was achieved by inserting an additional bipolar pulse pair into each waveform (figure 3.18, page 106).

The magnitudes of the new gradient pulse pairs were calculated, using the fact that the phase change in the presence of constant velocity motion due to the new pulse pair, should exactly cancel the phase change due to the existing pulse pair. Therefore, (from section 3.5.1),

$$\partial vGtT = \partial vG't'T' \qquad 4.2$$

where G is the gradient magnitude, t is the pulse width, T is the pulse separation and G', t' and T' are the new pulse pair parameters. This equation assumes that each of the existng pulse pairs are symmetrical, whereas in fact this is not the case for either the frequency-encoding or the slice-selection gradient waveforms. A more generalised formulation is therefore required.

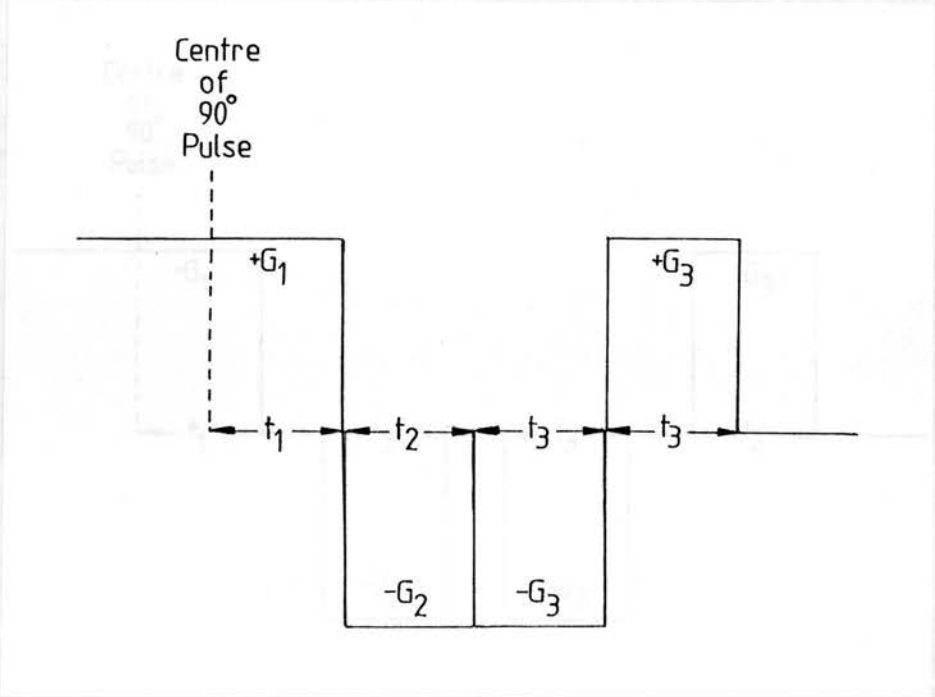

Figure 4.4.

The velocity-compensated slice selection gradient waveform showing the notation used in equations 4.4 and 4.5.

In order to derive this formulation, the gradient waveform is assumed to consist of perfectly rectangular pulses, although in practice, the gradient pulse edges are generated using a combination of linear and exponential functions. For the slice selection waveform, we shall use the notation shown in figure 4.4. Since the rephasing condition requires the phase modulation to be zero for constant velocity, from equation 3.7b (section 3.5.2),

$$0 = \gamma v \int G(t)\, t\, dt \qquad 4.3$$

Using the notation of figure 4.4 and expanding gives:

$$0 = \int_{0}^{t_1} G_1 t \, dt - \int_{t_1}^{t_1+t_2} G_2 t \, dt - \int_{t_1+t_2}^{t_1+t_2+t_3} G_3 t \, dt + \int_{t_1+t_2+t_3}^{t_1+t_2+2t_3} G_3 t \, dt \qquad 4.4$$

Integrating this obtains:

$$0 = G_1 t_1^{\,2} - 2G_1 t_1 t_2 - G_2 t_2^{\,2} + 2G_3 t_3^{\,2} \qquad 4.5$$

The value of G_1 is dictated by the width of the slice being acquired (section A2.6.4). If the existing gradient pulses are not changed and the durations of the new pulses are fixed, then G_3, the magnitude of the two new pulses, is the only unknown in equation 4.4 and can therefore be calculated. This calculation was performed for slice widths of 8, 10, 12, 14, 16, 18 and 20 millimetres, and values of $t_1 = t_2 = t_3 = 3.6$ milliseconds. The values of G_1, G_2 and G_3 for each of these slice widths are shown below in table 4.1. The values given are entered into the random access memory of the timing boards, which generate the gradient waveforms.

Slice Width	G_1	G_2	G_3
8mm	764	824	854
10mm	611	660	685
12mm	509	550	570
14mm	437	471	488
16mm	382	413	429
18mm	340	363	375
20mm	306	330	342

Table 4.1.

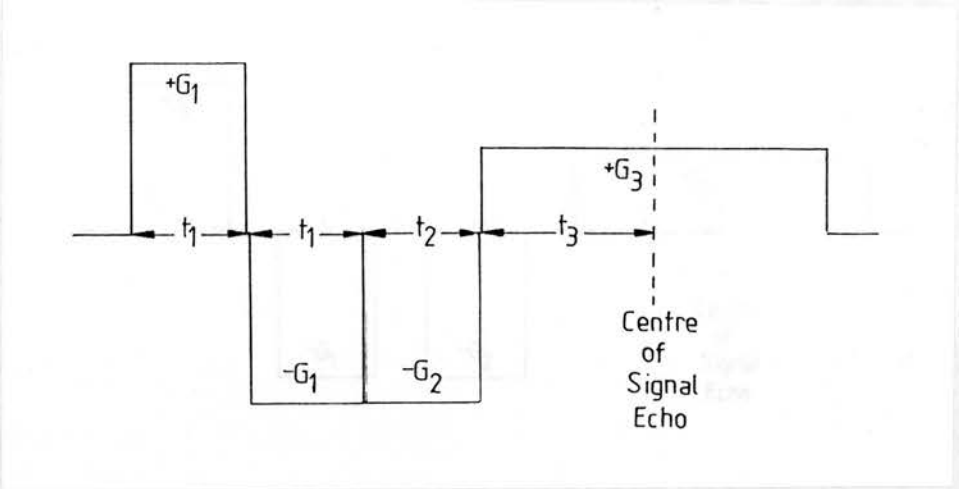

Figure 4.5.

The velocity-compensated frequency-encoding gradient waveform, showing the notation used in equation 4.6.

Similar calculations were performed for the frequency-encoding gradient waveform. The notation is shown in figure 4.5. The corresponding equation is

$$0 = -2G_1t_1^2 - G_2(t_2^2+4t_1t_2) + G_3(4t_1t_3+2t_2t_3+t_3^2) \quad 4.6$$

In this case, the value of G_3 is dictated by the field of view, the number of data samples acquired and by the sampling frequency of the data acquisition period. (section A2.6.2). The pulse widths and the gradient magnitude, G_2, are fixed, leaving the magnitude of the new pulses, G_1, as the only unknown in equation 4.6. This equation was solved for all the combinations of field of view, sampling frequency, and sample number which were to be used for flow imaging. The values of G_1, G_2, and G_3 are given in table 4.2 for each field of view and data sampling configuration.

Field of View	No of Samples	Sampling Frequency	G_1	G_2	G_3
160mm	128	10kHz	522	853	384
200mm	128	10kHz	419	684	308
200mm	128	5kHz	906	684	154
256mm	128	10kHz	327	533	240
256mm	128	5kHz	706	533	120
288mm	128	10kHz	281	474	212
288mm	128	5kHz	615	474	106
384mm	128	10kHz	211	358	160
384mm	128	5kHz	464	358	160
384mm	256	10kHz	940	711	160
448mm	128	10kHz	167	312	137
448mm	256	10kHz	789	615	137

Table 4.2.

Table showing the values of G_1, G_2 and G_3, (figure 4.5), calculated for each field of view and data sampling configuration.

4.2.2. Acceleration-Related Phase Modulation.

The addition of the second bipolar pulse pair to the field echo pulse sequence, causes accidental phase modulation in the presence of acceleration (section 3.7.1). For a sequence of four rectangular pulses, as shown in figure 4.6, the phase change, ϕ, in the presence of motion with a constant acceleration a, is given by

$$\phi = Gvt(T_1-T_2) + \tfrac{1}{2}\gamma Gat_w\{4t_w^2+t_w(7T_2+2T_o-T_1) + (T_2^2-T_1^2)+T_1T_2+T_2T_o\} \quad 4.7$$

The first term of the right hand side of equation 4.6 is the velocity-dependent part of the phase modulation.

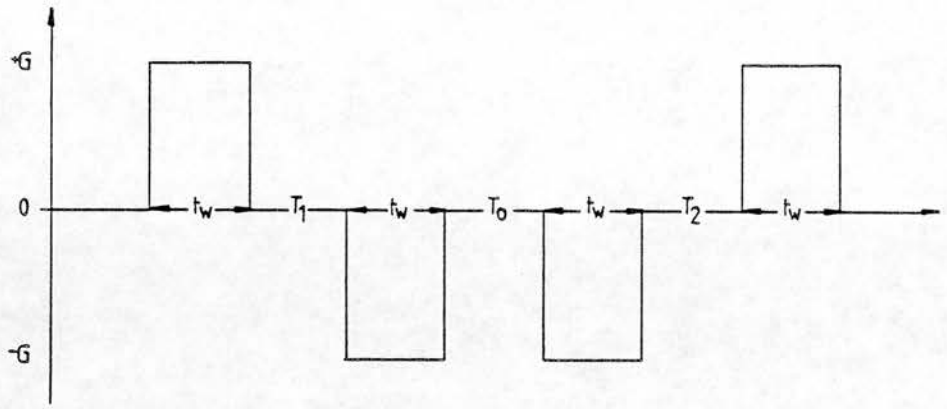

Figure 4.6.

Sequence of four quadrapolar gradient pulses showing the notation used in equation 4.7.

The second term of equation 4.6 is the acceleration-dependent part of the phase modulation. Accidental phase modulation due to acceleration is kept to a minimum if $T_o=T_1=T_2=0$. The desensitised pulse sequence is therefore designed with no time delay between the gradient pulses. The effective time separation, T_o, can be further reduced by merging the two middle pulses. In the pulse sequence described here, however, this was not done in order to retain the possibility of performing acceleration-encoded phase mapping. This could be achieved by varying T_o to control the acceleration-related phase modulation. There is no velocity-related phase modulation if $T_1=T_2$.

4.2.3. Velocity Imaging Using the New Pulse Sequence

In order to achieve velocity-dependent phase modulation, by consideration of the first term in the equation 4.6, either T_1 or T_2 must be non-zero for one of the two interleaved pulse sequences. By examining the second term, we see that a non-zero value for T_2 introduces a greater acceleration-related accidental phase modulation than T_1. It is therefore preferable to introduce a time delay, between the first and second pulse of the quadrapolar gradient waveform, in order to produce the required velocity-related phase modulation, whilst minimising the effects of acceleration. The resultant phase modulation is then linearly proportional to the velocity component in the direction of the gradient, and to the time shift introduced between the gradient pulses (section 3.9.5).

The above technique allows the imaging of velocity components in the slice-selection and frequency-encoding directions. Velocity components in the remaining direction can be measured in one of two ways: either the same technique could be used after switching the frequency-encoding direction with the phase-encoding direction, or a small bipolar pulse could be introduced into the phase-encoding gradient waveform in one of the interleaved pulse sequences (figure 4.7).

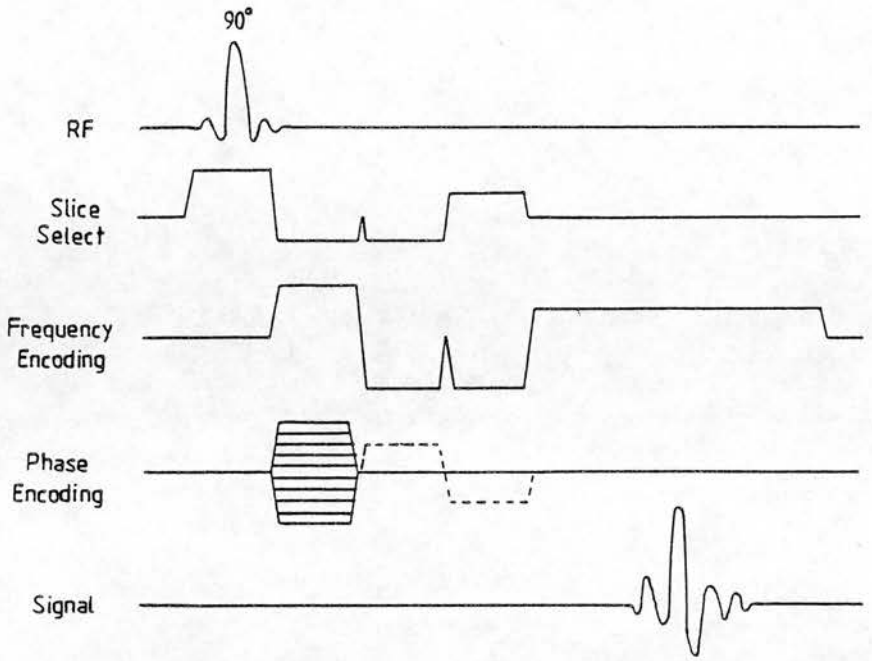

Figure 4.7

One method of performing velocity-encoded phase mapping, for velocity components in the phase-encoding direction, is to insert a pair of bipolar pulses in to the phase encoding gradient waveform (dotted line).

The flow measurement pulse sequence described in the previous sections was implemented on the Edinburgh MRI system by generating new gradient waveforms and pulse sequence timing data. In order to describe how this was done, it is first necessary to describe the operation of the electronic timing boards and the acquisition software in more detail.

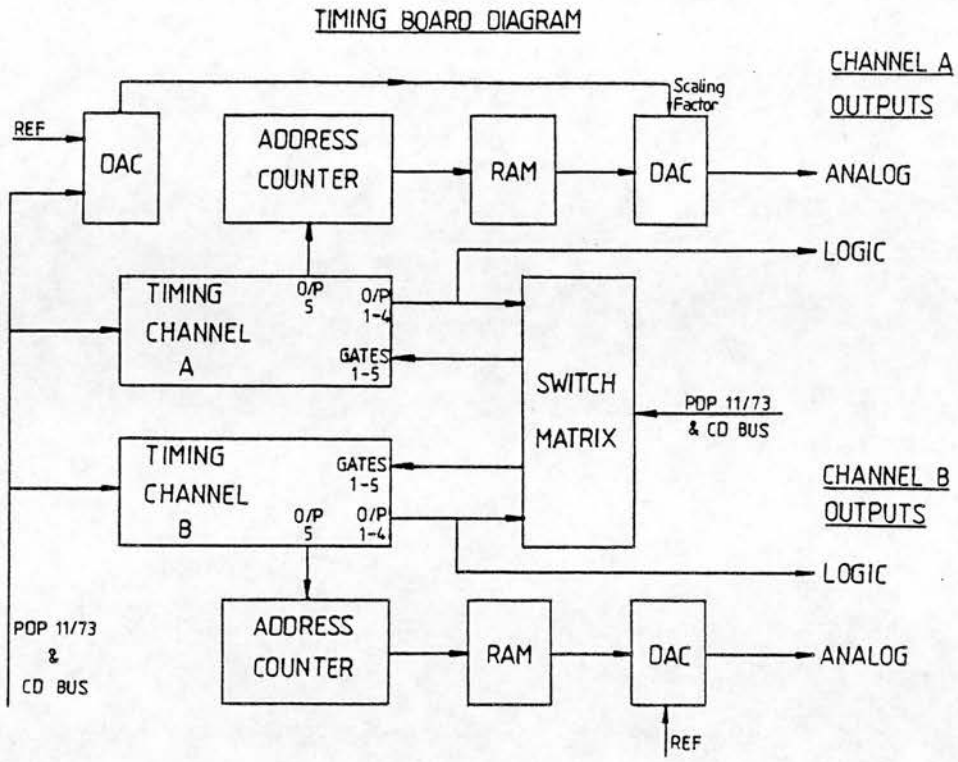

Figure 4.8.

Schematic diagram showing the layout of one of the electronic timing boards.

4.2.4. The Electronic Timing Boards

Each of the electronic timing boards (figure 4.8) is based on two programmable system timing controllers (Advanced Micro Devices; Am9513) forming two channels, A and B. Two kilobytes of random access memory (RAM) are allocated to each channel and are used to store the radiofrequency pulse envelopes and gradient pulse waveforms. The waveforms are output through a digital-to-analogue converter (DAC) to the inputs of the

gradient power supplies and the radiofrequency pulse modulator. The analogue output of the 'A' channels can be controlled by using a scaling factor, which can be updated by the acquisition software during a scan.

Each timing controller (and therefore each channel), has five timer-counter outputs. The fifth output is dedicated to act as a clock which increments the RAM address counter. The four remaining outputs can be used to gate or trigger any of the other counters on the same board, as determined by a programmable switch matrix. All the boards share the same clock signal which is passed from board 1 to the other boards via the C-D bus of the PDP11 backplane. The clock signal is derived from a frequency synthesiser (Model: PTS 500, Programmed Test Sources Inc.), which also generates the MRI system reference frequencies. The timer-counter outputs can also be passed between different boards using the switch matrix and the C-D bus, and can also be designated as clock sources for other counters, and as interrupt sources to the 11/73 processor using the switch matrix.

The counting mode of each individual timer-counter can be specified, (for example, whether it is to be gated, one-shot triggered, free running). The output of each timer-counter can be specified as a +ve edge pulse, a -ve edge pulse or as a toggled hi/lo output. Each timer-counter has two registers; a LOAD register and a

HOLD register. Depending on the mode selected, the counter can be loaded from the LOAD register only, so that it will always count the same period, or from both the LOAD and the HOLD register alternately, allowing two unequal time periods to be counted. The time period represented by the LOAD and HOLD register values is dependent on the frequency of the clock source for that counter.

The analogue outputs of each channel of the four timing boards are designated to particular tasks as follows:

Board 1 Channel A:	Phase-Encoding gradient pulse to the x-gradient amplifier.
Board 1 Channel B:	Frequency-Encoding and Slice-Selection gradient waveforms to the x-gradient amplifier.
Board 2 Channel A:	Phase-Encoding gradient pulse to the y-gradient amplifier.
Board 2 Channel B:	Frequency-Encoding and Slice-Selection gradient waveforms to the y-gradient amplifier.
Board 3 Channel A:	Phase-Encoding gradient pulse to the z-gradient amplifier.
Board 3 Channel B:	Frequency-Encoding and Slice Selection gradient waveforms to the z-gradient amplifier.
Board 4 Channel A:	RF 90° pulse envelope to the rf amplifier.
Board 4 Channel B:	RF 180° pulse envelope and AFP inversion pulse edges to the rf pulse modulator.

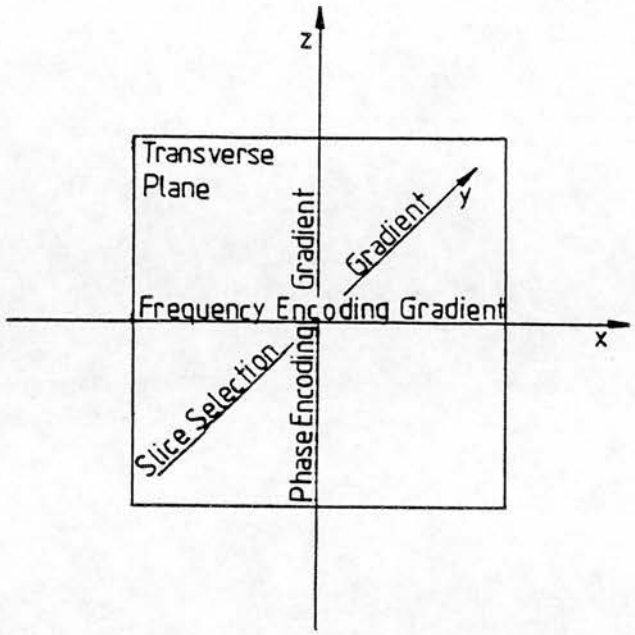

Figure 4.9.

Diagram showing the allocation of gradient waveforms to the x, y and z axes for imaging in the transverse plane.

The scaling factors applied to the outputs of channel A of boards 1,2 and 3 are used to increment the amplitude of the phase-encoding gradient pulse. The scaling factor of channel A of board 4 is used to alter the amplitude of the excitation pulse. This allows the excitation angle to be varied in field echo pulse sequences (section A2.1.2).

The scan orientation (section A2.6.6), is determined by scaling the gradient waveforms before they are loaded into RAM. For example, as shown in figure 4.9, imaging in the transverse plane requires the frequency-encoding gradient to be applied along the x axis, the slice-

selection gradient to be applied along the y axis, and the phase encoding gradient to be applied along the z axis. In order to achieve this, the frequency-encoding gradient waveform is given a scaling factor of unity when loaded into RAM on board 1, and a scaling factor of zero when loaded into RAM on boards 2 and 3. Similarly, the slice-selection gradient waveform is scaled by unity on board 2, and zero on boards 1 and 3, and the phase encoding gradient waveform is scaled by unity on board 3 and by zero on boards 1 and 2.

This arrangement has the advantage that the nine scaling factors can be calculated to mix the gradient waveforms and produce a scan orientation at any arbitrary angle. The main disadvantage is that the RAM address counter must step through the gradient waveforms even though they may have been set to zero. This is wasteful of the timer-counter allocation and RAM and, as we shall see, creates difficulties when time-shifting the velocity-encoding gradient pulses in an interleaved pulse sequence.

4.2.5. The Acquisition Software

The timing data for each pulse sequence is stored in a 'timing file'. The timing file contains the LOAD and HOLD register values for each timer counter, a code for the selected MODE of each timer counter, and a code for the setting of the switch matrix that designates the inputs and outputs of each of the timer-counters. The gradient pulse waveforms and rf pulse envelopes are also stored in a 'shapes file' in a form in which they can be loaded directly into RAM on the timing boards.

In the upgraded system, the timing and shapes files are generated and stored on one of the removable hard discs of the 11/23+. Before each scan is performed, the appropriate files are passed to the acquisition computer via a parallel interface. The timing files are then modified, depending on the imaging parameters set by the operator. Similarly, gradient pulse waveforms are modified depending on the selected scan orientation. The modified timing and shapes data are then downloaded onto the timing boards.

During a scan, up to five interrupt service routines (ISRs) are active on the acquisition computer. The first two of these ISRs perform a number of essential functions, including the updating of the phase encoding pulse amplitude, the switching of the acquisition

computer into a low-priority (quiet) state to reduce radiofrequency interference during data acquisition, and the disarming or re-arming of timer-counters as required. The third ISR updates the system frequency, by remote control of the frequency synthesiser. This controls the slice positioning in multiple slice acquisitions. The fourth ISR sets up the phase of the 180^{o} refocussing pulse in spin echo pulse sequences. The fifth ISR is only active when the cardiac synchronisation mode is selected. This routine initiates a pulse sequence on receiving an external trigger via one of the I/O channels. This is the only interrupt routine which is not initiated by the timing boards.

A background data acquisition program stores the digitised NMR data in a temporary buffer array as it is received from the ADC channels. Each data line is passed to the operator's console and is stored in extended memory, as the next line is acquired. If signal averaging is being performed, all the data corresponding to each line is summed in an accummulative buffer until the required number of data sets to be averaged is reached. This averaged data set is then transferred to the operator's console to be stored as before.

4.2.6. Pulse Sequence Implementation

In the pre-upgraded system, a simple form of the flow imaging pulse sequence was implemented, as described in section 4.2. In this case, the acquisition software was modified to shift the position of either the rephasing pulse of the slice-selection gradient waveform, or the dephasing pulse of the frequency-encoding gradient waveform, before each successive pulse sequence (section 4.2). This was achieved by adding extra program code to the interrupt service routine which was activated at the end of each pulse sequence to re-arm the timer-counters. The modified ISR updates the position of the gradient pulse by changing the value in the LOAD register of the appropriate timer-counter. The allocation of the timer-counters defined in the timing files were also modified to make this possible.

The increased number of timing boards in the upgraded system allows much greater flexibility when programming the flow imaging pulse sequences. However, a number of changes are required to the allocation of timing tasks to the timer counters: The B channels of boards 1,2 and 3 each has four timer-counters available for the slice-selection and frequency-encoding gradients.

The allocation of the channels to the gradient waveforms was dependent on the scan orientation. The mixing of

gradient waveforms to produce angled slices introduces a complication: the slice-selection and the frequency-encoding gradient waveforms overlap so that if the waveforms are mixed together, they become controlled by the same timer-counters. It is therefore impossible to re-position a pulse in one waveform without affecting the other. In order to avoid this problem it is necessary to create separate shapes files and timing files for angled slice acquisitions in which the slice selection and frequency encoding gradient waveforms do not overlap. This substantially increases the length of the velocity -compensated gradient waveform, and hence, the echo time.

The whole of each gradient waveform is stored in RAM with the exception of the readout pulse, for which only the pulse edges are stored. Whilst this reduces the number of timer-counters required to produce a series of consecutive gradient pulses, it uses a lot of space in RAM, and imposes a limitation on the maximum length of gradient waveform that can be used.

The allocation of tasks to the channel B timer-counters in a standard field echo pulse sequence is the same for boards 1, 2 and 3 (figure 4.10). Timer-counter B1 is allocated to a spoiler gradient which is applied in the slice selection direction between each pulse sequence. Timer-counter B2 is unused and timer-counter B3 is allocated to the gradient waveform preceding the

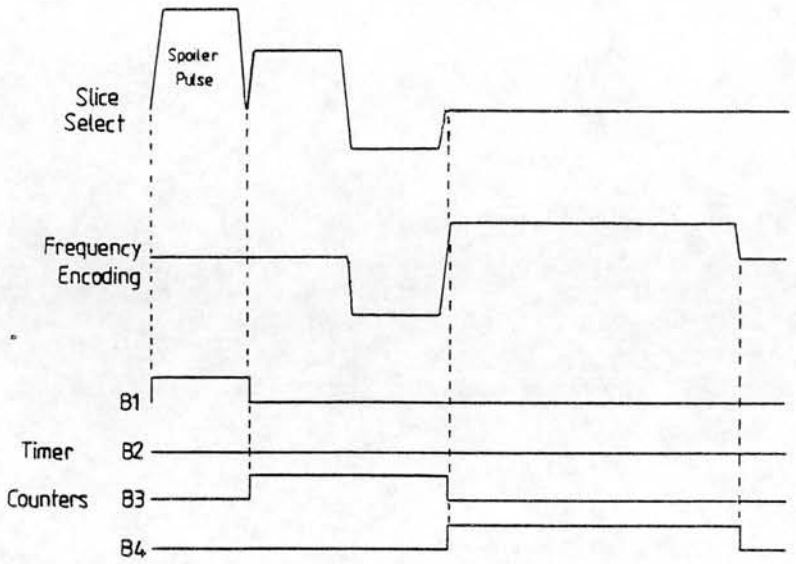

Figure 4.10.

Timing diagram showing the allocation of the channel B timer-counters to the gradient pulses for a field echo pulse sequence.

readout pulse. Timer-counter B4 is allocated to the readout pulse edges. The phase encoding gradient is controlled by timer-counter A4 on each board.

Three separate timing files are generated for the field echo pulse sequence, which correspond to three different data sampling times. The sampling time selected depends on the number of data samples being acquired, which is dependent on the resolution in the frequency encoding direction, and the sampling frequency, which is determined by the imaging bandwidth selected (sections A2.6.2 and A2.6.3).

In order to implement the flow imaging pulse sequences for both angled and non-angled slices, two separate timing files have been produced for each sampling time. In both files, the allocation of timer-counter B4 to the readout pulse edges was unchanged. The spoiler gradient pulse is attached to the front of the slice select waveform so that it occurs at the beginning of the pulse sequence, immediately before the excitation pulse. The excitation pulse is set 10 milliseconds later to accommodate this change. Figures 4.11 and 4.12 show the modified timing diagram for the slice-selection and frequency-encoding gradient waveforms for both non-angled and angled slice acquisitions, and indicate the allocation of timer counters in each case. Alternative timer-counter allocations are shown, depending on whether flow is being measured in the slice-selection direction, or in the frequency-encoding direction.

For the imaging of flow in either the slice-selection or frequency-encoding directions for non-angled slice acquisitions, timer-counter B3 is allocated to the spoiler pulse and the slice selection pulse. Timer-counters B1 and B2 are allocated to the three remaining gradient pulses of both the slice-selection and frequency-encoding waveforms, which overlap between the slice selection pulse and the readout pulse. The timer-counter allocation is modified by the acquisition

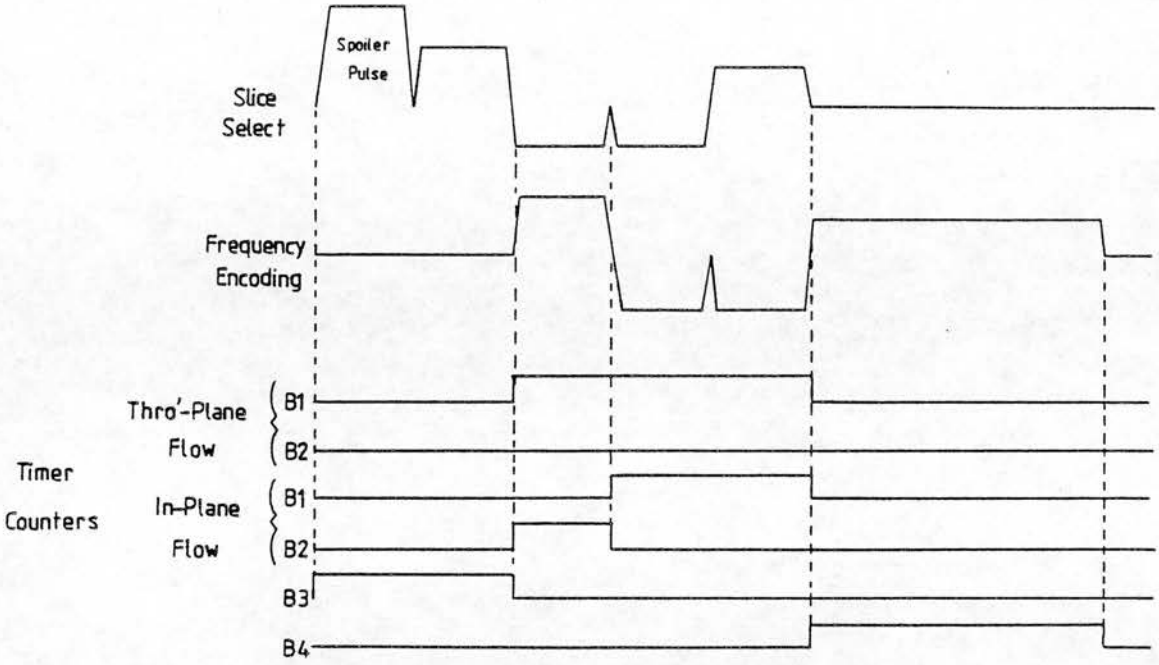

Figure 4.11.

Timing diagram showing the timer-counter allocation to the slice-selection and frequency-encoding grdaient waveforms for the flow imaging pulse sequence in the case of a non-angled slice acquisition. Alternative allocations are shown depending on whether through-plane or in-plane flow is being measured.

software before the timing data is loaded into the timing boards, depending on the direction of velocity encoding required (figure 4.11). For imaging of velocity components for flow in the slice, timer-counter B2 was allocated to the first of the three pulses and timer-counter B1 was allocated to the second and third pulses. This allowed the position of the first pulse of

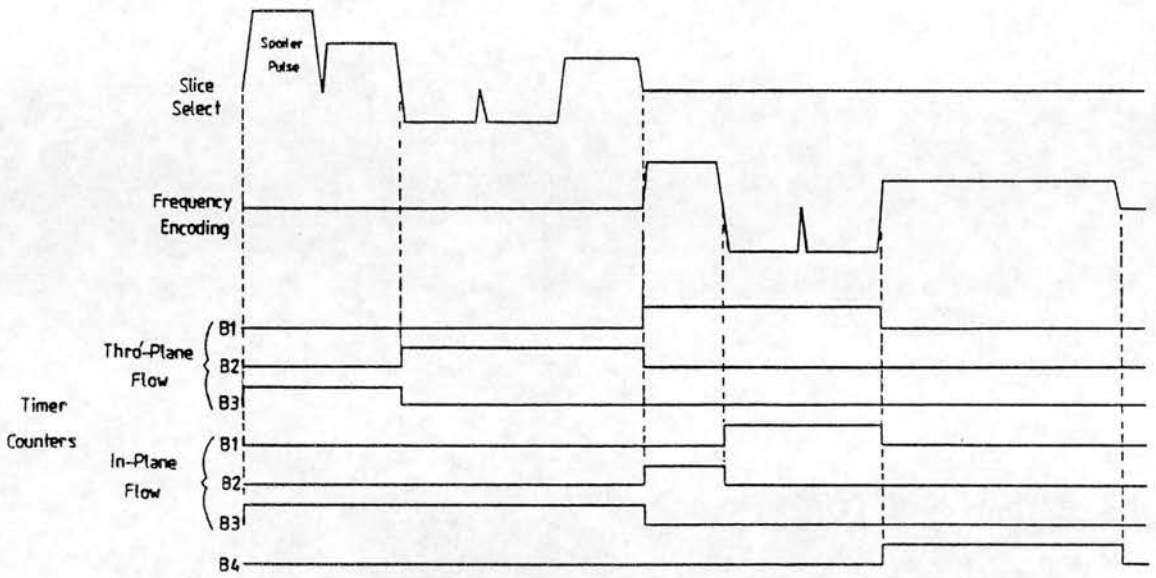

Figure 4.12.

Timing diagram showing the timer-counter allocation to the slice selection and frequency encoding grdaient waveforms for the flow imaging pulse sequence in the case of an angled slice acquisition.

the frequency encoding gradient to be changed by altering the value in the LOAD register of timer-counter B2. For imaging of velocity components of flow through the slice timer-counter B1 was not used, and timer-counter B2 was allocated to all three of the overlapping gradient pulses. This allowed the position of the three gradients in the slice-selection waveform to be changed by updating the LOAD register of timer-counter B2.

For the imaging of flow in either the slice select or frequency encoding directions for angled slice acquisitions, the slice-selection and frequency-encoding waveforms do not overlap. As with the non-angled slice acquisitions, the allocation of the timer-counters was modified, depending on the direction of velocity encoding required (figure 4.12).

For the imaging of velocity components of flow through the slice, timer-counter B1 was allocated to the spoiler pulse and the slice-selection pulse, timer-counter B2 was allocated to the three pulses following the slice-selection pulse and timer-counter B3 was allocated to the three pulses preceding the readout gradient. This allowed the position of the three pulses following the slice-selection pulse to be changed by altering the value in the LOAD register of timer-counter B2.

For imaging of velocity components of flow in the frequency-encoding direction, timer-counter B3 was allocated to the whole slice select gradient waveform, timer-counter B2 was allocated to the first of the frequency encoding pulses and timer-counter B1 was allocated to the second and third frequency encoding pulses. This allowed the position of the first frequency encoding gradient to be changed by updating the LOAD register of timer-counter B2.

The acquisition software was modified to perform the reallocation of LOAD and HOLD values to the timer-counters, prior to downloading the timing data to the timing boards. The timer-counter allocation is so arranged that velocity encoding can be achieved by altering the value in the LOAD register of counter B2. This register is updated whilst the interleaved sequence is in progress, by one of the interrupt service routines which re-arms the one-shot mode timer-counters between each pulse sequence. For non-angled slice acquisitions, the timer-counter B2 on only one of the timing boards has to be updated (figure 4.11). For angled slice acquisitions, the timer-counter B2 on all three of the boards must be updated (figure 4.12).

4.2.7. Cardiac Synchronisation

The repetition time, TR, of the pulse sequence in the upgraded system is controlled by timer-counter 4A1, operating in a free running mode. In this mode, the counter automatically reloads alternately from the LOAD and HOLD registers at the end of each counting period and restarts counting. The TR interval is determined by the sum of the LOAD and HOLD register values. The timer-counter can be armed or dis-armed by software control in order to start or stop counting.

If the pulse sequence is to be synchronised with the cardiac cycle, timer counter 4A1 is dis-armed until a synchronisation pulse is received by one of the parallel ports on the I/O board. When such a pulse is received, the timer-counter is armed by an interrupt service routine (ISR), and once the pulse sequence is complete a dis-arm command is issued by a second ISR. If multiple frames are being acquired, the timer-counter is allowed to count repeatedly through the TR period until all the frames have been acquired, and it is then dis-armed.

Since the timer-counter mode is the same whether the scan is gated or ungated, it is not necessary to generate separate timing files for gated pulse sequences. The ISRs which arm and dis-arm timer-counter 4A1 were already written into the upgraded software by the manufacturer, although some de-bugging of the commercial software was required, in order to make it function correctly.

4.3. Calculation and Subtraction of the Phase Maps

4.3.1. Initial Software Development

Initially, the software to calculate phase maps from the raw signal data, acquired on the pre-upgraded MRI system, was developed on a separate PDP 11/23+ computer which was used for in-house development of MRI system software. The raw data was stored and transferred to the development computer system on removeable hard discs, prior to undergoing Fourier transformation. Software was written on the development system to perform a two-dimensional Fourier transformation on this raw data, and then to calculate 'real', 'imaginary', magnitude and phase images from the result (section 3.1).

The phase maps were calculated by dividing the imaginary data by the real data and using a look-up table to determine the phase angles. The look-up table was used, in preference to the FORTRAN arctangent function, in order to increase processing speed. The software written on the development system was adapted and transferred on to the MRI system, and some initial results were obtained using the phase mapping technique, before the MRI system was upgraded (Ridgway and Smith, 1986; Appendix IV).

Phase-related banding was frequently observed on the real and imaginary images, and on the unsubtracted phase

images. The presence of these bands indicated that the centre of the NMR signal echo was offset from the centre of the data collection period (section 3.6.4). This could be caused either by mis-timing of the data collection period, or by the presence of an unwanted magnetic field gradient, in either the frequency-encoding or the phase encoding-directions. This phase variation can be corrected by adjusting the dc voltage offset on the appropriate gradient power supply. If there are no unwanted gradients, and the pulse sequence timing and the gradient waveforms are set up correctly, the phase image should have no obvious horizontal or vertical banding present.

4.3.2. Upgraded MRI System Software Development

In order to incorporate the phase mapping technique fully into the upgraded MRI system, software was written to calculate and subtract the two phase maps generated by the interleaved pulse sequence, and to convert the data into a suitable format for storage and display which was compatible with the new system software. The software developed makes full use of the array processor, in order to maximise processing speed. Considerable effort was made to limit the additional memory space utilised, both by the extra image data that was generated, and by the extra program code.

The large area of extended memory on the data processing computer (4 Megabytes) is accessed using an addressing function, 'VIR', which was supplied as part of the array processor software library. This function allows lines of data to be moved by the array processor around extended memory, and also between extended memory and virtual memory. The array processor performs all the steps in the image calculation. The time taken to reconstruct a magnitude image from the raw data is 9 seconds for a 128x128 image and 40 seconds for a 256x256 image.

The memory allocation of the data arrays, declared by the reconstruction software, is shown in figure 4.13. The digitised NMR signal data is received by the data processing computer from the acquisition computer and is stored in extended memory, until the data acquisition is completed. The image reconstruction software reconstructs one image at a time by converting the data from integer to real values, and then moving all the data lines for that image into the 128 x 128-element virtual array, A1. (If the image data has been acquired for a 256 x 256 matrix, the data occupies all four arrays, A1, A2, A3 and A4). A two-dimensional Fourier transformation is then applied to the raw data using the Fast Fourier Transform (FFT) subroutines, from the array processor software library, and the result replaces the data in array A1.

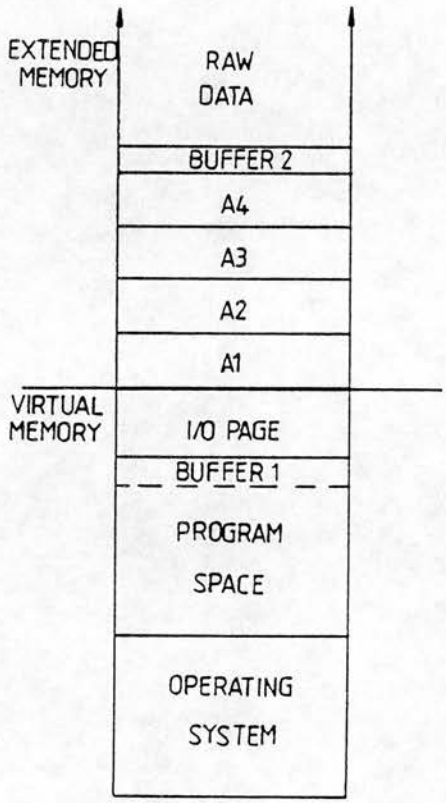

Figure 4.13. Schematic diagram showing the usage of virtual and extended memory by the reconstruction software.

Following the Fourier transformation, the data in array A1 represents the spatial distribution of the NMR signal over the selected image slice (section 3.1). Each array element has two components which represent the two orthogonal components of the NMR signal (section A2.4.2), and therefore it is possible to calculate both the magnitude and the phase of the NMR signal for each element at this stage.

When the magnitude is calculated using the existing software, the real and imaginary data is partially over-written by the result of the calculation, which causes the phase information to be lost. In the same way, if the phase calculation were to be done before the magnitude calculation, the result would also overwrite the real and imaginary data, and the signal magnitude information would be lost. It was therefore necessary to devise a method of storing the result of one calculation without over-writing the data needed for the second calculation.

An additional problem arises because of the form of the arctangent function. This function only yields phase values in the range +/- $\pi/2$, whereas there is sufficient information from the sign of the real and imaginary values to calculate phase values up to the range +/- π (figure 4.14). For example, if both the real and imaginary values are negative, the true phase value should be in the range between $-\pi/2$ and $-\pi$. However, the phase value calculated using the arctangent function is in the range between 0 and $+\pi/2$. In order to overcome this problem, bit maps are created which take account of the sign of the real and imaginary data using the convention shown in table 4.3. These bit maps are used to add or subtract values of π from the result of the arctangent calculation. The bit map of the signs of the imaginary data is subtracted from the bit map of the

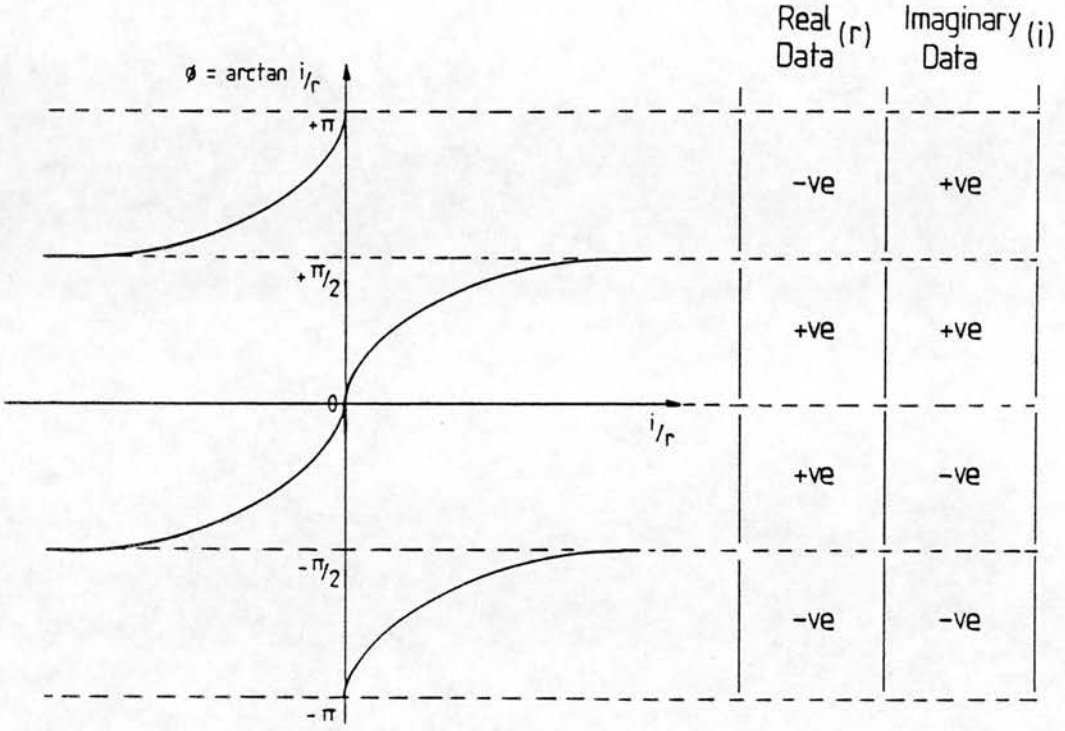

Figure 4.14.

Unless additional information is available, the arctangent function only yields phase values in the range of +/- π/2. In order to calculate phase values over the full range of +/- π, the sign of the real and imaginary data must be taken account of.

signs of the imaginary data, divided by the real data. The result is multiplied by π/2 and added to the phase values calculated by the arctangent function. In the above example, the bit map of the imaginary data gives a value of -1, and the bit map of the imaginary data divided by the real data gives a value of +1 (table 4.3).

Subtracting and multiplying by $\pi/2$ gives a value of $-\pi$. This is added to the phase value to place it in the correct range.

Bit Map Convention

'r' data sign:	-ve	+ve	+ve	-ve
'i' data sign:	-ve	-ve	+ve	+ve
'i' bit map:	-1	-1	+1	+1
'i'/'r' bit map:	+1	-1	+1	-1
subtracted bit map:	-2	0	0	+2
correction factor:	$-\pi$	0	0	$+\pi$

Table 4.3.

Table showing the convention used to generate the bit maps. Two bit maps are generated, which take account of the sign of the imaginay data, ('i'), and the sign of the imaginary data divided by the real data ('i'/'r'). A value of +1 is used for positive values and a value of -1 is used for negative values. These bit maps are subtracted and multiplied by $\pi/2$ to generate correction factors of $-\pi$, 0 or $+\pi$, which are added to the phase values calculated by the arctangent function.

To reconstruct both the magnitude and the phase data, an algorithm was developed which involved only minor changes to the reconstruction software. This algorithm involves a number of distinct steps which are given below. One line of data is processed at a time, which allows the use of temporary buffer space during each pass of the algorithm. The arrays refered to are shown in figure 4.13.

a) The imaginary components of one line of data elements in array A1 are divided by the corresponding real components and the result is stored in a temporary buffer array, BUFFER 1. This step preserves the phase information.

b) Two bit maps are created from the line of data elements in array A1; one representing the sign of the imaginary data, and one representing the sign of the real divided by the imaginary data. The bit maps are placed in the temporary buffer array, BUFFER 2.

c) The magnitude of the line of real and imaginary elements in array A1 is calculated and the result is stored by over-writing the first half of the line of real and imaginary data. (The result only takes up half the space since a single magnitude value is calculated from two separate components).

d) The arctangent of each element of the result of (a) in BUFFER 1 is calculated, and the resultant phase values are placed in array A1, overwriting the second half of the line of real and imaginary data.

e) The two bit maps in the temporary array, BUFFER 2 are subtracted. The result is multiplied by n/2 and then added to the phase values stored in array A1.

These steps are performed on each line until the magnitude and phase has been calculated for the whole image. Array A1 then holds two separate arrays of real numbers which represent the magnitude and phase images.

These arrays are then scaled and converted to 8 bit values suitable for disc storage and display. The phase data is scaled so that a pixel value of 255 represents a phase value of $+180^{o}$, a pixel value of 127 represents a phase value of zero, and a pixel value of zero represents a phase value of -179^{o}.

Before being displayed, the random background noise was removed from the phase image by referring to the magnitude image. If the signal magnitude was below a predefined threshold value, the phase value was set to zero. A linear grey scale was used for displaying the images. This resulted in zero phase being represented by the mid-grey level of the grey scale.

The two NMR image data sets, produced by the interleaved flow imaging pulse sequence, are processed in the same way. The two phase maps are subtracted as each block of the second set of image data is being written to disc and displayed. The corresponding block from the first set of data is read from disc into a temporary buffer array. A composite magnitude image is derived by taking the lower value of corresponding pixels from the two original

magnitude images. The two phase maps are subtracted to obtain the velocity-encoded flow image (Figure 4.15). The first pair of phase and magnitude images are over-written, both on disc and on the display, by the composite magnitude image and the subtracted phase image. A data file header is generated which contains data scaling parameters and scan information, so that the phase maps can be displayed and annotated by the MRI image display software.

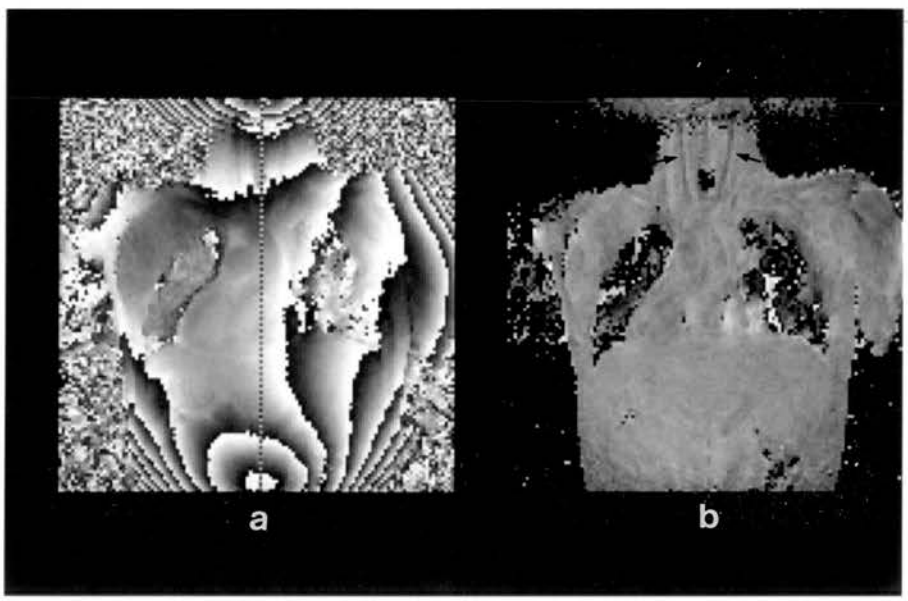

Figure 4.15.

Phase maps obtained in the coronal plane (a) before subtraction, and (b) after subtraction. In the subtracted image the phase modulation caused by magnetic field inhomogeneity has been removed, whilst that caused by flow with velocity components in the frequency-encoding direction can be seen in the carotid arteries (arrows).

4.4. Modification of the Operators Software

The selection of the scan type and setting of the pulse sequence parameters by the operator, is performed using a menu-driven software package known as the Protocol Builder. A particular set of parameters can be saved on hard disc in a 'protocol' file. This software also selects the appropriate system timing files and gradient waveforms from those stored on the disc.

The protocol builder was modified so that the operator can select the flow imaging pulse sequence and set up the relevant imaging parameters. The modified software also selects the appropriate timing files and shapes files from those newly generated for the flow imaging pulse sequences. The velocity-encoding direction can be selected to measure flow velocity components either perpendicular to the slice, or in the frequency-encoding direction. The separation of the bipolar velocity-encoding gradient pulse which is required can be selected within the range of 0 to 10 milliseconds. This value increases the field echo time, TE. The mininum field echo values, (i.e. with no velocity-encoding), are given in table 4.4, for both non-angled and angled slice acquisitions, and for both the sampling frequencies used.

Acquisition Type	Sampling Frequency 10KHz	5kHz
Non-Angled Slices	22.6ms	29.0ms
Angled Slices	33.4ms	39.8ms

Table 4.4.

Table of the mimimum field echo times, in milliseconds, possible using the velocity-compensated gradient waveforms, for both non-angled and angled slice acquisitions. These echo times are extended by the gradient pulse separation added to achieve velocity encoding.

4.5. Development of the Cardiac Gating Facility

A cardiac gating facility (figure 4.16), has been developed at Edinburgh, primarily for use in the investigation of ischaemic heart disease (Smith et al, 1986), and has since had extensive clinical use (Been et al, 1985; Been et al, 1988; Turnbull et al, 1988). This facility is also used to synchronise the flow imaging pulse sequence with the cardiac cycle.

The synchronisation pulse, which is used to act as an external trigger for the MRI system, is derived from the R-wave of the subject's Electrocardiogram (ECG).

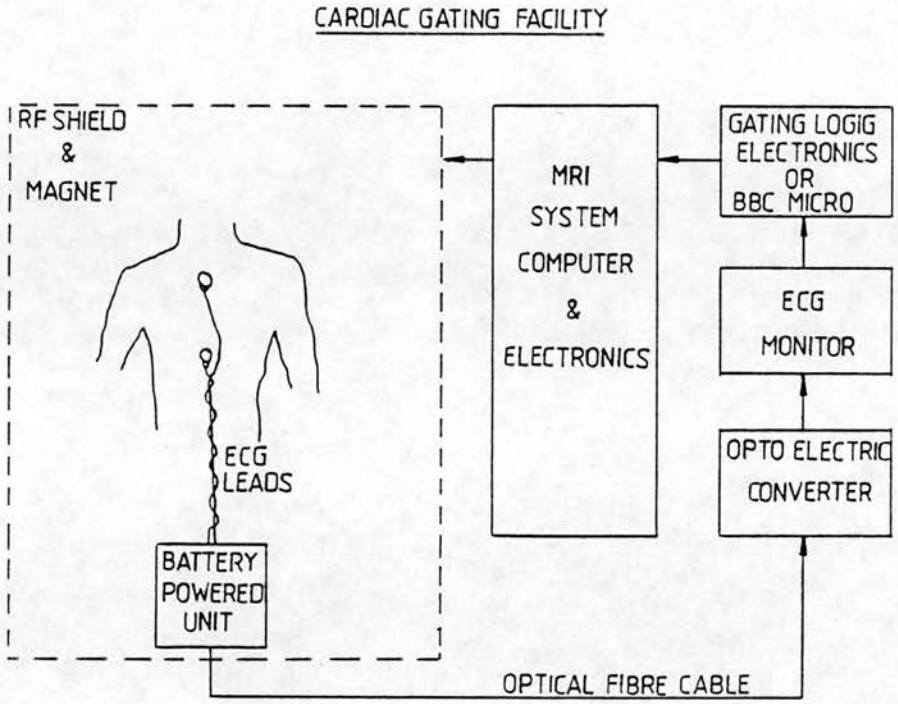

Figure 4.16.

Schematic diagram showing the main features of the cardiac gating facility.

A two-lead ECG is obtained from the subject and transmitted to an external ECG monitor as a frequency-modulated signal along an optical fibre link. This link serves to isolate the subject from any source of external electrical interference. A variable time delay can be added after the R-wave synchronising pulse, to control the point of data acquisition in the cardiac cycle.

4.5.1. ECG Electrodes and Leads

Initially, standard disposable electrodes with metal press-stud connections were used. On some of these electrodes, the press-studs were made of stainless steel, which causes a large local defect in the magnetic field. Electrodes with aluminium press-studs were therefore preferred. The ECG leads were electrically screened to reduce the pick-up of external noise and rf pulses from the imager. The screened leads were made of steel wire and therefore caused some artefact on the image. The use of thin, unscreened leads gave a negligible field defect but the external noise pick-up was greater. As a later development, the use of thin (0.1mm dia.), twin core, screened wire reduced the lead artefact. Ferrite beads were added to the leads to increase their inductance and therefore reduce the interference from the 3.4 MHz rf pulses.

The positioning of the electrodes on the body was found to be crucial, in order to maximise the R-wave signal, whilst minimising pick-up of the rf pulses. It was also necessary to ensure that any artefact on the image, caused by the electrodes and leads, was a reasonable distance from the region being imaged. Two electrode positions have been used using the standard electrodes. Initially the electrodes were placed above and below the heart on a line parallel to the midline, but on the

right-anterior chest wall. (Smith et al, 1986). This alignment of the eletrodes was found to reduce the pick-up from the rf pulses, although the amount of pick-up still seemed to vary considerably from one patient to another. Placing the electrodes on the right-anterior chest wall, ensured that the artefact caused by the ECG leads was far from the heart.

In an attempt to further reduce this pick-up of induced currents from the rf pulses and to remove the lead artefact completely away from the chest wall, the electrodes were positioned on the left-anterior abdominal wall and on the right wrist. The right wrist was then placed on the left-anterior abdominal wall so that the two electrodes lay on top of one another (figure 4.17a). With both these electrode arrangements, it was necesary to vary the position of the electrodes considerably, in order to obtain a satisfactory ECG signal. Many of the patients studied had abnormal ECG traces, which made positioning more difficult. Recently, graphite electrodes and carbon fibre leads have been used. Because of the total lack of artefact from this material, they can be positioned close to the heart, at the manubrium and the xiphisternum (figure 4.17b). This lead positioning is known as the MX configuration. Although they are not screened, the carbon fibre leads do not appear to suffer from the pick-up of noise and the gradient pick-up seems to be much less than with the conventional leads.

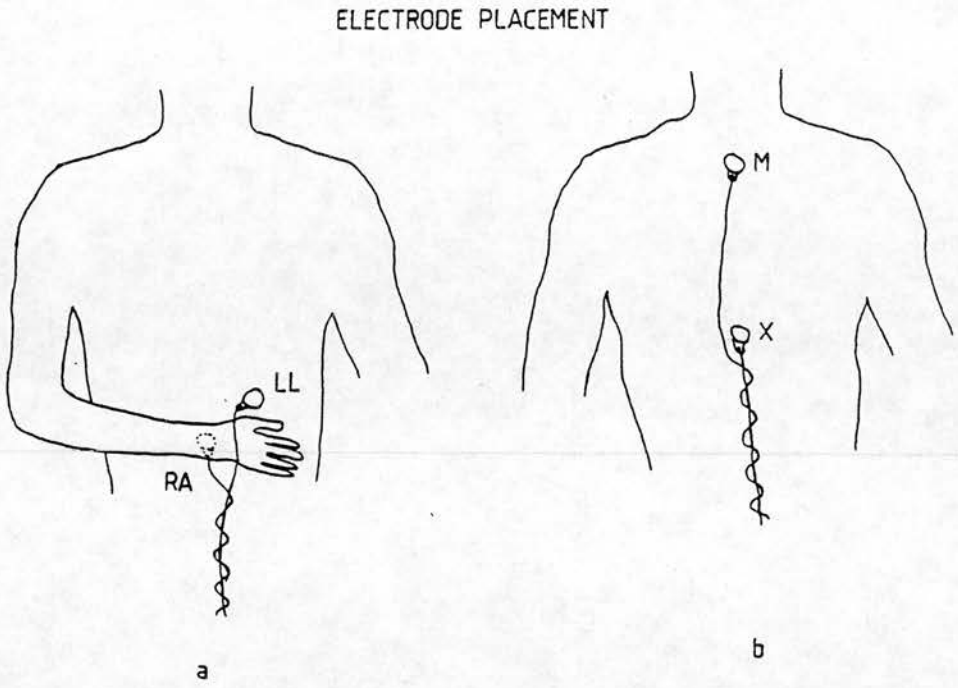

Figure 4.17.

Diagrams showing the positioning of ECG leads to reduce magnetic field distortion and pick-up of induced currents from the magnetic field gradients in the case of a) conventional electrodes, and b) carbon electrodes.

4.5.2. Opto-Electric Converter and Fibre-Optic link.

The ECG leads carry the ECG signal to a battery-powered unit, which amplifies the signal (figure 4.18). This signal is then used to modulate a carrier frequency (4.5MHz), which is then converted to an optical signal, which is transmitted along an optic fibre (figure 4.16).

Figure 4.18.

The ECG leads are connected to a battery-powered unit, which transmits the ECG signal to an external ECG monitor via a fibre optic cable. The optimum position for this unit is level with the rf shield of the MRI imager.

Positioning of the battery-powered unit within the MRI imager is important; placing the unit too far inside the magnet rf shielding allows interference from the unit to be picked up by the NMR receiver coil; placing the unit too far outside the magnet rf shield causes the pick-up of external noise by the ECG leads. The optimum position of the unit is therefore level with the opening in the magnet shield where the patient enters.

At the opposite end of the fibre-optic link, the optical signals are converted back to electrical signals, and are demodulated to obtain the original ECG signal. The battery-powered unit has recently been modified to accommodate respiratory gating (Amoore and Ridgway, 1989; Appendix IV).

4.5.3. The ECG Monitor and MRI System Interface

The demodulated ECG signal is input to a conventional ECG monitor (Model: Kontron Micromon 7142), in order to display the ECG trace and to perform R-wave detection. On the detection of an R-wave, the monitor generates a logic pulse which is used as a synchronisation pulse for the MRI system. An operator-controlled time delay is added between R-wave detection and the onset of the MRI pulse sequence. This function was performed initially by a BBC microcomputer, using its user port and the timer-counters in its internal Versatile Interface Adapter (VIA). The delay (in milliseconds) could be entered from the BBC keyboard. Ectopic beat rejection was made possible by comparing a running average of the last six R-R intervals with the latest one. A range of acceptable R-R intervals could be defined using a window, displayed schematically on the BBC video screen (figure 4.19). The MRI pulse sequence trigger was disabled for R-R intervals lying outside this range.

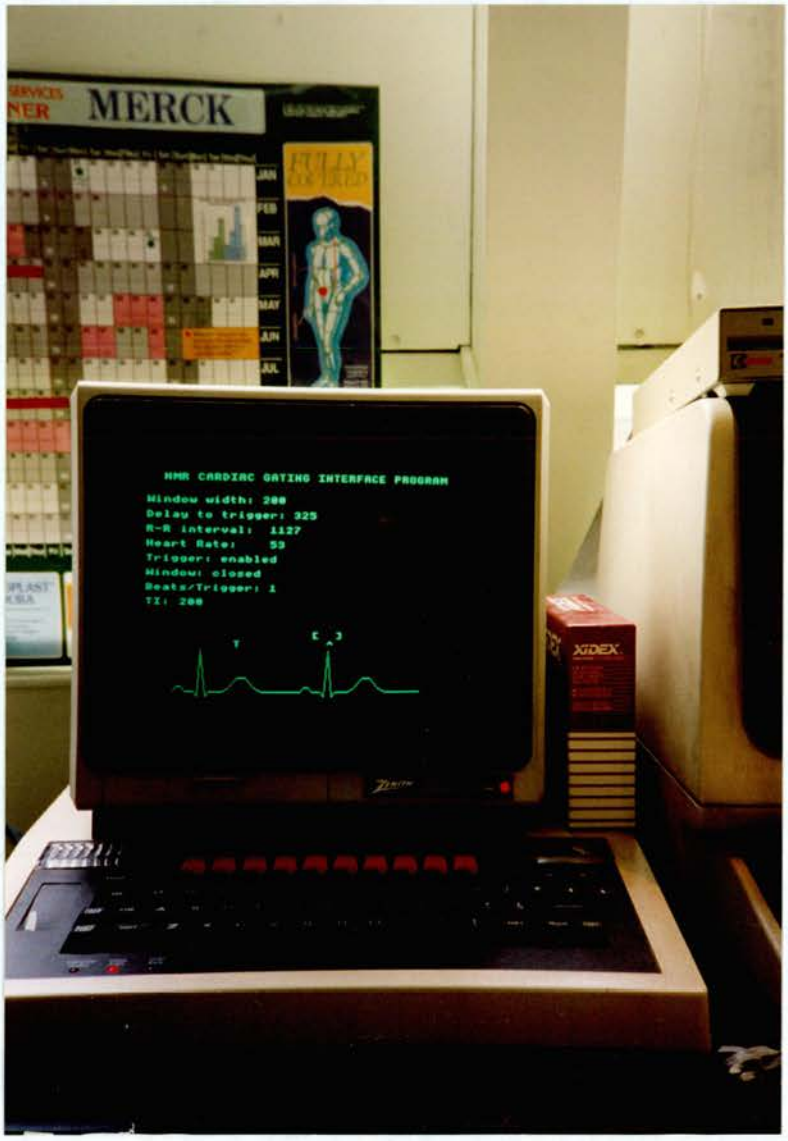

Figure 4.19.

The schematic display, on the BBC microcomputer, of the ECG, showing the position of the MRI synchronisation pulse, T, the window settings, [ ], and the position of the last R-wave, ^. The time base is defined by the running average of the previous six R-R intervals. Values for the synchronisation pulse delay, the heart rate and the R-R interval are also displayed in milliseconds.

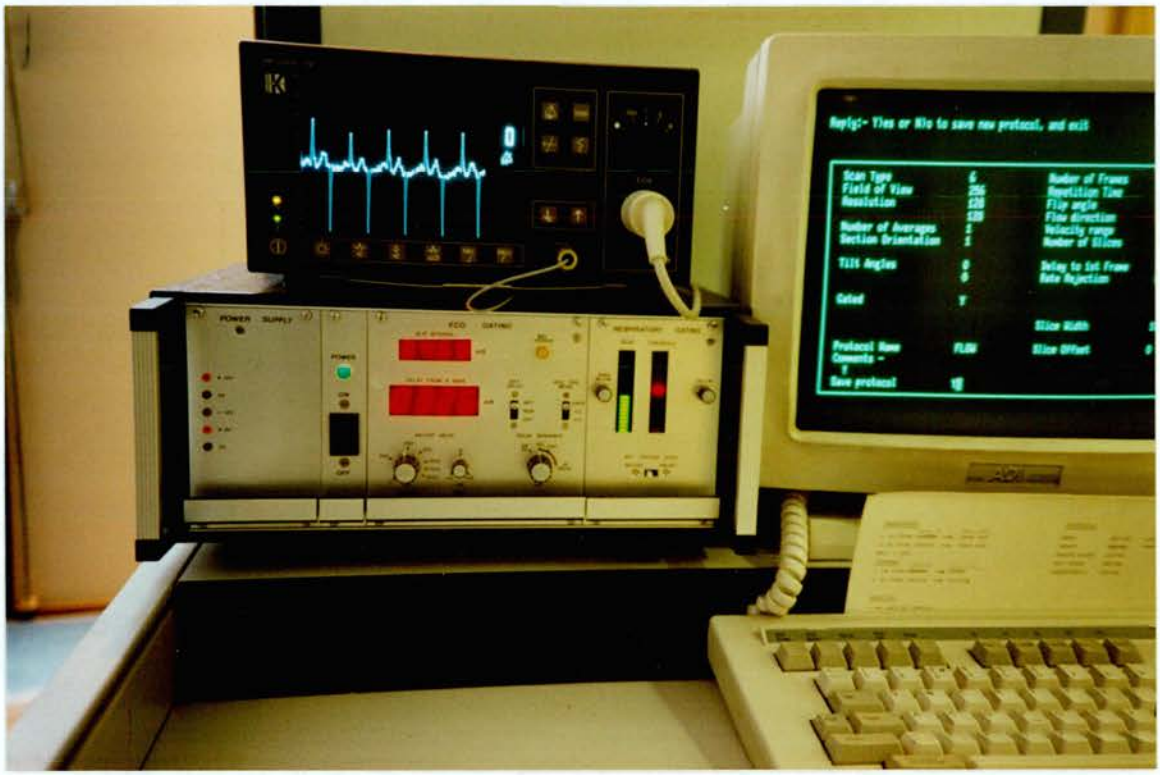

Figure 4.20.

Electronic gating logic unit and ECG monitor. The ECG trace displayed has a marker pulse superimposed on it, (seen as a downward spike), which shows the position of the MRI excitation pulse relative to the ECG.

The BBC has recently been replaced by a purpose-built, electronic gating logic module (Amoore and Ridgway, 1989; Appendix IV), shown in figure 4.20. This module was primarily developed to incorporate a respiratory gating facility, but at the same time it allowed improvements to the cardiac gating facility to be made. The current R-R interval and synchronisation pulse delay are shown on

digital LED displays on the front panel. The delay is set using coarse and fine setting potentiometers. The defibrillator input of the ECG monitor allows a marker pulse to be superimposed on the ECG trace, to show the position of the synchronisation pulse relative to the cardiac cycle (figure 4.20). During a scan, the marker pulse can be used to show the position of the rf pulses relative to the ECG trace.

4.6. The Phase Mapping Technique In Use

The phase mapping technique has been used to image a number of different vessels, encoding velocity in both the frequency-encoding direction, and in the slice-selection direction. The following pages contain examples of the images obtained.

Imaging of the major vessels was performed using the phase mapping technique, both with and without velocity compensation. The velocity-compensated gradient waveforms reduce the signal losses caused by phase dispersion in the presence of velocity gradients. Figure 4.21 shows two data sets acquired consecutively, in the transverse plane at the level of the major vessels in the same volunteer. In these images motion is predominantly in the slice-selection direction, due to blood flow in the ascending and descending aorta. The left hand images were acquired without any velocity compensation (figure 4.21a), while the right hand images were acquired using a velocity-compensated, slice-selection gradient waveform (figure 4.21b). For the data set acquired using the uncompensated pulse sequence, phase dispersion is observed in the magnitude image as a dark ring around both the ascending and descending aorta and noise is observed in the corresponding position on the phase map. Phase dispersion is much less apparent in the images acquired with the compensated pulse sequence.

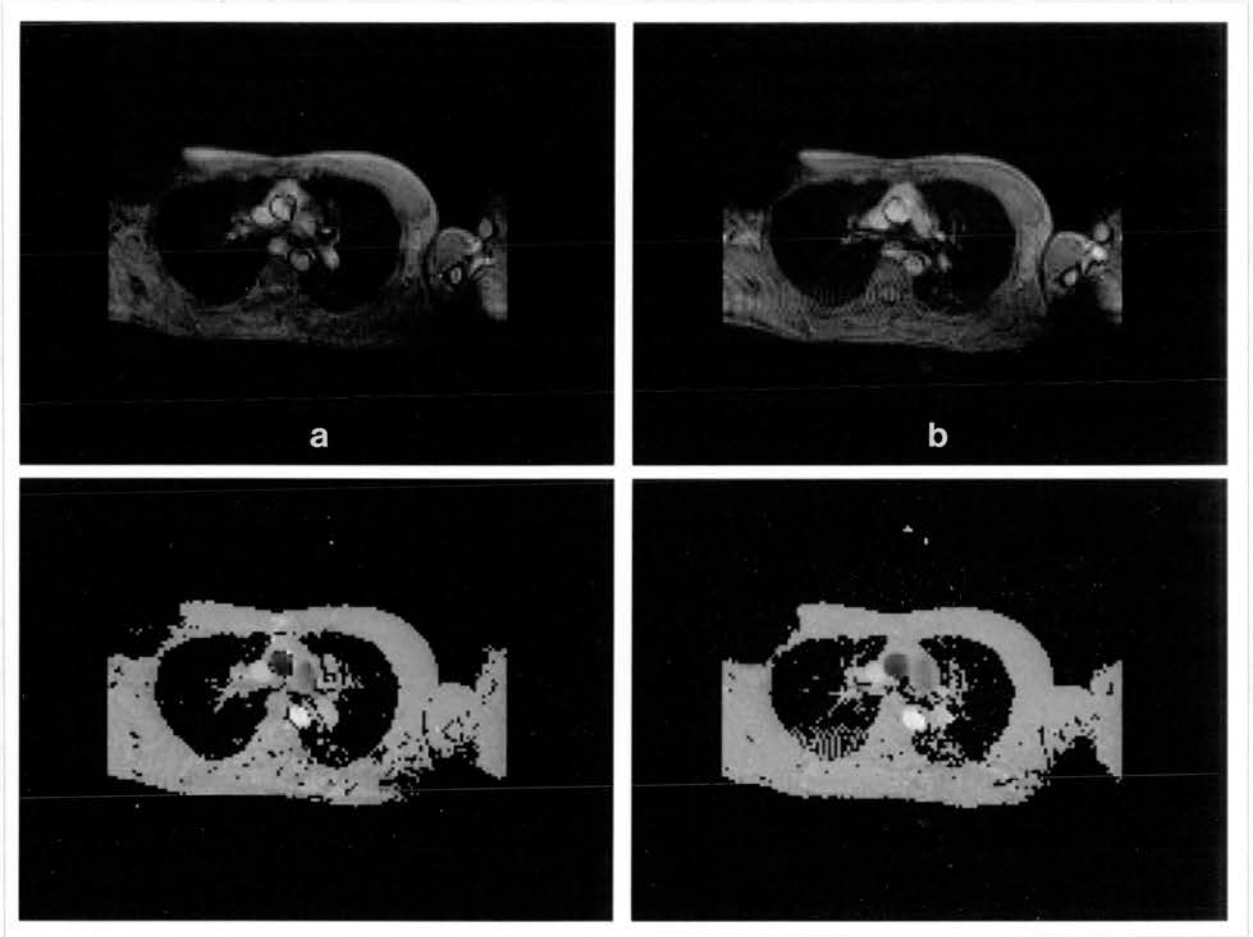

Figure 4.21.

Images obtained at the level of the major vessels using the flow imaging pulse sequence a) without velocity compensation, and b) with velocity compensation in the slice selection direction. The phase maps clearly show flow in the ascending (black) and descending (white) aorta. Reduced flow is also seen in the superior vena cava and the pulmonary artery. These images were acquired during mid-systole, using ECG synchronisation. In these early images, the background values set to zero by the thresholding algorithm are displayed as black, although stationary tissue is displayed as mid-grey.

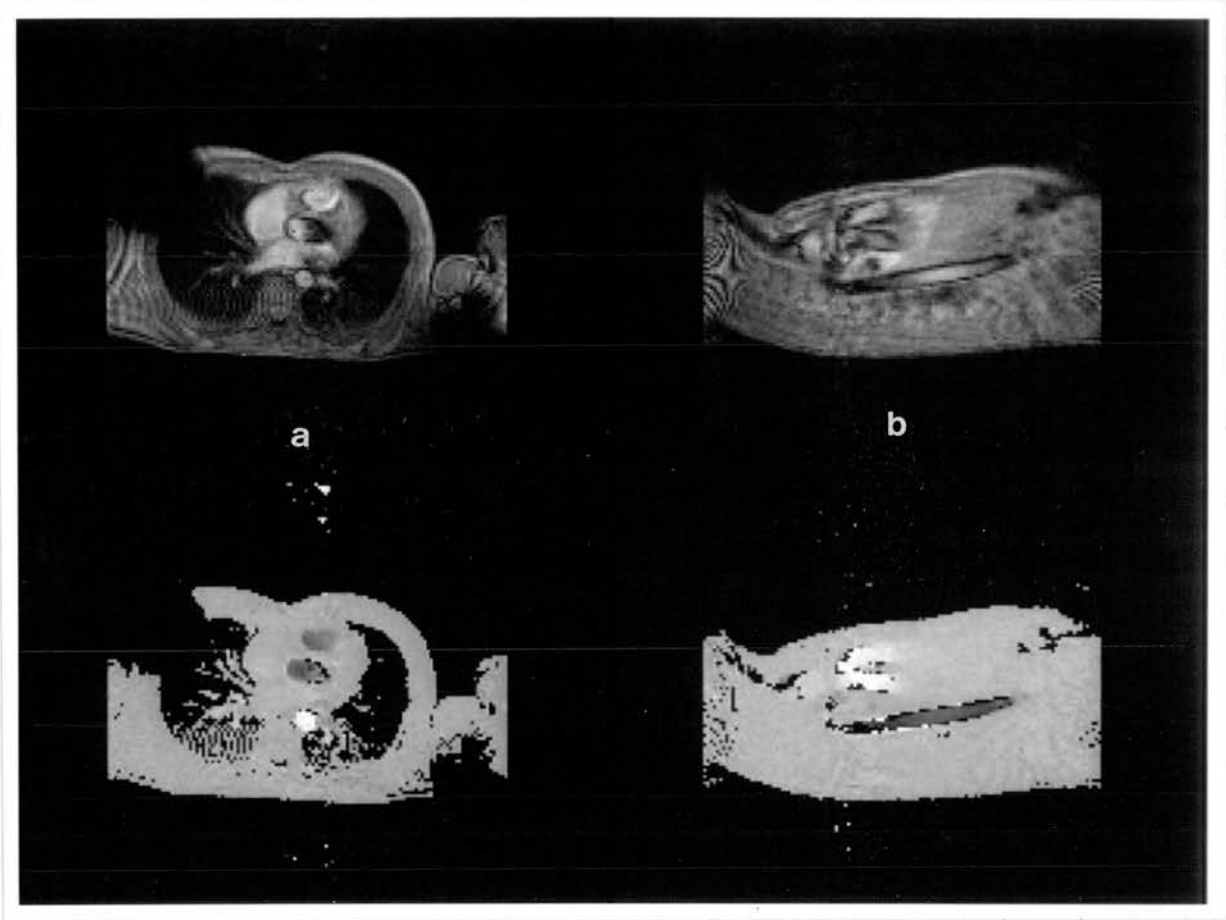

Figure 4.22.

Magnitude and phase images acquired through the descending aorta and the outflow tracts of the left and right ventricle a) in the transverse plane, imaging velocities through the slice (the ouflow tracts are observed as dark grey; the aorta is white), and b) in the sagittal plane, imaging velocities in the frequency-encoding direction, (the outflow tracts are white and the aorta is dark grey) . These images were acquired during mid-systole.

Phase maps were also acquired in the heart using the velocity-compensated pulse sequence. Figure 4.22a shows transverse images acquired at the level of the outflow tracts of the left and right ventricles, encoding flow velocities in the slice selection direction. A large degree of phase dispersion can be seen on the magnitude image in the left ventricular outflow tract, caused by higher order terms of motion. The phase dispersion across a voxel will be increased at this point because the flow is at an angle to the image plane at this level. Figure 4.22b shows the outflow tracts imaged in the sagittal plane by encoding velocity in the frequency-encoding direction. Flow in the descending aorta is also observed in this image.

Flow has been imaged in-the-slice in a number of other vessels. Figure 4.23a shows phase and magnitude images acquired using a 10mm slice width, showing the common carotid arteries and jugular veins, and figure 4.23b shows images acquired using a 20mm slice width which include the lower portion of the abdominal aorta, the aortic bifurcation, and the right iliac artery. Both these sets of images were acquired using oblique slices, in order to maximise the extent of the vessel included in the image slice. However, even with the use of oblique slices, it is difficult to include a reasonable length of vessel. Increasing the slice width reduces this problem, but increases the problems of phase dispersion.

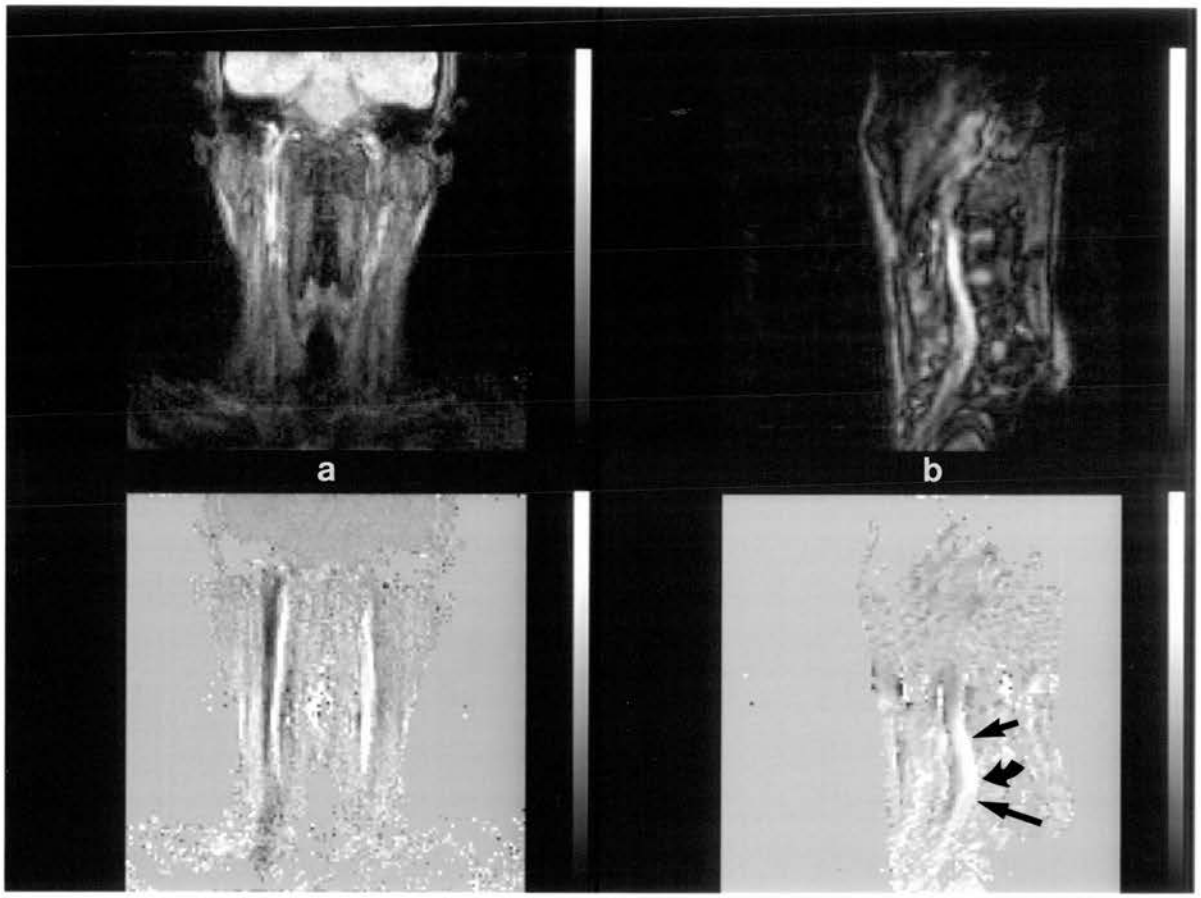

Figure 4.23.

Phase and magnitude images acquired using velocity-encoding in the frequency encoding direction. a) shows images of the common carotid arteries (white) and jugular veins (dark grey), acquired using oblique slices of width 10mm, angled at 20° to the coronal plane. b) shows images which include the lower extent of the abdominal aorta (short arrow), the aortic bifurcation (curved arrow), and the right iliac artery (long arrow), acquired using an oblique slice of width 20mm, angled at 30° to the sagittal plane.

Whilst imaging of flow velocities in the image plane, using phase mapping, is useful for the visualisation of flow, it is not suitable for flow measurement. The voxel dimension defined by the slice width is much greater than that defined by the in-plane resolution. When imaging vessels which are orientated parallel to the image plane, the velocity profile across the vessel diameter therefore leads to a greater degree of phase dispersion within voxels that contain velocity gradients. Whilst this is corrected for by the velocity-compensated gradients in the case of constant velocity flow, this is not so in the case of pulsatile flow, when higher order terms of motion are present. Furthermore, when imaging vessels which have a smaller diameter than the slice width, flow velocities may be underestimated beacuse of the inclusion of stationary tissue in the voxel. When imaging vessels which have diameters similar to, or larger than, the slice width, it is difficult to ensure that the slice is positioned at the centre of the vessel. Flow measurement is therefore better performed using an image plane which orientated perpendicular to the direction of flow.

Multiple frame imaging has been performed in a number of vessels to obtain flow velocity measurements throughout the cardiac cycle and encoding velocity perpendicular to the image plane. Figures 4.24 and 4.25 show a series of magnitude images and corresponding phase maps, acquired in the transverse plane at the level of the acsending and

descending aorta. These images were obtained using two separate acquisitions with a repetition time of 100 milliseconds. The first frame of the second acquisition was acquired with a delay of 50 milliseconds, so that the effective sampling interval of the cardiac cycle was 50 milliseconds.

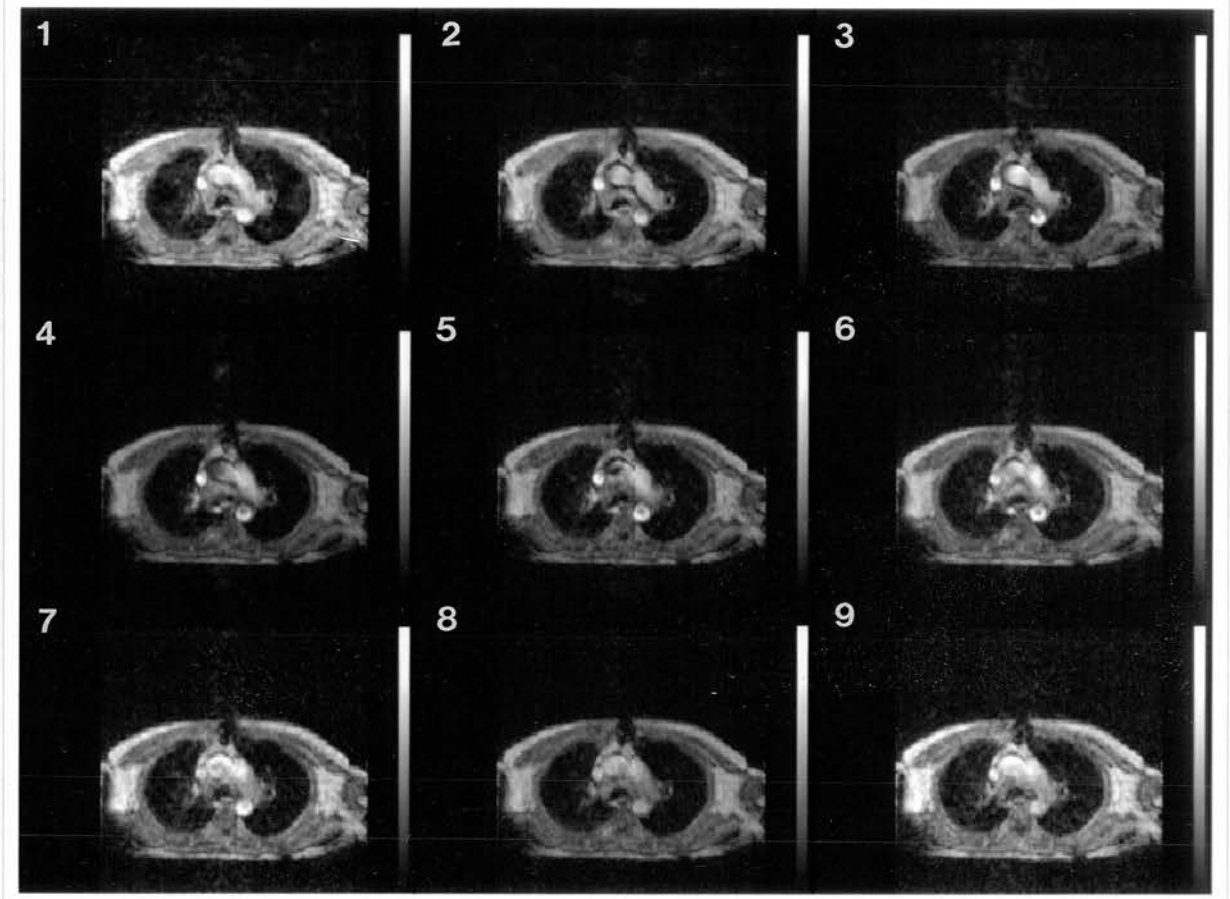

Figure 4.24.

Set of magnitude images acquired using two multiple frame acquisitions with a repetition time of 100ms, giving an effective sampling interval of 50ms. Phase dispersion is observed in frame 5, caused by bi-directional turbulent flow (see figure 4.25).

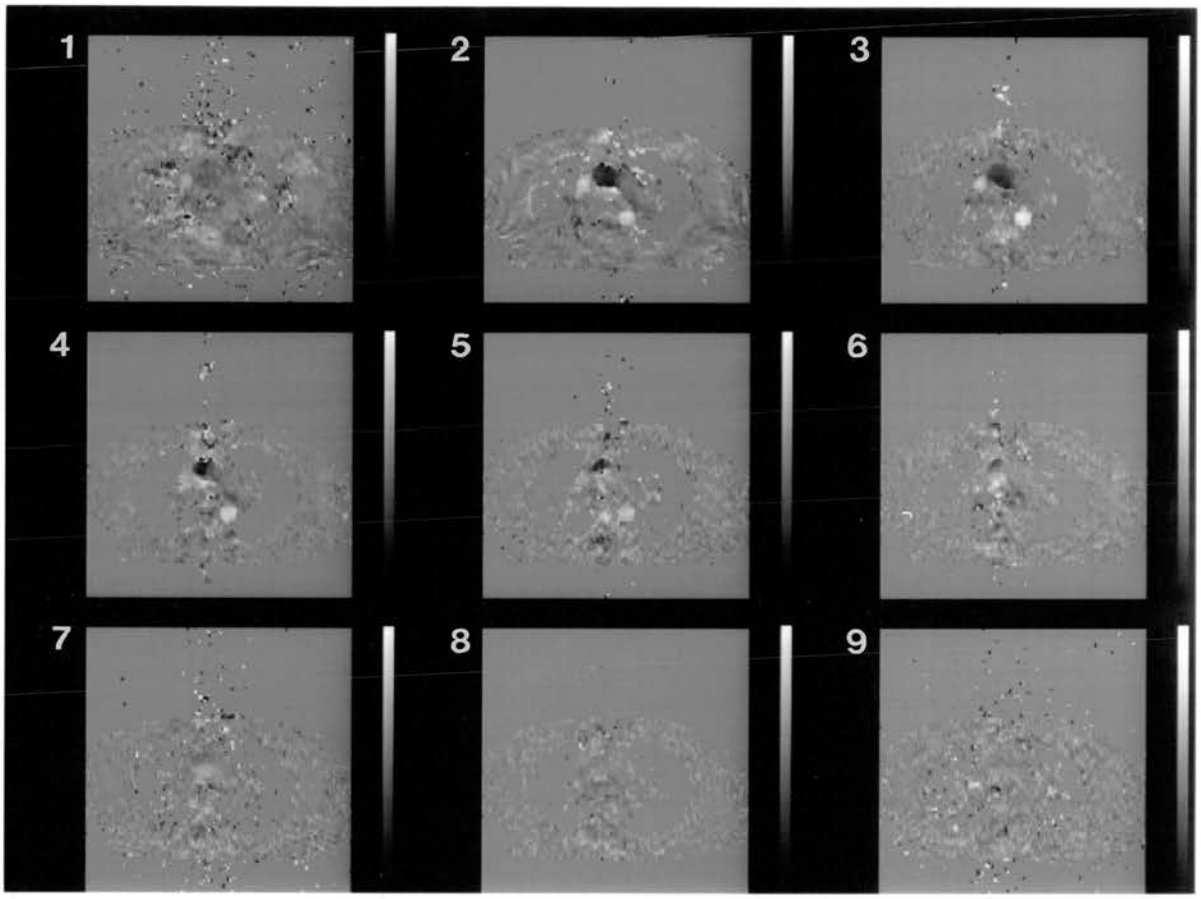

Figure 4.25.

Series of phase maps corresponding to the magnitude images in figure 4.24. The pulsatile flow in the ascending (black), and descending (white) aorta can clearly been seen, reaching a maximum in frames 2 and 3. Bi-directional turbulent flow is observed in the ascending aorta in frames 5 6 and 7. The flow velocity in the superior vena cava is also seen to reach a maximum in frames 2 and 3.

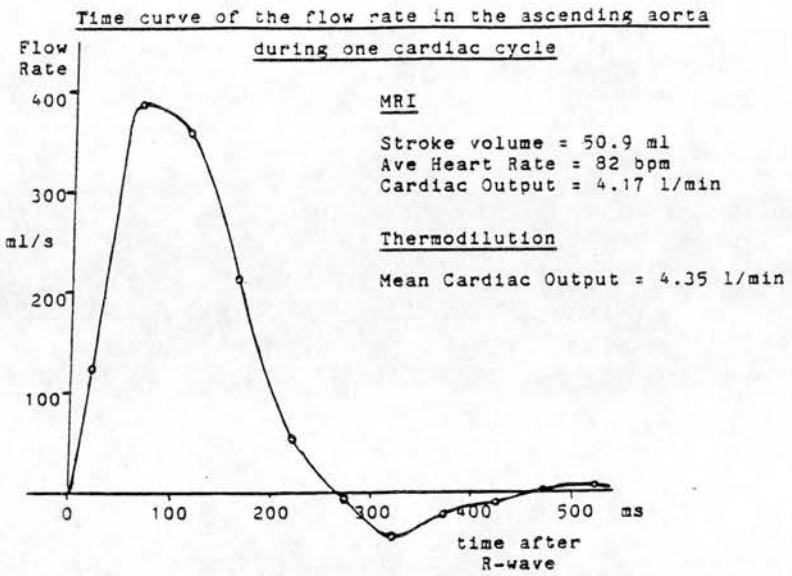

Figure 4.26.

The flow rate curve obtained from the phase maps in figure 4.25. The cardiac output obtained using MRI agrees well with that obtained using thermodilution.

Flow rates in the ascending aorta were obtained from each of the phase maps by measuring the mean velocity and area of the vessel. A flow curve (figure 4.26) was constructed and integrated in order to calculate the stroke volume and cardiac output (see appendix III). The cardiac output obtained using MRI was in close agreement with that measured using thermodilution. Whilst thermodilution cannot be regarded as a gold standard measurement for cardiac output, this agreement suggests that MRI flow measurement may be of use in the non-invasive measurement of stroke volume and cardiac output.

Calibration for Velocity Measurement by Phase Mapping

5.0. Introduction

The phase mapping technique was calibrated in order to relate the phase modulation to velocity, so that the technique could be used for flow velocity measurement. The calibration was performed using constant flow velocities in a direction perpendicular to the image plane. The expected relationship between phase and velocity was first derived from theory in order to aid in the choice of imaging parameters and velocity ranges.

5.1. Theoretical Prediction

As shown in chapter 3, the dependence of phase modulation on velocity components through the slice, can be predicted by calculating the phase modulation induced by the slice selection gradient waveform, in the presence of a constant velocity, v. The velocity-compensated, slice-selection gradient pulse waveform is shown in figure 5.1. The edges of the gradient pulses are assumed to be linear. Since the temporal position of only the last three pulses of the waveform is shifted to induce the velocity related phase modulation, the integral for the first gradient pulse, G_a, is not evaluated.

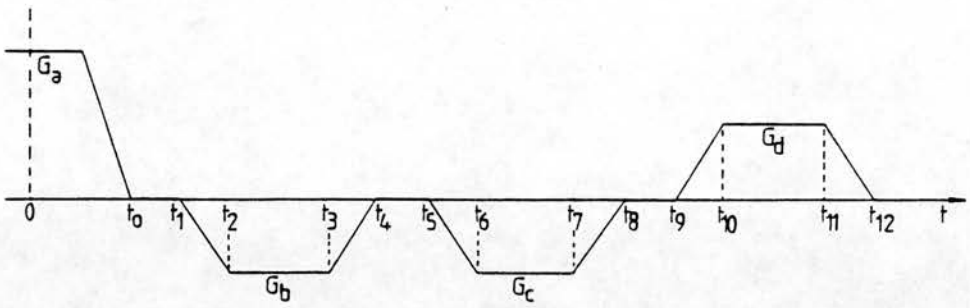

Figure 5.1.

The velocity-compensated, slice-selection gradient pulse waveform, showing the notation used in the theoretical prediction of the relationship between phase and velocity.

Using the notation of figure 5.1, the phase modulation, ϕ, induced by the slice-selection gradient, in the presence of constant flow of velocity, v, is given by

$$\phi = \int_0^{t_0} f(G_a, t)\,dt + \gamma v G_b \left\{ \int_{t_1}^{t_2} \frac{(t-t_1)}{t_2-t_1}\,t\,dt + \int_{t_2}^{t_3} t\,dt + \int_{t_3}^{t_4} \frac{(t_4-t)}{t_4-t_3}\,t\,dt \right\}$$

$$- \text{similar terms in } G_c + \text{similar terms in } G_d \qquad (5.1)$$

Evaluating the integrals of equation 5.1, and setting $t_2-t_1 = t_4-t_3 = t_e$ etc, gives

$$\phi = F(G_a,t) + \frac{\gamma vG_b}{6t_e}\left[2t_2^3-3t_1t_2^2+t_1^3\right] - \frac{\gamma vG_b}{2}\left[t_3^2-t_2^2\right]$$

$$- \frac{\gamma vG_b}{6t_e}\left[t_4^3-3t_4t_3^2+2t_3^3\right]$$

$$- \text{similar terms in } G_c + \text{similar terms in } G_d \qquad (5.2)$$

Equation 5.2 gives the phase modulation induced by the general form of the slice-selection gradient. The flow measurement technique is performed by obtaining two phase maps using two separate acquisitions. In the second of these acquisitions, the second, third and fourth gradient pulses occur at a time, T later than in the first acquisition, in order to increase the velocity dependence. Hence $t_1 \rightarrow t_1+T$, $t_2 \rightarrow t_2+T$, etc. By substituting these new time coordinates into equation 5.2, it is possible to calculate the additional phase modulation, ϕ_{diff}, corresponding to the temporal gradient shift, T, as

$$\phi_{diff}(T) = \phi(t+T) - \phi(t) \qquad (5.3)$$

where $\phi(t+T)$ and $\phi(t)$ are the phase modulations with and without the temporal gradient shift evaluated from equation 5.2.

Hence, substituting equation 5.2 into equation 5.3 obtains,

$$\phi_{diff} = - \gamma v G_b [\frac{Tt}{2}e + T(t_3-t_2) + \frac{Tt}{2}e]$$

$$- \gamma v G_c [\frac{Tt}{2}e + T(t_7-t_6) + \frac{Tt}{2}e] \qquad (5.4)$$

$$+ \gamma v G_d [\frac{Tt}{2}e + T(t_{11}-t_{10}) + \frac{Tt}{2}e]$$

Finally, setting $t_3-t_2 = t_7-t_6 = t_{11}-t_{10} = t_w$ (i.e. t_w = the gradient pulse width), gives

$$\phi_{diff} = vT(t_w+t_e)[-G_b-G_c+G_d] \qquad (5.5)$$

In order to continue with this derivation, it is necessary to evaluate some of the constants in the above equation. The time duration of the gradient pulse widths and edges are the same for all the slice thicknesses. Hence we have

$$t_w+t_e = 3.2ms \qquad (5.6)$$

The magnetic field gradient magnitude stored in RAM, G_{RAM}, is related to the actual magnetic field gradient strength, G, by

$$G = G_{RAM} 3.65x10^{-3} \ mT/m \qquad (5.7)$$

Finally, the gyromagnetic ratio, $\gamma = 2.8 \times 10^{8} s^{-1} T^{-1}$. Thus evaluating equation 5.5 gives,

$$\phi_{diff}(\text{radians}) = 3.27vT[-G_b - G_c + G_d] \qquad (5.8)$$

or

$$\phi_{diff}(\text{degrees}) = 187vT[-G_b - G_c + G_d] \qquad (5.9)$$

where v is expressed in metres per second, T is expressed in seconds and G_b, G_c and G_d are the gradient values stored in RAM.

Since $G_c = G_d$ for all the slice-selection gradient waveforms (table 4.1) and the choice of sign for phase modulation is arbitrary, equation 5.9 can be simplified further to

$$\phi_{diff} = 187vTG_b \qquad (5.10)$$

Equation 5.10 is used to derive the theoretical relationships in the following sections.

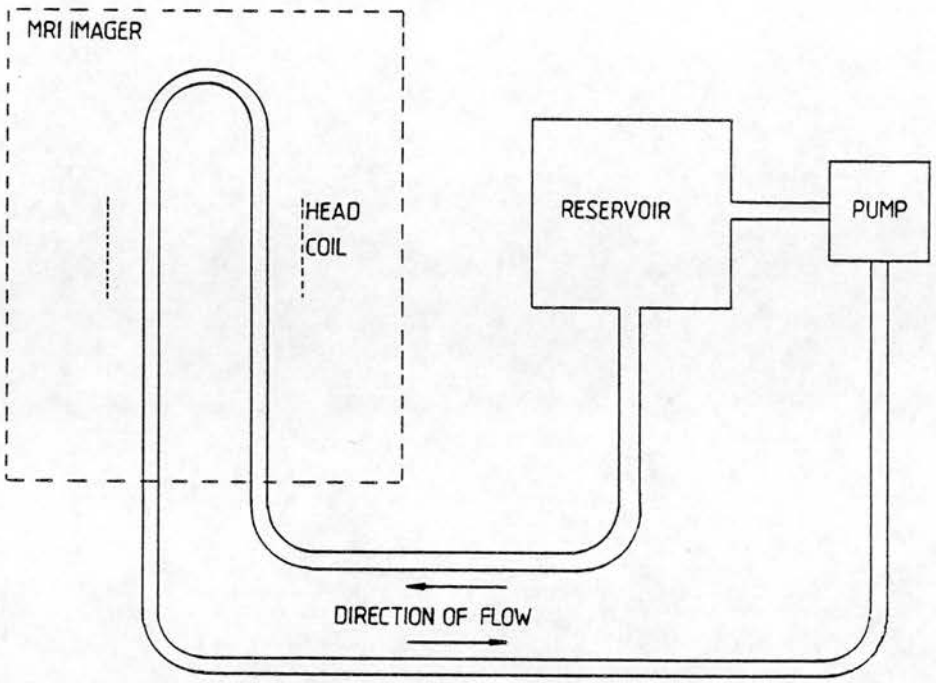

Figure 5.2.

Schematic diagram showing the experimental set-up used for the calibration procedure.

5.2. Calibration Procedure

The calibration was carried out using a plastic pipe of 1.0cm internal diameter, containing a mixture of glycerol and water (730ml glycerol: 1270ml water), which was doped with copper sulphate to give a T1 of around 400ms. This mixture has a viscosity similar to that of blood (0.004 $Kgm^{-1}s^{-1}$), when kept at room temperature ($20^{o}C$), and helps to maintain laminar flow at the higher flow rates used in this experiment.

The pipe was formed into a U-shape and placed inside the imager to provide two opposed directions of flow (figure 5.2). The pipe was of sufficient length to connect to a pump and reservoir, positioned outside the radiofrequency shield of the magnetic resonance imager. The pump was driven by a stepper motor to provide a wide range of constant flow velocities. A perspex container filled with copper sulphate solution (T1=250ms) was placed beneath the pipe at the centre of the imager, in order to provide a reference phase measurement from stationary fluid (figure 5.3). Imaging was performed using the patient head coil.

Flow rates were determined by diverting the return flow from the reservoir into a measuring cylinder and measuring the time taken to collect a certain volume of fluid. The mean flow velocity, v_{mean}, was calculated using the equation

$$v_{mean} = Q/A$$

where Q is the flow rate in millilitres per second and A is the cross sectional area of the pipe. The maximum velocity is calculated as twice the mean velocity, by assuming the presence of laminar flow with a symmetric, parabolic flow profile across the diameter of the pipe. In order to ensure that the flow profile was symmetric, the upstream section of the pipe was straightened for a distance of over one metre, before it entered the imaging

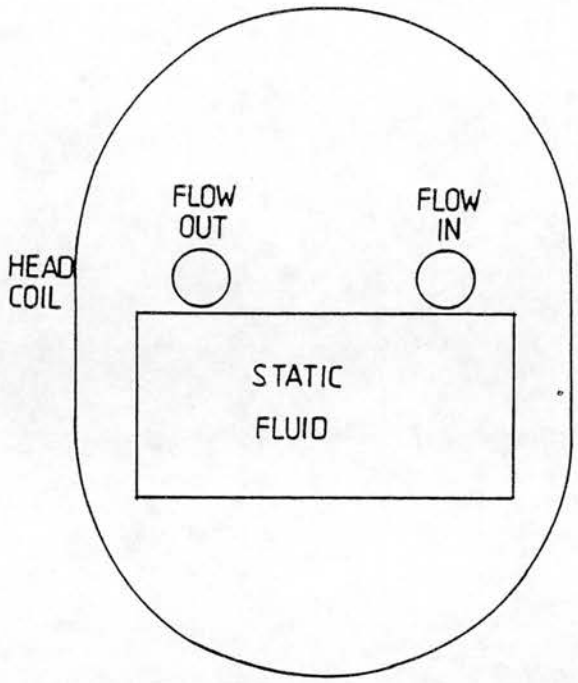

Figure 5.3.

Cross-sectional diagram of the experimental arrangement inside the head coil.

volume. The limiting threshold for the mean velocity before turbulence will occur in a circular pipe is given by (MacDonald, 1960),

$$v_{mean} = R_e \nu / D$$

where R_e is the Reynolds number, ν is the kinematic viscosity (for the water glycerol mixture, $\nu = 0.004$ $Kgm^{-1}s^{-1}$), and D is the diameter of the pipe. If the critical value of R_e is taken as 2000, the greatest mean velocity attainable before turbulence occurs for a pipe of 1.0cm internal diameter is 80cm/s.

Imaging was performed in the transverse plane, using the flow measurement pulse sequence to measure flow velocities perpendicular to the imaged plane. Images were acquired on a matrix of 128 x 128 pixels, using a field of view of 256mm x 256mm, to give an in-plane resolution of 2mm. The repetition time (TR) of the field echo pulse sequence was 400ms, the time to echo (TE) was 29ms and the flip angle was 90 degrees. No signal averaging was performed.

The phase maps were displayed using a mask derived from the corresponding magnitude image: where the signal was less than 25% of the maximum value, the phase map was set to zero. The mean phase value, ϕ_{mean}, within the pipe was measured by placing an irregular region of interest over the pipe cross section as seen on the image (figure 5.4). Values within the region of interest which were set to zero by the masking procedure were excluded from the mean. The total cross sectional area corresponding to the pixels included in the mean value was recorded, as was the maximum phase value, ϕ_{max}, within each region of interest. A background phase measurement was taken from the phantom containing stationary fluid for each image and was subtracted from the mean and maximum phase measurements. Following the background subtraction, the mean phase values and cross-sectional areas were multiplied to obtain a quantity ϕ_{sum}, which represents the total flow through the pipe.

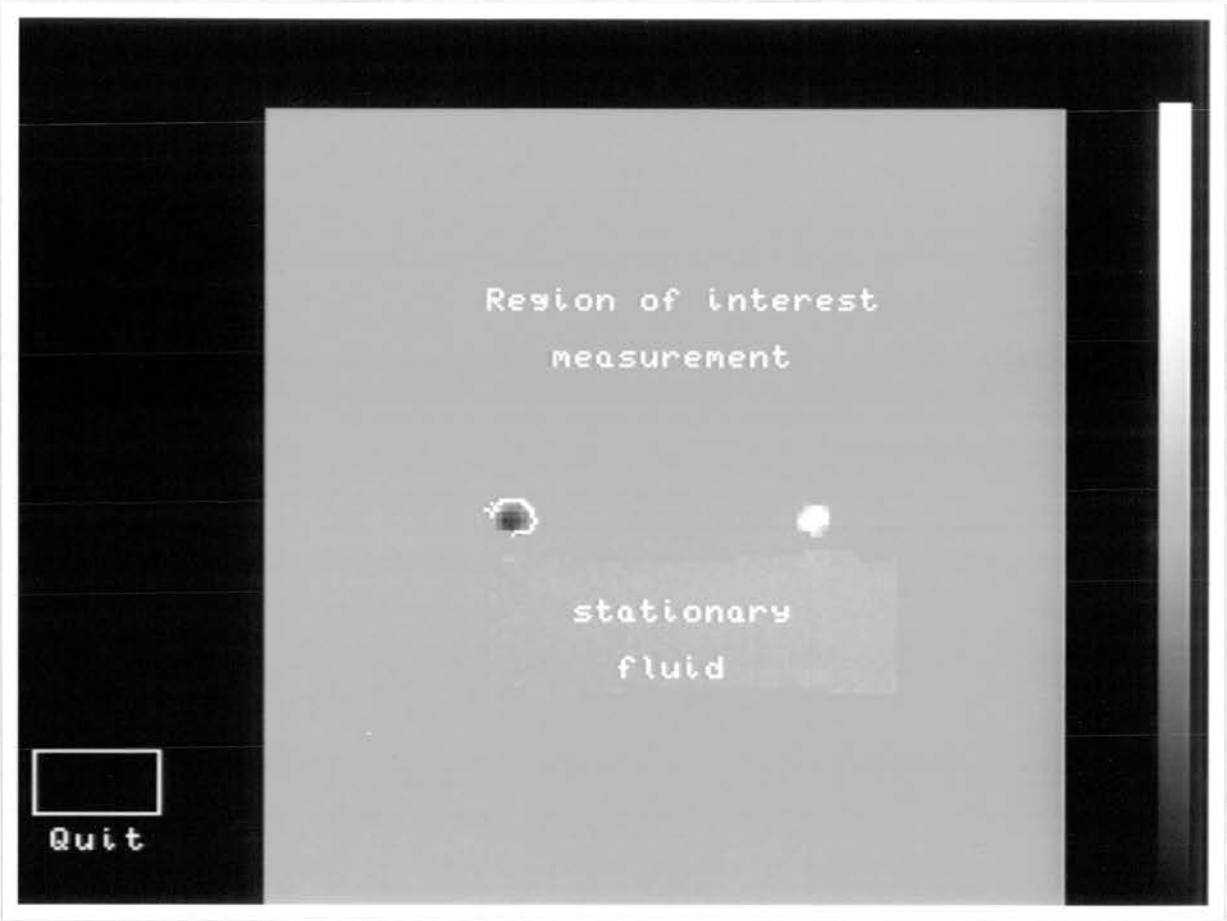

Figure 5.4.

An example of one of the phase maps obtained during the calibration procedure, showing a partially completed region of interest around the left hand pipe.

There were two separate stages in the calibration procedure. The first stage of the calibration investigated the dependence of phase modulation both on the time separation of the flow encoding pulses and on the selected slice width, in the presence of constant velocity flow.

The second stage of the calibration investigated the dependence of phase modulation on velocity, over different velocity ranges.

5.2.1. Stage 1 - Method

The speed of the stepper motor was adjusted so that the mean flow rate along the pipe was approximately 10ml/s. The flow imaging pulse sequence was used to acquire images in the transverse plane, perpendicular to the direction of flow. Imaging was performed to measure the flow velocity component through the slice, at slice thicknesses of 8, 10, 12, 14, 16, 18 and 20 millimeters, using a gradient pulse separation of 5 milliseconds. Each image was acquired three times to assess the random variation in the measurement and the flow rate was checked after each acquisition. Imaging was also performed at slice thicknesses of 10mm and 16mm, using gradient pulse separations of between 1 and 8 milliseconds in steps of 1 millisecond.

5.2.2. Stage 1 - Results

Table 5.1 shows the results obtained by varying the slice thickness, whilst maintaining a constant flow rate through the phantom.

Table of Calibration Results - Varying slice Width

Pipe c/s area = 0.785 cm^2 T = 5.0 ms
Average Mean velocity = 12.9 cm/s

Slice Width (mm)	Gradient Strength	Flow Rate (ml/s)	Area (cm^2)	ϕ_{mean}	ϕ_{sum}
8	824	10.2	0.84	94.3	83.5
8	824	10.1	0.81	95.0	81.1
8	824	10.2	0.84	92.5	77.4
10	660	10.2	0.77	93.6	60.1
10	660	10.2	0.76	98.4	63.9
10	660	10.2	0.76	93.8	59.4
12	550	10.2	0.84	63.0	54.7
12	550	10.2	0.84	65.1	56.3
12	550	10.1	0.84	64.2	56.3
14	471	10.2	0.84	55.9	47.0
14	471	10.2	0.84	56.1	48.1
14	471	10.1	0.84	58.5	47.0
16	413	10.1	0.80	50.6	40.5
16	413	10.2	0.84	49.1	41.4
16	413	10.2	0.83	49.8	40.3
18	363	10.2	0.84	44.9	37.5
18	363	10.2	0.84	43.0	35.0
18	363	10.2	0.80	47.4	38.0
20	330	10.2	0.75	42.3	31.4
20	330	10.2	0.73	42.2	29.9
20	330	10.2	0.76	40.3	29.8

Table 5.1.

Table of results from stage 1 of the calibration procedure, measuring the phase modulation produced for a constant velocity at different slice widths.

A linear relationship is shown in figure 5.5 between the gradient strength, G, and the summed phase shift, ϕ_{sum}. The theoretical relationship predicted by equation 5.10 for T=5.0ms and v=12.9cm/s is also shown as a dotted line.

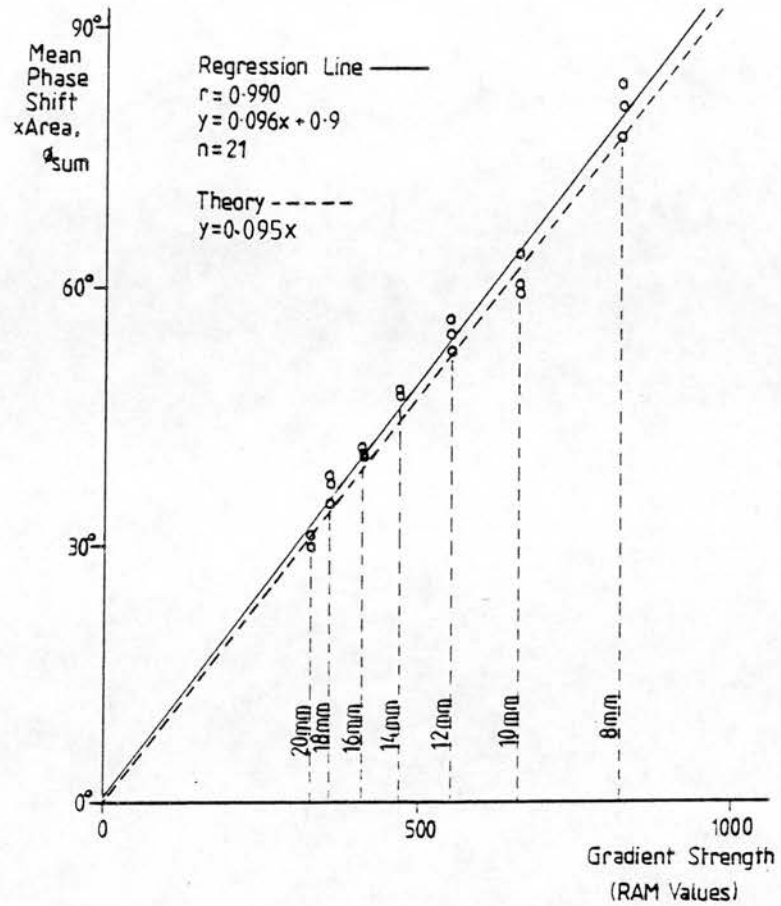

Figure 5.5.

Graph showing ϕ_{sum} plotted against the gradient strength for the different slice widths. The regression line is also shown, and the dotted line indicates the theoretical relationship predicted by equation 5.10.

Tables 5.2 and 5.3 and figures 5.6 and 5.7 show the results obtained by varying the gradient pulse separation, T, whilst maintaining a constant flow rate. A linear relationship is again demonstrated. In each case there is a close agreement with theory (shown by the dotted lines).

Table of Calibration Results - Varying T

Pipe c/s area = 0.785 cm^2 Slice Width = 10mm
Average mean velocity = 13.0 cm/s

T (ms)	Flow Rate (ml/s)	Area (cm^2)	ϕ_{mean}	ϕ_{sum}
1	10.1	0.80	20.3	13.4
1	10.2	0.76	21.0	12.8
1	10.2	0.75	20.9	13.1
2	10.2	0.76	43.1	24.0
2	10.2	0.76	44.6	25.1
2	10.2	0.72	44.4	22.9
3	10.2	0.76	51.1	34.0
3	10.2	0.76	49.9	33.7
3	10.1	0.76	50.7	34.9
4	10.1	0.72	78.0	45.8
4	10.2	0.76	73.6	44.2
4	10.2	0.76	73.3	44.5
5	10.2	0.80	93.1	61.2
5	10.2	0.80	94.0	62.0
5	10.2	0.80	90.9	59.8
6	10.2	0.79	109.0	73.3
6	10.2	0.80	107.4	73.4
6	10.2	0.84	107.4	76.2

Table 5.2.

Table of results from stage 1 of the calibration procedure, measuring the phase modulation produced for a constant velocity whilst varying the velocity-encoding gradient separation, T, for a slice width of 10mm.

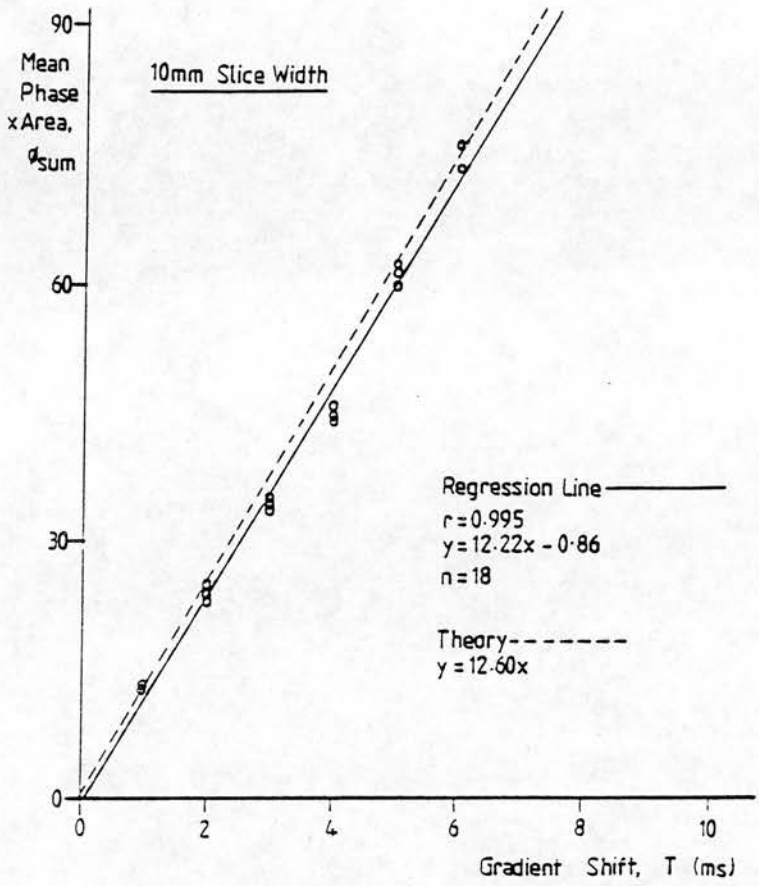

Figure 5.6.

Graph showing ϕ_{sum} plotted against the separation, T, of the velocity-encoding gradient for a slice width of 10mm. The regression line is also shown, and the dotted line indicates the theoretical relationship predicted by equation 5.10.

Table of Calibration Results - Varying T

Pipe c/s area = 0.785 cm^2 Slice Width = 16mm
Average mean velocity = 12.9 cm/s

T (ms)	Flow Rate (ml/s)	Area (cm^2)	ϕ_{mean}	ϕ_{sum}
1	10.2	0.84	14.6	8.7
1	10.2	0.75	13.8	7.3
1	10.1	0.83	14.6	8.9
2	10.1	0.83	25.0	17.3
2	10.1	0.68	27.5	14.8
2	10.1	0.72	26.5	14.3
3	10.1	0.74	31.5	21.6
3	10.1	0.79	32.5	24.3
3	10.1	0.74	33.3	23.6
4	10.2	0.72	44.5	28.2
4	10.1	0.77	43.0	28.8
4	10.1	0.79	43.5	28.8
5	10.2	0.75	52.6	38.8
5	10.1	0.75	53.5	40.0
5	10.2	0.75	54.0	39.9
6	10.1	0.72	61.9	49.8
6	10.1	0.81	53.7	48.8
6	10.1	0.80	58.3	54.2
7	10.1	0.80	68.0	61.0
7	10.1	0.83	62.5	60.3
7	10.1	0.81	62.8	59.1
8	10.0	0.80	86.2	66.7
8	10.0	0.80	88.7	68.5
8	10.0	0.76	89.2	64.5

Table 5.3.

Table of results from stage 1 of the calibration procedure, measuring the phase modulation produced for a constant velocity whilst varying the velocity-encoding gradient separation, T, for a slice width of 16mm.

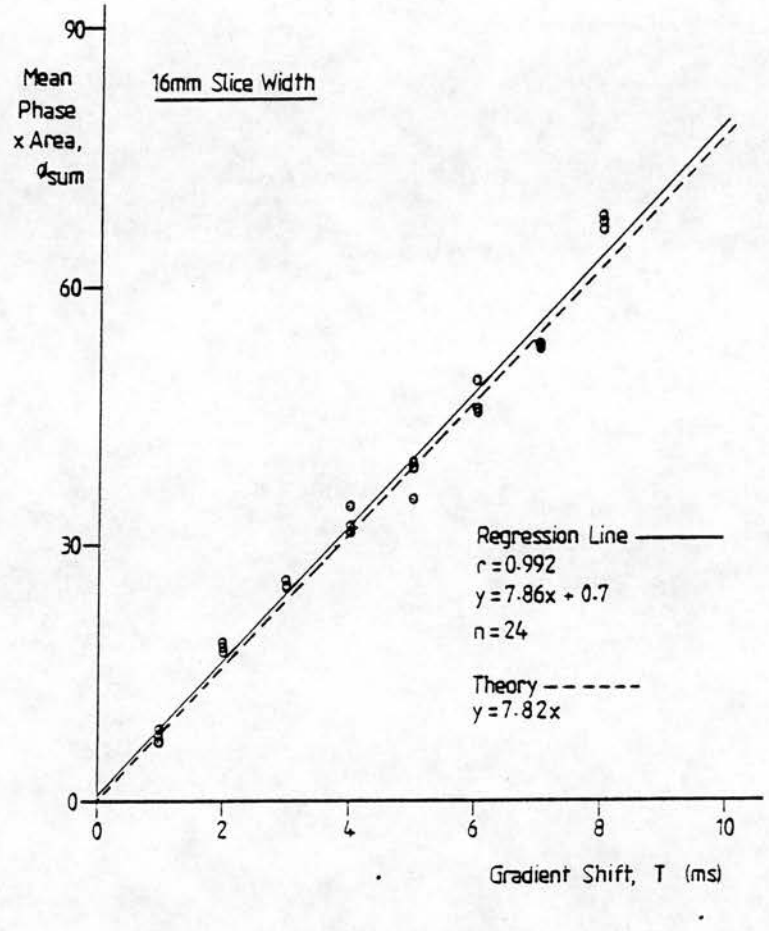

Figure 5.7.

Graph showing ϕ_{sum} plotted against the separation, T, of the velocity-encoding gradient for a slice width of 16mm. The regression line is also shown, and the dotted line indicates the theoretical relationship predicted by equation 5.10.

5.2.3. Stage 1 - Summary

It has been shown that the relationship between phase modulation, ϕ, in the presence of constant velocity, and the strength, G, and separation, T, of the velocity encoding gradient pulses, is linear and agrees well with the relationship predicted by equation 5.10. It is therefore possible to use equation 5.10 to predict the maximum velocity that can be measured without phase wrap-around, for a given slice thickness and value of T. The maximum velocities calculated using equation 5.10, for a number of slice thicknesses and values of T, are tabulated below in table 5.4 and are shown graphically in figure 5.8.

T (ms)	Slice Width 8mm	10mm	12mm	14mm	16mm	18mm	20mm
1.00	116.8	145.8	175.0	204.4	233.1	265.2	291.7
1.25	93.5	116.7	140.0	163.5	186.5	212.1	233.4
1.50	77.9	97.2	116.7	136.2	155.4	176.8	194.5
1.75	66.8	83.3	100.0	116.8	133.2	151.5	166.7
2.00	58.4	72.9	87.5	102.2	116.5	132.6	145.8
2.50	46.7	58.3	70.0	81.7	93.2	106.1	116.7
3.00	38.9	48.6	58.3	68.1	77.7	88.4	97.2
3.50	33.4	41.7	50.0	58.4	66.6	75.8	83.3
4.00	29.2	36.5	43.8	51.1	58.3	66.3	72.9
5.00	23.4	29.2	35.0	40.9	46.6	53.0	58.3
6.00	19.5	24.3	29.2	34.1	38.8	44.2	48.6
8.00	14.6	18.2	21.9	25.5	29.1	33.1	36.5
10.00	11.7	14.6	17.5	20.4	23.3	26.5	29.2

Table 5.4.

Table of maximum velocities predicted by equation 5.10, that can be measured without wrap-around of phase values, for different slice widths and values of T.

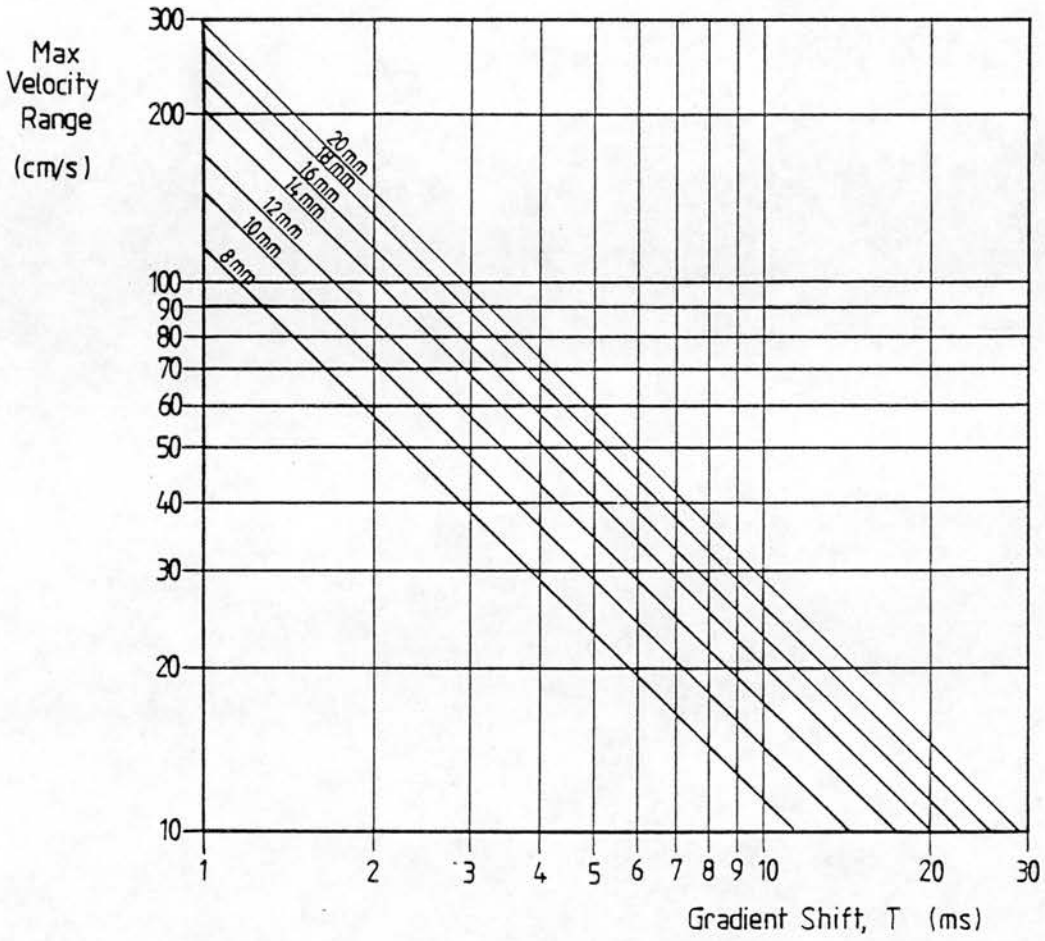

Figure 5.8.

Graph plotting the relationship predicted by equation 5.10, between the maximum velocity that can be measured without phase wrap-around and the velocity-encoding gradient pulse separation, T, for slice widths of 8, 10, 12, 14, 16, 18, and 20 millimetres. This graph can be used to select an appropriate value of T, to image velocities within a given range.

5.2.4. Stage 2 - Method

The second stage of the calibration measured the phase modulations produced by different flow velocities at slice thicknesses of 10 and 16 millimetres. Both high velocity (100cm/s maximum) and low velocity (30cm/s maximum) ranges were calibrated for each slice thickness. The gradient pulse separation, T, was determined in each case by the velocity range to be calibrated, using the data obtained from stage 1 (table 5.4). For the 10mm slice thickness a value of T=1.5ms was chosen for the high velocity range (maximum veloctiy = 92.7cm/s), and a value of T=5.0ms was chosen for the low velocity range (maximum velocity = 29.2cm/s). For the 16mm slice thickness a value of T=2.5ms was chosen for the high velocity range (max. velocity = 93.2cm/s), and a value of T=8.0ms was chosen for the low velocity range (max. velocity = 29.1cm/s). Each image was acquired three times at each different flow rate, in order to account for any random variation in the measurement and the actual flow rate was measured after each acquisition. The mean phase value, ϕ_{mean}, the maximum phase value, ϕ_{max}, and the cross-sectional area, were measured on each of the phase maps, and ϕ_{sum} was calculated using the same method as in stage 1 of the calibration procedure. These measurements were made for both the outward and inward sections of the pipe in order, to calibrate the flow measurement in both directions.

5.2.5. Stage 2 - Results

The four sets of results are given in tables 5.5-5.8, showing the measured flow rates and mean velocities, and the values of ϕ_{max} and ϕ_{sum} for both the inward (left) and outward (right) sections of the pipe. Also shown are the maximum velocities expected, assuming laminar flow.

The values for ϕ_{sum} are plotted against the flow rates, in order to derive the relationship between phase shift and velocity in each case (figures 5.9-5.12). There is good agreement with the predicted relationships derived from equation 5.10 (shown by the dotted lines). The maximum phase values are also plotted against the maximum velocities expected for laminar flow (figures 5.13-5.16). In this case the agreement with the predicted relationship was less good, particularly at higher velocities.

High Velocity Calibration Slice Width = 10mm

Pipe c/s area = 0.785sqcm T = 1.5ms

Flow Rate (ml/s)	Mean Velocity (cm/s)	Maximum Velocity (cm/s)	Left ϕ_{sum}	Left ϕ_{max}	Right ϕ_{sum}	Right ϕ_{max}
39.4	50.2	100.3	71.1	167	69.9	161
40.0	51.0	101.9	70.7	158	73.3	161
39.5	50.4	100.7	72.6	165	71.0	161
34.4	43.8	87.6	64.6	139	68.6	151
34.6	44.1	88.2	65.2	140	67.5	149
34.5	43.9	87.9	65.4	145	65.3	152
29.9	38.1	76.3	53.7	127	58.4	129
29.9	38.1	76.3	55.6	121	57.2	135
29.9	38.0	76.1	54.5	125	56.2	126
25.1	32.0	64.0	43.5	109	49.1	111
25.1	32.0	64.0	46.1	108	48.1	115
25.3	32.2	64.3	46.5	114	47.2	107
19.8	25.2	50.4	37.4	95	36.7	87
19.7	25.1	50.2	37.5	98	39.6	89
19.7	25.1	50.3	38.1	93	36.2	85
15.0	19.1	38.3	26.0	75	29.4	68
15.0	19.1	38.1	28.7	82	27.6	65
15.0	19.1	38.3	29.0	81	31.9	75
10.0	12.8	25.5	19.2	55	19.0	47
10.1	12.8	25.6	20.4	53	20.9	55
10.0	12.7	25.4	19.7	53	21.9	53
5.3	6.7	13.4	12.3	33	10.1	26
5.3	6.7	13.4	8.6	32	10.8	28
5.3	6.8	13.5	11.6	28	11.9	28

Table 5.5.

Table of results from stage 2 of the calibration procedure for the high velocity range and a 10mm slice width.

High Velocity Calibration Slice Width = 16mm

Pipe c/s area = 0.785sqcm T = 2.5ms

Flow Rate (ml/s)	Mean Velocity (cm/s)	Maximum Velocity (cm/s)	Left ϕ_{sum}	Left ϕ_{max}	Right ϕ_{sum}	Right ϕ_{max}
39.2	50.0	99.9	70.0	161	80.6	164
40.0	51.0	101.9	72.3	163	81.4	166
39.8	50.8	101.5	74.3	168	73.2	164
34.6	44.1	88.2	64.7	150	65.7	153
34.6	44.1	88.2	66.7	148	64.8	152
34.5	43.9	87.9	63.1	147	69.1	156
29.9	38.0	76.1	54.9	127	58.9	131
29.9	38.1	76.3	52.3	130	54.7	135
29.9	38.1	76.3	51.9	126	60.5	129
25.1	32.0	64.0	44.0	102	52.7	113
25.2	32.1	64.2	46.7	111	50.2	117
25.1	32.0	64.0	46.7	111	49.9	109
19.7	25.1	50.2	36.0	99	31.9	88
19.6	25.0	50.0	33.3	87	43.8	93
19.6	25.0	50.1	35.7	96	36.8	87
15.0	19.1	38.1	25.7	82	27.1	69
14.9	19.0	37.9	30.0	75	28.9	69
15.0	19.1	38.3	28.9	80	27.0	74
10.0	12.7	25.5	17.9	45	19.4	50
10.0	12.7	25.5	17.3	52	16.8	57
10.0	12.8	25.6	16.4	48	21.7	55
5.2	6.7	13.3	8.8	27	8.9	29
5.3	6.7	13.4	9.4	29	8.8	29
5.3	6.8	13.5	7.3	28	9.9	30

Table 5.6.

Table of results from stage 2 of the calibration procedure for the high velocity range and a 16mm slice width.

Low Velocity Calibration Slice Width = 10mm

Pipe c/s area = 0.785sqcm T = 5.0ms

Flow Rate (ml/s)	Mean Velocity (cm/s)	Maximum Velocity (cm/s)	Left ϕ_{sum}	Left ϕ_{max}	Right ϕ_{sum}	Right ϕ_{max}
10.6	13.5	26.9	63.6	166	70.0	162
10.6	13.5	26.9	61.0	172	72.3	157
10.6	13.5	27.0	63.9	175	74.1	161
9.2	11.7	23.4	56.2	152	58.9	142
9.2	11.8	23.5	54.8	153	61.6	137
9.2	11.8	23.5	54.3	154	58.9	140
8.2	10.5	21.0	48.7	141	51.7	129
8.2	10.4	20.9	48.4	139	53.6	127
8.2	10.4	20.8	48.3	139	55.4	124
7.2	9.1	18.2	43.3	123	44.9	111
7.2	9.1	18.3	43.0	125	45.3	108
7.2	9.1	18.3	41.1	124	47.0	110
6.2	7.9	15.7	36.7	109	38.9	98
6.2	7.9	15.9	36.2	109	38.1	97
6.3	8.0	16.1	35.6	107	38.7	98
5.2	6.6	13.2	30.9	91	31.3	89
5.2	6.7	13.3	30.3	90	31.6	83
5.1	6.6	13.1	29.8	87	32.4	84
4.0	5.1	10.1	21.3	71	24.6	64
4.0	5.1	10.3	20.6	66	23.3	62
4.0	5.1	10.1	22.8	64	22.9	63
2.9	3.8	7.5	16.3	50	16.3	51
3.0	3.8	7.6	15.2	49	16.2	48
3.0	3.8	7.6	16.2	50	16.3	48
1.7	2.2	4.5	8.6	34	10.5	28
1.8	2.2	4.5	7.5	28	9.7	28
1.8	2.3	4.6	7.1	29	8.9	29

Table 5.7.

Table of results from stage 2 of the calibration procedure for the low velocity range and a 10mm slice width.

Low Velocity Calibration Slice Width = 16mm

Pipe c/s area = 0.785sqcm T = 8.0ms

Flow Rate (ml/s)	Mean Velocity (cm/s)	Maximum Velocity (cm/s)	Left ϕ_{sum}	Left ϕ_{max}	Right ϕ_{sum}	Right ϕ_{max}
10.1	12.9	25.7	61.8	168	59.0	154
10.1	12.8	25.6	56.0	155	64.8	162
10.1	12.9	25.7	58.8	165	60.7	156
9.1	11.6	23.1	50.4	142	55.2	145
9.1	11.5	23.1	50.7	144	56.8	143
9.1	11.5	23.1	48.8	144	55.5	153
8.3	10.6	21.2	50.2	140	52.2	144
8.2	10.5	21.0	49.7	137	51.8	146
8.3	10.5	21.1	50.5	139	54.6	148
7.2	9.2	18.4	44.2	123	47.8	133
7.3	9.3	18.5	41.6	122	49.3	133
7.3	9.3	18.6	41.8	122	45.4	136
6.2	7.9	15.9	35.6	111	41.8	115
6.2	7.9	15.8	33.5	107	41.8	111
6.2	7.9	15.7	38.6	109	41.4	117
5.3	6.7	13.4	30.9	107	36.3	99
5.3	6.8	13.5	31.6	90	36.2	101
5.3	6.7	13.4	29.6	90	35.4	97
4.1	5.2	10.4	23.0	69	25.0	72
4.1	5.2	10.4	21.6	68	26.9	76
4.0	5.1	10.2	22.9	66	23.5	73
3.2	4.0	8.1	19.3	56	19.6	57
3.1	4.0	8.0	20.4	55	17.6	54
3.2	4.0	8.0	16.4	53	22.3	59
1.8	2.3	4.5	10.6	30	8.1	29
1.8	2.2	4.5	9.4	29	10.0	34
1.8	2.3	4.5	11.1	30	11.4	33

Table 5.8.

Table of results from stage 2 of the calibration procedure for the low velocity range and a 16mm slice width.

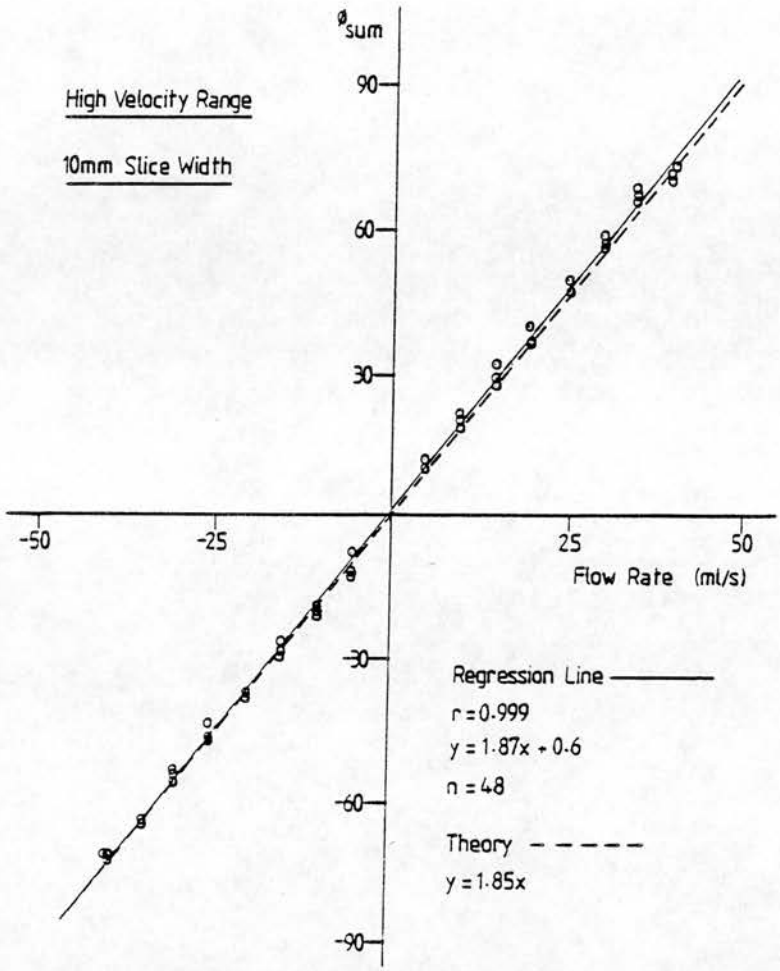

Figure 5.9.

Graph plotting ϕ_{sum} against flow rate (in millilitres per second) for flow in the high velocity range and a slice width of 10 millimetres. The regression line is shown and agrees well with the theoretical relationship predicted by equation 5.10 (dotted line). The mean standard error of estimating flow rate from ϕ_{sum} is +/- 1.02 ml/s.

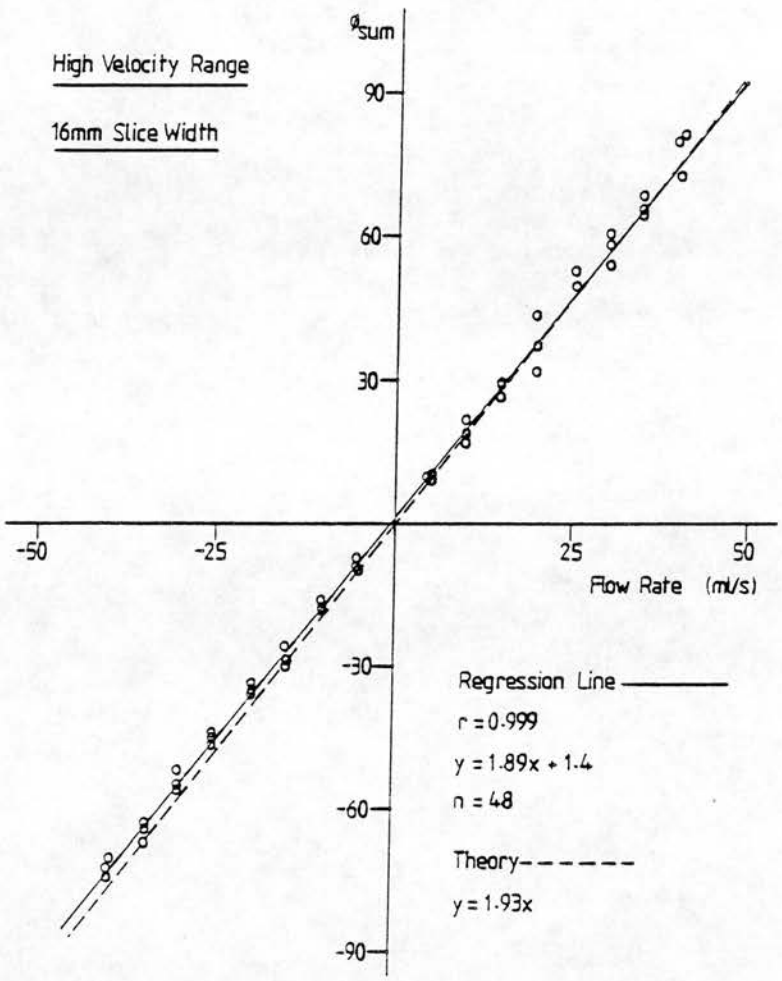

Figure 5.10.

Graph plotting ϕ_{sum} against flow rate (in millilitres per second) for flow in the high velocity range and a slice width of 16 millimetres. The regression line is shown and agrees well with the theoretical relationship predicted by equation 5.10 (dotted line). The mean standard error of estimating flow rate from ϕ_{sum} is +/- 1.36 ml/s.

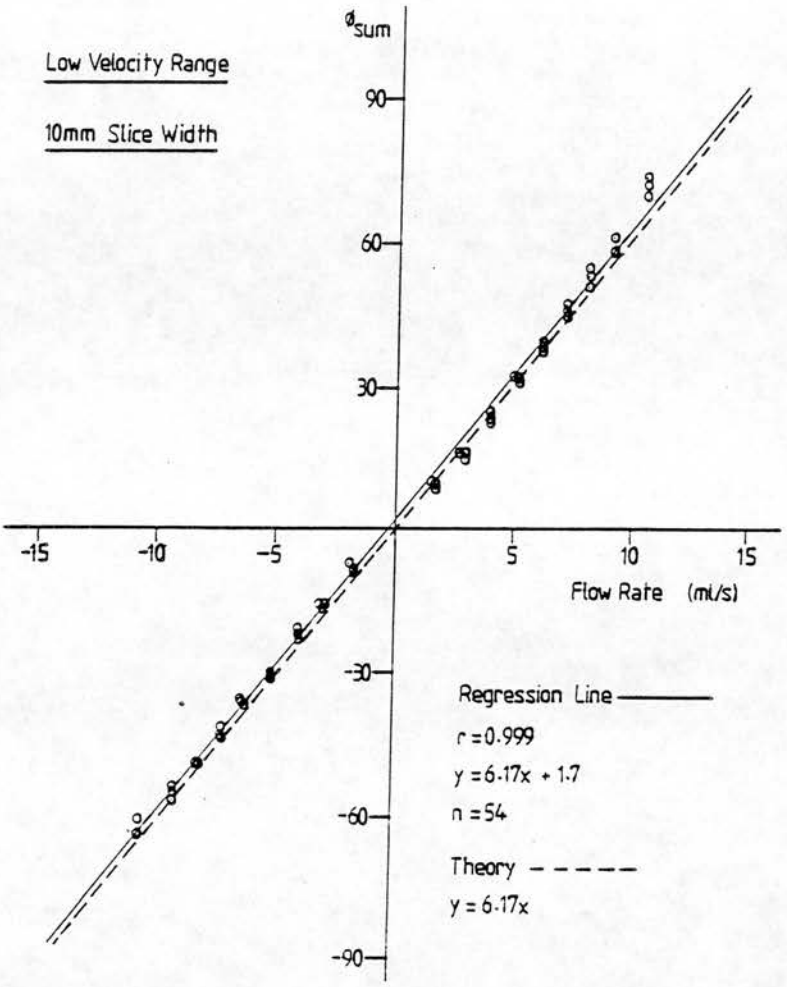

Figure 5.11.

Graph plotting ϕ_{sum} against flow rate (in millilitres per second) for flow in the low velocity range and a slice width of 10 millimetres. The regression line is shown and agrees well with the theoretical relationship predicted by equation 5.10 (dotted line). The mean standard error of estimating flow rate from ϕ_{sum} is +/- 0.37 ml/s.

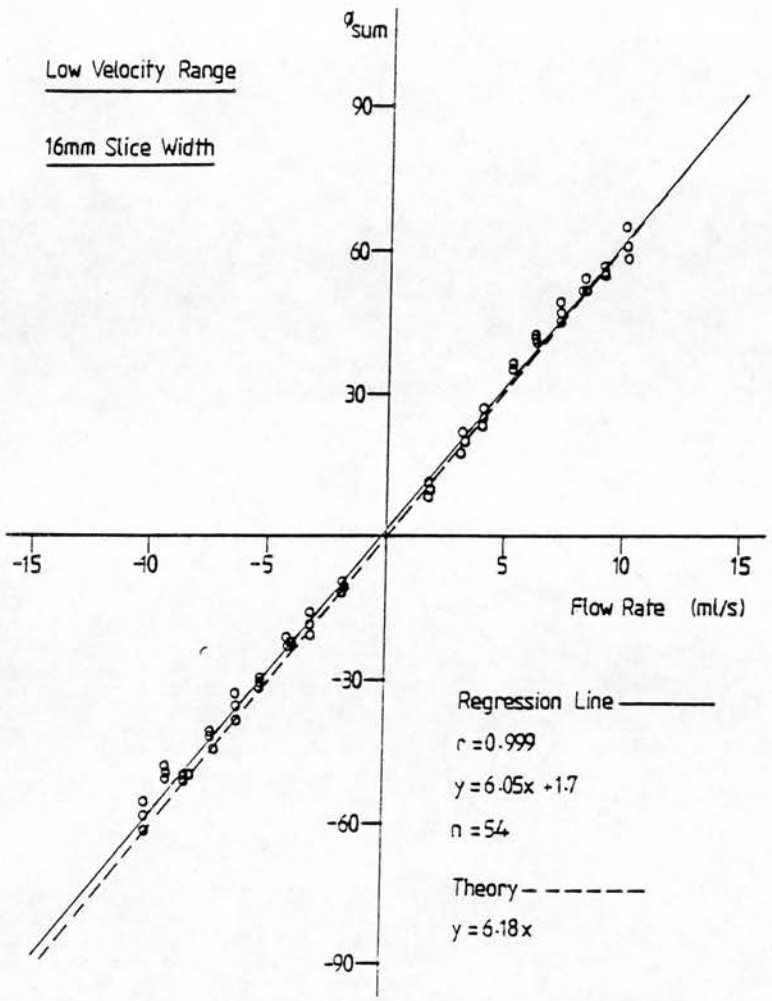

Figure 5.12.

Graph plotting ϕ_{sum} against flow rate (in millilitres per second) for flow in the low velocity range and a slice width of 16 millimetres. The regression line is shown and agrees well with the theoretical relationship predicted by equation 5.10 (dotted line). The mean standard error of estimating flow rate from ϕ_{sum} is +/- 0.37 ml/s.

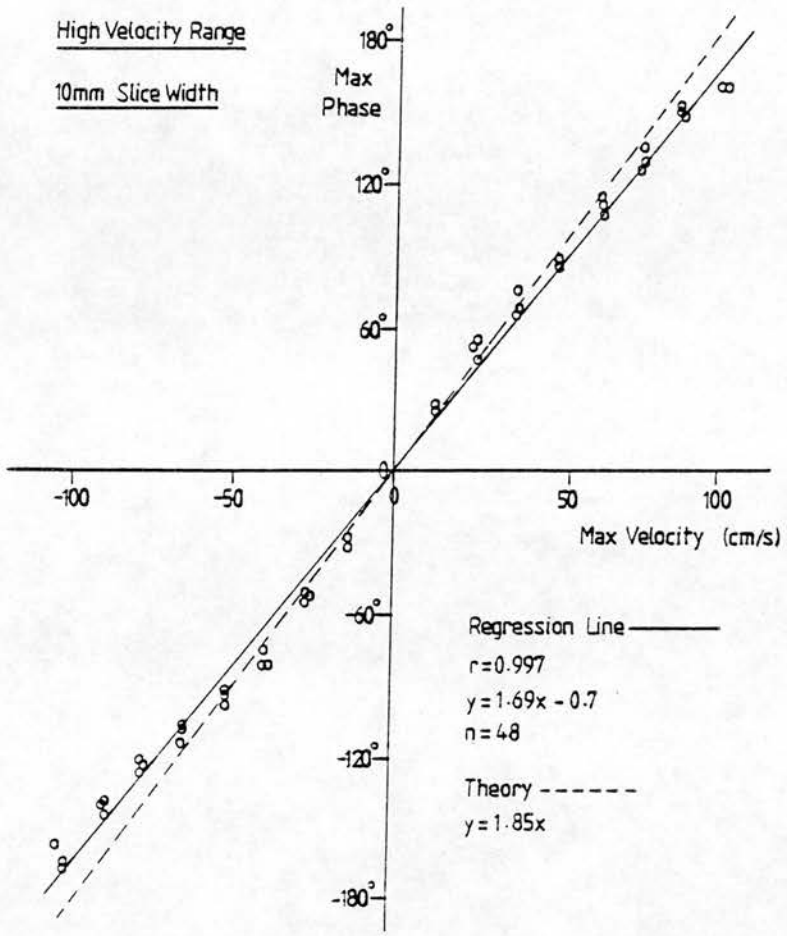

Figure 5.13.

Graph plotting ϕ_{max} against the expected maximum velocity (in centimetres per second), assuming laminar flow for a high velocity range and a slice width of 10 millimetres. The regression line is shown and differs slightly from the theoretical relationship predicted by equation 5.10 (dotted line). The mean standard error of estimating maximum velocity from ϕ_{max} is +/- 4.8 cm/s.

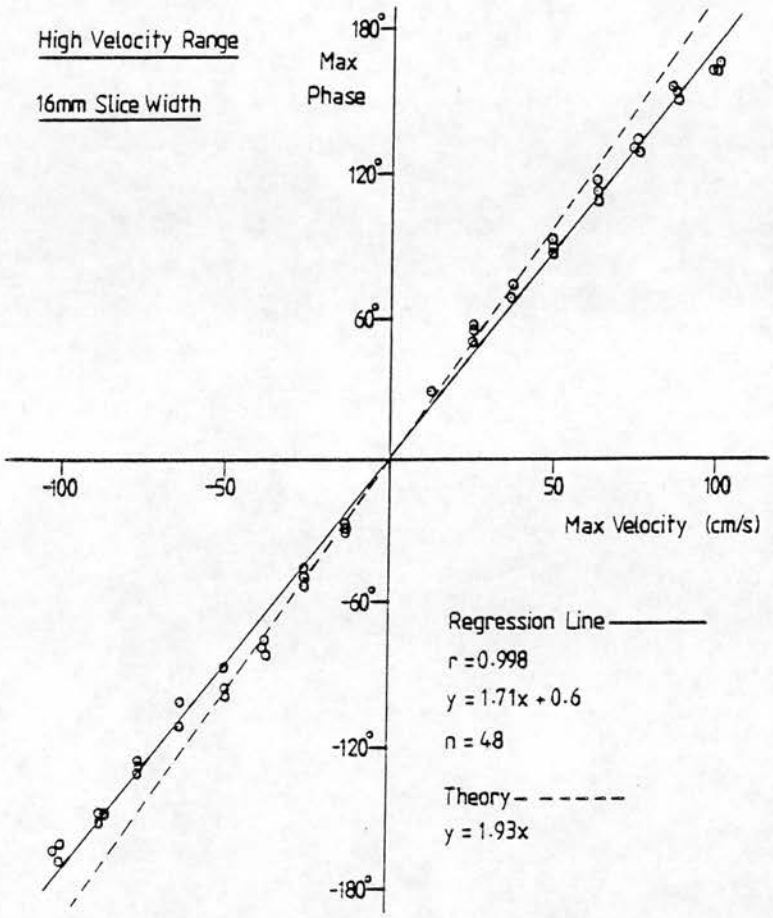

Figure 5.14.

Graph plotting ϕ_{max} against the expected maximum velocity (in centimetres per second), assuming laminar flow for a high velocity range and a slice width of 16 millimetres. The regression line is shown and differs slightly from the theoretical relationship predicted by equation 5.10 (dotted line). The mean standard error of estimating maximum velocity from ϕ_{max} is +/- 4.3 cm/s.

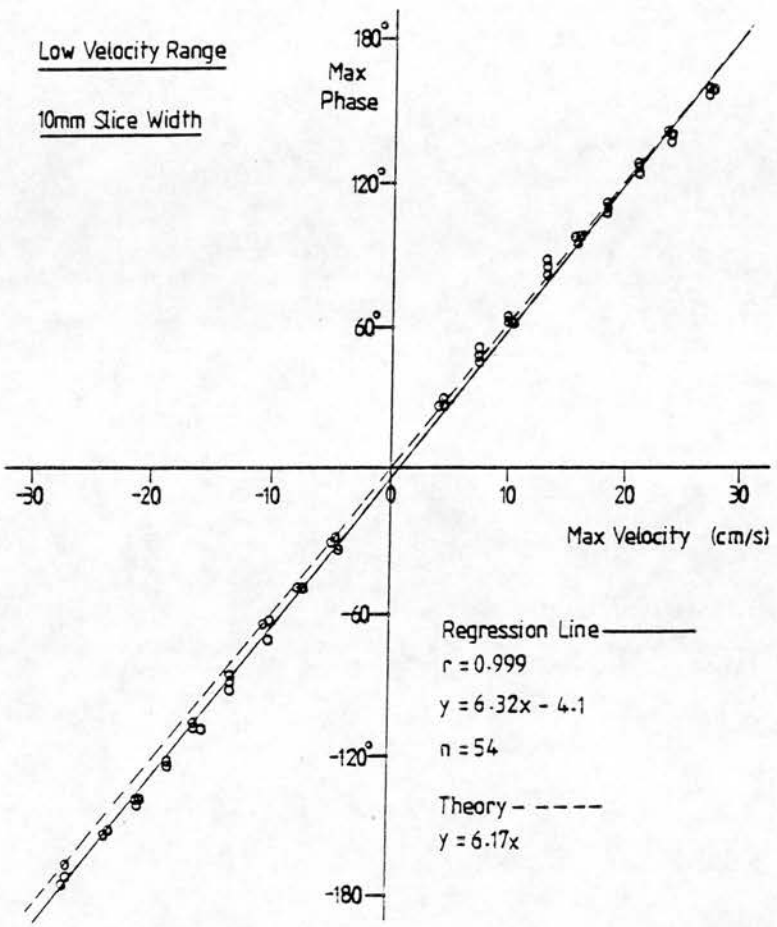

Figure 5.15.

Graph plotting ϕ_{max} against the expected maximum velocity (in centimetres per second), assuming laminar flow for a low velocity range and a slice width of 10 millimetres. The regression line is shown and agrees well with the the theoretical relationship predicted by equation 5.10 (dotted line). The mean standard error of estimating maximum velocity from ϕ_{max} is +/- 0.66 cm/s.

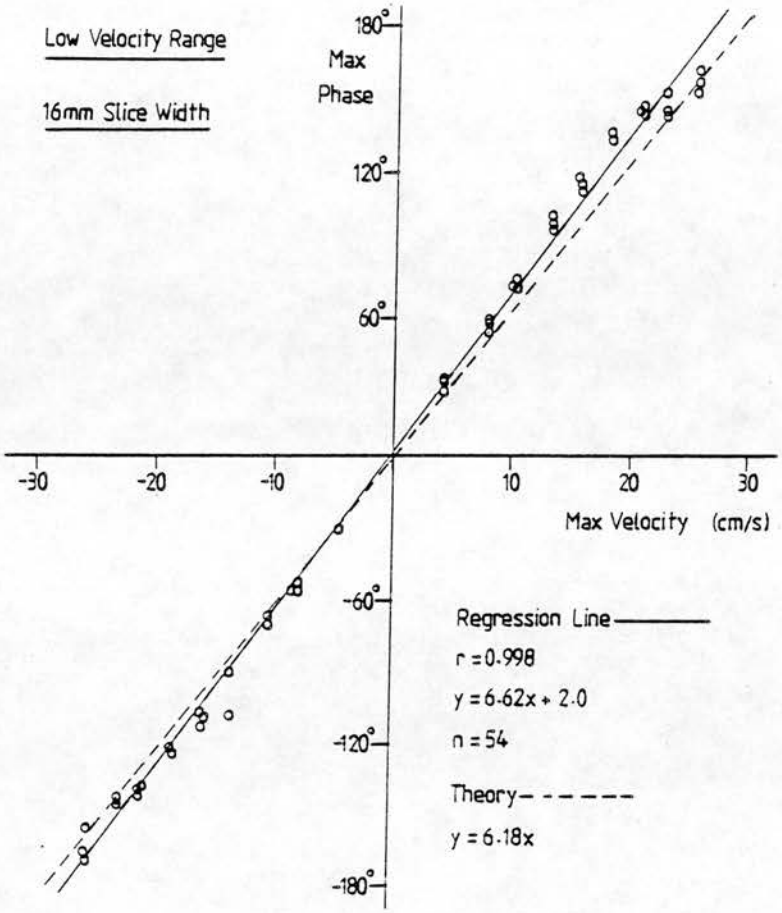

Figure 5.16.

Graph plotting ϕ_{max} against the expected maximum velocity (in centimetres per second), assuming laminar flow for a low velocity range and a slice width of 16 millimetres. The regression line is shown and differs slightly from the theoretical relationship predicted by equation 5.10 (dotted line). The mean standard error of estimating maximum velocity from ϕ_{max} is +/- 1.1 cm/s.

5.2.6. Stage 2 - Summary

Tables 5.9 and 5.10 summarise the results of stage 2 of the calibration, comparing the calibrated and predicted slopes of the relationship between velocity and phase and showing standard error of estimating flow rate and maximum velocity from ϕ_{sum} and ϕ_{max}.

Results of Calibration of ϕ_{sum} against Flow Rate

	High Velocity Range		Low Velocity Range	
Slice Width	10mm	16mm	10mm	16mm
Slope of Theoretical Prediction	1.85	1.93	6.17	6.18
Slope of Regression Line	1.87	1.89	6.17	6.05
y-intercept	+0.6	+1.4	+1.7	+1.7
S.E.E. of flow rate from ϕ_{sum} (ml/s)	+/-1.02	+/-1.36	+/-0.37	+/-0.37

Table 5.9.

Table summarising the results of the calibration of ϕ_{sum} against flow rate, showing the slope aand y-intercept of the regression line, the slope of the line predicted by equation 5.10, and the standard error of estimate (S.E.E) in millilitres per second for estimating flow rate from ϕ_{sum}.

Results of Calibration of ϕ_{max} against Maximum Velocity

	High Velocity Range		Low Velocity Range	
Slice Width	10mm	16mm	10mm	16mm
Slope of Theoretical Prediction	1.85	1.93	6.17	6.18
Slope of Regression Line	1.69	1.71	6.32	6.62
y-intercept	-0.7	+0.6	-4.1	+2.0
S.E.E. of max. velocity from ϕ_{max} (cm/s)	+/-4.8	+/-4.3	+/-0.66	+/-1.1

Table 5.10.

Table summarising the results of the calibration of ϕ_{max} against maximum velocity, showing the slope and y-intercept of the regression line, the slope of the line predicted by equation 5.10, and the standard error of estimate (S.E.E), in cntimetres per second for estimating maximum velocity from ϕ_{max}.

The relationship between ϕ_{sum} and flow rate is linear and agrees well with the predicted relationship. The relationship between ϕ_{max} and maximum velocity agrees less well with the predicted relationship, particularly in the high velocity range. The standard error of estimating flow rate from ϕ_{sum} is small suggesting that the technique is precise.

The standard error of estimating maximum velocity from ϕ_{max} is greater, particularly at high velocities, suggesting that the measurement of maximum velocity using phase mapping is less precise than the measurement of flow rate.

5.3. Discussion of Errors in the Calibration

The maximum and mean velocities are derived from the flow rate which is measured by recording the time it takes to collect a certain volume of fluid in a measuring cylinder. Typically a volume of 500mls was acquired in around 50 seconds. If it is assumed that the error is +/-0.005 litre (half a division on the measuring cylinder) for the volume measurement, and +/-0.5 seconds for the time measurement, these constitute errors of around 1.0% each. The actual flow rate is therefore known to within +/-2%. The internal diameter of the plastic pipe is accurately known and contributes a negligible error to the calculation of the mean velocity from the flow rate. The mean velocity can therefore be determined to within +/-2%.

Measurement of the mean phase value within the region of interest on the phase image is difficult. The internal cicumference of the pipe is often difficult to define, which leads to a wide variation in the measurement of the cross-sectional area and mean phase value.

In order to minimise this source of error, the quantity ϕ_{sum} was calculated by multiplying the mean phase measured within the pipe (after subtraction of the background phase value), by the area corresponding to the number of pixels measured. This quantity represents the flow rate through the pipe, and has the same relationship to the actual flow rate as the mean phase value has to the mean velocity. If the area measured is smaller than the pipe, the mean phase value is overestimated, but the value of ϕ_{sum} is compensated by the smaller area. The quantity ϕ_{sum} was therefore used to generate the calibration graphs, which showed an excellent agreement with the relationships predicted by equation 5.10.

The maximum velocity was calculated as twice the mean veloctiy, assuming a symmetric parabolic flow profile in the presence of laminar flow. The flow rates used in this experiment were well within the values at which turbulence was expected to occur given the geometry of the pipe.

Measurement of maximum phase value is obtained from the maximum pixel value within the region of interest. Since the in-plane resolution is large (2mm x 2mm), compared to the pipe diameter (1.0cm), there is a distribution of velocities within each pixel. The phase shift recorded by each pixel is dependent on the distribution of phase values corresponding to this velocity distribution.

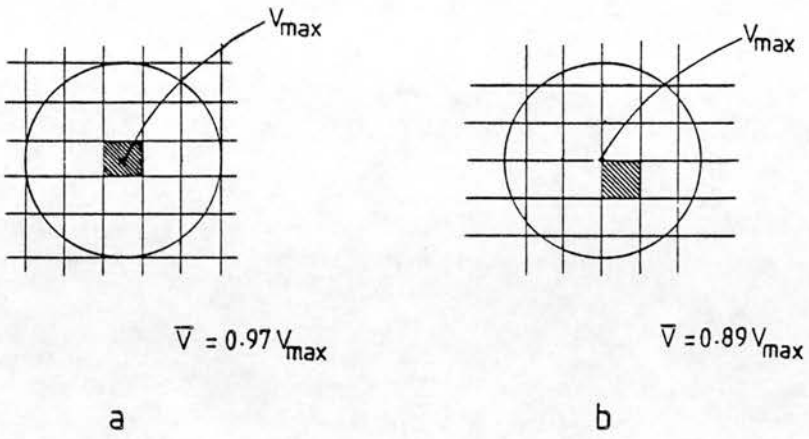

Figure 5.17.

Diagram showing the average velocity, $\bar{V}$, expected over the area of a 2mm x 2mm pixel (shaded area), at the centre of a 1.0cm diameter pipe, expressed as a fraction of the maximum velocity, V_{max}, and assuming a symmetric, parabolic flow profile. In a) the pixel is exactly coincident with the centre of the pipe, while in b) the pixel is displaced the maximum possible distance from the centre.

The average velocity expected in a pixel at the centre of the pipe cross section can be calculated, assuming the existence of laminar flow with a symmetric parabolic profile. Figure 5.17a shows the average velocity, expressed as a fraction of the maximum velocity, expected for a pixel which is exactly coincident with the centre of the pipe. In figure 5.17b the pixel is displaced away from the centre of the pipe. As result of the relatively large pixel dimensions used for the calibration procedure, the average velocity within the pixel can be

within a range 0.89 and 0.97 of the true maximum velocity. The maximum phase measurement will reflect this discrepency, and may account for the difference between the calibrated and theoretical relationships between the maximum phase values, ϕ_{max}, and the expected maximum velocities.

In Vivo Comparison with Doppler Ultrasound

6.0. Introduction.

The MRI flow measurement technique has been compared, in vivo, with velocity measurements obtained using Doppler ultrasound. The measurements were performed on the common carotid arteries of 4 healthy volunteers. The MRI technique used a multiple frame acquisition, synchronised with the R-wave of the subject's ECG, to obtain instantaneous velocity measurements at multiple points throughout the cardiac cycle. These measurements were compared with measurements taken from corresponding points on the velocity waveforms obtained using Doppler ultrasound.

6.1. Methods

The common carotid arteries of 4 healthy volunteers were studied. The common carotid artery was chosen because of its large size and for ease of access by ultrasound. The measurements were performed approximately two centimeters below the carotid bifurcation, where there was relatively little turbulence. The volunteers remained supine and their heart rates were monitored throughout both the MRI and the Doppler ultrasound examinations.

6.1.1. Method - MRI

The MRI flow technique was performed using the MRI system and flow measurement technique described in chapter 4. An ECG signal was obtained from the subject, using either conventional or carbon electrodes. The radiofrequency receiver coil, which is normally used for imaging the head, was used to image the neck of the volunteers by positioning the lower edge of the coil against their shoulders.

The bifurcation of the carotid arteries was located by acquiring a series of ungated multiple slices in the sagittal plane, using the flow imaging pulse sequence. The sequence was velocity-encoded in the frequency-encoding direction, corresponding to the direction of flow in the carotid arteries. From the resultant phase maps, the position of the carotid bifurcation could be seen (figure 6.1), and a transverse plane was prescribed at a position 20mm below the most distal of the two carotid bifurcations.

A gated, multiple-frame scan was then performed in the prescribed plane, using a slice thickness of 10mm and an acquisition mmatrix of 128 x 64 elements, giving an in-plane resolution of 4mm x 2mm. Signal averaging was performed using two signal acquisitions. The repetition rate of each frame was 120 milliseconds, and 6-8 frames

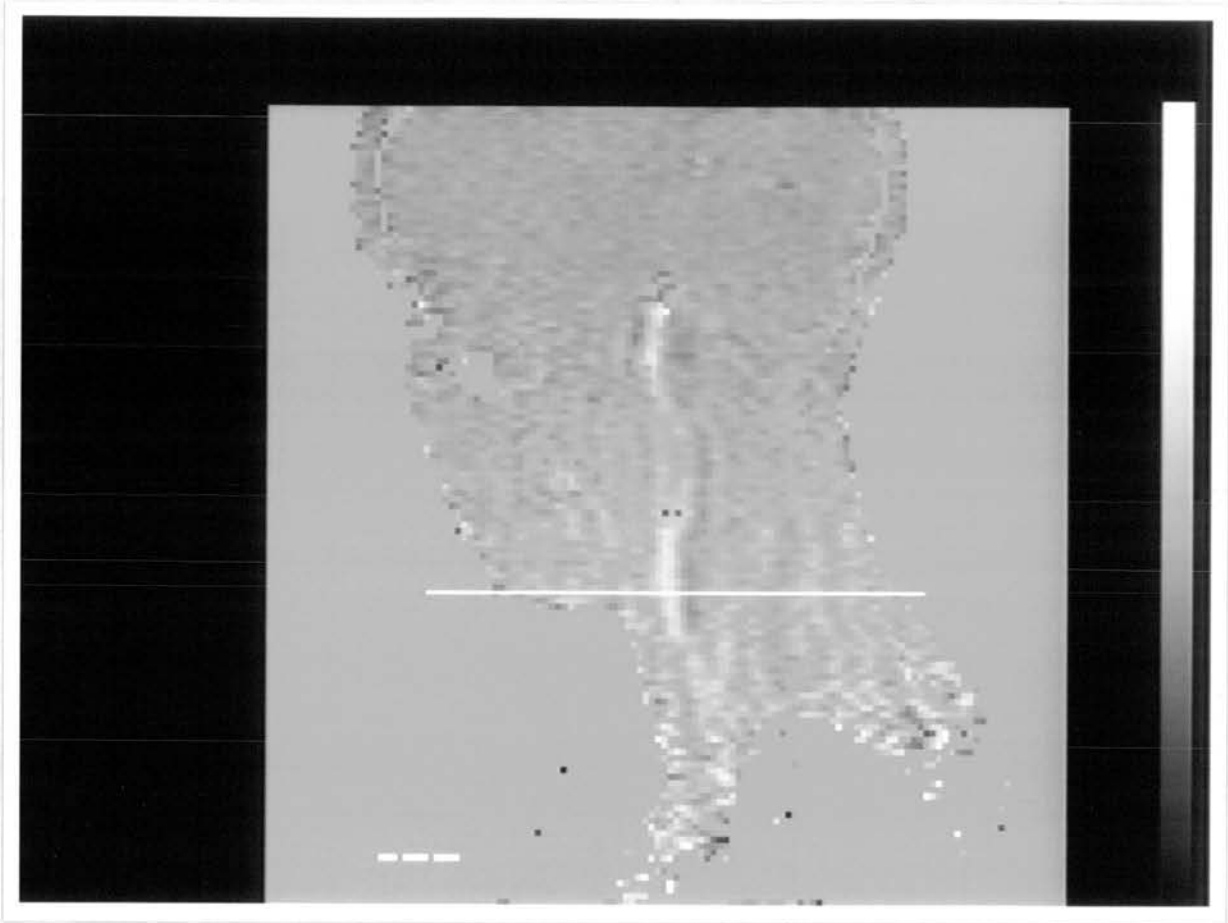

Figure 6.1.

An example of one of the phase maps acquired in the sagittal plane showing the carotid bifurcation. These phase maps were used to prescribe a transverse plane 2cm below the bifurcation (white line).

were acquired following each R-wave synchronisation pulse. Two further acquisitions were performed with additional delays of 40 and 80 milliseconds inserted between the R-wave and the first frame. Therfore, between 18 to 24 frames were acquired at different points in the cardiac cycle, with an effective time separation of 40 milliseconds (Figure 6.2).

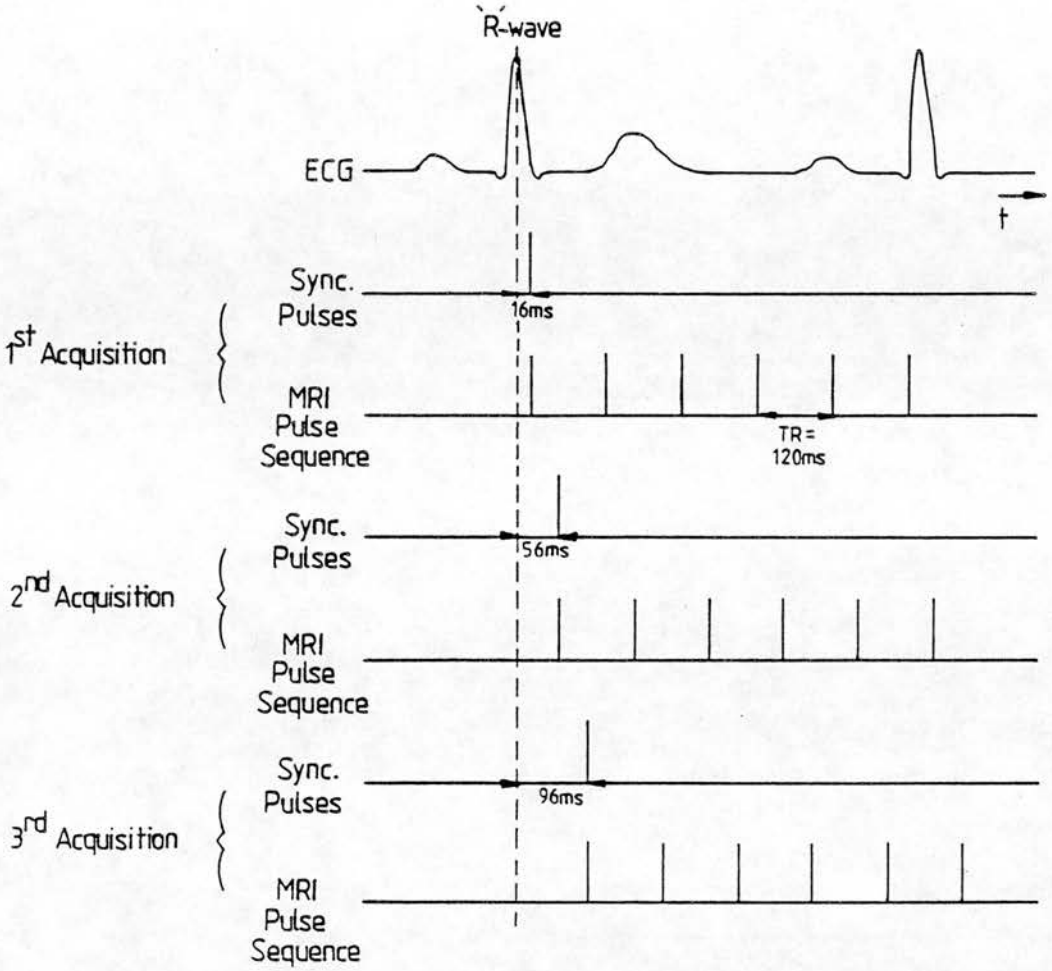

Figure 6.2.

Three multiple-frame acquisitions, using a repetition time of 120ms, were performed with delays of 16, 56, and 96ms between the R-wave and the first frame. Images were therefore acquired at 40ms intervals throughout the cardiac cycle.

The excitation angle was set to 90° in order to maximise the signal from flowing blood. The shortest sampling time was selected (table 4.4), and so the field echo occured at time equal to 22.6 millseconds plus the time delay introduced for velocity encoding, T. For this study T was

chosen to be 2.0ms, corresponding to a velocity range of +/-72.8cm/s (table 5.4).

The mean and maximum phase values, and the region of interest areas, were recorded for both the left and right carotids from each of the phase maps. Pixels which had corresponding values on the magnitude image of less than 25% maximum signal were excluded from the phase measurement. Pixels for which the velocity was overrange (i.e. causing phase values of greater than 180^{o}), were corrected for. The background phase measurement was subtracted from the mean and maximum phase values and the summed phase shift was calculated for each carotid as the product of the mean phase shift and the region of interest area. Flow rates and maximum velocities were calculated using a scaling factor derived from the calibration. Mean velocities were derived from the flow rates by using an average value for the region of interest area.

6.1.2. Method - Doppler

The velocity waveforms were measured using Doppler ultrasound, immediately following the MRI examination, while the subject was still supine on the patient couch. Measurement was performed using an ACUSON 128 duplex Doppler ultrasound system operating at 3.0 Megahertz. The

operator was familiar with the machine in clinical use.

Both the right and left carotid arteries were examined separately. The carotid bifurcation was located from the two-dimensional ultrasound display and the sample volume for the doppler measurement was positioned interactively using a cursor. The sample volume was positioned approximately two centimetres below the bifurcation, in order to obtain velocity waveforms from a site similar to that imaged by the MRI technique. The size of the sample volume was adjusted to include as much of the vessel lumen as possible, whilst avoiding the inclusion of Doppler signals from wall motion.

The visual display and the audio frequency shift signal was recorded on video tape. Estimates of the peak maximum and mean velocities, and of the time-averaged mean velocity, were recorded using the software available on the ACUSON system. The recorded waveforms were later sampled by a BBC microcomputer and were smoothed and averaged to match the number of sampled points obtained using the MRI technique.

6.2. Results

Figure 6.3 shows the magnitude images and phase maps of two of the frames obtained from one of the volunteers.

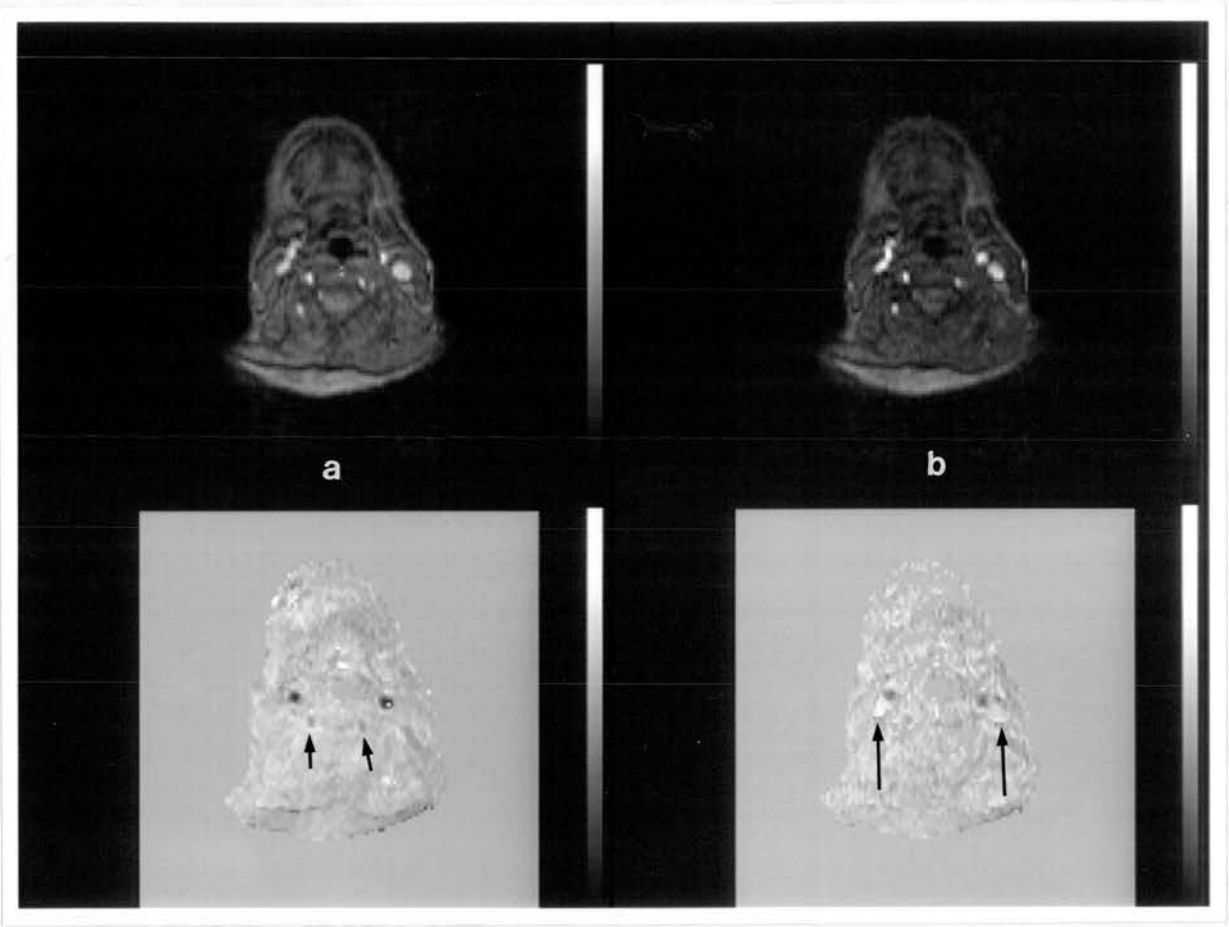

Figure 6.3.

The magnitude images (top) and corresponding phase maps (bottom) obtained from two of the frames acquired from one of the volunteers. In (a) the images were acquired at peak systole. The white dot observed in the left common carotid artery, (seen on the right), indicates that the velocity is overrange. In (b) the images were acquired at late systole when the velocities were reduced. Flow in the vertebral arteries (small arrows) can be clearly seen in (a), while flow in the jugular veins (long arrows) is clearly seen in (b).

Figure 6.4 shows a typical Doppler display obtained for one of the volunteers.

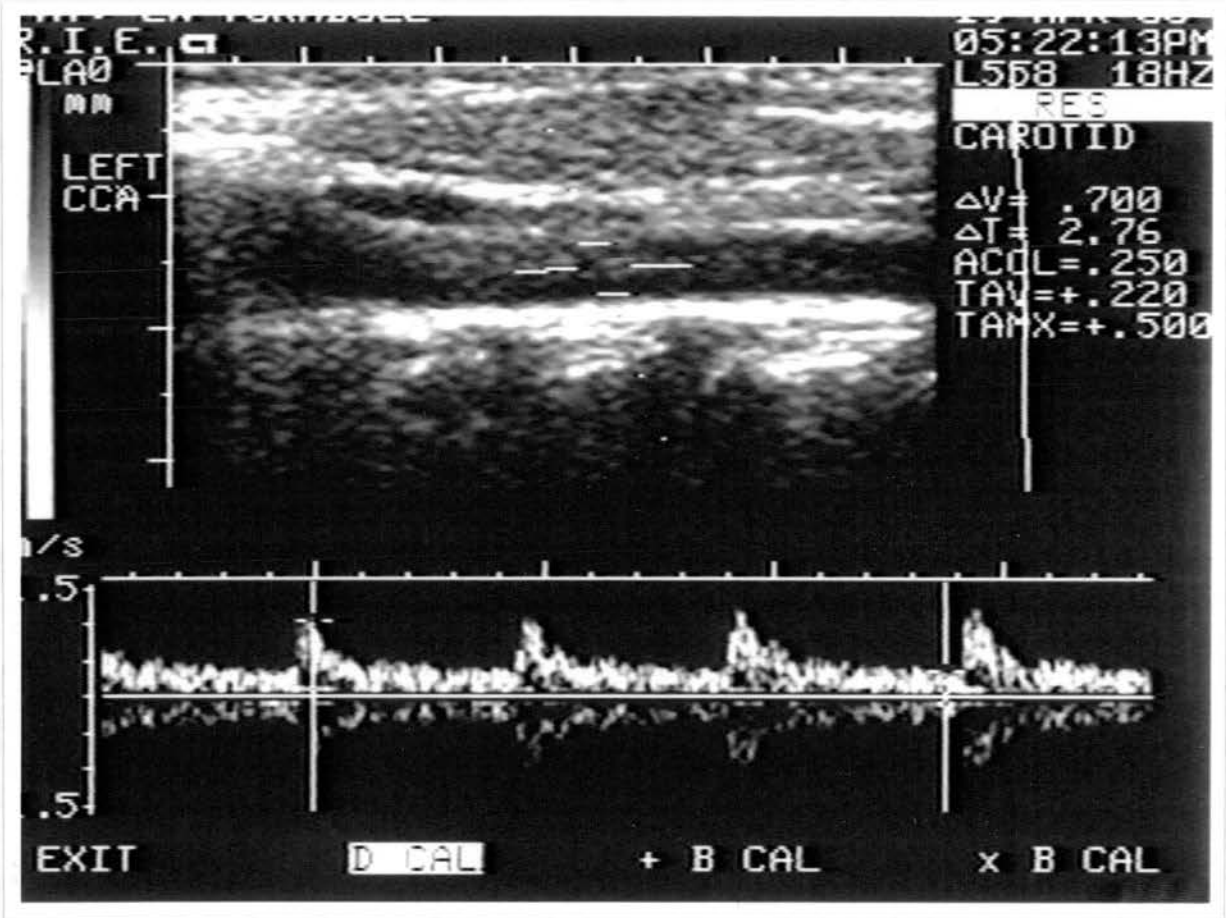

Figure 6.4.

An example of the display obtained during the Doppler ultrasound examination. The position of the sample volume can be seen on the two-dimensional echo image, below which is seen the velocity waveform. Measurements from the velocity waveform can be performed using a cursor. In this case the time-averaged-velocity over three cardiac cycles is being measured.

The third acquisition of the MRI examination of one of the volunteers (JA) was discarded, as the magnetic field of the MRI system became unstable during that acquisition. In another volunteer (LWT) it was not possible to image at a point in the cardiac cycle before peak velocities were attained.

Tables 6.1 to 6.4 give the flow rates and mean and maximum velocities measured by MRI, and the maximum velocities measured by Doppler ultrasound, at each point in the cardiac cycle for the left and right common carotid arteries of the four volunteers.

Table of Results of MRI and Doppler Comparison - Volunteer JA

Gradient Shift, T = 2.0 ms
Gradient Magnitude = 660
Mean Area of RCCA = 0.64 sqcm
Velocity Range = 72.8 cm/s
Scaling Factor = 0.405
Mean Area of LCCA = 0.69 sqcm

	Right CCA				Left CCA			
Time after R-Wave (ms)	MRI Flow Rate (ml/s)	MRI Mean Velocity (cm/s)	MRI Maximum Velocity (cm/s)	Doppler Maximum Velocity (cm/s)	MRI Flow Rate (ml/s)	MRI Mean Velocity (cm/s)	MRI Maximum Velocity (cm/s)	Doppler Maximum Velocity (cm/s)
16	13.2	20.5	62.3	83.8	6.8	9.9	33.2	52.3
56	20.5	31.8	67.8	90.3	28.8	41.8	74.7	89.1
136	14.0	21.8	56.8	66.3	12.1	17.5	43.0	82.3
176	12.0	18.7	38.2	49.4	16.6	24.0	45.1	60.0
256	14.5	22.5	42.6	49.7	15.7	22.7	38.5	48.9
296	8.8	13.7	29.2	50.7	16.2	23.5	36.5	50.4
376	13.7	21.3	34.6	46.6	13.9	20.1	37.4	48.7
416	9.9	15.3	31.2	32.2	16.5	23.9	36.9	41.9
496	12.1	18.8	32.4	35.5	10.9	15.8	28.7	34.7
536	7.0	10.8	31.2	39.5	11.3	16.4	29.6	40.8
616	10.5	16.3	32.2	38.3	8.4	12.2	25.3	41.9
656	8.9	13.8	35.3	36.7	14.2	20.5	28.4	39.1
736	9.5	14.7	23.9	33.0	8.3	12.1	22.7	35.2
776	8.9	13.8	16.3	30.2	13.4	19.4	30.0	31.5
856	8.0	12.4	20.5	29.4	7.3	10.5	20.9	30.1

Table 6.1.

Table of the flow rates and mean and maximum velocities measured by MRI, and the maximum velocities measured by Doppler ultrasound for the left and right common carotid arteries of volunteer JA.

Table of Results of MRI and Doppler Comparison - Volunteer DP

Gradient Shift, T = 2.0 ms
Gradient Magnitude = 660
Mean Area of RCCA = 0.63 sqcm
Velocity Range = 72.8 cm/s
Scaling Factor = 0.405
Mean Area of LCCA = 0.59 sqcm

	Right CCA				Left CCA			
Time after R-Wave (ms)	MRI Flow Rate (ml/s)	MRI Mean Velocity (cm/s)	MRI Maximum Velocity (cm/s)	Doppler Maximum Velocity (cm/s)	MRI Flow Rate (ml/s)	MRI Mean Velocity (cm/s)	MRI Maximum Velocity (cm/s)	Doppler Maximum Velocity (cm/s)
16	5.8	9.3	25.9	49.1	6.2	10.5	22.2	78.1
56	27.3	43.6	81.8	100.5	23.2	39.3	67.6	115.2
96	26.3	42.0	73.1	115.2	23.5	39.8	58.1	99.6
136	14.1	22.6	60.8	92.4	15.1	25.6	44.3	67.9
176	10.3	16.4	40.3	60.8	8.7	14.8	28.5	44.7
216	9.4	15.0	39.0	46.8	8.4	14.3	26.1	40.3
256	10.0	16.0	40.0	45.3	10.7	18.1	29.9	36.7
296	7.5	11.9	28.7	37.3	6.3	10.7	44.1	32.7
336	11.4	18.2	32.0	40.7	10.2	17.2	27.1	41.0
376	12.9	20.6	41.1	48.1	13.8	23.3	33.4	46.7
416	10.3	16.4	45.0	50.2	8.7	14.8	38.9	43.4
456	8.8	14.0	35.2	46.0	7.8	13.2	20.6	36.6
496	8.8	14.1	36.2	42.1	9.4	16.0	31.3	34.2
536	8.2	13.2	26.8	40.8	7.0	11.9	34.5	36.9
576	10.0	16.0	28.2	39.4	9.0	15.2	24.2	36.1
616	8.7	13.9	32.3	38.4	9.3	15.7	25.8	34.9
656	5.3	8.4	38.3	37.7	4.5	7.6	31.4	34.2
696	10.2	16.2	31.0	37.0	9.1	15.4	27.4	32.4
736	6.5	10.4	30.9	34.5	7.0	11.8	22.8	33.1

Table 6.2.

Table of the flow rates and mean and maximum velocities measured by MRI, and the maximum velocities measured by Doppler ultrasound for the left and right common carotid arteries of volunteer DP.

Table of Results of MRI and Doppler Comparison - Volunteer HM

Gradient Shift, T = 2.0 ms
Gradient Magnitude = 660
Mean Area of RCCA = 0.68 sqcm

Velocity Range = 72.8 cm/s
Scaling Factor = 0.405
Mean Area of LCCA = 0.58 sqcm

	Right CCA				Left CCA			
Time after R-Wave (ms)	MRI Flow Rate (ml/s)	MRI Mean Velocity (cm/s)	MRI Maximum Velocity (cm/s)	Doppler Maximum Velocity (cm/s)	MRI Flow Rate (ml/s)	MRI Mean Velocity (cm/s)	MRI Maximum Velocity (cm/s)	Doppler Maximum Velocity (cm/s)
16	10.1	14.9	27.3	49.4	9.3	16.2	23.3	28.6
56	23.1	34.0	71.4	123.1	8.5	14.7	54.5	90.2
96	21.2	31.4	64.7	110.0	17.7	30.6	66.3	102.2
136	13.6	20.0	37.4	66.5	10.5	18.1	28.5	69.0
176	11.0	16.3	40.3	45.4	10.9	18.8	37.5	47.4
216	11.6	17.1	39.2	46.0	10.0	17.3	30.7	44.9
256	13.5	20.0	39.6	45.4	11.1	19.2	28.7	43.2
296	11.0	16.3	37.2	34.3	11.3	19.5	33.9	35.6
336	6.7	9.9	26.8	31.7	7.3	12.7	28.4	27.6
376	13.7	20.3	35.7	41.8	10.2	17.7	28.4	37.3
416	12.5	18.5	29.0	42.1	12.1	20.9	37.9	41.1
456	9.1	13.4	25.4	36.7	8.9	15.4	31.9	38.4
496	9.1	13.4	25.9	31.7	6.8	11.8	20.7	32.7
536	9.8	14.5	27.3	30.3	9.2	15.9	28.9	30.5
576	7.0	10.3	26.1	28.9	9.3	16.0	32.6	29.5
616	7.7	11.3	21.6	28.2	6.0	10.3	17.1	27.6
656	7.2	10.6	23.8	28.2	7.5	12.9	26.3	27.0
696	6.9	10.2	17.6	27.4	6.4	11.0	23.3	26.0
736	6.1	9.1	18.7	27.5	4.9	8.4	15.5	26.2
776	7.6	11.2	22.6	27.5	8.2	14.2	26.3	26.3
816	6.1	9.0	16.6	28.5	6.4	11.0	30.7	26.5
856					7.6	13.2	18.9	26.4

Table 6.3.

Table of the flow rates and mean and maximum velocities measured by MRI, and the maximum velocities measured by Doppler ultrasound for the left and right common carotid arteries of volunteer HM.

Table of Results of MRI and Doppler Comparison - Volunteer LT

Gradient Shift, T = 2.0 ms
Gradient Magnitude = 660
Mean Area of RCCA = 0.63 sqcm
Velocity Range = 72.8 cm/s
Scaling Factor = 0.405
Mean Area of LCCA = 0.62 sqcm

	Right CCA				Left CCA			
Time after R-Wave (ms)	MRI Flow Rate (ml/s)	MRI Mean Velocity (cm/s)	MRI Maximum Velocity (cm/s)	Doppler Maximum Velocity (cm/s)	MRI Flow Rate (ml/s)	MRI Mean Velocity (cm/s)	MRI Maximum Velocity (cm/s)	Doppler Maximum Velocity (cm/s)
16	29.9	47.4	74.7	97.0	30.3	48.9	75.5	90.5
56	15.6	24.7	47.7	75.4	17.3	27.9	61.5	74.7
96	5.1	8.0	24.3	61.7	4.7	7.6	25.9	61.3
136	13.6	21.5	36.0	58.1	13.6	21.9	34.8	56.8
176	8.2	12.9	31.0	57.6	8.8	14.1	31.4	51.9
216	8.6	13.7	28.2	49.5	8.4	13.5	27.4	43.8
256	5.9	9.3	20.4	41.2	7.1	11.5	20.8	37.0
296	7.2	11.4	21.3	46.0	6.9	11.1	24.2	38.9
336	7.4	11.8	24.2	48.2	7.4	11.9	22.5	41.8
376	9.4	14.8	25.6	46.2	9.1	14.6	28.4	42.1
416	8.0	12.6	23.3	44.0	6.9	11.0	21.3	39.5
456	7.4	11.7	22.2	43.2	5.4	8.7	17.0	35.7
496	5.7	9.1	26.3	41.8	6.4	10.3	20.6	35.5
536	6.8	10.8	20.8	41.8	6.1	9.8	20.4	33.8
576	5.4	8.5	18.6	40.5	4.1	6.7	18.6	33.6
616	6.3	10.0	19.1	38.0	4.9	7.9	22.7	32.9
656	5.2	8.2	17.6	37.6	6.3	10.1	16.0	31.5
696	3.8	6.1	14.9	37.5	4.3	6.9	17.0	30.9
736	4.6	7.4	17.8		6.3	10.2	19.0	30.2

Table 6.4.

Table of the flow rates and mean and maximum velocities measured by MRI, and the maximum velocities measured by Doppler ultrasound for the left and right common carotid arteries of volunteer LT.

The maximum velocities measured by MRI and Doppler ultrasound, and the mean velocities measured by MRI, are plotted against time through the cardiac cycle for each of the volunteers in figures 6.5 to 6.8. In all cases, the maximum velocities measured by Doppler are greater than those measured by MRI. A point by point correlation was also carried out on the two velocity waveforms in each case as shown in figures 6.9 to 6.12. Although the points do not lie on the line of identity, a reasonable correlation is shown between the maximum velocities measured by the two techniques.

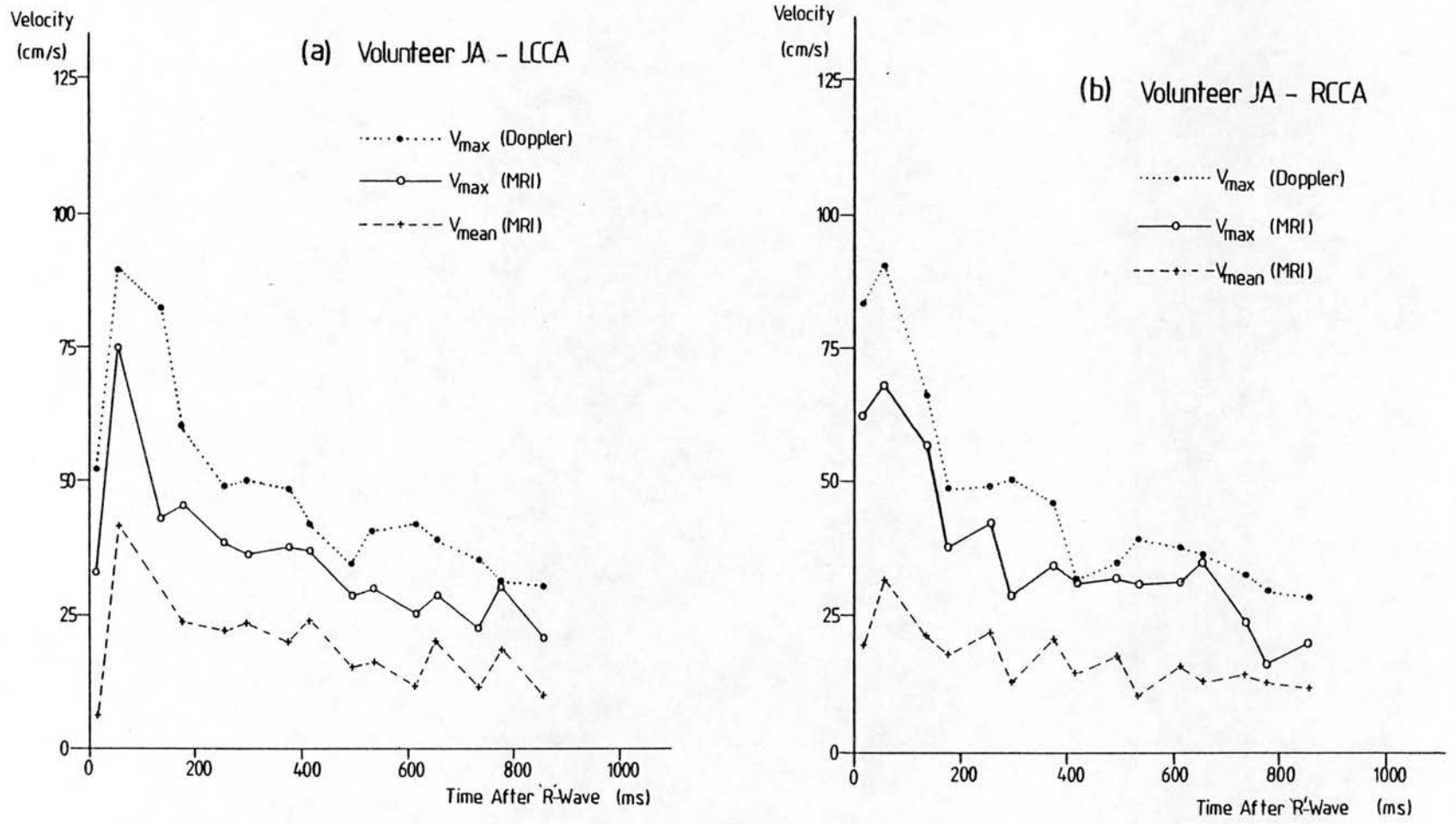

Figure 6.5.

The mean and maximum velocities measured using MRI, and the maximum velocities measured using Doppler ultrasound in (a) the left and (b) the right common carotid artery of volunteer JA.

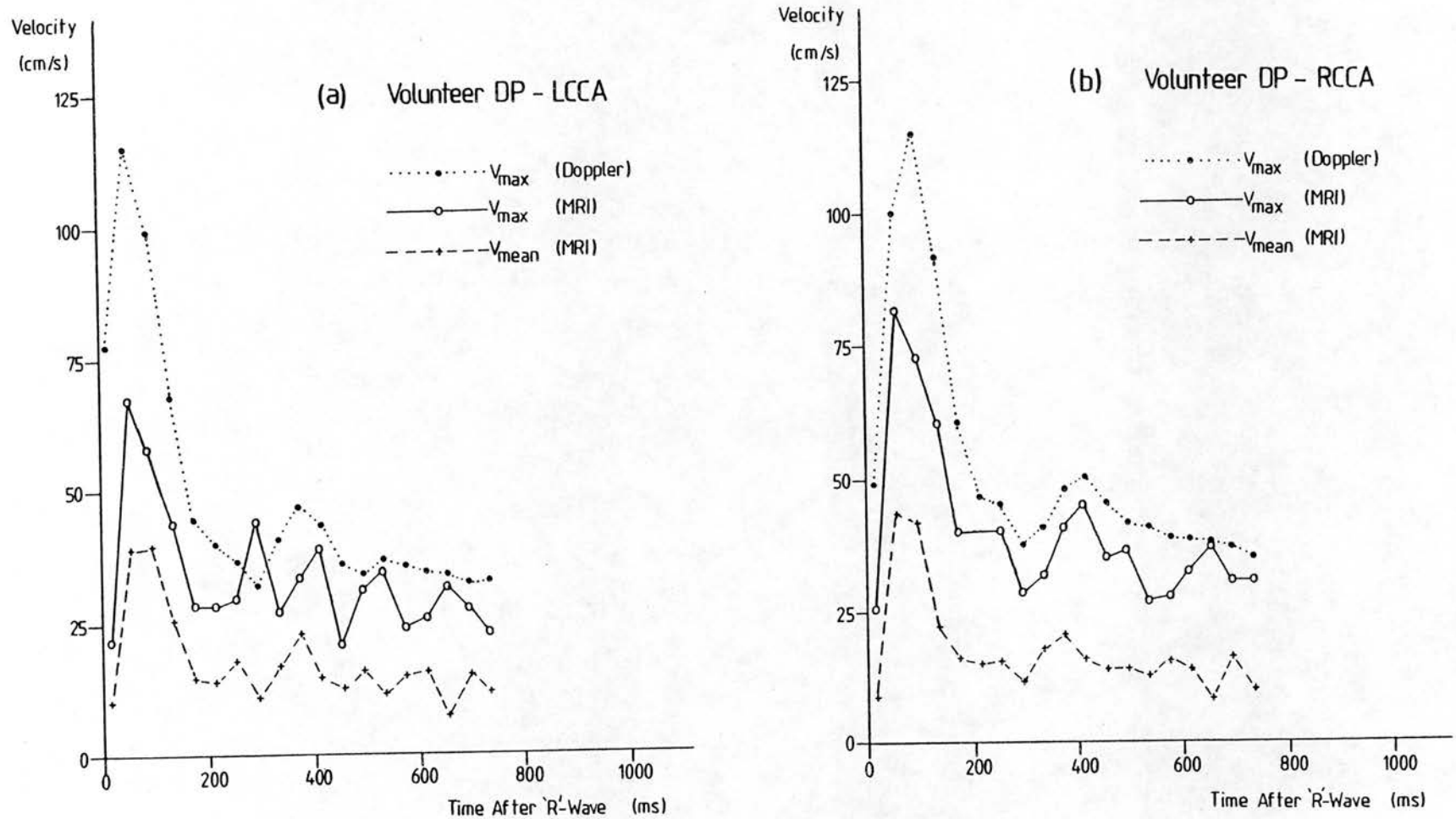

Figure 6.6.

The mean and maximum velocities measured using MRI, and the maximum velocities measured using Doppler ultrasound in (a) the left and (b) the right common carotid artery of volunteer DP.

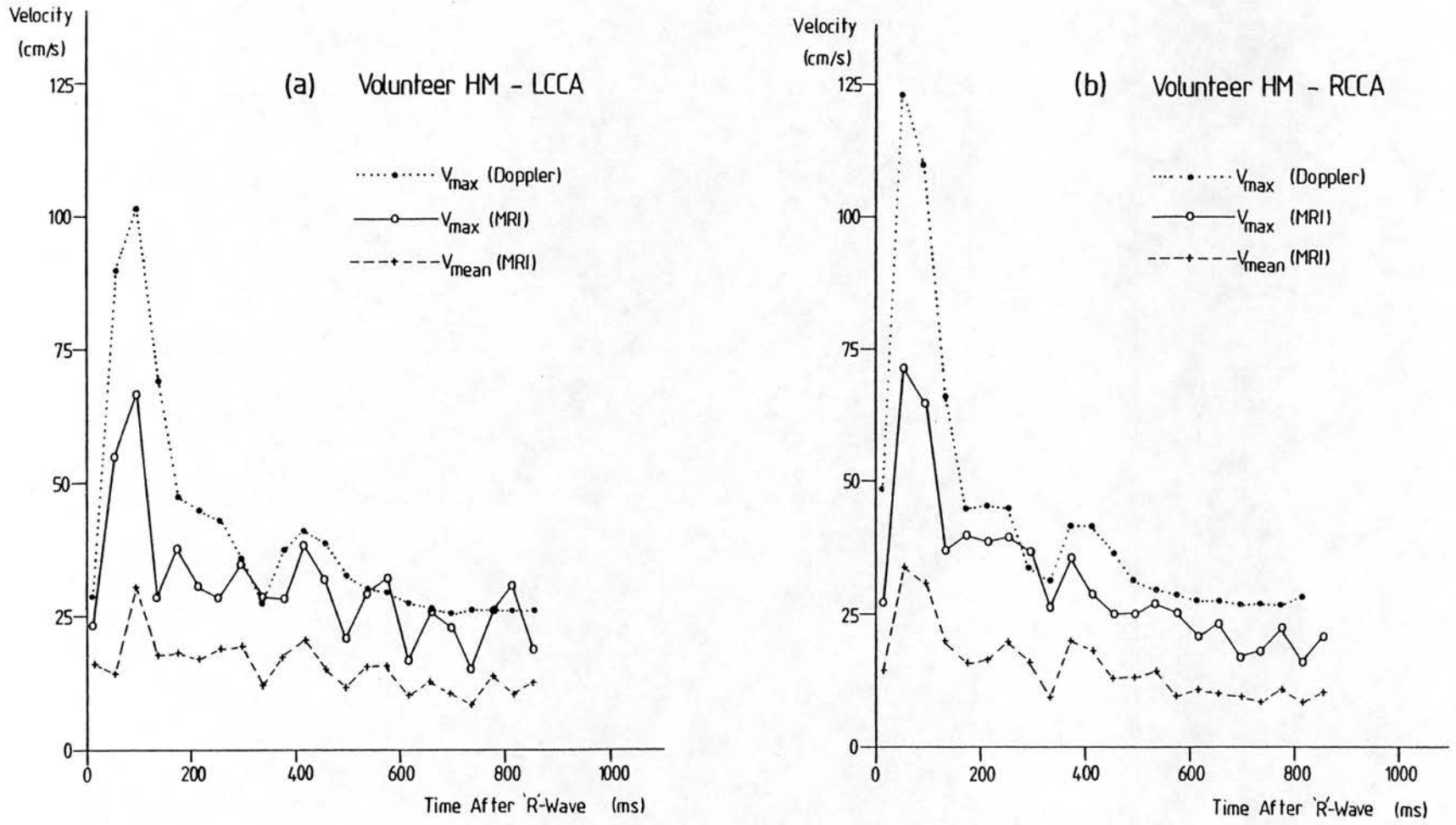

Figure 6.7.

The mean and maximum velocities measured using MRI, and the maximum velocities measured using Doppler ultrasound in (a) the left and (b) the right common carotid artery of volunteer HM.

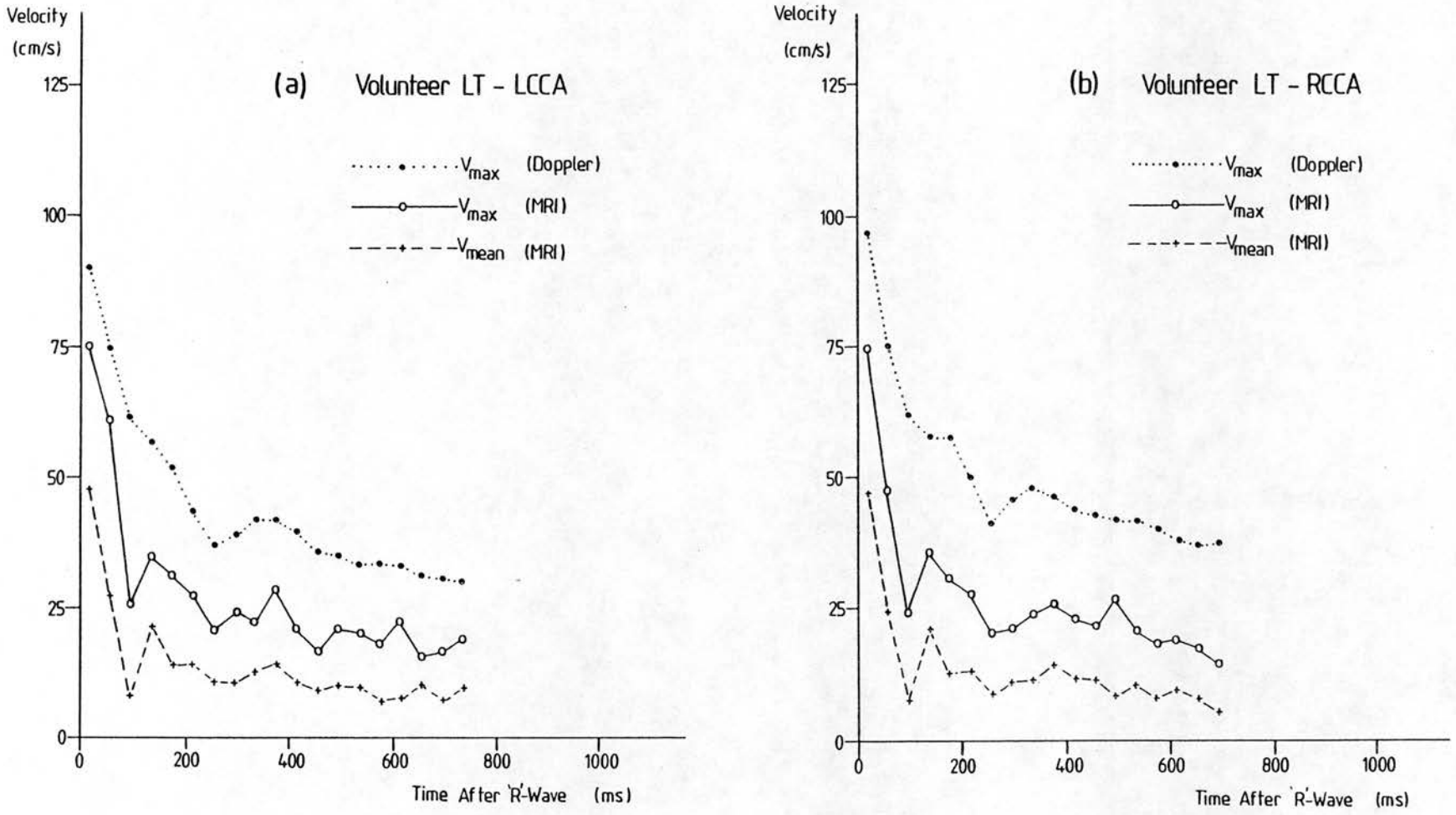

Figure 6.8.

The mean and maximum velocities measured using MRI, and the maximum velocities measured using Doppler ultrasound in (a) the left and (b) the right common carotid artery of volunteer LT.

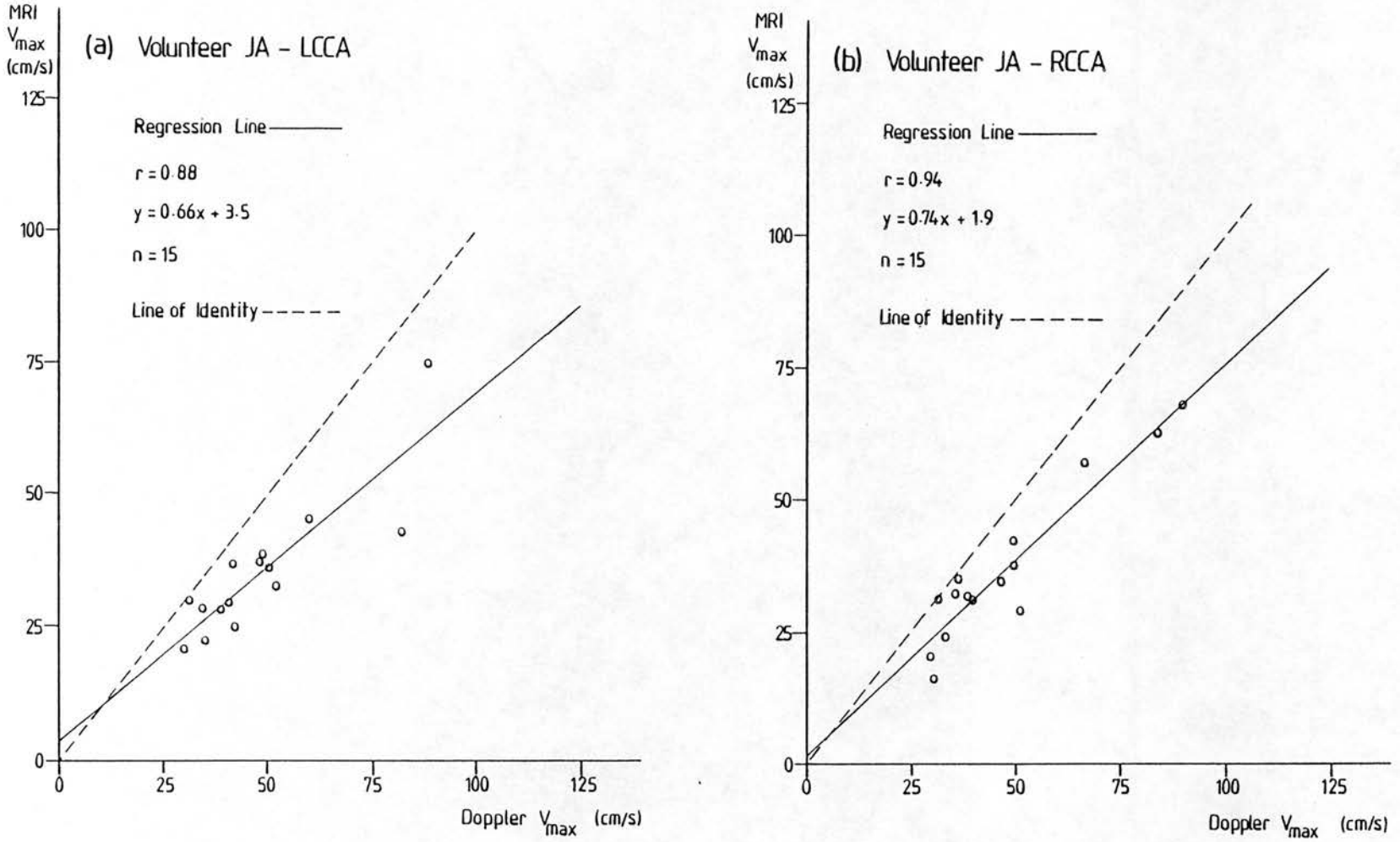

Figure 6.9.

The point by point correlation of the two maximum velocity waveforms obtained using MRI and Doppler ultrasound for (a) the left, and (b) the right common carotid artery of volunteer JA. The line of identity is also shown as a dotted line.

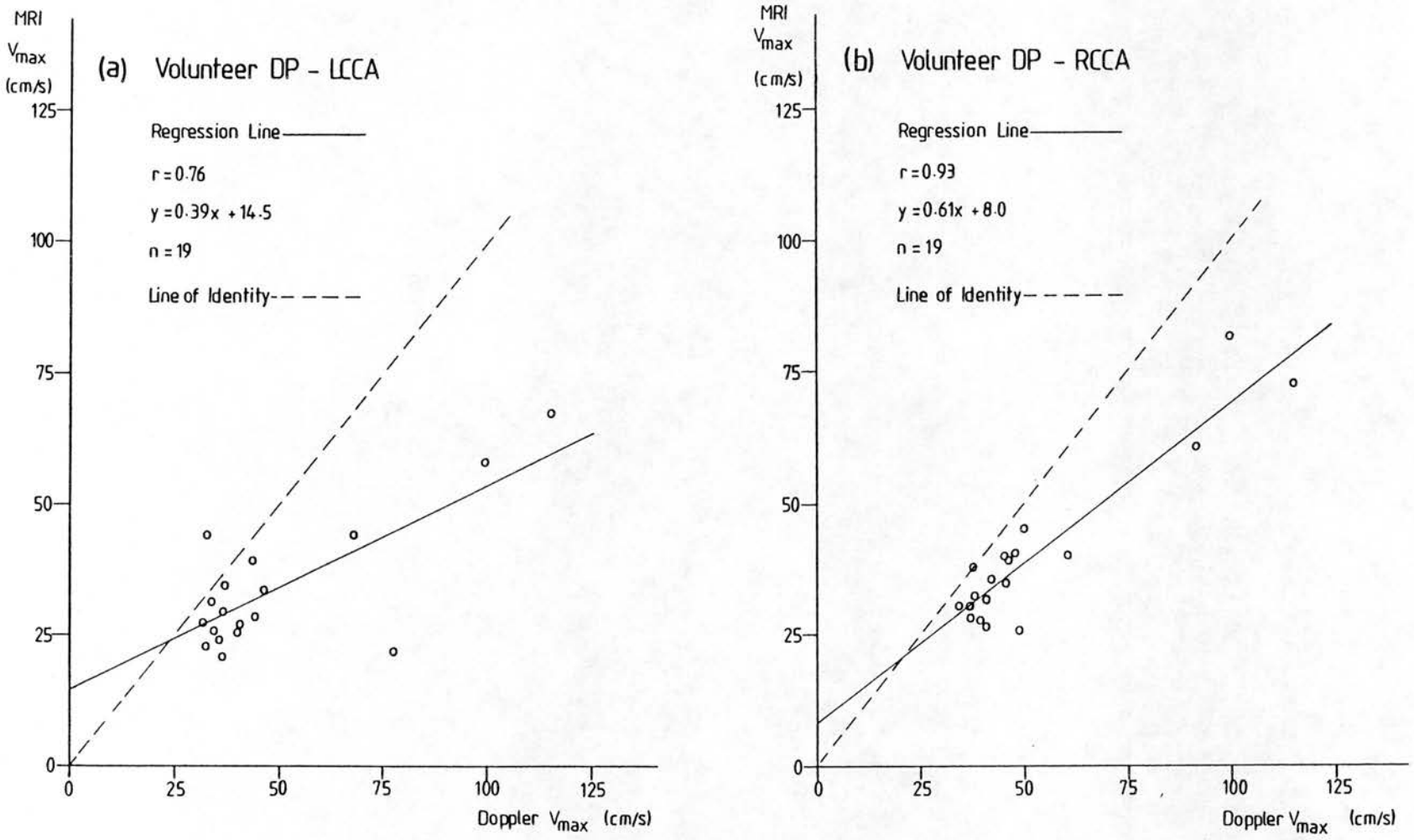

Figure 6.10.

The point by point correlation of the two maximum velocity waveforms obtained using MRI and Doppler ultrasound for (a) the left, and (b) the right common carotid artery of volunteer DP. The line of identity is also shown as a dotted line.

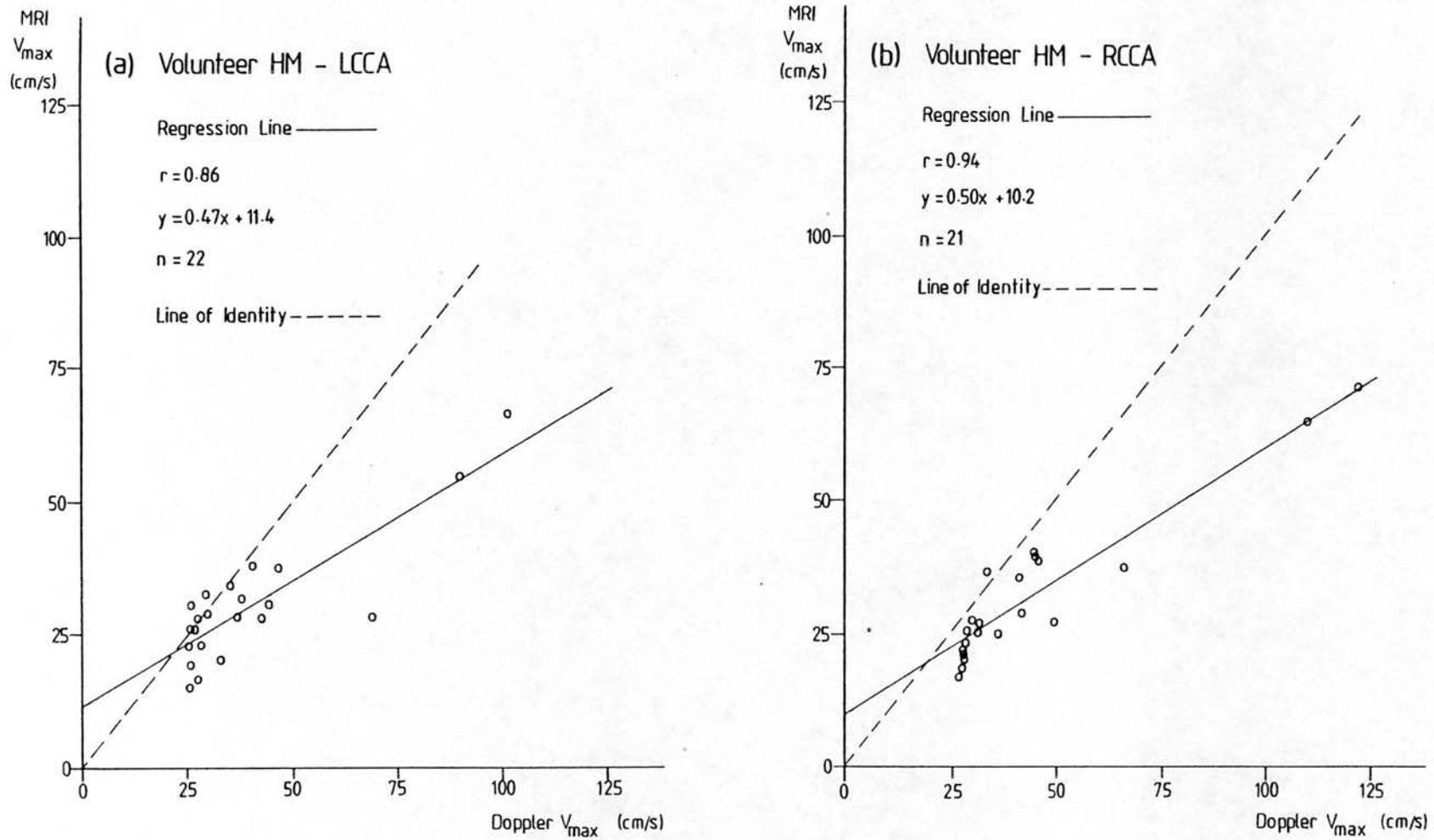

Figure 6.11.

The point by point correlation of the two maximum velocity waveforms obtained using MRI and Doppler ultrasound for (a) the left, and (b) the right common carotid artery of volunteer HM. The line of identity is also shown as a dotted line.

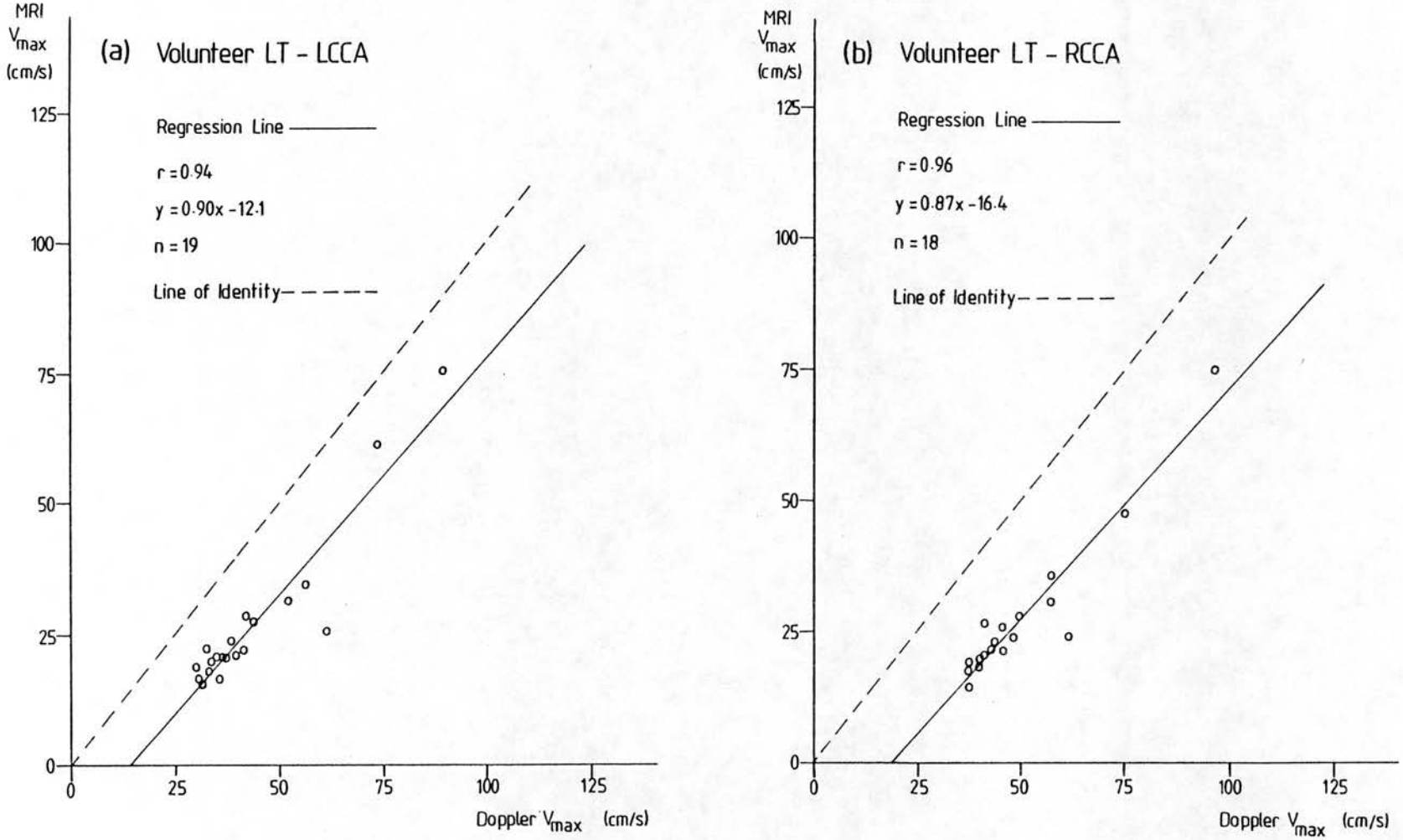

Figure 6.12.

The point by point correlation of the two maximum velocity waveforms obtained using MRI and Doppler ultrasound for (a) the left, and (b) the right common carotid artery of volunteer LT. The line of identity is also shown as a dotted line.

The mean velocity waveforms in figures 6.5-6.8 were integrated to obtain the time-averaged mean velocity for each carotid artery and these values, along with the peak maximum and mean velocities, are compared in table 6.5 below, with the values obtained from Doppler ultrasound.

Table of Velocity Measurements.

	Modality	Volunteer JA LCCA	Volunteer JA RCCA	Volunteer DP LCCA	Volunteer DP RCCA	Volunteer HM LCCA	Volunteer HM RCCA	Volunteer LT LCCA	Volunteer LT RCCA
Peak Maximum Velocity (cm/s)	MRI	75	68	68	82	66	71	76	75
	Doppler	89	90	115	115	102	123	91	97
Peak Mean Velocity (cm/s)	MRI	42	32	40	44	30	34	49	47
	Doppler	38	20	57	39	51	29	67	71
Time-Averaged Velocity (cm/s)	MRI	19	18	17	17	16	16	13	13
	Doppler	17	15	22	20	22	23	14	20
Heart Rate (bpm)	MRI	65	65	70	70	62	61	62	62
	Doppler	66	68	65	66	70	71	62	67

Table 6.5

Table comparing the peak mean and maximum velocities, and the time-averaged mean velocities measured by MRI and Doppler ultrasound in the left and right carotid arteries of the four volunteers. Also shown are the heart rates which were recorded during MRI and Doppler measurements.

6.3. Discussion

The maximum velocity waveforms measured by MRI compare well with those obtained using Doppler ultrasound and the point by point correlations between the maximum velocities measured by the two techniques show good qualitative agreement. However, the MRI measurement is consistently lower than the Doppler measurement. This is to be expected because of the relatively large effective sample volume used in the MRI examination. The maximum velocity measurement is derived from a voxel of dimensions 2mm x 4mm x 10mm. The voxel containing the maximum velocity also contains a range of lower velocities (section 5.2). The observed phase shift within that voxel therefore corresponds to the average velocity in the voxel, rather than the maximum velocity. This partial volume effect can be reduced by decreasing the voxel size, but this requires a substantial increase in the imaging time in order to maintain the same signal to noise ratio.

In three out of four of the volunteers (figures 6.5 to 6.7 and figures 6.9 to 6.11), the maximum velocities are in closer quantitative agreement during diastole compared with during systole, while in the remaining volunteer (figures 6.8 and 6.12), the MRI measurements are consistently very much lower than the Doppler measurements throughout the cardiac cycle. In this case

the correlation between the two techniques is excellent and the discrepency appears more likely to be due to an error related to the background phase measurement.

In all cases, the maximum velocities measured by MRI during systole are much lower than those measured by Doppler ultrasound. The presence of high flow acceleration and deceleration at this point may lead to errors in the phase measurement. The flow velocity measurement pulse sequence is also sensitive to acceleration (section 4.1.2). An expression can be derived from equation 4.7 giving the phase modulation ϕ_{diff} due to both velocity, v, and constant acceleration a, when using the interleaved pulse sequence,

$$\phi_{diff} = \gamma(t_w+t_e)GT\left[v + \frac{a}{2}[t_w+t_e+T]\right] \qquad 6.1$$

From equation 6.1, in the case of acceleration the phase shift has the same sign as that due to velocity, however in the case of deceleration the phase shift is of opposite sign. The maximum values of acceleration that occurred during systole were estimated from the measurements of maximum velocity obtained using Doppler ultrasound on three of the four volunteers. These values are shown in table 6.6, along with the calculated error in phase modulation, and the corresponding error in the velocity measurement. These errors are small and do not account for the large descrepancy between the MRI and Doppler ultrasound techniques.

		Peak Acceleration (m/s/s)	Error in Phase (degrees)	Error in Velocity (cm/s)
Volunteer JA	LCCA	9.2	5.9	2.4
	RCCA	1.6	1.0	0.4
Volunteer DP	LCCA	14.0	9.0	3.6
	RCCA	12.9	8.3	3.3
Volunteer HM	LCCA	11.0	7.0	2.8
	RCCA	18.4	11.8	4.8

Table 6.6.

Table showing the values of peak acceleration in the common carotid arteries of three of the four volunteers, and the corresponding errors in the measurement of velocity-dependent phase modulation and flow velocity.

The largest potential source of error in the estimation of the peak maximum velocity, using the MRI technique, is the relatively coarse sampling interval used. Even with three acquisitions, the minimum sampling interval is 40 milliseconds, and so it is quite likely that the peak velocity will be missed.

There is reasonable agreement in three out of four of the volunteers between the peak mean velocities, and the time-averaged mean velocities measured by the two techniques (table 6.5). The time-averaged mean velocity may be used in conjunction with the vessel cross-

sectional area to calculate the average flow rate in the vessel. The area is difficult to estimate accurately using either MRI or ultrasound, however in the case of MRI the summed phase measurement does not require accurate measurement of the area but gives a direct measurement, corresponding to the flow rate in the vessel. Although the voxels around the edge of the vessel may include some stationary tissue, the measured phase value will be reduced accordingly by the phase dipersion effect and any overestimation of the vessel is compensated for.

Measurement of Velocities in Pulsatile CSF Motion

7.0. Introduction

The existence of pulsatile motion of cerebrospinal fluid (CSF) within the subarachnoid space has been known for some time. Such motion has been observed with fluoroscopy during Pantopaque myelography and with cineradiology during myelography and encephalography (du Boulay, 1966; du Boulay et al, 1972). This pulsatile motion is related to the cardiac cycle and is thought to be caused by an increase in arterial volume in the brain during systole, which momentarily displaces CSF down the spinal column.

Estimations of pulsatile CSF flow have been made from a video monitor using the above techniques, but such estimates were inevitably imprecise. Bergstrand and co-workers have used MRI to demonstrate pulsatile CSF flow in the cerebral aqueduct and pontine cistern, by measuring signal intensity variations over the cardiac cycle (Bergstrand et al, 1985). The MR phase imaging technique, described in the previous chapters, has been used to measure the low velocities in pulsatile CSF motion more accurately. Five volunteers were imaged to obtain pulsatile CSF velocity waveforms in the subarachnoid space, at the level of the second cervical vertebra (C2). This study was performed before the MRI

system was upgraded and so it was necessary to calibrate the phase mapping technique for the measurement of low flow velocities on the old MRI system prior to this study. Details of this calibration are therefore also described in this chapter.

7.1. Method

The phase mapping technique was used to measure low flow velocity components, perpendicular to the imaging slice by extending the separation of the biploar flow-encoding gradient pulses of the slice selection gradient waveform to 12 milliseconds (Ridgway et al, 1987; Appendix IV). The corresponding increase in echo time for the pulse sequence resulted in a significant reduction in signal to noise ratio, however the images were still of sufficient quality to obtain the calculation of phase images for velocity measurement. For this gradient pulse separation, the maximum velocity range was approximately +/-20cm/s, corresponding to a phase modulation range of +/-180^{o}.

7.1.1. Method - Low Velocity Calibration

The technique was calibrated for mean flow velocities in the range from 1 to 11 centimetres per second, using a similar method to that described in chapter 5. Images were acquired using exactly the same MRI pulse sequence as that which was to be used in the volunteer studies; a slice thickness of 10mm was used, with an acquisition matrix of 128 x 128 elements, and the pulse sequence was synchronised using an external source at a repetition rate corresponding to a heart rate of 75 beats per minute. Each scan was repeated three times and the flow rate was recorded each time. The phase images were analysed using region of interest software to obtain the mean phase value within the tube relative to the background phase value measured within stationary fluid.

7.1.2. Method - Volunteer Studies

Five healthy volunteers were imaged by synchronising the pulse sequence to the R-wave of the subject's electrocardiogram. The volunteers' average heart rates were recorded, and images were obtained with delays of 110, 140, 165, 190, 215, 240, 290, 390, 490, 590, 690, 790 and 840 milliseconds following the R-wave. More images were acquired within the systolic period where the velocity variation appeared to be more rapid. Multiple-

frame imaging was not available at the time of this study and so the images were obtained in separate acquisitions. The duration of each volunteer study was therefore approximately one hour.

All five volunteers were imaged in the transverse plane at the level of the second cervical vertebra (C2). A previous study of CSF velocities, in the head and the neck of one volunteer, suggested that the peak velocity was higher in the neck than in the head (figure 7.2). However, imaging too low in the neck resulted in a loss of sensitivity as one moved out of range of the head coil. The level of C2 was chosen as a compromise.

The phase images obtained from the five volunteers were analysed, using region of interest software, to obtain the mean phase shifts and areas within the subarachnoid space. In the transverse plane, the subarachnoid space appears as an annular-shaped region. In order to obtain mean phase values within this region, measurements were obtained from two regions; one included both the CSF space and the spinal cord, and the other included only the spinal cord. From these two regions the mean phase value within the subarachnoid space and its area could be determined. The reproducibility of the technique was assessed by scanning one volunteer six times, at the time at which the peak velocity was observed.

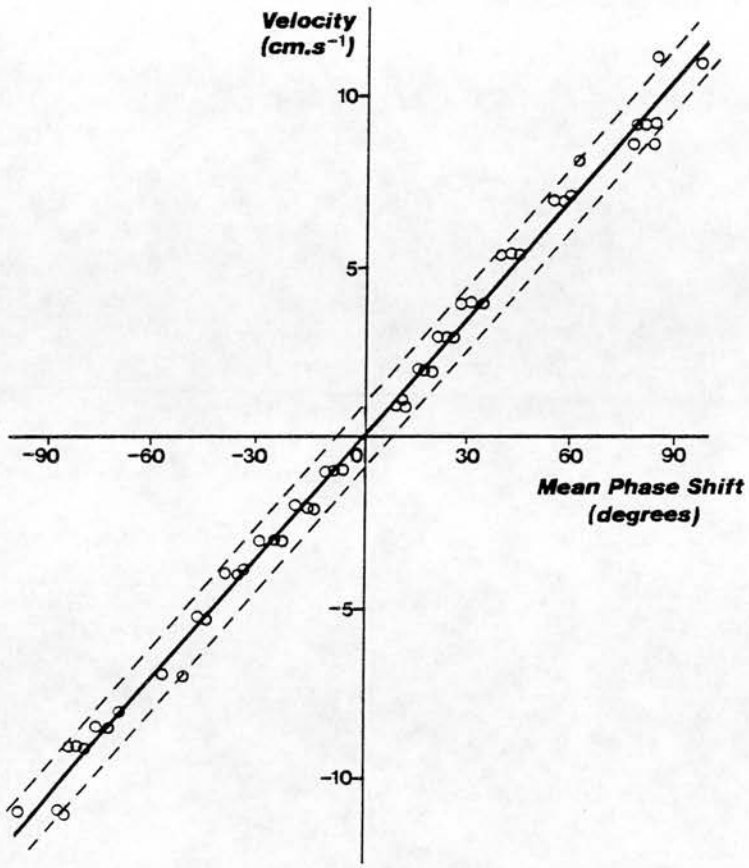

Figure 7.1.

A graph showing the results of the low-velocity calibration. There is good linear relationship between mean velocity and mean phase shift ($r=0.998$; $p<0.001$). The 95% confidence limits for the prediction of velocity from phase shift are shown (+/-0.92cm/s). The slope of the regression line is 0.118 and the y-intercept is 0.06cm/s.

7.2. Results

The results of the velocity calibration are plotted in figure 7.1. A good linear relationship is demonstrated between the mean velocity and the mean phase shift.

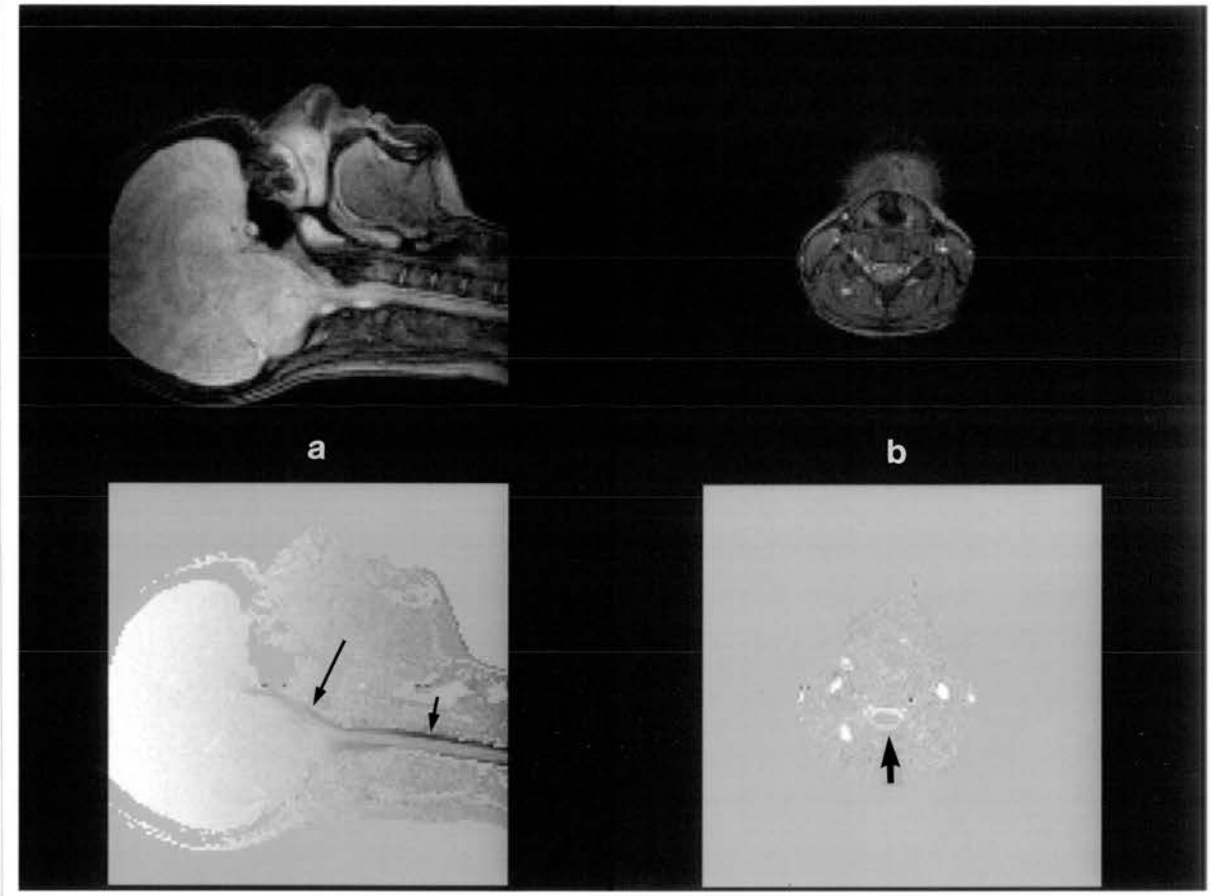

Figure 7.2.

Magnitude and phase images obtained of CSF flow, when peak caudad velocity is attained. In (a) images in the sagittal plane demonstrate that the velocities attained in the neck (short arrow) are greater than those attained in the head (long arrow). In (b) the images are representative of those obtained in the transverse plane from the five volunteers. Caudad motion of CSF can be seen on the phase map as a bright ring (arrow).

Figure 7.2 shows the magnitude and phase images obtained of CSF motion in one of the volunteers. The phase imaging technique demonstrated pulsatile CSF motion in all four volunteers. Caudad motion was demonstrated during systole, while cephalad motion was demonstrated during diastole. Figure 7.3 shows the mean velocity waveforms obtained for the five volunteers. The peak mean velocities and flow rates in both caudad and cephalad directions, and the times at which they occurred following the R-wave, are tabulated in table 7.1. The maximum variation in heart rate for any one volunteer, was from 65 to 83 beats per minute.

The measurements obtained from the six repeated scans were used to estimate the reproducibility of the CSF velocity measurement. The reproducibility for these six scans, expressed as a coefficient of variation, is 14.4%, This figure includes the error associated with the estimation of phase information from a single image. Repeated analysis of the same image showed this error to be 8.7%. The reproducibility of the velocity measurement technique alone is therefore 11.5%.

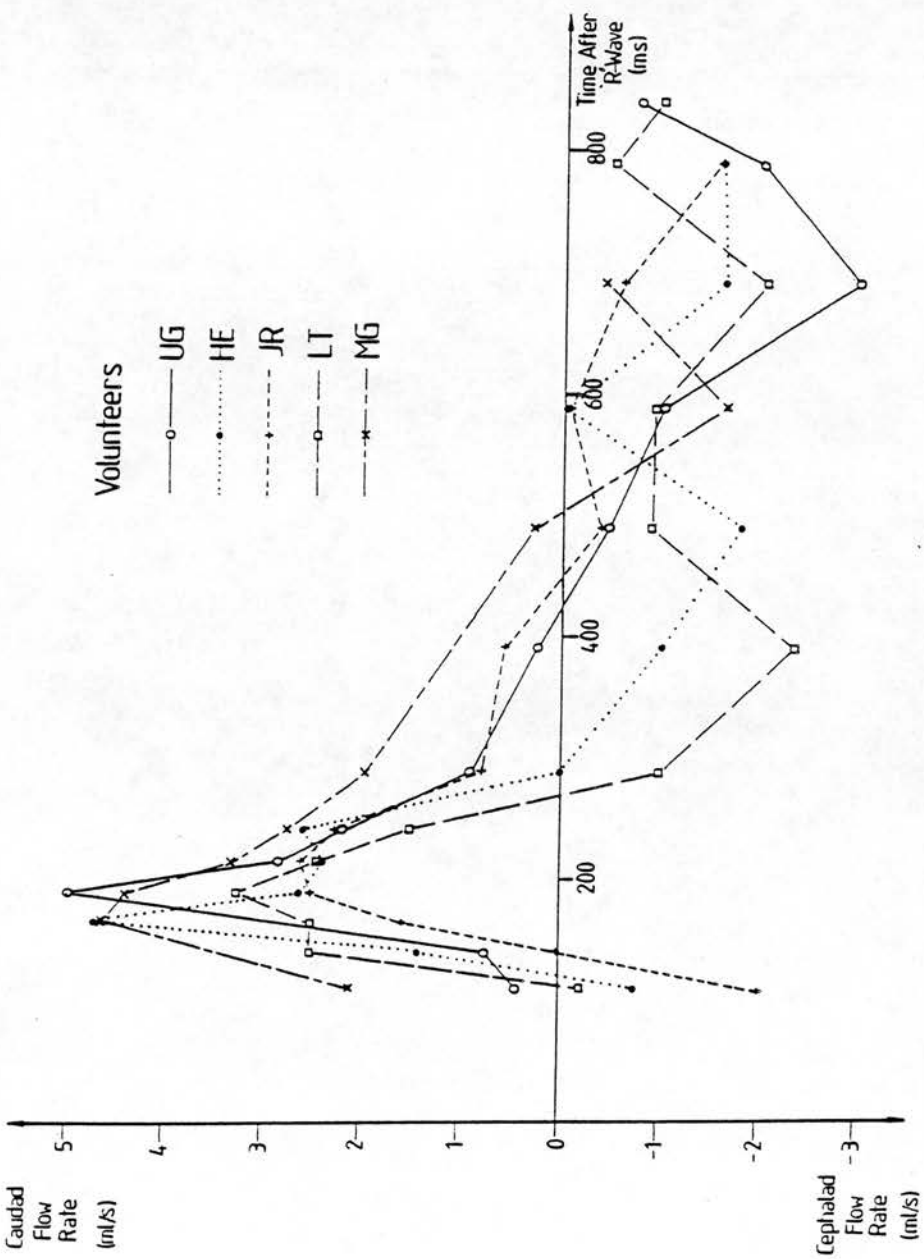

Figure 7.3.

Flow rate curves obtained in the five volunteers plotted against time after the R-wave. Both cephalad and caudad flow is demonstrated for all five volunteers. Peak caudad flow is attained at the same point during systole in each case.

Table of Peak Mean Velocities and Flow Rates Measured in CSF Motion

	Caudad Motion			Cephalad Motion			
Volunteer	Peak Mean Velocity (cm/s)	Peak Flow Rate (ml/s)	Time after R-wave (ms)	Peak Mean Velocity (cm/s)	Peak Flow Rate (ml/s)	Time After R-wave (ms)	Approx. Mean R-R Interval (ms)
UG	3.12	4.98	190	1.74	2.99	690	800
HE	3.57	4.71	165	1.47	1.80	490	800
JR	1.78	2.61	215	1.10	1.96	110	750
LT	3.17	3.24	190	1.52	2.35	390	750
MG	2.82	4.42	190	0.72	1.64	590	1000

Table 7.1.

Table showing the peak mean velocities and flow rates for CSF motion measured in the five volunteers. The velocities and flow rates in the cephalad direction are less than the caudad direction in all the volunteers.

7.3. Discussion of Results

This study demonstrates that it is possible to obtain velocity waveforms of pulsatile CSF motion within the subarachnoid space, both non-invasively and with reasonable precision. The direction of motion can also be identified and therefore the technique has advantages over the earlier technique proposed by Bergstrand et al. (Bergstrand et al, 1985). However, the technique does not appear to be as sensitive as that of Bergstrand, as we have been unable to demonstrate flow within the cerebral aqueduct. This may be due partly to the much lower

velocities in that region, and partly to the poorer resolution of our imager.

Good agreement is found between the flow measurements obtained in three out of the four volunteers. The peak velocities may be underestimated however, due to insufficient sampling of the cardiac cycle. Shorter sampling intervals may enable the peak values to be established more accurately, although this would increase the imaging time still further. The total imaging time for the volunteer study is too long for clinical use. The same technique has been developed for use in conjunction with multiple frame imaging and this significantly reduces the imaging time. However, the partial saturation effect reduces the signal-to-noise ratio to almost unacceptable levels, particularly in CSF where the T1 relaxation time is long. The signal-to-noise ratio can be optimised to some extent, by reducing the excitation angle to the Ernst angle value (section A2.5.5).

7.4. Clinical Potential of CSF Flow Measurement

This technique may be of use in the non-invasive investigation of disorders in the CSF circulation. For example, if there is complete obstruction, pulsatile motion distal to the obstruction will cease, whereas it will persist on the cranial side. If the subarachnoid

space is narrowed but not occluded, the amplitude of pulsatile motion at the site of narrowing may be increased (du Boulay, 1966).

One particular application of the technique may be to distinguish communicating syringomyelia from cystic intraspinal lesions (Turnbull et al, 1987). Whilst MRI is the method of choice to image the spinal cord and canal (Norman et el, 1983), differentiation between CSF contained within a syrinx and a cystic tumour is difficult, as both have similar relaxation parameters. The use of phase imaging to detect pulsatile flow within a communicating syrinx may be of help in this differential diagnosis.

One patient has been investigated in whom the MRI scan showed a possible syrinx, extending from the level of the first cervical vertebra to at least the second thoracic vertebra (fig. 7.4). Phase images were obtained in the transverse plane at 50, 225, 300 and 325 milliseconds following the R-wave. The cross sectional area of the syrinx was measured from the images and the flow rates, and mean velocities of CSF within the syrinx were calculated (Table 7.2). The maximum caudad flow velocity measured was 1.63cm/s and the corresponding flow rate calculated using the area of the syrinx ($0.87cm^2$) was 1.27ml/s. The maximum cephalad flow velocity observed, was 0.86cm/s with a corresponding flow rate of 0.64ml/s.

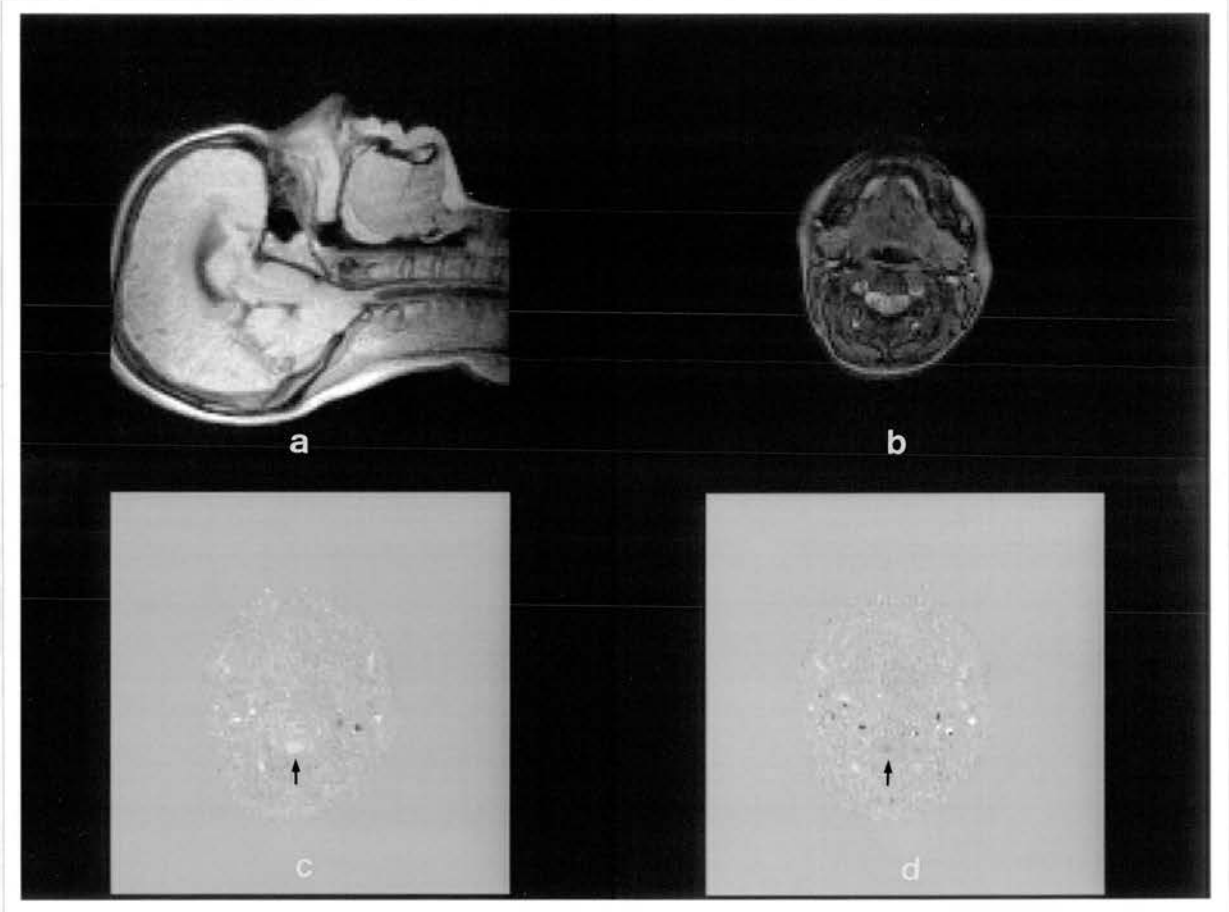

Figure 7.4.

Images obtained in a patient with syringomyelia. In (a) the magnitude image acquired in the sagittal plane clearly shows the syrinx (arrow). (b) shows a magnitude image obtained in the transverse plane, using the flow measurement technique. (c) shows a phase map obtained during systole at the same level as (b). CSF motion can be seen within the syrinx (arrow). (d) shows reduced flow on the phase map acquired during diastole (arrow).

Table of Peak Mean Velocities and Flow Rates for the Syrinx Patient

	Peak Mean Velocity (cm/s)	Peak Flow Rate (ml/s)	Time after R-wave (ms)
Caudad Motion	1.63	1.27	300
Cephalad Motion	0.86	0.64	50

Table 7.2.

Table of peak mean velocities and flow rates of CSF motion measured within the syrinx. These velocities and flow rates are reduced relative to those measured in the subarachnoid space of normal volunteers (see table 7.1).

Whilst it has not been possible to perform the same flow measurement technique on a patient with non-communicating sryingomyelia, it is possible that the absence of flow in such cases will allow for a differential diagnosis to be made.

Discussion of the Phase Mapping Technique

8.0. Introduction

A technique has been developed to measure the velocity of fluid motion within human subjects using nuclear magnetic resonance phase mapping and details of the technique have been published (Ridgway and Smith, 1986; See appendix IV). This technique overcomes some of the technical problems encountered by earlier techniques. In particular, it does not suffer from signal losses caused by the spin washout effect, and is less susceptible to phase dispersion and artefacts caused by magnetic field inhomogeneity, chemical shift and changes in magnetic susceptibility. The phase mapping technique has been implemented on an MRI system operating at 0.08 Tesla and has been used in vivo to image blood flow in a variety of large vessels. The technique has been calibrated to enable accurate measurement of flow velocity. It has been compared with Doppler ultrasound in the common carotid arteries of healthy volunteers, and has been used to study pulsatile CSF motion. The findings and limitations of this phase mapping technique, as a method of flow measurement, are summarised in the following section.

8.1. Summary of Findings and Limitations

The use of a field echo pulse sequence, with velocity compensated slice-selection and frequency-encoding gradient waveforms, prevents signal losses caused by spin washout and phase dispersion from occurring in most situations. NMR phase mapping provides a non-invasive method to measure flow through large vessels and is not restricted by site or orientation. Velocity encoding is easily achieved in either the slice selection or frequency encoding directions, but has not been implemented in the phase encoding direction because of technical limitations. Signal losses still occur in the presence of turbulence or higher order terms of motion in pulsatile flow, (section 4.6), which suggests that the velocity-compensation of the gradient waveforms is not adequate in these situations.

The phase mapping technique has been calibrated to enable the accurate measurement of flow velocity perpendicular to the image slice. The measured phase modulation shows a linear relationship with actual flow velocity, which was very close to that predicted by theory. The best agreement with theory was obtained when comparing the phase values integrated over the cross-sectional area of the pipe containing the flow, with the flow rate. Measurement of the mean velocity was found to be less accurate.

In the in vivo study, the maximum velocity waveforms measured in the common carotid artery, derived from maximum phase values measured by MRI, were compared with the maximum velocity waveforms measured using Doppler ultrasound. In all cases, the maximum velocities measured using MRI were much lower than the maximum velocities measured using Doppler ultrasound. This was particularly true during systole, when the peak maximum velocities were attained. This disagreement between the two techniques underlines two specific limitations of the MRI phase mapping technique.

Firstly, the measurement of the maximum phase shift underestimates the maximum velocity. The observed maximum phase value represents the net phase value within a voxel of relatively large dimensions. In most instances, there will be a range of velocities present in the voxel and the resultant phase dispersion will cause the observed maximum phase value to be less than the true value (section 2.2.7). This was demonstrated in the case of laminar flow, during the calibration of the phase mapping technique, when the observed relationship between maximum phase shift and maximum velocity deviated from the predicted relationship. The measurement of maximum phase values could be improved to give a better representation maximum velocity by decreasing the voxel size. However, this would require substantial increases in imaging time in order to maintain the same signal to noise ratio.

In these studies, the voxel size was restricted by the relatively low signal-to-noise ratio available on the imager. The implementation of this technique on an MRI system operating at a higher magnetic field strength would allow smaller voxels to be used.

The second limitation of the use of the phase mapping technique to measure maximum velocities, is due to the relatively poor sampling of the velocity waveform throughout the cardiac cycle, when measuring pulsatile flow. This inevitably leads to an under-estimation of the peak maximum velocity attained during systole and is the most likely cause of the large difference found between the Doppler ultrasound and MRI techniques. The sampling interval used in the study of the common carotid artery was particularly long. The minimum length of this sampling interval was restricted by technical constraints, and by the low signal-to-noise ratio caused by partial saturation effects. The technical contraints were dictated by the time required for data processing and by the relatively long duration of the gradient and radiofrequency pulses. MRI systems operating at higher field strengths would improve the signal-to-noise ratio. The use of rf pulses with a gaussian profile rather than a 'sinc' function profile, and shorter gradient pulses would allow shorter sampling times to be achieved.

Whilst the accurate measurement of maximum velocity has proved to be difficult using this phase mapping technique, its use to measure mean velocities and flow rates has produced encouraging results. Pulsatile CSF motion, as well as pulsatile blood flow, can be studied and measured. However, the technique cannot measure flow velocity in 'real time', and the velocity waveforms obtained are averaged over the total acquisition time. The acquisition times of the MRI technique are relatively long, making the technique largely inappropriate for routine clinical use as it stands.

8.2. Review of Current Literature

Phase mapping techniques similar to the one described here have been developed by other research groups. In 1986, Young and co-workers described a flow measurement technique using a field echo pulse sequence in which the velocity encoding was achieved by the same method as described in this thesis (Young et al, 1986b). However the authors state that their technique 'does not distinguish between phase differences due to flow, field errors or chemical shift effects', contrary to the findings in this thesis.

The same technique, incorporating motion-compensated gradient waveforms, was also published later in 1986 by the research group working at the National Heart Hospital, London and Picker International (Naylor et al, 1986). Their technique, named FEER (Field Even Echo Rephasing), was used with sampling intervals of between 50 and 100ms to obtain velocity waveforms throughout the cardiac cycle. This technique was subsequently validated in vivo (Firmin et al, 1986), and has been used to study blood flow patterns in the aorta (Klipstein et al, 1987) and to study a number of congenital heart abnormalities and stenoses in major vessels (Underwood et al, 1987). Recently, the signal losses experienced in the presence of turbulence have been significantly reduced by using very short gradient and rf pulses, and fast sampling rates (Firmin et al, 1989). Using these short pulses and sampling times, FEER sequences with echo times of between 3.5ms and 6ms are possible, compared with 14ms-22ms in the conventional FEER pulse sequence. In addition, very short pulse sequence repetition rates of 8.5ms were possible, enabling acceleration velocity measurements to be obtained at high temporal resolution.

In vivo comparisons of the phase mapping technique with Doppler ultrasound have also been performed in the abdominal aorta (Meier et al, 1988; Vieli et al, 1989). The correlations between the spatial and temporal velocity profiles, obtained by the two techniques, showed

good agreement. This technique was performed with an in-plane resolution of 1.5mm, allowing much better accuracy of velocity profile measurement.

The main limitation of the phase mapping techniques discussed so far, is the long acquisition time required. Two approaches have recently been suggested to reduce the acquisition time of the phase mapping technique. The first approach involves the use of echo planar imaging (Howseman et al, 1988). This enables phase images to be obtained using just one or two signal excitations (Firmin et al, 1988). The second approach involves the continuous acquisition of signal data, without synchronisation with the cardiac cycle. This has the effect of randomly sampling the pulsatile waveform, giving a direct measure of the time-averaged flow velocity and flow rate (Tarnawski et al, 1989).

Pulsatile CSF motion has been studied in healthy volunteers using the 'Zebra Stripe' display described in section 3.7.3, (Edelmann et al, 1986), and in patients with syringomyelia using phase mapping (Enzmann and Pelc, 1989). In both these studies, the velocities obtained were consistent with those recorded in this thesis. Studies observing variations in signal intensity due to CSF flow in the aqueduct (Bradley et al, 1986; Mascalchi et al, 1989), suggest that higher flow rates occur in patients with normal pressure hydrocephalus (NPH), whilst

lower velocities occur in patients with atrophy. Measurement of CSF flow velocity in the aqueduct may therefore help in the differential diagniosis of NPH and atrophy.

8.3. Conclusion

NMR phase mapping techniques provide a non-invasive measurement of in-vivo flow velocities and flow rates in large vessels. The phase mapping technique described in this thesis has been successfully implemented and overcomes many of the problems encountered by early techniques. The use of a field echo pulse sequence avoids the spin washout effect and allows fast repetition rates to be used to acquire multiple frames throughout the cardiac cycle. Velocity-compensation of the gradient waveforms reduces signal losses caused by high velocity gradients. Signal losses caused by the presence of turbulent flow still occur, although the use of much shorter gradient pulses could significantly reduce this problem. The chosen method of velocity-encoding is easy to control and calibrate. The subtraction of two phase maps, with different velocity-encoded phase modulation, removes unwanted phase modulation caused by magnetic field inhomogeneity, chemical shift and changes in magnetic susceptibility. Interleaving of the two flow-encoding pulse sequences avoids spatial mis-registration

of the two phase maps when they are subtracted.

The velocity-dependent phase modulation has a linear relationship with velocity and is in excellent agreement with theory. The technique is reasonably accurate and precise in vivo when measuring non-turbulent flow perpendicular to the imaging plane. Flow rates can be measured with reasonable accuracy by integrating the phase modulation over the vessel cross section. Mean velocities are subject to errors in the measurement of vessel area. Maximum velocity tends to be underestimated, although the use of smaller voxel sizes would improve this measurement.

The velocity waveforms of pulsatile flow, studied in the common carotid artery, show a good correlation with those obtained using Doppler ultrasound. The peak velocities measured during systole by MRI are much less than those measured by ultrasound. This is probably caused by the relatively poor sampling of the waveform achieved with MRI. The use of faster pulse sequence repetition rates would improve the temporal resolution of the velocity measurement.

In comparison with Doppler ultrasound, the MRI technique requires a much longer acquisition time and is not able to acquire data in 'real time'. However, techniques such as echo planar imaging are currently being developed by

other workers, that will significantly decrease these acquisition times. Unlike ultrasound, MRI is not restricted by the site or orientation of the vessel. Two-dimensional velocity profiles are directly obtainable, allowing flow rates to be calculated, without making any assumption about the geometry of the vessel cross-section.

The phase mapping technique has shown potential in a number of clinical situations. It allows accurate, non-invasive measurement of left ventricular stroke volume and the calculation of flow rates in large diameter vessels. Pulsatile CSF motion, related to the cardiac cycle, has also been studied using phase mapping. The non-invasive analysis of CSF flow waveforms may give a better understanding of CSF flow dynamics in patients with syringomyelia and hydrocephalus, and may help in the differential diagnosis of these diseases.

Bibliography

Alfidi, R. J., Haaga, J. R., El Yousef, S. J., Bryan, P. J., Fletcher, et al., (1982). Preliminary experimental results in humans and animals with a superconducting whole body nuclear magnetic resonance scanner. Radiology, 143, 175-181.

Amoore, J. N., and Ridgway, J. P., (1989). A system for cardiac and respiratory gating of a magnetic resonance imager. Clinical Physics and Physiological Measurement, 10, 283-286. (See Appendix IV).

Axel, L., (1984). Blood flow effects in magnetic resonance imaging. American Journal of Roentgenology, 143, 1157-1166.

Beall, P. T., Amtey, S. R. and Kasturi, S. R., (1984). NMR data handbook for biomedical applications. Pergammon Press, New York.

Been, M., Smith, M. A., Ridgway, J. P., Brydon, J. W. E., Douglas, R. H. B., Kean, D. M., Best, J. J. K. and Muir, A. L., (1985). Characterisation of acute myocardial infarction by gated magnetic resonance imaging. Lancet ii, 348-350.

Been, M., Smith, M. A., Ridgway, J. P., Douglas, R. H. B., De Bono, D. P., Best, J. J. K. and Muir, A. L., (1988). Serial changes in the T1 magnetic resonance relaxation parameter after myocardial infarction in man. British Heart Journal, 59, 1-8.

Bergstrand, G., Bergstrom, M., Nordell, B., Stahlberg, F., Ericsson, A., Hemmingson, A., Sperber, G., Thomas, K. and Jung, B., (1985). Cardiac gated MR imaging of cerebrospinal fluid flow. Journal of Computer Assisted Tomography, 8, 588-593.

Bloch, F., Hansen, W. W. and Packard, M., (1946). The nuclear induction experiment. Physiological Reviews, 70 474-485.

Bradley, W. G., Waluch, V., Lai, K-S., Fernandez, E. J. and Spalter, C., (1984). The appearance of rapidy flowing blood on magnetic resonance images. American Journal of Roentgenology, 143, 1167-1174.

Bradley, W. G., Kortman, K. E. and Burgoyne, B., (1986). Flowing cerebrospinal fluid in normal and hydrocephalic states: Appearance on MR images. Radiology, 159, 611-616.

Bryant, D. J., Payne J. A., Firmin, D. N. and Longmore, D. B., (1984). Measurement of flow with NMR imaging using a gradient pulse and phase difference technique. Journal of Computer Assisted Tomography, 8, 588-593.

Burns, P. N. and Jaffe, C. C., (1985). Quantitative flow measurements with Doppler ultrasound: Techniques, accuracy, and limitations. In: The Radiologic Clinics of North America (Advances in Cardiac Imaging). ed. S. W. Miller. Saunders, Philadelphia 23, pp 641-657.

Bydder, G.M., (1988). Magnetic resonance imaging: present status and future perspectives. British Journal of Radiology, 61, 889-887.

Crooks, L. E., Mills, C. M., Davis, P. L., Brant-Zawadzki, M., Hoenninger, J., Arakawa, M., Watts, J. and Kaufman, L., (1982). Visualisation of cerebral and vascular abnormalities by NMR imaging. The effects of imaging parameters on contrast. Radiology, 144, 843-852.

Crooks, L. E., Barker, B., Chang, H., Feinberg, D., Hoenninger, J. C., et al., (1984). Magnetic resonance imaging strategies for heart studies. Radiology, 153, 459-465.

Cunningham, A. D., (1986). Cardiac catheterisation. In: Physics in Medicine & Biology Encyclopedia. ed. T. F. McAinish, Pergammon Press, Oxford. pp 121-126.

Damadian, R., (1971). Tumour detection by nuclear magnetic resonance. Science, 171, 1151-1153.

Damadian, R., Goldsmith, M. and Minkoff, L., (1977). NMR in cancer. FONAR image of the live human body. Physiological Chemistry and Physics, 9, 97-100.

Du Boulay, G. H., (1966). Pulsatile movements in the CSF pathways. British Journal of Radiology, 39, 255-262.

Du Boulay, G. H., O'Connell, J., Currie, J., Bostick, T. and Verity, P., (1972). Further investigations on pulsatile movements in the cerebrospinal fluid pathways. Acta Radiologica Diagnostica, 13, 496-523.

Edelman, R. R., Wedeen, V. J., Davis, K. R., Widder, D., Hahn, P., Shoukimas, G. and Brady, T. J., (1986). Multiphasic MR imaging: A new method for direct imaging of pulsatile CSF flow. Radiology, 161, 779-783.

Edelstein, W. A., Hutchison, J. M. S., Johnson, G. and Redpath, T. W., (1980). Spin-warp NMR imaging and applications of human whole body imaging. Physics in Medicine and Biology, 25, 751-753.

Enzmann, D. R. and Pelc, N., (1989). CSF dynamics in normal and syringomyelia patients using phase contrast cine MR. In: Proceedings of the Eighth Annual Meeting of the Society of Magnetic Resonance in Medicine, Amsterdam, August 12-18, 1989, p 11.

Ernst, R. R., (1966). Sensitivity enhancement in magnetic resonance. Advances in Magnetic Resonance, 2, 1-135.

Farrar, T. C. and Becker, E. D., (1971). Pulse and Fourier transform NMR. Academic Press, London.

Feinberg, D. A., Crooks, L., Hoenninger, J., Arakawa, M. and Watts, J., (1984). Pulsatile blood velocity in human arteries displayed by magnetic resonance imaging. Radiology, 153, 177-180.

Firmin, D. N., Nayler, G. L., Klipstein, R. H., Underwood, S. R., Rees, R. S. O. and Longmore, D. B., (1987). In vivo validation of MR velocity imaging. Journal of Computer Assisted Tomography, 11, 751-756.

Firmin, D. N., Hounsfield, G. N., Paley, M. P. and Longmore, D. B., (1988). A multi-field echo data acquisition technique designed to reduce blood flow artefacts in cardiac imaging. In: Proceedings of the Seventh Annual Meeting of the Society of Magnetic Resonance in Medicine, San Francisco, August 20-26, 1988, p 894.

Firmin, D. N., Kilner, P. J., Pennell, D. J., Underwood, S. R., Mohiaddin, R. H., Rees, R. S. O. and Longmore, D. B., (1989). In: Proceedings of the Eighth Annual Meeting of the Society of Magnetic Resonance in Medicine, Amsterdam, August 12-18, 1989, p 888.

Fisher, M. R., von Schultess, G. K. and Higgins, C. B., (1985). Multiphasic cardiac magnetic resonance imaging: Normal LV wall thickening. American Journal of Roentgenology, 145, 27-30.

George, C. R., Jacobs, G., MacIntyre, W. J., Lorig, R. J., Go, R. T., Nose, Y. and Meaney, T. F., (1984). Magnetic resonance signal intensity patterns obtained from continuous and pulsatile flow models. Radiology, 151, 421-428.

Herfkens, R. J., Higgins, C. B., Hricak, H., Lipton, M. J., Crooks, L. E., Lanzer, P., Botvinick, E., Brundage, B., Sheldon, P. E. and Kaufman, L., (1983). Nuclear magnetic resonance imaging of the cardiovascular system: Normal and pathologic findings. Radiology, 147, 749-759.

Hinshaw, W. S., Andrew, E. R., Bottomley, P. A., Holland, G. N., Moore, W. S. and Worthington, B. S., (1978). Internal structural mapping by nuclear magnetic resonance. Neuroradiology, 16, 607-609.

Howseman, A. M., Stehling, M. K., Chapman, B., Coxon, R., Turner, R., Ordidge, R. J., Cawley, M. G., Glover, P., Mansfield, P. and Coupland, R. E., (1988). Improvements in snap-shot nuclear magnetic resonance imaging. British Journal of Radiology, 61, 822-828.

Hutchison, J. M. S., Sutherland, R. J. and Mallard, J. R., (1978). NMR imaging: image recovery under magnetic fields with large non-uniformties. Journal of Physics E: Scientific Instruments, 11, 217-221.

Hutchison, J. M. S., Edelstein, W. A. and Johnson, G., (1980). A whole body NMR imaging machine. Journal of Physics, E: Scientific Instruments, 13, 947-955.

Hymen, C. and Windsor, T., (1961). History of plethysmography. Journal of Cardiovascular Surgery, 2, 506-518.

Jackson, J. A., (1968). Whole Body Spectrometer. Reviews on Scientific Instrumentaion, 39 510-515.

Jones, T., (1986). Cerebral blood flow: Regional measurement. In: Physics in Medicine & Biology Encyclopedia. ed. T. F. McAinish, Pergammon Press, Oxford. pp 157-160.

Klipstein, R. H., Firmin, D. N., Underwood, S. R., Rees, R. S. O. and Longmore, D. B., (1987). Blood flow patterns in the human aorta studied by magnetic resonance. British Heart Journal, 58, 316-323.

Lanzer, P., Botvinick, E. H., Schiller, N. B., Crooks, L. E., Arakawa, M., et al., (1984). Cardiac imaging using gated magnetic resonance. Radiology, 150, 121-127.

Lanzer, P., Barta, C., Botvinick, E. H., Wiesendanger, H. U. D., Modin, G. and Higgins, C. B., (1985). ECG-Synchronised cardiac MR imaging: Method and evaluation. Radiology, 155, 681-686.

Lauterbur, P., (1973). Image formation by induced local interactions: examples employing nuclear magnetic resonance zeugmatography. Nature, 242, 190-191.

Leach, M. O., (1988). Spatially localised nuclear magnetic resonance. In: The Physics of Medical Imaging. ed. S. Webb. IOP Publishing, Bristol.

Le Roux, P. and Floch, J., (1985). Cancellation of the shear rate influence on flow velocity imaging. In: Proceedings of the Fourth Annual Meeting of the Society of Magnetic Resonance in Medicine, London, August 19-23, 1985, pp. 585-586.

Ligon, T. R., (1967). Coil design for low field NMR experiments and NMR measurements on the human arm. M.S. Thesis, Oklamhoma State University, 1967.

Lorimer, A. R., Hillis, W. S. and Tweddel, A. C., (1986). Cardiac output measurement. In: Physics in Medicine & Biology Encyclopedia. ed. T. F. McAinish, Pergammon Press, Oxford. pp 132-139.

McDonald, D. A., (1974). Blood flow in arteries. (2nd ed). Edward Arnold, London.

Mansfield, P. and Maudsley, A. A., (1977). Medical imaging by NMR. British Journal of Radiology, 50, 188-194.

Martin, W., (1986). Dynamic cardiac studies. In: Physics in Medicine & Biology Encyclopedia. ed. T. F. McAinish, Pergammon Press, Oxford. pp 282-285.

Mascalchi, M., Ciraolo, L., Bucciolini, M., Inzitari, D., Arnetoli, G. and Dal Pozzo, G., (1989). Fast multiphase MR imaging of aqueductal CSF flow in demented patients with hydrocephalus. In: Proceedings of the Eighth Annual Meeting of the Society of Magnetic Resonance in Medicine, Amsterdam, August 12-18, 1989, p. 12.

Meier, D., Maier, S. and Bosiger, P., (1988). Quantitative flow measurements on phantoms and on blood vessels with MR. Magnetic Resonance in Medicine, 8, 25-34.

Moores, B. M., (1986). Digital fluorography. In: Physics in Medicine & Biology Encyclopedia. ed. T. F. McAinish, Pergammon Press, Oxford. pp 269-274.

Moran, R., (1982). A flow velocity zeugmatographic interlace for NMR imaging in humans. Magnetic Resonance Imaging, 1, 197-203.

Moran, P. R. and Moran, R. A., (1984). Imaging true motion velocity and higher order motion quantities by phase gradient modulation techniques in NMR scanners. In: Technology of Nuclear Magnetic Resonance. Ed. P. D. Esser and R. E. Johnston (Society for Nuclear Medicine Inc., New York), pp 149-166.

Morris, P. G., (1986). Nuclear Magnetic Resonance Imaging in Medicine and Biology. Clarendon Press, Oxford.

Morse, O. C. and Singer, J. R., (1970). Blood velocity measurements in intact subjects. Science 170, 440-442.

Naylor, G. L., Firmin, D. N. and Longmore, D. B., (1986). Blood flow imaging by cine magnetic resonance. Journal of Computer Assisted Tomography, 10, 715-722.

Norman, D., Mills, C. M., Brant-Zawadzki, M., Yeates, A., Crooks, L. E. and Kaufman, L, (1983). Magnetic resonance imaging of the spinal cord and canal: Potentials and limitations. American Journal of Roentgenology, 141, 1147-1152.

Norris, D. G., (1985a). Phase errors in NMR images. In: Proceedings of the Fourth Annual Meeting of the Society of Magnetic Resonance in Medicine, London, August 19-23, 1985, pp. 1037-1038.

Norris, D. G., (1985b). Acceleration imaging by NMR. In: Proceedings of the Fourth Annual Meeting of the Society of Magnetic Resonance in Medicine, London, August 19-23, 1985, pp. 593-594.

Odeblad, E. and Lindstrom, G., (1955). Some preliminary observations on the PMR in biological samples. Acta Radiologica, 43, 469-476.

Pattany, P. M. and Nayler, G. L., (1985). High velocity flow imaging by even echo rephasing. In: Proceedings of the Fourth Annual Meeting of the Society of Magnetic Resonance in Medicine, London, August 19-23, 1985, pp. 599-600.

Pattany, P. M., Phillips, J. J., Chiu, L. C., Lipcamon, J. D., Duerk, J. L., McNally, J. M. and Mohapatra, S. N., (1987). Motion artifact suppression technique (MAST) for MR imaging. Journal of Computer Assisted Tomography, 11, 369-377.

Purcell, E. M., Torrey, H. C. and Pound, R. V., (1946). Resonance absorption by nuclear magnetic moments in a solid. Physiological Reviews, 69: 37-43.

Pykett, I. L., (1982). NMR imaging in medicine. Scientific American, 246, 78-88.

Redpath, T. W., Norris, D. G., Jones, R. A. and Hutchison, J. M. S., (1984). A new method of NMR flow imaging. Physics in Medicine and Biology, 29, 891-898.

Redpath, T. W., Hutchison, J. M. S., Eastwood, L. M., Selbie, R. D., Johnson, G., Jones, R. A. and Mallard, J. R., (1987). A low field NMR imager for clinical use. Journal of Physics, E: Scientific Instruments, 20, 1228-1234.

Ridgway, J. P. and Smith, M. A., (1986). A technique for velocity imaging using magnetic resonance imaging. British Journal of Radiology, 59, 603-607. (See appendix IV).

Ridgway, J. P., Turnbull, L. W. and Smith, M. A., (1987). Demonstration of pulsatile cerebrospinal-fluid flow using magnetic resonance phase imaging. British Journal of Radiology, 60, 423-427. (See appendix IV).

Shaw, D., (1986a). Nuclear magnetic resonance: General principles. In: Physics in Medicine & Biology Encyclopedia. ed. T. F. McAinish, Pergammon Press, Oxford. pp 529-535.

Shaw, D., (1986b). Nuclear magnetic resonance imaging. In: Physics in Medicine & Biology Encyclopedia. ed. T. F. McAinish, Pergammon Press, Oxford. pp 535-544.

Simpson, I. A., Houston, A. B., Sheldon, C. D., Hutton, I., and Lawrie, T. V. D., (1985). Clinical value of Doppler echocardiography in the assessment of adults with aortic stenosis. British Heart Journal, 53, 636-639.

Singer, J. R., (1959). Blood flow rates by nuclear magnetic resonance measurements. Science, 130, 1652-1653.

Singer, J. R., (1981). Blood flow measurements by NMR. In: Nuclear Magnetic Resonance Imaging in Medicine. eds: L. Kaufman, L. E. Crooks and A. R. Margulis. Igaku-Shoin, Tokyo. pp 128-144.

Singer, J. R. and Crooks, L., (1983). Nuclear magnetic resonance blood flow measurements in the human brain. Science, 221, 654-656.

Smith, M. A., Best, J. J. K., Douglas, R. H. B. and Kean, D. M., (1984). The installation of a commercial resitive NMR imager. British Journal of Radiology, 57, 1145-1148.

Smith, M. A., Ridgway, J. P., Brydon, J. W. E., Been, M, Douglas, R. H. B., Kean, D. M., Muir, A. L. and Best, J. J. K., (1986). ECG-gated Tl images of the heart. Physics in Medicine and Biology, 3, 771-778. (See Appendix IV).

Steiner, R. E., Bydder, G. M., Selwyn, A., Deanfield, J., Longmore, D. B., Klipstein, R. H. and Firmin, D., (1983). Review: Nuclear magnetic resonance imaging of the heart. British Heart Journal, 50, 202-208.

Taylor, D. G., Inamdar, R. and Bushell, M-C., (1988). NMR imaging in theory and in practice. Physics in Medicine and Biology, 33, 635-670.

Tarnawski, M., Padayachee, T. S., Graves, M., Taylor, M. G. and Smith M. A., (1989). Measurement of time-averaged flow in the middle cerebral artery. In: Proceedings of the Eighth Annual Meeting of the Society of Magnetic Resonance in Medicine, Amsterdam, August 12-18, 1989, p. 895.

Terry, H. J., (1986). Blood flow: Invasive and non-invasive measurement. In: Physics in Medicine & Biology Encyclopedia. ed. T. F. McAinish, Pergammon Press, Oxford. pp 85-89.

Turnbull, L. W., Ridgway, J. P. and Smith, M. A., (1987). MRI flow imaging: A possible method of distinguishing communicating syringomyelia from cystic intraspinal lesions. British Journal of Radiology, 60, 517-518.

Turnbull, L. W., Bell, D, Nicoll, J. J., Ridgway, J. P., Muir, A. L. and Best, J. J. K., (1988). Myocardial infarct sizing by magnetic resonance imaging and 99mTc pyrophosphate. In: Proceedings of the 46th Annual Congress of the BIR, Glasgow, British Journal of Radiology., 61, 779.

Underwood, S. R., Firmin, D. N., Klipstein, R. H., Rees, R. S. O. and Longmore, D. B., (1987). Magnetic resonance velocity mapping: clinical application of a new technique. British Heart Journal, 57, 404-412.

Van Dijk, P., (1984). Direct cardiac NMR imaging of heart wall and blood flow velocity. Journal of Computer Assisted Tomography, 8, 429-436.

Vieli, A., Moser, U., Maier, S., Meier, D. and Boesiger, P., (1989). Velocity profiles in the normal human abdominal aorta: A comparison between ultrasound and magnetic resonance data. Ultrasound in Medicine and Biology, 15, 113-119.

Waluch, V. and Bradley, W. G., (1984). NMR even echo rephasing in slow laminar flow. Journal of Computer Assisted Tomography, 8, 594-598.

Waterton, J. C., Jenkins, J. P. R., Zhu, X. P., Love, H. G., Isherwood, I. and Rowlands, D. J., (1985). Magnetic resonance (MR) cine imaging of the human heart. British Journal of Radiology, 58, 711-716.

Wedeen, V. J., Rosen, B. R. and Brady, T. J, (1987). Magnetic resonance angiography. In: Magnetic Resonance Annual, 1987. ed. H. Y. Kressel. Raven Press, New York. pp 113-178.

Wehrli, F. W., Shimakawa, A., MacFall, J. R., Axel, L. and Perman, W., (1985). MR imaging of venous and arterial flow by a selective saturation-recovery spin echo (SSRSE) method. Journal of Computer Assisted Tomography, 9, 537-545.

Wells, P. N. T., (1986). Doppler blood flow measurement. In: Physics in Medicine & Biology Encyclopedia. ed. T. F. McAinish, Pergammon Press, Oxford. pp 274-278.

Woodcock, J. P., (1986). Plethysmography. In: Physics in Medicine & Biology Encyclopedia. ed. T. F. McAinish, Pergammon Press, Oxford. pp 585-588.

Young, I. R., Burl, M., and Bydder, G. M., (1986a). Comparative efficiency of different pulse sequences in MR imaging. Journal of Computer Assisted Tomography, 10, 271-286.

Young, I. R., Bydder, G. M. and Payne, J. A., (1986b). Flow measurement by the development of phase differences during slice formation in MR imaging. Magnetic Resonance in Medicine, 3, 175-179.

Young, I. R., Khenia, S., Thomas, D. G. T., Davis, C. H., Gadian, D. G., Cox, I. J., Ross, B. D. and Bydder, G. M., (1987). Clinical magnetic susceptibility mapping of the brain. Journal of Computer Assited Tomography, 11, 2-6.

Appendix I

Basic Principles of Nuclear Magnetic Resonance (NMR)

A1.0. Introduction

This appendix gives a brief description of the basic principles of NMR. A fuller description can be found, for example, in Farrar and Becker (1971), or in Shaw (1986a).

The phenomenon of nuclear magnetic resonance (NMR) occurs when energy in the form of radiofreqeuncy (rf) radiation is absorbed by a system of nuclei, in the presence of a strong external magnetic field. Absorption only occurs when the rf radiation is applied at a particular resonant frequency, known as the Larmor frequency (expressed here as an angular frequency, ω_L, in radians per second). The Larmor frequency is related to the external magnetic field strength B_o by the relation

$$\omega_L = \gamma B_o$$

The constant γ is known as the gyromagnetic ratio, and is dependent on the nucleus involved.

A1.1. Nuclear Magnetic Moment.

Only certain nuclei have suitable properties for NMR to take place. In particular, they must possess a non-zero nuclear magnetic moment, μ. The presence of a nuclear magnetic moment is dependent on the value of the nuclear spin quantum number I, which is in turn dependent on the arrangement of the protons and neutrons in the nucleus. Both protons and neutrons possess a spin of ½. Governed by the laws of quantum mechanics, pairs of protons or neutrons combine so that their individual spin quantum numbers cancel. Hence a nucleus containing even numbers of both neutrons and protons (even-even nuclei) have a value of $I = 0$ and a net zero nuclear magnetic moment (eg. ^{12}C, ^{16}O, ^{32}S, ^{40}Ca). Most nuclei studied in biological systems have an odd number of either protons or neutrons (odd-even nuclei) and therefore have a value of $I=½$. The most commonly studied nuclei are shown in table A1.1, along with their corresponding values for $\gamma/2\pi$ (MHz/Tesla), their isotopic abundance, and their occurrence in biological systems.

Nucleus	$\gamma/2\pi$	Abundance	Occurrence
^{1}H	42.6	99.8%	All
^{2}H	6.5	0.2%	^{1}H Substitute
^{13}C	10.7	1.0%	All
^{14}N	3.1	99.6%	Amino Acids, Peptides, Proteins.
^{19}F	40.1	100.0%	^{1}H Substitute
^{31}P	17.2	100.0%	Nucleotides, Phospholipids

Table A1.1.

The ^{2}H and ^{14}N nuclei are of the odd-odd type, having an odd number of both protons and neutrons and a value of I= 1. Whilst these nuclei exhibit the same NMR properties as the nuclei with I=½, they also possess electric quadrapole moments, which complicate their behaviour. The proton clearly has advantages for NMR studies over the other nuclei listed. It is the dominant stable isotope of the hydrogen nucleus and it is present in high concentrations in biological tissues.

A1.2. Behaviour of the Proton in a Static Magnetic Field

Since the proton has a spin quantum number value of I=½, it adopts one of two energy states, in the presence of an external magnetic field. These two states correspond to the magnetic moment being aligned, either parallel (lower energy) or anti-parallel (higher energy), to the direction of the field. The energy difference, ΔE, of the two states is proportional to the external magnetic field strength, B_o, ie

$$\Delta E \propto B_o$$

A proton can be excited from the lower to the higher energy state by supplying exactly the right amount of energy.

The energy, ΔE, of the electromagnetic radiation is related to the Larmor frequency, ω_L, by Plank's law:

$$\Delta E = \hbar\omega_L$$

where $\hbar$ is Planck's constant.

A1.3. Bulk Magnetisation and the Net Magnetic Moment

When there is no external magnetic field applied, the proton magnetic moments are randomly aligned with respect to one another. For a large population of nuclei in thermal equilibrium, the net magnetic moment is zero. In the presence of a magnetic field, however, the protons align themselves with the field and the two energy states are populated by roughly equal numbers of protons, although a slightly greater number will occupy the lower energy state, producing a net magnetisation. This can be thought of as the net magnetic moment of the proton population. The population difference between the two states is proportional to the magnetic field strength. As the field strength increases, the net magnetisation increases, and therefore the NMR signal increases. It follows from this that the imagers of higher magnetic field strength should produce images of a greater signal-to-noise ratio.

When energy is applied at the Larmor frequency, protons are excited from the lower to the higher energy states. If sufficient energy is supplied, the population difference will become equal and opposite to the difference at equilibrium. This is known as a poulation inversion.

A1.4. Classical Vector Model and Frames of Reference.

In the following sections a classical vector model shall be used to describe the NMR phenomenon. The vectors are defined relative to a laboratory frame of reference using the cartesian axes x,y, and z with the z axis defined in the direction of the external magnetic field. The net magnetic moment is represented by the Bulk Magnetisation vector $\overline{M}_o$ of magnitude M_o and components M_x, M_y, and M_z. The external magnetic field is represented by the vector $\overline{B}_o$ of magnitude B_o. It is also convenient to define a rotating frame of reference which rotates about the z axis at the Larmor frequency. The cartesian axes x', y' and z' shall be used for the rotating frame of reference. (z and z' are common axes).

A1.5. Resonance and Precession

In the classical model, resonance is accompanied by a rotational motion of the bulk magnetisation vector about the direction of the external magnetic field. This rotational motion is known as precession and is analogous to the precessional motion of the axis of a spinning top or gyroscope about the earth's gravitational field. In this analogy, the spin axis of the top is equivalent to the magnetic moment of the proton and the bulk magnetisation vector.

At equilibrium, the bulk magnetisation vector is aligned with the magnetic field and there is no precession. When perturbed with an energy source, applied at the resonant frequency, the vector $\overline{M}_o$ makes angle ϕ with the z axis and begins to precess about it (figure A1.1). This angle increases for as long as the energy source is applied.

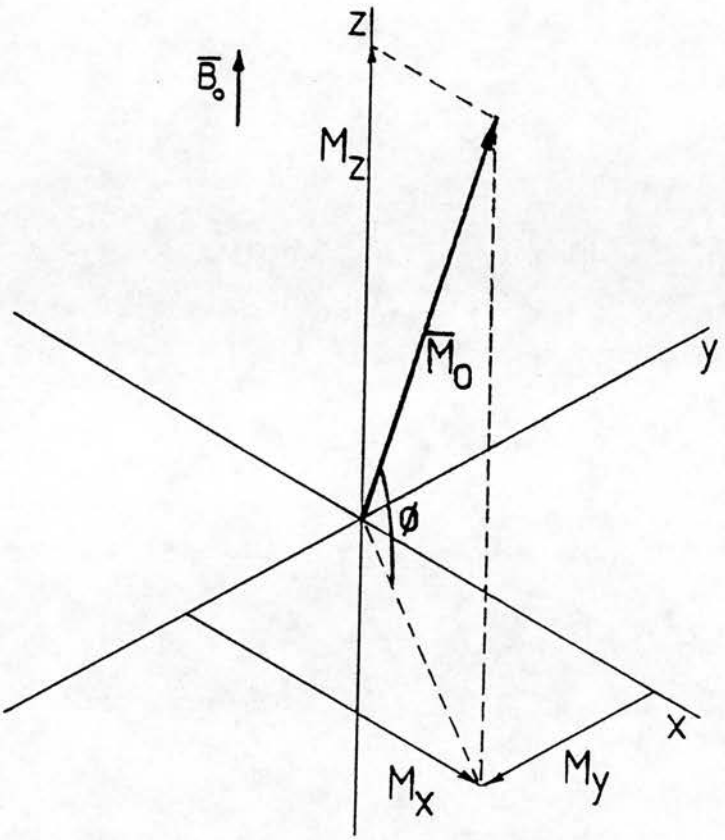

Figure A1.1

Figure showing the bulk magnetisation vector, $\overline{M}_o$, and the angle of precession, ϕ, relative to the cartesian axes defined in section A1.4. Also shown are the three orthogonal components of M_o; M_x, M_y, and M_z.

A1.6. Continuous and Pulsed NMR and Signal Detection

Initially, NMR experiments were performed using continuous excitation by an energy source. The excitation frequency was swept through the range of interest and resonance was detected by observing peaks in the absorbed energy. Most present day NMR, including NMR in the application of medical imaging, is performed using pulses of radiofrequency energy. Radiofrequency energy which is supplied in pulsed form comprises a range of frequencies, known as the bandwith. Following the excitation pulse, energy is emitted by the irradiated sample in the form of radiofrequency electromagnetic radiation, also at the Larmor frequency, and a radiofrequency signal can be detected, known as the Free Induction Decay Signal (FID).

Excitation pulses which cause the bulk magnetisation vector to make an angle of 90^{o} with the z axis are known as 90^{o} pulses. Excitation pulses which rotate the magnetisation vector through 180^{o} are known as 180^{o} pulses. 180^{o} pulses can be used both for inversion of the magnetisation vector and to produce signal echoes (see section A1.8).

The FID signal is detected by a radiofrequency receiver coil which is similar in design to that which transmits the rf power used for excitation. The rf coil is sensitive to time varying magnetic components of

radiation which lie in the xy plane and so long as these transverse components of magnetisation exist, a signal can be detected. The amplitude of the FID is therefore at a maximum following a 90° excitation pulse.

A1.7. The Decay Characteristics of the NMR Signal

Like all excited systems, the population of protons returns to its equilibrium state following excitation, via a relaxation process in which energy is emitted. In NMR there are two main relaxation processes to consider; one which characterises the return of the magnetisation vector to its equilibrium value along the z axis, and one which characterises the initial decay of the transverse component of the magnetisation vector. Both these processes have characteristic exponential decay times, known respectively as the Longitudinal Relaxation Time, T1, and the Transverse Relaxation Time, T2.

A1.7.1. Longitudinal Relaxation Time, T1

Following excitation, the component of the magnetisation vector along the z axis, M_z, will have changed from its equilibrium value ($M_z = +M_o$). For example, for a 90° pulse, $M_z = 0$, or for a 180° pulse $M_z = -M_o$. M_z will then return to its equilibrium value, $M_z = +M_o$, with an

exponential decay time constant denoted T1. This time constant is also known as the longitudinal relaxation time or the spin-lattice relaxation time.

A1.7.2. Transverse Relaxation Time, T2

Following an excitation pulse, the existence of the transverse component of the bulk magnetisation vector requires coherent precessional motion of the proton population. Whilst individual protons may retain their transverse magnetisation for some time, the bulk magnetisation vector may very quickly lose its transverse component as the precessional motion of the population of protons loses its coherence. Incoherence arises from the existence of interaction between adjacent proton spins and from the existence of local inhomogeneities in the the external magnetic field. These both affect the precessional frequency of the individual protons, causing them to move out of phase with one another. Their magnetic moments therefore cancel,causing the tranverse component of the magnetisation vector to reduce and the signal magnitude to decay. This decay is exponential with a time constant denoted $T2^*$, known as the 'observed' transverse relaxation time. The exponential decay time constant, due to the interaction of adjacent protons alone, is denoted T2, and is also known as the transverse relaxation time, or the spin-spin relaxation time.

For protons in biological tissues, the T1 relaxation process takes longer than the T2 relaxation process. Typical values in biological systems range from 100 to 1500 for T1, and 40 to 300 for T2, although T1 is dependent on field strength. The measurement of T1 and T2 values is of use for tissue discrimination both in vitro and, in the case of NMR imaging, in vivo. The different T1 and T2 relaxation times that characterise different tissues can be used to generate contrast in the NMR image.

A1.8. Measurement Pulse Sequences

The measurement of the peak amplitude of the FID represents the magnitude of the magnetisation vector, and therefore reflects the population density of magnetised protons, often referred to as the proton density, ρ. Whilst it is difficult to obtain an absolute measure of ρ, it is possible to perform quantitative measurement of the relaxation times T1 and T2, by using particular measurement RF pulse sequences. The NMR signal strengths obtained are dependent in a quantifiable way on the T1 and T2 values of the measured sample. The four most commonly used sequences for measurement are the Saturation Recovery, Inversion Recovery, Spin-Echo and Multiple-Spin-Echo sequences, and these are described below.

A1.8.1. The Saturation Recovery Pulse Sequence

The saturation recovery pulse sequence is used to measure the longitudinal relaxation time, T1 and consists of two 90° RF pulses separated by a time interval, T, i.e.,

$$90^{\circ}\text{-T-}90^{\circ}\text{-(FID)}$$

Following the first 90° pulse, the z component of the magnetisation, M_z, is zero, and during the time interval, T, it begins to return to its equilibrium value, $M_z=M_0$. The signal obtained following the second 90° pulse is dependent on the value of M_z attained after the time T, given by

$$M_z = M_o[1-\exp(-T/T1)]$$

If this sequence is repeated for different values of T, the T1 can be calculated. A further development of the saturation recovery pulse sequence is the Steady State, or Progressive Saturation Recovery sequence,

$$90^{\circ}\text{-T-}90^{\circ}\text{-T-}90^{\circ}\text{-T-}.....$$

This sequence can be regarded as an infinite train of 90° pulses, each separated by a time T. The value of $M_{z(T)}$ reaches a steady state value after the initial pulses given by

$$M_z(T) = M_o[1-\exp(-T/T1)]$$

A1.8.2. The Inversion Recovery Pulse Sequence

The inversion recovery pulse sequence is also used to measure the T1 relaxation time and has the form,

$$180^{\circ}\text{-}T\text{-}90^{\circ}\text{-}(FID)$$

In this case, the magnetisation vector is inverted by a 180° pulse so that $M_z=-M_o$. Following a time, T, a 90° pulse is applied and the signal obtained is a measure of the value of M_z attained, given by

$$M_z(T) = M_o[1-2\exp(-T/T1)]$$

The sequence is repeated for a number of values of T, in order to determine the T_1. This technique is more accurate for T1 measurement than the saturation recovery sequence. Errors in the 180° pulse value, caused by non-uniformities of the rf field, have less effect on the initial value of M_z, than do errors in a 90° pulse. Any error caused by the 180° can be further reduced by using an Adiabatic Fast Passage, (AFP), to invert the magnetisation vector. This is a swept-frequency pulse, which is more efficient than the 180° pulse at inverting a population of nuclei. This is particularly the case over the large volumes encountered in imaging, where RF homogeneity becomes a significant source of error.

A1.8.3. The Spin Echo Pulse Sequence

The spin echo pulse sequence consists of a 90^{o} excitation pulse, followed at a time, T, by a 180^{o} pulse. During the period, T, the proton nuclear magnetic moments move out of phase with each another as they experience slightly different local magnetic field values, since the field is not perfectly homogeneous. This results in a loss of coherence and the FID signal decays rapidly.

The 180^{o} pulse changes the sign of the phase shift gained by each individual proton, by rotating the proton magnetic moments vector through 180^{o} about the x' axis. During a second time period, T, following the 180^{o} pulse, the nuclear magnetic moments experience the same phase changes as in the first period, T, since they experience the same local field values. The net phase changes due to the local magnetic field inhomogeneity will therefore cancel, and coherence is re-established for an instant to form a signal echo, at a time 2T, following the excitation pulse. As the phase changes continue, the nuclei will again lose coherence.

The 180^{o} pulse does not compensate for loss of coherence due to spin-spin interactions, and therefore the magnitude of the signal echo will depend on the T2 of the sample and the value of T. The maximum signal magnitude of the echo depends on the transverse magnetisation

present after a time 2T, and is given by

$$M_{xy}(2T) = M_o[\exp(-2T/T2)]$$

If this pulse sequence is repeated for different values of T, T2 can be calculated.

A1.8.4. The Multiple-Spin Echo Pulse Sequence

Repeated single spin echo experiments are time consuming, and are affected by molecular diffusion. Multiple-echo pulse sequences where further 180^o pulses are applied at intervals of 2T following the first 180^o, such as

$$90^o\text{-T-}180^o\text{-T-(echo)-T-}180^o\text{-T-(echo)-T-}180^o\text{-T-(echo)....}$$

can be used to speed up the measurement and to reduce diffusion effects. A signal echo occurs after each 180^o pulse. This sequence is known as the Carr-Purcell sequence. If T is kept small, diffusion effects will be minimised and T2 can be calculated by measuring the magnitude of the signal echoes. A modification of this sequence is the Carr-Purcell-Meiboom-Gill (CPMG) sequence in which the 180^o pulses are applied with a phase shift of 90^o relative to the initial 90^o pulse. This sequence eliminates problems due to diffusion.

Appendix II

Basic Principles of Magnetic Resonance Imaging (MRI)

A2.0. Introduction

This appendix gives a brief description of the basic principles of MRI. A fuller description can be found, for example in Morris (1986), Shaw (1986b), Leach (1988), or Taylor et al (1988),

There are two main specific requirements which must be fullfilled when adapting the technique of NMR to perform whole body imaging. Firstly, magnets must be developed with a large enough central bore to accommodate the whole body. Magnets used for NMR spectroscopy need only to accommodate small samples and have typical bore diameters of just a few centimetres. Whole body imaging requires the magnetic field to be uniform over a large volume, (typically around 20ppm over a 40cm sphere). Magnet design and technology has improved significantly over the last decade in order to meet this requirement.

The second requirement of whole body NMR imaging is that the NMR signal must be spatially localised and spatially encoded, in order to provide enough information for an image to be reconstructed. This is achieved by superimposing magnetic field gradients onto the existing

magnetic field, by using additional electromagnetic coils. In this appendix a general description is given of the spatial localisation and encoding techniques, the signal detection, and of the pulse sequences, parameters and effects exploited in MRI. The equipment associated with each aspect of the technique is also described. In this description, special emphasis is given to Spin Warp Imaging (Edelstein et al, 1980), which forms the basis of the imaging techniques used by most MRI system manufacturers.

The convention for the right handed cartesian axes used both in this appendix and in the main text, is shown in figure A2.1. For the purposes of this thesis, the axes are defined for a vertically oriented magnetic field and a human subject lying in the supine position. The z axis is in the vertical direction, parallel to the magnetic field, B_o, (+ve is upwards). The y axis is from the feet towards the head of the subject, and the x axis is from right to left of the subject. The transverse, sagittal and coronal planes are also shown. This convention is for a magnetic field, B_o which is orientated vertically. A horizontally orientated magnetic field is normally oriented in the y direction.

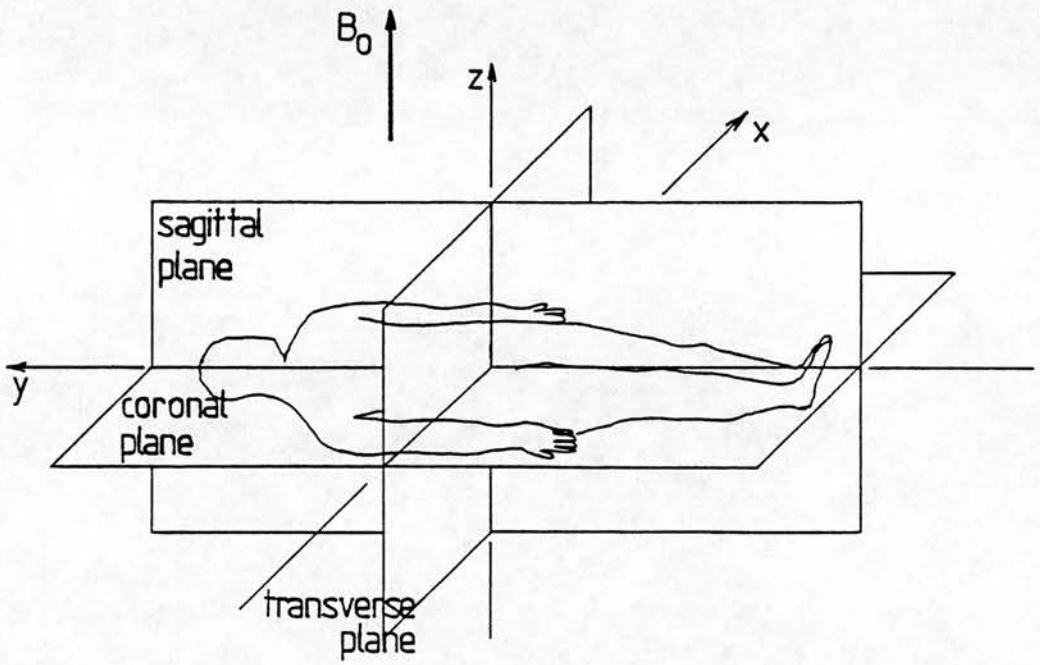

Figure A2.1.

Schematic diagram showing the cartesian axes defined in this appendix relative to a patient lying supine, and a vertically oriented magnetic field, B_o. The sagittal, coronal and transverse planes are also shown.

A magnetic field gradient, which is superimposed on the main magnetic field B_o, results in a spatially-dependent magnetic field, B(x), given by

$$B(x) = B_o + xG_x$$

where G_x is the magnitude of the magnetic field gradient, expressed in milli-Tesla per metre, and x is the spatial coordinate in the direction of the gradient. There are three orthogonal magnetic field gradients, corresponding to each of the cartesian axes. Each gradient has a null point, where the additional magnetic field contributed by the gradient is zero. The null points of the three gradients usually coincide at the geometric centre of the main magnet.

A2.1. Spatial Localisation by Selective Excitation

When performing NMR on a large object, the NMR signal is obtained from the whole object, provided that the static magnetic field and radiofrequency (rf) field extend uniformly over the whole object, and that the frequency of the rf field matches the Larmor frequency at each point. Usually, images of only one part of the object are required. Therefore, the origin of the signal is restricted to a smaller region by using selective excitation.

Selective excitation of part of an object is achieved by applying a magnetic field gradient at the same time as the RF excitation pulse. Selective excitation methods can be categorised as sensitive point, sensitive line or planar methods. In each case, the NMR signal is obtained from a point, line or plane, (all of finite volume), and is used to build up a two-dimensional image. In practice, the most commonly used of the three methods is planar imaging in which the NMR signal from an excited plane, (also referred to as a slice), is spatially encoded in two dimensions, to allow reconstruction of a two-dimensional image (see Section A2.3).

If an excitation pulse of a single fixed frequency, ω, is applied in the presence of a magnetic field gradient, excitation only occurs where the magnetic field strength corresponds to the Larmor frequency of the same value. For a gradient of magnitude, G_x, applied along the x-direction, the excited region is a slice, which is in a plane perpendicular to the gradient direction, at a point x along the gradient where the Larmor frequency is given by

$$\omega = \gamma(B_o + xG_x)$$

Using the convention of figure A2.1, this would be a sagittal slice. This magnetic field gradient is known as the slice selection gradient. The slice position, x, can be varied by varying the frequency ω.

A2.1.1. RF Pulse Shape, Slice Width and Slice Profile

Since the rf excitation energy is applied in pulsed form, the excitation occurs over a range of frequencies. The frequency distribution is related to the envelope of the rf pulse, and determines the slice profile. The bandwidth of the frequency distribution is determined by the pulse width and determines the slice thickness, for a given magnetic field gradient magnitude. The slice profile is the Fourier transform of the pulse envelope. For a rectangular slice profile, the pulse envelope should be a sinc function. Theoretically, such a pulse should have an infinite number of side lobes, but in practice this envelope is truncated after the first one or two side lobes. A gaussian pulse envelope gives a gaussian slice profile.

A2.1.2. Pulse Magnitude and Flip Angle

The magnitude of the rf pulse of a given width and envelope, determines the rf power delivered by the pulse and therefore, determines the angle of precession achieved during excitation (See secion A1.6). This excitation angle is often referred to as the Flip Angle, α, although the more commonly used pulses have $\alpha = 90^{\circ}$ and $\alpha = 180^{\circ}$.

A2.1.3. Slice-Selection and Rephasing Gradient Pulses

The slice-selection magnetic field gradient is also applied in pulsed form, and is only switched on when the rf excitation pulse is applied, so that it does not interfere with the spatial encoding of the NMR signal which follows. Since the rf pulse is applied over a finite length of time, however, the gradient will have a significant dephasing effect on the excited nuclei, over the latter part of the time for which it is applied. The dephasing effect causes loss of coherence and a reduction in the signal magnitude and so it is compensated for by a second gradient pulse of the same magnitude and direction, but of opposite sign to the first. This second gradient pulse is known as the rephasing pulse and has a time integral which is half that of the slice-selection pulse. The magnitude of the slice-selection gradient pulse is used to control the slice width, for a given rf pulse bandwidth.

A2.1.4. RF Transmission Hardware and Electronics

This description refers to the hardware on the Edinburgh MRI system, however this hardware configuration is common to many other systems. The rf-pulse carrier frequency is generated by a frequency synthesiser, which is under

computer control. The carrier frequency is set to obtain the desired slice position. The bandwidth of the rf pulse is fixed at 1 kHz, and the magnetic field gradient strength is chosen to obtain the desired slice thickness. The envelope of the RF pulse is computer generated as a digital waveform, which is converted to an analogue signal by a Digital-to-Analogue Converter (DAC). The relative amplitude of the pulse envelope is set at this stage and the envelope is then used to modulate the carrier frequency to produce the shaped rf pulse. The rf pulse is then amplified by a power amplifier. The amplified pulse is transmitted down a cable to the rf transmitter coil within the imager.

A2.2. NMR Signal Production

Following the excitation pulse, the slice-selection magnetic field gradient is switched off and an FID signal is produced (section A1.6). Whilst the FID can be detected and used to provide the necessary information for image reconstruction, it is more common to produce a signal echo.

A2.2.1. The Spin Echo

A spin echo is produced at a time, TE, following the excitation pulse, by applying a 180° pulse at a time TE/2. (See section A1.8.3). This pulse sequence can be expressed in notation form,

$$90^{\circ}\text{-TE/2-}180^{\circ}\text{-TE/2-(signal echo)}$$

A gradient is applied before and after the 180° pulse, in a direction which is perpendicular to the slice-selection gradient. These two gradient pulses have the same sign. and the presence of the 180° pulse enables the second gradient pulse to compensate for the dephasing effect of the first pulse. The second gradient pulse is used to spatially encode the signal in the direction in which it is applied (see section A2.4.1). This gradient pulse is known as either the Readout Pulse or the Frequency-Encoding Gradient Pulse. The magnitude of the readout pulse is used to control both the field of view of the two-dimensional image, and the imaging bandwidth (See section A2.4.3.). For a given bandwidth, the field of view decreases as the gradient magnitude increases.

A2.2.2. The Field Echo

The field echo is produced without the application of a 180° pulse. Instead, dephasing and rephasing magnetic field gradients are solely responsible for the generation of the signal echo. In notation form, the field echo pulse sequence is

$$90^{\circ}\text{-TE-(signal echo)}$$

Because the 180° pulse is not present, the rephasing pulse is of opposite sign to the dephasing pulse. This pulse sequence does not correct for the loss of coherence caused by local magnetic field inhomogeneity, and so the field echo has a smaller amplitude than the spin echo (See sections A1.7.2. and A1.8.3).

A2.3. Spatial Encoding of the NMR Signal

In two-dimensional imaging techniques, the NMR signal is obtained from a plane or slice, produced using selective excitation. In order to reconstruct an image, the signal is spatially encoded by using magnetic field gradients. This idea was first used by Lauterbur, who used magnetic field gradients to produce a two-dimensional cross-sectional image of two testubes (Lauterbur, 1973).

A2.3.1. Frequency Encoding

The simplest application of spatial encoding uses the frequency of the NMR signal. A magnetic field gradient is applied, in a direction which is parallel to the selected plane, during the formation of the signal echo. The resultant signal is composed of a range of frequencies. Fourier transformation of this signal produces the distribution of the frequency components contained within the signal. Since the frequency of the signal is related to the position along the gradient, this distribution represents a one-dimensional projection of the proton density of the sample, in the direction of the frequency-encoding gradient. The number of frequency components evaluated, is directly related to the matrix size of the reconstructed image.

In order to reconstruct a two-dimensional image, a number of signals must be acquired. For each of the signal acquisitions, the frequency encoding gradient can be applied along a number of different directions within the selected plane, to obtain one-dimensional projections of the slice at different angles. It is then possible to reconstruct a two-dimensional image from these projections, using a back-projection reconstruction technique.

A2.3.2. Phase Encoding

An alternative method, known as two-dimensional Fourier transform imaging, uses the phase of the signal to spatially encode the remaining direction. In this method, the signal is acquired a number of times with the frequency encoding gradient applied in a fixed direction, whilst a second gradient is applied, in the direction perpendicular both to the slice-selection, and the frequency-encoding directions, for a short time before the signal echo is formed. This short pulsed gradient, known as the phase-encoding gradient, introduces a phase shift in the NMR signal, which is dependent on the position along its direction. Whilst this alone does not produce enough information for a two-dimensional image to be reconstructed, the pulse sequence is repeated a number of times using different amplitudes of the phase-encoding gradient, increasing from a negative value to a positive value equal in magnitude to the starting value.

All of the signals acquired with different phase-encoding are stored in computer memory. After the first Fourier transform has been applied to each signal to obtain the frequency distribution of the signal, a second Fourier transform is applied to the total number of signals to translate the phase encoding into positional information. This second application of the Fourier transform completes the reconstruction of the two-dimensional

image. This technique is also known as Spin Warp Imaging (Edelstein et al, 1980), because of the use of a phase encoding gradient. The number of phase encoding steps required is also directly related to the matrix size of the final reconstructed image. For example, a square image matrix of 128 x 128 elements requires 128 frequency components to be evaluated and 128 phase encoding steps to be used. Therfore, the pulse sequence must be applied 128 times.

A2.3.3. Three-Dimensional Fourier Transform Imaging.

Three-dimensional Fourier transform imaging is a natural extension of the two-dimensional technique to three dimensions. In this case, the signal is acquired from a selectively excited volume rather than from a slice. Two-dimensional spatial encoding is then applied in the usual way described above, but for each phase encoding step in the phase encoding direction, a second phase encoding gradient is applied in what would normally be the slice selection direction. Image reconstruction is performed in a similar fashion to the two-dimensional case, except that the Fourier transform is applied three times and the reconstructed image data exists as a cubic matrix. The third dimension of this matrix and the increase in scan time are related to the number of additional phase encoding steps used.

A2.4 NMR Signal Detection

The NMR signal can be detected, so long as there is an oscillating transverse component of the bulk magnetisation vector within the excited volume. This results in a rf signal with an oscillating magnetic field, in a plane perpendicular to the main magnetic field (the x-y plane). This signal can be detected by rf receiver coils. The geometry of the coil depends on the orientation of the main magnetic field relative to the body, and on the part of the body being imaged. The detected signal is small and so it is immediately pre-amplified before it is transmitted along a cable to the MRI system electronics. In order to extract information from the NMR signal, it is processed in analog form before it is stored by the computer in digital form.

A2.4.1. Amplification and Demodulation

After the NMR signal has been pre-amplified, its amplitude may vary over a wide range depending on the pulse sequence and the subject or sample being imaged. Before the signal is digitised, therefore, the signal amplitude is first optimised using a variable-gain amplifier to bring it within a suitable range for the analogue to digital converters (ADCs).

At this stage, the signal will consist of a range of frequencies close to the system operating frequency, f_o. System operating frequencies lie typically in the range 1-100 Mhz (depending on the operating field strength), and are difficult to sample fast enough. The signal is therefore demodulated with respect to f_o. The demodulated signal is then much easier to sample, being typically in the range 1-10kHz.

A2.4.2. Quadrature Detection, Frequency and Phase.

The detected signal represents only one time-varying component of the magnetisation vector. In order to determine the magnitude and phase of the magnetisation vector at any instant, both the components of the magnetisation vector in the x-y plane are required. Since this information is required for the two-dimensional, Fourier-transform reconstruction, a method known as Quadrature detection is used to overcome this problem: During the demodulation process, the signal is split into two channels and each channel is detected synchronously by two demodulators, with the reference frequency phase-shifted by 90^o between the two demodulators.

The two channels generated by quadrature detection represent the two components, M_x and M_y, of the transverse magnetisation vector. From these two components, it is possible to calculate the phase, ϕ_m,

and magnitude, M_o, of the transverse magnetisation at any instant, given by:

$$\phi_m = \tan^{-1}(M_y/M_x) \quad ; \quad M_o = \sqrt{M_x + M_y}$$

The two components, M_x and M_y, derive what are often referred to as the real and imaginary components of the signal. This terminology is derived from the mathematical concept of complex numbers and is used here because the two-dimensional Fourier transform treats the two components of each matrix element as a complex number. Following the Fourier transformation, the phase and magnitude information is preserved. Therefore, each image matrix element also has real and imaginary components, which represent the two orthogonal components of the NMR signal, at the location represented by that element. Usually, the magnitude of the signal for each element is calculated and used to generate an image. It is also possible however, to generate images from either of the real and imaginary components, or from the phase calculated for each element.

A2.4.2. Filtering and Digitisation of the NMR Signal

The region of the imaged object included in the selected slice often extends outside the chosen field of view. In the frequency-encoding direction, the magnitude of the

frequency-encoding gradient is designed so that the edge of the field of view corresponds to a frequency shift which is equal to half the imaging bandwidth selected. Frequencies outwith this range are removed by a low pass filter. This filtering also removes rf interference occuring at higher frequencies. As the imaging bandwidth is decreased, the signal-to-noise ratio is increased. If the sample extends outside the field of view in the phase encoding direction, the influence on the signal cannot be filtered out in the same way. In this case, the extended region is superimposed on the opposite edge of the image. This is known as the wrap-around effect.

In order to obtain sufficient sampling of the frequencies present in the signal, the analogue-to-digital converters must sample at a rate of twice the maximum frequency present after low-pass filtering. This minimum sampling frequency is known as the Nyquist frequency and it is equal to the imaging bandwidth. As the imaging bandwidth decreases, the sampling time required increases and therefore the echo time has to be extended to accommodate it. The gain in signal to noise ratio therefore has to be balanced against T2-related losses.

A2.5. Imaging Pulse Sequences

Every imaging pulse sequence has a number of common features which are listed below:

Radiofrequency Pulse Sequence, $B_1(t)$
Magnetic Field Gradient Pulse Sequence, G(t)
Signal, (FID, Spin Echo, or Field Echo)
Data Collection Period
Echo Time, TE, (spin echo and field echo only)
Repetition Time, TR

The radiofrequency pulse sequence, $B_1(t)$, is comprised of all the rf pulses which are required to produce the NMR signal, including the excitation pulse, the 180° refocussing pulse used in spin echo sequences, and the inversion pulse used in inversion recovery sequences.

The gradient pulse sequence, G(t), includes all the gradient pulses, applied in order to achieve spatial localisation and encoding of the NMR signal. It therefore includes the magnetic field gradient pulses applied in the three orthogonal directions, including the slice-selection gradient, the readout gradient (or frequency-encoding gradient), and the phase-encoding gradient. Additional gradient pulses may be added to generate specialised pulse sequences, or to improve the performance of the existing pulse sequences.

The NMR signal can be detected as an FID, a field echo, (FE), or a spin echo, (SE), (see section A2.2). The period of detection is known as the data collection period and ADC sampling is enabled during this period. The FE and SE are the most common forms of NMR signal, and therefore the time to echo, (TE), is usually quoted.

The pulse sequence is repeated a number of times, in order to obtain sufficient information to reconstruct an image. (See section A2.3.2.). The time interval between successive applications of the pulse sequence is known as the Repetition Time, (TR). Both the TR and the TE are usually quoted as they greatly influence the image contrast.

The rf pulse sequence also influences the image contrast obtained, and the following sections describe some of the more common sequences in clinical use.

A2.5.1. Saturation Recovery and Partial Saturation

The Saturation Recovery (SR) and Partial Saturation (PS) pulse sequences are similar in form. The PS sequence is the steady state form of the SR sequence (See section A1.8.1.). Using the RF pulse sequence notation, the general form of the SR sequence is,

$$90^{\circ}\text{-T-}90^{\circ}\text{-signal}$$

The signal can be an FID, a spin echo or a field echo and is detected after the second 90° pulse. The pulse sequence is repeated with a repetition time TR. The PS sequence is obtained by setting the time interval, T, equal to the TR and collecting the signal after every 90° pulse.

Images obtained using the SR sequence have contrast which is related to the T1 relaxation time. The T1-related contrast increses as T decreases. Similarly, the T1-related contrast in the PS sequence increases as the TR decreases. For values of TR (or T) >> T1, the T1-contrast is minimal. Provided that the T2-contrast is also minimal, such pulse sequences are sometimes called Proton Density sequences as the image pixel intensity is related only to the proton density.

A2.5.2. Inversion Recovery

The Inversion Recovery (IR) sequence is similar to the SR sequence, however the first 90^{o} pulse is replaced by an inverting pulse. This pulse is usually a 180^{o} pulse, but an Adiabatic Fast Passage (AFP) pulse can also be used (See section A1.8.3.). The IR sequence has the form,

180^{o}-TI-90^{o}-signal

or

AFP-TI-90^{o}-signal

The signal can again have the form of an FID, an SE or an FE. The time interval between the inversion pulse and the 90^{o} excitation pulse is known as the time from inversion, denoted TI. Images produced by this pulse sequence are very dependent upon T1 relaxation time, and exhibit superior T1-related contrast to the SR or PS sequences. The IR sequence is commonly used for in vivo measurement of the T1 relaxation time, although accurate measurement requires long TR values, making it a time consuming method.

A2.5.3. Spin Echo

The Spin Echo (SE) imaging pulse sequence (see sections A1.8.3. and A2.2.1.), has the form,

$$90^{\circ}\text{-TE/2-}180^{\circ}\text{-TE/2-(signal)}$$

If the TR is short relative to T1, and the TE is also short (TE<<T2), this sequence is effectively the same as a PS sequence and the image contrast is dependent upon T1. The main application of this pulse sequence is to obtain image contrast which is heavily T2 weighted by setting the TR and TE to longer values, (TR>>T1; TE≈T2). Generally speaking, the T1-related contrast increases as the TR and the TE decrease, whilst the T2-related contrast increases as the TR and the TE increase.

A2.5.4. Multiple Spin Echo

The Multiple Spin Echo (MSE) pulse sequence is a spin echo sequence in which the 180° refocussing pulse is repeated and an echo is detected following each 180° pulse (see section A1.3.4). The form of the MSE sequence is

$$90^{\circ}\text{-TE/2-}180^{\circ}\text{-TE/2-echo-TE/2-}180^{\circ}\text{-TE/2-echo....}$$

A separate image is calculated which corresponds to each

echo. The T2-related contrast is increased for the later echoes. The CPMG pulse sequence (see section A1.3.4.) is often used to measure T2 relaxation times in vivo.

A2.5.5. Field Echo

The Field Echo (FE) imaging pulse sequence (section A2.2.2), has the form,

$$\alpha\text{-TE-signal}$$

Here the angle of precession, denoted by α, generated by the excitation pulse, can be varied within the range $0^{o} < \alpha < 180^{o}$. The excitation angle is also known as the flip angle (see section A2.1.2.), and it gives the FE sequence the advantage of further control over image contrast. Whilst the signal echo is produced by a magnetic field gradient reversal, rather than by a 180^{o} refocussing pulse, the FE sequence has similar properties to the SE sequence. The T1-related contrast increases as the TR and TE are decreased and the T2-related contrast increases as the TR and the TE increase. As the flip angle is increased, the T1-related contrast increases. At intermediate values of TR and TE, the T1- and T2-related contrast tend to cancel one-another. Decreasing the flip angle decreases the T1-related contrast, making the T2-related contrast more evident at intermediate values of TR.

Reducing the flip angle to a value which is too close to zero reduces the signal magnitude to below acceptable values, however it is possible to optimise the value of the flip angle to maximise the signal-to-noise ratio for a given T1 value. This value, α_E, is known as the Ernst angle (Ernst, 1966), and is given by

$$\alpha_E = \cos^{-1}[\exp(-TR/T1)]$$

A2.6. Pulse Sequences - Other General Parameters

A number of pulse sequence parameters have been already considered and their effect on the image contrast has been stated. These parameters are the pulse sequence type, (which determines the RF and magnetic field gradient pulse sequences), the Flip Angle, (FE sequences only), and the various pulse sequence timing parameters, (TR, TE, TI).

There are a number of other parameters which affect the appearance and quality of the NMR image, some of which have been mentioned previously in this appendix. These are discussed in the following sections.

A2.6.1. Magnetic Field Strength and Homogeneity

The magnetic field strength of an MRI system determines the maximum signal-to-noise ratio obtainable. As discussed in section A1.3, the signal-to-noise ratio increases as the operating field strength increases. High field strength machines (B_o>1.5 Tesla), can also be used to perform in vivo spectroscopy measurements. However, the T1-related contrast is reduced at higher field strengths, and at very high field strengths (B_o>2.0 Tesla), absorption of the RF frequency radiation by surrounding tissues significantly attenuates the NMR signal, which offsets the advantage of increased signal to noise ratio. High installation, purchase and running costs are further disadvantages of high field systems.

The magnetic field can be produced using three main types of magnet; resistive electromagnets, superconducting electromagnets and permanent magnets. Low field strength systems (between 0.02 and 0.15 Tesla), use air-cored, resitive electromagnets. Field strengths of up to 0.4 Tesla can be achieved using iron-cored resitive magnets, but power and weight restrictions prevent resistive magnets from producing field strengths higher than this. Most of the medium and high field strength systems (above 0.5 Tesla), use superconducting electromagnets which have a low power consumption, but require liquid helium and nitrogen to cool the magnet

rings to the temperature necessary for superconduction. Permanent magnets, made from blocks of magnetic material, can produce magnetic fields in the low to medium field strength range, but they suffer from instability due to temperature variations, and require special preparation of the installation site because of their weight.

Electromagnetically-produced magnetic fields may be orientated either vertically or horizontally, depending on the orientation of the electromagnet rings. Rings which are orientated in the horizontal plane produce a field in the vertical direction, and the subject lies horizontally between the central two rings. Vertically oriented magnet rings produce a horizontal field and the subject lies along direction of the field.

The magnetic field homogeneity, often denoted ΔB_o, is usually defined over a sphere at the centre of the imager, and is expressed as the variation in the magnetic field, relative to the field strength, in parts-per-million. It does not usually have a great effect on the appearance of the image, however, signal losses due to ΔB_o can sometimes be seen when scanning extremities which fall outside this sphere. This effect is particularly noticeable on Field Echo images. The homogeneity of the magnetic field can be improved by a process called shimming. Shimming modifies the magnetic field, using small electromagnetic coils, or pieces of iron.

A2.6.2. Spatial Resolution, Field of View & Matrix Size

In MRI, the spatial resolution usually refers to the in-plane resolution of a two-dimensional slice. Provided that the signal-to-noise ratio is adequate, the resolution is equal to the pixel dimensions. The resolution in a given direction is therefore related to the field of view and the matrix size (i.e. the number of pixels along that direction), such that,

$$\text{Resolution} = \text{Field of View} / \text{Matrix Size}$$

The field of view is determined by the magnitude G, of the frequency-encoding and phase-encoding gradients (see sections A2.3.1. and A2.3.2.) and by the imaging bandwidth, Δf:

$$\text{Field of View} = \Delta f / \gamma G$$

The matrix size is directly related to the number of samples used to digitise each NMR signal, (and therefore, the number of frequency components evaluated), and to the number of phase-encoding steps used. For example, if each NMR signal is digitised using 256 samples and 128 phase encoding steps, the image matrix size will be 256 x 128 pixels.

A2.6.3. Bandwidth

The imaging bandwidth is determined by the sampling rate of the analogue-to-digital converters. Decreasing the bandwidth increases the signal-to-noise ratio. However, a narrower bandwidth also requires a longer sampling time which may lengthen the TE unacceptably (see section A2.4.2.).

A2.6.4. Slice Thickness

The slice thickness, d, refers to the thickness of the excited plane following selective excitation (see section A2.1 et seq.). It is determined by the bandwidth of the excitation pulse, Δf_o, (which is normally fixed), and the magnitude of the magnetic field gradient, G_s, which is used for selective excitation, such that,

$$d = \Delta f_o / \gamma G_s$$

An increase in slice thickness gives a proportional increase in the signal-to-noise ratio. However, when using thick slices, small structures become less well defined and separate structures may overlap and appear to be connected. This effect is known as the partial volume effect. The slice thickness is chosen in order to obtain the best signal-to-noise ratio and the best definition.

A2.6.5. Signal Averaging

Signal averaging can be used to increase the signal-to-noise ratio, while keeping all other imaging parameters the same. This is achieved by repeating the signal acquisition a number of times for each phase encoding step, and then taking the average of the collected signals. The signal to noise ratio increases as the square root of the number of acquisitions, N. For example, for signal averaging using four acquisitions, the signal to noise ratio is doubled. Signal averaging has the disadvantage of causing an N-fold increase in the imaging time.

A2.6.6. Slice Orientation

The slice orientation is determined purely by the applied direction of the magnetic field gradients. The electromagnetic gradient magnetic field coils are designed to produce gradients in three orthogonal directions which coincide with the transverse, sagittal and coronal planes of a subject, lying in a supine position in the imager. By assigning the slice-selection, frequency-encoding and phase-encoding gradient pulse waveforms to the appropriate gradient coils, the transverse, sagittal and coronal slice orientations are obtained. The assignment of gradient pulse waveforms to

the coils is shown in table A2.1, using the convention defined in section A2.0. Arbitrary slice angulation is achieved by mixing the gradient pulse waveforms assigned to each coil.

Slice Orientation	Gradient Pulse Waveform		
	Slice-Selection	Frequency-Encoding	Phase-Encoding
Transverse	y coil	x coil	z coil
Sagittal	x coil	y coil	z coil
Coronal	z coil	y coil	x coil

Table A2.1

Assignment of Gradient Pulse Waveforms to the Magnetic Field Gradient Coils for Transverse, Sagittal and Coronal Slice Orientations.

A2.6.7. Simultaneous Multiple Slice Imaging

Most examinations usually require several slices to be acquired at different levels in order to cover the region of interest. Whilst each slice can be acquired separately, the total examination time is increased in proportion to the number of slices acquired.

Simultaneous multiple-slice imaging avoids this problem, by selectively exciting several slices at different times during the pulse sequence repetition period, TR. The maximum number of slices that can be obtained during a single scan is limited only by the number of pulse

sequences that can be applied during the period TR. Provided that all the RF pulses are applied using selective excitation, the relaxation process within slices already excited is not affected by the selective excitation of a slice at a different level.

A2.6.8. Scan Time

The scan time is determined by the repetition time, TR, the number of phase encoding steps required, n, and the number, N, of signal acquisitions acquired for signal averaging. If the TR is expressed in milliseconds, the scan time in seconds is given by

$$\text{Scan Time} = (TR \times n \times N)/1000$$

Thus for scan with a TR=500ms, using 2 aquisitions to obtain image matrix of 256 x 128, the scan time is 128 seconds. Other factors may increase the scan time; for example, some types of scan use two interleaved pulse sequences, which doubles the scan time.

A2.7. Other Factors Affecting Pixel Intensity

The main factors which affect image pixel intensity have been discussed, however there are a number of other factors which influence the image pixel intensity, which are encountered less frequently. These are the effects of chemical shift, magnetic susceptibility and motion. The effects of motion, including blood flow, and cardiac and respiratory motion, are discussed in the main text. Chemical Shift and Magnetic Susceptibility are discussed in the following sections.

A2.7.1. Chemical Shift

Chemical shift phenomena occur when there is a small change in resonant frequency, due to a difference in chemical structure. The most apparent chemical shift observable in proton NMR imaging is between fat (or lipid) and water. At high field strengths (>1.0T), this frequency shift can give rise to the overlapping of structures in the frequency encoding direction, at the boundaries between structures with a high fat content and structures with a high water content. As the receiver bandwidth is decreased, the effect becomes more prominent.

At low field strengths, this frequency shift is negligible compared with the imaging bandwidth and there is no observable overlapping of structures. However, due to the difference in frequencies, a phase shift develops between the signals from fat and water, as the NMR signal evolves. A symmetric spin echo sequence cancels the phase shifts developed. For a field echo sequence however, the phase shift increases linearly, throughout the period of evolution, so that at the time of the echo, TE, the phase shift, ϕ, is given by,

$$\phi \propto \gamma\sigma B_o TE.$$

If TE is sufficiently long for the phase shift to be close to π, the signal from voxels which contain a fat/water boundary is reduced. This gives rise to the appearance of dark lines on field echo images at fat/water boundaries.

2.7.2. Magnetic Susceptibility

The magnetic susceptibility, χ_m, of a material causes changes in the local magnetic field strength, due to the magnetisation induced in the material by the magnetising field H_o. The effect can be either paramagnetic, which increases the local field strength (χ_m is +ve), or diamagnetic, which decreases the local field strength (χ_m is -ve). The resultant local magnetic field strength is given by

$$B_o = \mu_o (H_o + \chi_m) \quad .$$

This change in local field strength gives rise to a change in the Larmor frequency, and so a phase shift develops in the same way as the chemical shift. For this reason, the two effects cannot be easily distinguished.

Appendix III

Existing Techniques for Blood Flow Measurement

A3.0. Introduction

This appendix gives a brief overview of the major techniques in existence, which are used for flow measurement. In each case, details of the method are given and the accuracy and limitations of each technique are indicated. Two of the measurements, performed using these techniques to assess cardiac function, are those of ejection fraction and cardiac output. These are defined as follows: The left ventricular (LV) ejection fraction (EF) is a dimensionless quantity, giving the ratio of the volume of blood ejected from the left ventricle in each cardiac cycle (the stroke volume), to the volume of the LV chamber at end-diastole, ie:

$$EF = \frac{\text{(end-diastolic LV volume) - (end-systolic LV volume)}}{\text{(end-diastolic LV volume)}}$$

$$= \frac{\text{Stroke Volume}}{\text{(end-diastolic LV volume)}}$$

The cardiac output is related to the stroke volume by the heart rate, such that,

$$\text{Cardiac Output} = \text{Stroke volume} \times \text{Heart rate}$$

A3.1. Plethysmography

Plethysmography is one of the oldest techniques used to measure blood flow. The measurement is performed by detecting a change in volume of the whole, or segment, of a limb during a temporary occlusion of the venous drainage from that limb (Woodcock, 1986; Terry, 1986). The original form of the technique involves placing the limb in a rigid chamber filled with water or air. During venous occlusion, the limb expands and the displacement of fluid gives a direct measure of the change in volume from which the blood flow rate to the limb can be calculated. Whilst this method, known as direct-volume displacement plethysmography, is simple to use, there are a number of problems relating to its accuracy. If a water-filled chamber is used, the hydrostatic effect of the water may reduce the blood flow into the limb. Alternatively, the high coefficient of expansion of air can cause baseline drift if an air filled-tube is used.

In strain-gauge plethysmography, a strain-gauge consisting of a thin, mercury-filled, rubber tube can be used to measure the change in circumference of the limb. As the gauge is stretched by the expanding limb, the resistance of the gauge changes. The change in volume is inferred by assuming that the limb has cylindrical symmetry.

The change in volume of the limb can also be measured indirectly, by impedance plethysmography and capacitance plethysmography. However, fluid-displacement plethysmography and strain-gauge plethysmography are the most accurate and widely used methods. Impedance plethysmography can be used to monitor changes in cardiac output non-invasively (Lorimer et al, 1986). One general disadvantage of plethysmography is that the subject must lie still during the measurement.

A3.2. Tracers

Tracers have been used to measure the blood flow to organs for over a century. Initially, coloured dyes were used, but they have now largely been replaced by the use of radioisotopes. The principles of use for both these tracers are similar, although the methods used to measure the tracer concentrations are different. Various methods have been developed. The earliest and most basic methods used the Fick principle, based on the law of conservation of matter, which states that the blood flow through an organ can be estimated if a measurable substance is either removed, or added, as blood flows through it (Lorimer et al, 1986). Either the total blood flow to an organ can be measured, or the organ perfusion (flow per unit mass) can be measured using tracer techniques. Tracer methods generally require an injection of the

tracer into the blood stream. One exception to this is in the estimation of cardiac output by measuring the difference in oxygen concentration between systemic arterial blood and venous blood taken from the pulmonary artery. (Lorimer et al, 1986). Oxygen consumption is measured by spirometric collection of expired air.

A3.3. Indicator Dilution Method

Cardiac output can be calculated by measuring the dilution of indicators which have been introduced into the blood stream in a central vein, either by continuous infusion or by a bolus injection (Lorimer et al, 1986). If continous infusion is used, the concentration is measured within the pulmonary artery, until a plateau level of maximum concentration is reached. The flow rate can then be deduced from the known rate of infusion. If a bolus injection is used, a 'concentration-versus-time' curve (dilution curve) is obtained. The area under this curve is found and by knowing the amount of indicator injected the flow rate can be calculated. The indicator dilution method also applies to any vessel or organ where mixing of the indicator with blood occurs (Terry, 1986). Dyes such as indocyanine green are used as indicators and their concentration in the blood stream can be measured by withdrawing blood through a sampling cuvette and obtaining absorption spectra, or by using optical fibres.

A3.4. Thermodilution

A thermal indicator, such as cooled saline, can be used instead of dye, to measure cardiac output (Lorimer et al, 1986). The saline is injected through a catheter into the blood entering the heart. The dilution curve is obtained by recording the temperature, as measured by a thermister at the tip of a catheter, inserted into the pulmonary artery. In order to calculate the cardiac output, the specific heats and gravities of the blood and the injectate must be known and the baseline temperature of the blood must be accurately determined. This technique is easy to use and is fairly safe, but there are many potential problems related to its accuracy.

A3.5. Indicator Clearance Method

Volume flow rates can be deduced by measuring the rate at which an indicator is removed from an organ or region of the body (Terry, 1986). Tissue perfusion can be measured using this method, by injecting a radioisotope tracer, indicator, such as Xenon 133 dissolved in saline, into tissue. The observed rate of radioactive decay within that region is proportional to the perfusion of the tissue. The method of thermal clearance can also be used in which a thermistor which has been embedded in tissue is kept at a constant temperature, which is a few degrees

above body temperature. The electrical power required to maintain this temperature, is proportional to the perfusion of that region of tissue.

A3.6. Hot Film Anemometry

The same principle of the thermal clearance method described above can be used to determine the velocity profile within a vessel. In this case, a thin film resistor, mounted at the tip of a needle, is inserted into the vessel and is advanced across the vessel diameter (Terry, 1986). The variation in power required to keep the resitor at a constant temperature at different points across the vessel, reflects the velocity profile.

A3.7. Cardiac Function by Radioisotope Imaging

The use of radioisotope imaging to assess cardiac function, by the measurement of the left ventricular ejection fraction, is now well established (Martin, 1986). The radioisotope, normally technetium 99m pertechnetate, is injected into the blood pool. Two techniques may then be employed to image the heart, both using gamma cameras. In the first, know as the first-pass method, the first passage of the isotope through the

right and left sides of the heart is rapidly recorded. A time-activity curve is obtained from a fixed region-of-interest, placed over the left ventricle, from which functional data can be derived. This technique is highly dependent on the integrity of the bolus, and on the definition of the region-of-interest boundaries.

The second technique is known as the dynamic recording method or, alternatively, as the multigate acquisition blood pool scanning method. In this case, the heart is scanned over many heart beats and the acquisition of data is gated, or synchronised, with the cardiac cycle so that a separate image 'frame' is obtained for each phase of the cycle. The activity within the left ventricle is obtained from regions-of-interest positioned on the images, which correspond most closely to end-systole and end - diastole. The ejection fraction can then be calculated. With this technique, the background count is high and it is difficult to delineate the boundary of the left ventricle.

Ventricular volumes can be estimated from the images acquired by both these methods, making it possible to estimate stroke volume and cardiac output. As with all radionuclide studies, these methods involve a small radiation dose to the subject.

A3.8. Regional Cerebral Blood Flow Measurement

Radionuclide techniques have also been developed to measure regional cerebral blood flow (rCBF), (Jones, 1986). The two main imaging techniques developed are tomographic and therefore, they have the potential to allow distribution of regional perfusion within brain tissue to be mapped out. Single photon emission computed tomography, (SPECT), can be performed either by using a special tomographic scanner or a rotating-head gamma camera. In both cases, the detectors rotate about the subject in order to obtain multiple views of the head from which tomographic images can be reconstructed.

The isotope originally used for SPECT imaging of cerebral blood flow was Xenon 133, although other isotopes have been used more recently. None of the tracers used so far have the ideal properties for this application. Flow rates are determined by observing the rate of clearance from cerebral tissue. The images have a poor signal-to-noise ratio and there are many sources of error in the estimation of flow rates, including those caused by tracer re-circulation and scattered radiation.

Positron emission tomography (PET) has been used to image up-take of the inert tracer, oxygen-15-labelled water, in cerebral tissue. The technique is non-invasive since the oxygen 15 is introduced by continuous inhalation of

$C^{15}O_2$. It then transfers to water molecules in the lungs, and is carried by the circulation to the peripheral tissues. The arterial concentration and cerebral tissue concentration reach equilibrium and the regional blood flow can be derived from these relative concentrations. Regional cerebral blood flow has also been determined from first-pass and rate-of-clearance measurements using PET. The main drawback of this technique is that it is expensive: an on-site cyclotron is required to produce the short-lived oxygen 13 isotope, and a specialised PET scanner is required to obtain the tomographic data.

A3.9. Electromagnetic Induction

Flowmeters, using the principle of eletromagnetic induction, have been used to measure blood flow in vessels for over 20 years. The flowmeter applies a uniform magnetic field across the vessel, at right angles to the direction of flow (Terry, 1986). Because blood is an electrical conductor, a potential difference, which is proportional to the mean flow velocity, is induced across the vessel, in a direction which is perpendicular to both the direction of flow and the direction of the magnetic field. Two main types of flowmeter probe are used: the cannulating-type probe is a rigid tube, which is plumbed directly into the vessel being measured. The cuff-type probe fits around the outside of the intact vessel wall.

Whilst the cuff-type probe is less invasive than the cannulating-type probe, its accuracy is dependent on the conductivity of the blood and the vessel wall. If the flow is not symmetrical about the vessel axis, large errors can occur with both types of probe. Flowmeters which are mounted on catheter tips can also be used, but they produce signals which are dominated by the flow velocities closest to the probe. It is therefore difficult to calculate the mean flow in the vessel using this type of probe.

A3.10. Doppler Ultrasound

The measurement of blood flow velocity by ultrasound is based on the Doppler effect (Wells, 1986). A beam of ultrasound is directed by a transducer at an angle, θ, across the vessel being measured, and back-scattered ultrasound is detected by the same transducer. Ultrasound which is back-scattered from the red blood cells in flowing blood moving at a velocity, v, will have experiencd a Doppler frequency shift (i.e. the difference between the transmitted and received frequencies), given by

$$f_D = \frac{2vf_o}{c} \cos \theta$$

where f_o is the transmitted frequency and c is the speed of ultrasound in tissue. If continuous wave ultrasound

is used, back-scattered ultrasound is received from all the tissue and blood which lies within the path of the beam. However, it is possible to filter out ultrasound, back-scattered by stationary structures, by demodulating the received signal. The demodulator output only contains the Doppler shift frequencies received from moving blood. The transmitted frequency, f_o, is typically between 2 and 10 Megahertz, while the Doppler shift frequencies lie within the audio range.

One drawback of continuous wave ultrasound, is that the demodulated signal may include Doppler shift frequencies derived from a number of vessels which lie in the beam and there is no way of separating them. The technique of pulsed Doppler ultrasound allows range discrimination, in which a sensitive volume (known as the resolution cell) is defined, so that only signals which originate from this sensitive volume are accepted. To achieve this, the transmitted ultrasound is pulsed, and the receiver is gated. The length of the pulse defines the length of the sensitive volume, and the time between the transmission of the pulse and the gating of the receiver defines the position of the sensitive volume along the beam. The maximum pulse repetition rate is limited by the time taken for each pulse to return to the receiving transducer. This sets an upper limit on the maximum velocity that can be measured unambiguously. (The sampling rate must be at least twice maximum Doppler

shift frequency).

Once the Doppler frequency shift signals have been acquired, they are analysed to obtain both quantitative and qualitative information. It is possible to deduce the direction of flow, depending on whether the received frequency is higher, or lower, than the transmitted frequency. Spectral analysis of the signal, using fast Fourier transformation techniques, allows the frequency components of the signal, (corresponding to the velocities present), to be displayed as the signal is acquired. The energy density of the spectrum, reflects the amount of blood flowing at a given velocity. This information can be used to quantify flow rates, however, great care must be taken, as the energy density is also subject to attenuation by tissue lying between the transducer and the vessel, and the flowing blood may not be uniformly insonated across the vessel. An additional source of error is introduced when quantifying the total flow through a vessel since, most machines filter out low frequencies, to remove signals arising from vessel wall motion. This can also remove the contribution from low-velocity flow.

Volume blood flow rates within a vessel can be calculated, either by finding the diameter and average velocity in the vessel, or by spectral analysis. Methods which measure the diameter and average flow velocity can

be subject to large errors, as they assume cylindrical symmetry of the vessel, and any error in the diameter measurement is squared when calculating the area of the vessel. In general, the most reliable measurement that can be made with this technique is that of maximum velocity, although the accuracy of this measurement depends on how accurately the angle of the ultrasound beam to the direction of flow is known, especially when this angle is large.

The blood flow velocity waveforms, obtained using Doppler ultrasound, can be used to characterise arterial disease. The damping factor, of a suspect segment of an artery, can be calculated as the ratio of the pulsatility index, measured from waveforms obtained, from above and below the segment. This, combined with measurement of the transit time of the arterial pulse through the segment, can be used to classify the disease. Indices, relating to arterial stiffness and distal peripheral resistance, can also be obtained from the time-velocity waveform. Other indicators of disease are the ratio of systolic and diastolic velocities, and spectral broadening of the Doppler shift frequency during systole.

Cardiac function can be assessed using Doppler flow measurements, either by placing a Doppler probe in the suprasternal notch to measure flow in the ascending or transverse aorta, which reflects left heart function, or

by measuring flow in the jugular vein, which reflects right-heart function. Measurement of the maximum instantaneous blood flow velocity in the aorta can be used to obtain a curve of velocity versus time. Integration of this curve during the systolic phase of the cardiac cycle yields a quantity known as the Systolic Velocity Integral (SVI). Changes in the SVI reflect changes in the stroke volume and although an absolute measurement of stroke volume cannot be obtained, this measurement is useful to monitor sequential changes in acutely ill patients. Doppler ultrasound has also been useful in the study of aortic stenosis and coarctation, and in the study of ventricular septal defects.

A3.11. Echocardiography

Echocardiography is an ultrasonic imaging technique, which presents either a real-time, two-dimensional image through cardiac structures, or a one-dimensional display of cardiac structure, plotted against a time base (Lorimer et al, 1986). In the latter case, structures are recognised by their pattern of motion. Whilst echo-cardiography cannot be used to measure blood flow, cardiac function can be determined by the measurement of heart wall motion and cardiac dimensions. In particular, left ventricular dimensions determined by echo-cardiography can be used to caculate end-systolic and

end-diastolic volumes and cardiac output. This calculation, however, makes assumptions about the geometry of the left ventricle which may not be accurate, especially in diseased hearts. However, this technique has been found to correlate well with indicator dilution methods and angiography, although it has a tendency to underestimate ventricular volumes.

A3.12. Angiography

Angiography is a technique which is used to image the heart and great vessels, by injecting an x-ray contrast medium into the heart chamber or vessel under high pressure and recording the event on cine film or video tape (Cunningham, 1986). The technique can be used to assess left ventricular function by power-injecting contrast into the left ventricle, through a narrow bore catheter (35-50 mls in 2-3 seconds). Timing of the cine film exposure is often recorded, with respect to the cardiac cycle, using either the subject's ECG, or pressure curve, in order to identify the phase of the cardiac cycle corresponding to each frame. Information about the contractility of the ventricle and incompetence of the inlet valve can be obtained (Cunningham, 1986). Left ventricular chamber volume can also be calculated and the stroke volume can be calculated from the difference of the end-systolic and end-diastolic volumes.

Catheter injection of smaller amounts of contrast material into the coronary arteries, a technique known as coronary arteriography, allows areas of narrowing or total block to be located.

The large amount of contrast required to image the left ventricle can itself affect cardiac function as, the high viscosity and ionic content of the contrast medium can induce ectopic beats and lower the contractility of the heart muscle (Cunningham, 1986). This problem has been partially overcome by the use of non-ionic contrast media, and the advent of digital subtraction angiography (DSA) has reduced the amount of contrast medium required. With these techniques, there is a possibility that the coronary arteries will fill with contrast medium, starving the heart muscle of oxygen and causing a cardiac arrest, although the actual mortality rate is low.

A3.13. Pressure Measurement

Intravascular pressure measurement can give valuable information about the degree of stenosis in vessels. In particular, stenosis of the aortic valve can be assessed using cardiac catheterisation, by measuring intracardiac pressure above and below the valve (Simpson et al, 1985). The pressure gradient across the valve is an indication of the severity of the disease. Aortic valve stenosis

causes increased pressure in the left ventricle, causing ventricular enlargement and eventual heart failure. It is necessary to determine the severity of the disease, before any surgery is undertaken.

Intracardiac pressures are measured using catheters filled with fluid, (usually saline), which are connected externally to a pressure transducer (Cunningham, 1986). Problems can arise with fluid-filled catheters, due to an underdamped response for fast-rising pressure waveforms, which is seen as an excessive 'ringing' artefact on the waveform. More expensive catheter-tip transducers avoid these problems.

Appendix IV

Publications and Presentations

This appendix lists the publications and presentations arising from and associated with the work described in this thesis. Reprints of the publications are enclosed at the back of this thesis where stated.

Publications.

1. Ridgway, J. P. and Smith, M. A. A technique for velocity imaging using magnetic resonance imaging. British Journal of Radiology, 59, 603-607, 1986. (Reprint enclosed).

2. Ridgway, J. P., Turnbull, L. W. and Smith, M. A. Demonstration of pulsatile cerebrospinal-fluid flow using magnetic resonance imaging. British Journal of Radiology, 60, 423-427, 1987. (Reprint enclosed).

3. Amoore, J. N. and Ridgway, J. P. A system for cardiac and respiratory gating of a magnetic resonance imager. Clinical Physics and Physiological Measurement, 10, 283-286, 1989. (Reprint enclosed).

4. Smith MA, Ridgway JP, Brydon JWE, Been M, Douglas RHB, Kean DM, Muir AL, and Best JJK. ECG gated Tl images of the heart. Phys. Med. Biol., 3, No 7, 771-778,

1986. (Reprint enclosed).

5. Been M, Smith MA, Ridgway JP, Brydon JWE, Douglas RHB, Kean DM, Best JJK, and Muir AL. Characterisation of acute myocardial infarction by gated magnetic resonace imaging. Lancet ii, 348-350, 1985.

6. Been M, Smith MA, Ridgway JP, Douglas RHB, De Bono DP, Best JJK, and Muir AL. Serial Changes in the T1 magnetic resonance relaxation parameter after myocardial infarction in man. Br. Heart J., 59, 1-8, 1988.

7. Turnbull LW, Ridgway JP, Smith MA, and Best JJK. MRI flow imaging: A possible method for distinguishing communicating syringomyelia from cystic intraspinal lesions. Brit. J. Radiol., 60, 517-518, 1987. [Letter].

Published Abstracts of Presentations

1. Ridgway JP, Turnbull LW, and Smith MA. A phase imaging technique and its use to measure low velocities in pulsatile CSF flow. Proc. 3rd Europ. Soc. Mag. Res. in Med. and Biol., Aberdeen 205, 1986.

2. Ridgway JP and Smith MA. A technique for velocity imaging using magnetic resonance imaging. Abstracts of the 44th Annual Congress of the BIR, Bristol, Brit. J. Radiol. 59, 817, 1986. [A]

3. Ridgway JP, Turnbull LW, and Smith MA. A phase imaging technique and its use to measure low velocities in pulsatile CSF flow. Proc. 5th Annual Meeting of Soc. Mag. Res. in Medicine, Montreal, 108-109, 1986.

4. Ridgway JP, Turnbull LW, Allan PL, Hoskins P and Best JJK. A quantitative comparison of velocity waveforms obtained in the common carotid artery using MR phase imaging and Doppler ultrasound. Works in Progress abstracts of the 7th Annual Meeting of the Society of Magnetic Resonance in Medicine, San Francisco, 146, 1988.

5. Amoore JN and Ridgway JP. A system for cardiac and respiratory gating of magnetic resonance images. Abstracts of the 45th Annual Conference of the HPA/IPSM, Canterbury, Kent, September 1988.

1986, *The British Journal of Radiology*, 59, 603–607 JUNE 1986

Technical note

A technique for velocity imaging using magnetic resonance imaging

By J. P. Ridgway, B.Sc., M.Sc. and M. A. Smith, B.Sc., M.Sc., Ph.D.

NMR Imaging Unit and Department of Medical Physics & Medical Engineering, University of Edinburgh, Royal Infirmary, Edinburgh

(*Received October 1985 and in revised form December 1985*)

Magnetic resonance imaging (MRI) is becoming well established as a technique which both shows anatomy and allows tissue characterisation. A further development of the technique allows the imaging of regular movement such as blood flow and cardiac wall motion. In particular, much effort has been put into developing techniques for imaging flowing blood and deducing such parameters as velocity and acceleration.

Early work by Singer (1959) described a technique of blood flow velocity measurement using a "time-of-flight" method. Velocity images have been obtained by this method using a modified version of a spin-echo pulse sequence (Feinberg et al, 1984). Normally, a slice is excited using a selective 90° radio-frequency (RF) pulse and an echo is produced at a later time by applying a selective 180° pulse to the same slice. If moving hydrogen nuclei have, in the meantime, moved out of the slice, no signal will be returned from them, resulting in a reduction in signal intensity from blood vessels in the image. This is the spin washout effect. If, however, the 180° RF pulse is applied to a slice downstream, an echo signal will be returned from excited nuclei having a velocity such that they coincide with the second slice selection. In this way, a series of images can be obtained, each corresponding to a certain range of velocities.

The standard spin-echo technique can also be exploited to produce flow-dependent signals in vessels (Axel, 1984; Bradley et al, 1984; Waluch & Bradley, 1984). The effect, known as paradoxical enhancement, results in vessels appearing to have a much higher intensity than the surrounding tissue. This effect becomes particularly noticeable for shorter repetition times since freshly saturated nuclei moving into the slice will give a stronger signal relative to the surrounding stationary tissue, which is only partially saturated.

In a multi-echo sequence a phenomenon known as even-echo rephasing is also present (Waluch & Bradley, 1984). The magnetic field gradient (subsequently referred to as the gradient) used for slice selection and the gradient used for readout are applied twice in a spin-echo sequence. The first time they are applied, nuclei dephase along the direction of the gradient; the second time, they are applied with opposite polarity and nuclei move back into phase along that direction. If the nuclei are stationary then they will move back exactly into phase with one another; however, if nuclei are moving along a gradient direction they will have a phase shift at the first echo, having only partially rephased. This phase shift will be linearly dependent on their velocity. All nuclei having the same velocity will have the same phase shift on odd echoes but will have zero phase shift on even echoes, the effect of the gradients having been reversed provided the velocity is constant. Thus, flow can be identified by comparing first and second echo images. On the first echo, flowing blood will appear to have a reduced signal while, on the second echo, the signal will be of higher intensity. We are, of course, neglecting dephasing effects caused by spin-spin relaxation.

Since the non-zero phase shift on the first echo is linearly dependent on velocity, it can be used to measure velocity directly (Bryant et al, 1984; Moran & Moran, 1984; Redpath et al, 1984; Van Dijk, 1984; Moran et al, 1985; Wedeen et al, 1985). In most MRI systems the signal is collected from two channels in quadrature, yielding a real and an imaginary data set. These are usually combined to calculate a modulus image used for diagnosis. These two data sets can, however, be used separately to produce a real or an imaginary image, or can be combined to calculate a phase image. All three of these contain phase information which is normally discarded in the calculation of the modulus image and it is this information which provides a way of imaging velocity.

Although real and imaginary images have been used to demonstrate imaging of velocity, they also contain spin-density information (Moran et al, 1985). The phase image is easiest to interpret and quantify since it contains only motion information and represents a direct linear map of a single velocity component. In order to quantify the velocity measurements accurately, standard spin-echo and field-echo sequences have been modified by adding extra gradient pulses in the direction of required velocity measurement.

To date, this has been done in two ways (Moran et al, 1985); either two identical gradient pulses separated by a 180° RF pulse are inserted, or a bipolar pulse consisting of two successive gradient pulses equal in magnitude and duration but of opposite sign is inserted into the pulse sequence between the 90° RF pulse and the readout gradient. The first of these

gradient pulses dephases the nuclei in the applied direction and the second pulse rephases them. Stationary nuclei are all brought back into phase, whereas for nuclei moving along the gradient the rephasing is not complete, leaving them with a phase shift proportional to velocity.

The accuracy of the technique is dependent on the two gradient pulses having exactly the same duration and magnitude over the imaging volume and on the uniformity of the RF, gradient and static fields. A non-uniform field will introduce a spatially dependent phase shift over the image (McVeigh et al, 1985; Norris, 1985b). A technique has been developed (Redpath et al, 1984) to overcome these difficulties by varying the size of the flow-encoding pulses for a number of data acquisitions and applying a 3D Fourier transform technique to the whole set of data. The resultant set of images will be coded in intensity, each corresponding to a certain velocity range, and may be used to reconstruct a simple velocity-coded image. A further limitation of the techniques is that velocities corresponding to a phase shift of greater than $+180°$ or less than $-180°$ will lead to an ambiguity of velocity measurement. This can be avoided by adjusting the magnitude of the gradient so that the resultant phase shifts lie within the range of $\pm 180°$. This paper presents a technique which uses the calculated phase image as a direct measurement of velocity. The problem of field non-uniformity is avoided by using two separate pulse sequences and subtracting the resultant phase images.

METHOD

The technique has been integrated into the standard spin-warp imaging sequence (Edelstein et al, 1980) used on an M&D 0.08 T resistive MRI system (Smith et al, 1984). The slice selection gradients, which are effectively of bipolar form, were initially used to provide the phase encoding for velocity components perpendicular to the imaging slice (Fig. 1). In order to avoid the appearance of phase shifts due to the spatial non-uniformities of the fields, two pulse sequences were used to produce two phase images which were subtracted to produce the final velocity image. The two pulse sequences were identical except that the timing of the rephasing gradient was later in one than in the other. Phase errors due to the time-independent inhomogeneities in the main field and the RF field would be the same in each case and would, thus, cancel in the final subtracted image. The only remaining phase differences are due to motion, such that for a given velocity component, v, in the direction of the applied slice selection gradient, G, the phase difference is:

$$\phi_{\text{diff}} = -\gamma G v t_w t_{\text{diff}}$$

where t_w is the duration of the rephasing pulse, t_{diff} is the difference in pulse separation for the two pulse sequences, and γ is the gyromagnetic ratio for protons (Fig. 1).

All the computer processing is performed within the acquisition program so that the subtracted phase images are displayed 8 s after acquisition. An ungated velocity image can be obtained in 64 s using a repetition time (TR) of 250 ms. For *in-vivo* imaging, however, the pulse sequences are gated (Been et al, 1985) in order to look at an instantaneous velocity, and consequently the imaging time is dependent on the heart rate. Typically, one section will take about 4 min. The two pulse sequences are interlaced so as to reduce the effects of gross patient movement between scans. The magnitude of the flow pulse gradient, G, is 1.25 mT m^{-1}. For the studies described here, the flow pulse timing was such that $t_{\text{diff}} = 2$ ms and $t_w = 2.4$ ms. The velocity sensitivity can be increased simply by increasing t_{diff}.

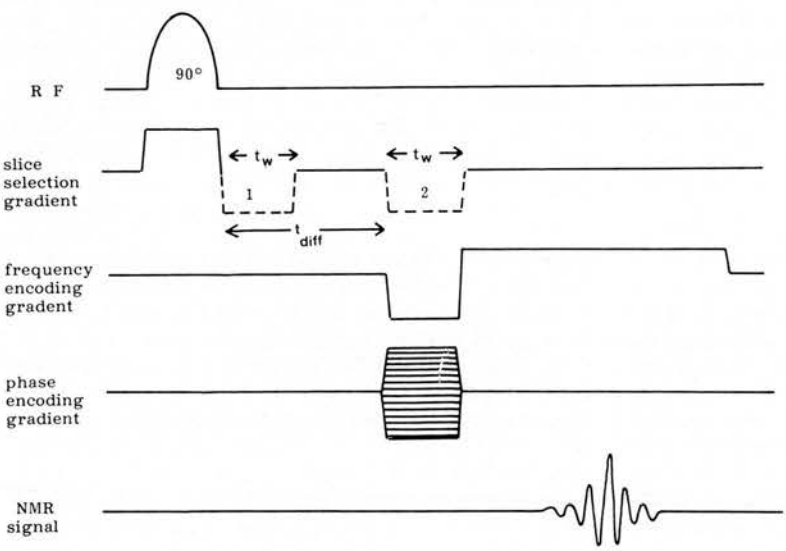

FIG. 1.

A simple adaption of the Aberdeen spin-warp pulse sequence for imaging of velocity through the slice by varying the position of the rephasing gradient (broken line) between positions 1 and 2. Two corresponding phase images are produced and then subtracted to produce the velocity-coded image.

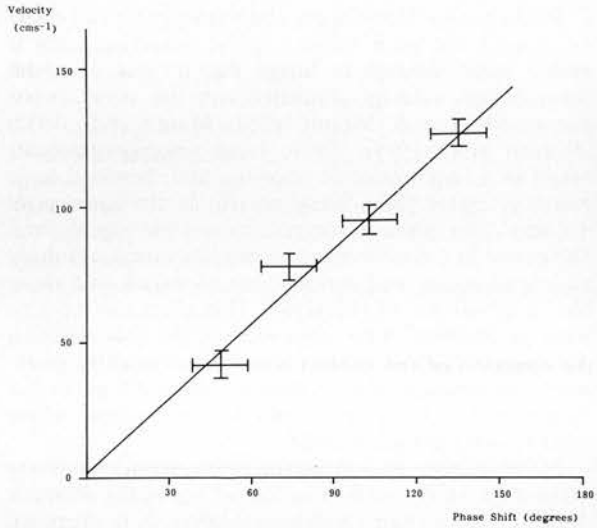

FIG. 2.

Velocity calibration of the flow measurement technique using the pulse sequence in Fig. 1.

Velocity measurements have been calibrated using a simple flow phantom consisting of a 1 cm-inside diameter polythene tube surrounded by a bath of 2.5 mM solution of copper sulphate. The same solution of copper sulphate was pumped through the tube at various known constant rates. The mean flow velocity for the tube was calculated and calibrated against the mean phase shift found within the tube. A number of normal volunteers have been imaged in the neck, thorax and abdomen using the interlaced gated sequence. An initial comparison with continuous wave Doppler ultrasound at 2.5 MHz has been carried out in the abdominal aorta using a Hewlett Packard 77020 Doppler imaging system. Using MRI, a number of delays were used from the electrocardiogram R-wave in order to plot the velocity in the abdominal aorta over the systolic period of the heart cycle. The sample volume for this measurement was taken at the centre of the aortic diameter.

RESULTS

The calibration of the velocity measurement shows a good linear relationship between velocity and phase shift (Fig. 2). Three examples of the volunteer studies are shown in Fig. 3. These images display zero phase shift as mid-grey, positive phase shift of 180° as white and negative phase shift of 180° as black. Where the values in the modulus image are below a certain threshold the phase values are not calculated.

Figure 4 shows the velocity measurements taken in the abdominal aorta compared with those taken from continuous-wave Doppler ultrasound measurements. There is a good agreement in profile shape and timing, although the velocities appear to be lower in the case of the Doppler measurements.

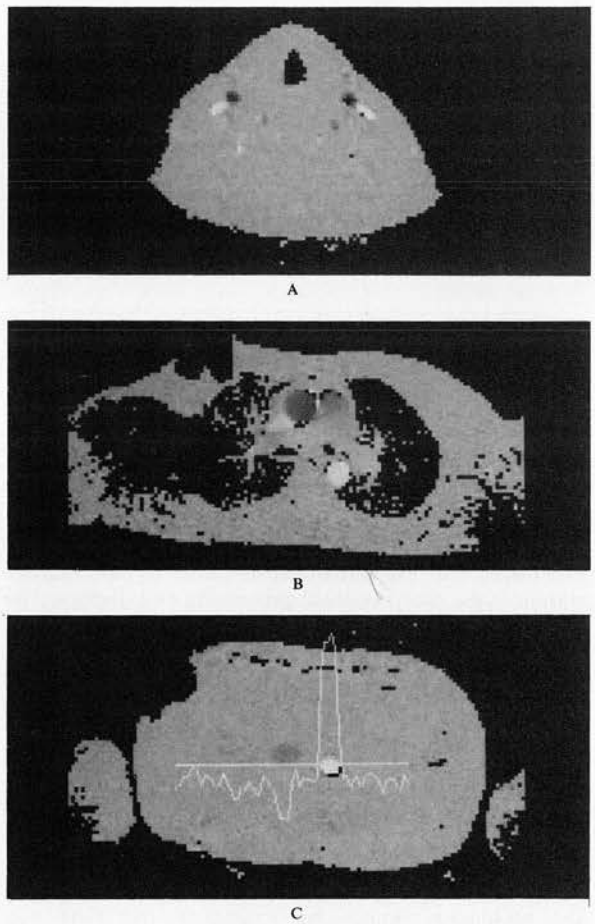

FIG. 3.

(A) A flow image of the neck using the pulse sequence of Fig. 1. This image demonstrates the common carotids and the vertebral arteries as the darker vessels, corresponding to a negative phase shift, and the jugular veins as the lighter vessels, corresponding to a positive phase shift. The surrounding stationary tissue is displayed as mid-grey. (B) A flow image of the thorax showing the ascending and descending aorta. (C) A flow image of the abdomen showing aorta and inferior vena cava. A line profile through both vessels clearly shows the differences in velocities.

DISCUSSION

It has been shown that velocity measurements are possible on the low field imaging system at Edinburgh with changes only to the pulse sequence and software and without any improvements required on the field homogeneity.

This technique, using phase as a direct measurement of velocity, has advantages over the other techniques

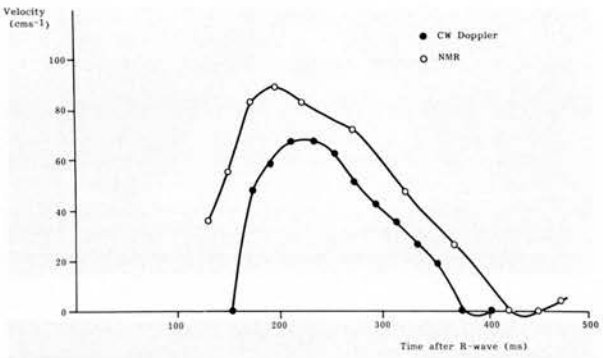

FIG. 4.

A velocity flow profile of the systolic period of the heart cycle for the abdominal aorta comparing the results from 11 flow images as shown in Fig. 3c, with results from Doppler ultrasound measurements.

mentioned in the introduction due to its relative simplicity in interpretation, processing and display. The time-of-flight method is restricted to imaging of one particular velocity range per image. Paradoxical enhancement and even echo rephasing are not quantitative measures of flow and can only be used to identify whether flow is present. The 3D Fourier transform method requires many flow encoding stages, whereas the technique described here requires only two sections to produce the final velocity image.

Initially, high flow velocities are being examined since they occur in the larger, better defined vessels. Lower velocities of the order of 1 cm s^{-1} have been imaged by the technique simply by extending the time t_{diff}. However, if this becomes too large then inhomogeneities in the field lead to loss of signal from the imaging slice, so it would be necessary instead to increase the magnitude of the flow gradient.

While peak velocity in the abdominal aorta can easily be imaged, the peak velocity in the ascending aorta is rather more difficult to image due to loss of signal around high velocity gradients over the vessel cross-section (Moran & Moran, 1984; Moran et al, 1985; Wedeen et al, 1985). These large velocity gradients result in a large range of velocities and, hence, a large range of phase shifts being present in the same pixel volume. This phase dispersion causes the signal from the nuclei in the same pixel volume to cancel, resulting in loss of signal, and is often seen as a dark line along the inner surface of the vessel. This effect can be seen even in standard pulse sequences, as the slice selection and signal readout gradients induce accidental phase shifts for nuclei moving in their direction. Of particular importance is the case of mitral-valve stenosis where high-velocity jets are present.

Methods have been suggested to overcome the phase dispersion which causes this loss of signal (Le Roux & Floch, 1985; Pattany & Naylor, 1985). It is proposed to use an adaption of the compensating bipolar pulse technique suggested by Le Roux and Floch, modifying it for use with the basic spin-warp pulse sequence. The compensating bipolar pulse is of opposite polarity to that already in the sequence, so that the dephasing effect is reversed. Figure 5 shows the suggested pulse sequence for use in further work, incorporating compensating bipolar pulses into the technique in all three directions. At present, this is not possible to do due to hardware limitations, although it is hoped to implement it in the near future.

It has already been shown (Norris, 1985a) that double bipolar pulses can be used to image acceleration. The greater the separation between the bipolar pulses, the greater the phase shift for a given acceleration. Thus, phase shifts due to acceleration can be minimised by merging the two middle pulses of the double bipolar flow pulse into one. The velocity measurement is achieved by varying the position in time

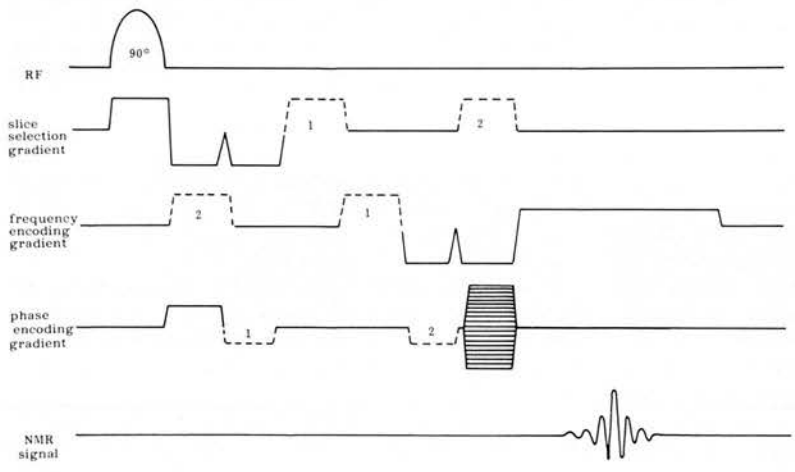

FIG. 5.

A further adaption of the flow pulse sequence of Fig. 1 for measurement of blood flow velocity in all three orthogonal directions. The gradient pulse sequences in the slice selection and frequency encoding directions have two bipolar pulses to compensate for the phase dispersion found in the normal imaging sequence.

of the broken line pulses in Fig. 5 between positions 1 and 2. Using the previous notation, the expression for phase shift is given by:

$$\phi_{diff} = \gamma G v t_w t_{diff} + \gamma G a t_w (7 t_w t_{diff} + t_{diff}^2)$$

where a is the constant acceleration.

Thus, for conditions where maximum acceleration occurs *in vivo* (200 cm s^{-2}) this would produce at most a 10% error in velocity measurement, given that typical velocities at this point are around 50 cm s^{-1}.

It is proposed to extend the technique to the measurement of flow in all directions in all phases and to pursue further volunteer studies and initial clinical trials. The technique will be compared directly with results from Doppler ultrasound measurements where possible.

ACKNOWLEDGMENTS

We would like to thank Dr W. N. McDicken and Dr M. Been for advice and assistance with the Doppler ultrasound measurements. We would also like to thank Mrs C. N. Rowan for secretarial services and Mr I. Lennox of the Department of Medical Illustration. This research is generously funded by a grant from the Scottish Home and Health Department. Finally we wish to thank Professor J. J. K. Best, Dr D. M. Kean, Ms R. H. B. Douglas, Mrs A. Blane and Mr P. Hoskins for their helpful comments and support.

REFERENCES

AXEL, L., 1984. Blood flow effects in magnetic resonance imaging. *American Journal of Roentgenology, 143,* 1157–1166.

BEEN, M., SMITH, M. A., RIDGWAY, J. P., BRYDON, J. W. E., DOUGLAS, R. H. B., KEAN, D. M., BEST, J. J. K. & MUIR, A. L., 1985. Characterisation of acute myocardial infarction by gated magnetic resonance imaging. *Lancet, ii,* 348–350.

BRADLEY, W. G., WALUCH, V., LAI, K. S., FERNANDEZ, E. J. & SPALTER, C., 1984. The appearance of rapidly flowing blood in magnetic resonance images. *American Journal of Roentgenology, 143,* 1167–1174.

BRYANT, D. J., PAYNE, J. A., FIRMIN, D. N. & LONGMORE, D. B., 1984. Measurement of flow with NMR imaging using a gradient pulse and phase difference technique. *Journal of Computer Assisted Tomography, 8,* 588–593.

EDELSTEIN, W. A., HUTCHISON, J. M. S., JOHNSON, G. & REDPATH, T. H., 1980. Spin warp imaging and applications to whole body imaging. *Physics in Medicine and Biology, 25,* 751–756.

FEINBERG, D. A., CROOKS, L., HOENNINGER, J., ARAKAWA, M. & WATTS, J., 1984. Pulsatile blood velocity in human arteries displayed by magnetic resonance imaging. *Radiology, 153,* 177–180.

LE ROUX, P. & FLOCH, J., 1985. Cancellation of the shear rate influence on flow velocity imaging. In *Proceedings of the Fourth Annual Meeting of the Society of Magnetic Resonance in Medicine, London, August 19–23, 1985,* pp. 585–586.

MCVEIGH, E. R., HENKELMAN, R. M. & BRONSKILL, M. J., 1985. Spatial dependence of phase in MR images. In *Proceedings of the Fourth Annual Meeting of the Society of Magnetic Resonance in Medicine, London, August 19–23, 1985,* pp. 1248–1249.

MORAN, P. R. & MORAN, R. A., 1984. Imaging true motion velocity and higher order motion quantities by phase gradient modulation techniques in NMR scanners. In *Technology of Nuclear Magnetic Resonance.* Ed. by P. D. Esser & R. E. Johnston (Society for Nuclear Medicine Inc., New York), pp. 149–166.

MORAN, P. R., MORAN, R. A. & KARSTAEDT, N., 1985. Verification and evaluation of internal flow and motion. *Radiology, 154,* 433–441.

NORRIS, D. G., 1985a. Acceleration by NMR. In *Proceedings of the Fourth Annual Meeting of the Society of Magnetic Resonance in Medicine, London, August 19–23, 1985,* pp. 593–594.

NORRIS, D. G., 1985b. Phase errors in NMR images. In *Proceedings of the Fourth Annual Meeting of the Society of Magnetic Resonance in Medicine, London, August 19–23, 1985,* pp. 1037–1038.

PATTANY, P. M. & NAYLOR, G. L., 1985. High velocity flow imaging by even echo rephasing. In *Proceedings of the Fourth Annual Meeting of the Society of Magnetic Resonance in Medicine, London, August 19–23, 1985,* pp. 599–600.

REDPATH, T. W., NORRIS, D. G., JONES, R. A. & HUTCHISON, J. M. S., 1984. A new method of NMR flow imaging. *Physics in Medicine and Biology, 29,* 891–898.

SINGER, J. R., 1959. Blood flow rates by nuclear magnetic resonance measurements. *Science, 130,* 1652–1653.

SMITH, M. A., BEST, J. J. K., DOUGLAS, R. H. B. & KEAN, D. M., 1984. The installation of a commercial resistive NMR imager. *British Journal of Radiology, 57,* 1145–1148.

VAN DIJK, P., 1984. Direct cardiac NMR imaging of heart wall and blood flow velocity. *Journal of Computer Assisted Tomography, 8,* 588–593.

WEDEEN, V. J., ROSEN, B. R., CHESLER, D. & BRADY, T. J., 1985. MR velocity imaging by phase display. *Journal of Computer Assisted Tomography, 9,* 530–536.

WALUCH, V. & BRADLEY, W. G., 1984. NMR even echo rephasing in slow laminar flow. *Journal of Computer Assisted Tomography, 8,* 594–598.

Book review

Radionuclide Imaging Techniques. By Peter F. Sharp, Philip P. Dendy and W. Ian Keyes, pp. 271, 1985 (Academic Press Inc. London), £58.00/$63.50 Hardback, £29.50 Paperback.
ISBN 0–12–639020–7

This latest book in the *Medical Physics* series covers the fundamentals of radionuclide imagings and the current state of scientific and technical developments. It has been written by three physicists who have clearly given much thought to concepts and the logical presentation of relevant material. The result is a work which is refreshingly original and yet very practical.

The nature of "The Imaging Problem" is described in a chapter which presents the physical, mathematical and radiochemical principles illustrated by well chosen examples of applications. Imaging systems are explained with the help of many clear diagrams, and the development of the gamma camera is traced to the most recent advances. An interesting chapter devoted to "Other Imaging Devices" includes such developments as the semi-conductor array and the multiwire proportional chamber. Particular attention is given to the measurement of performance with full description of theory and practice and examples of modern results.

Tomography is covered with a concise account of reconstruction theory (including attenuation correction), and of practical implementations, including positron techniques. The chapter on image display includes a thorough treatment of image evaluation methods, describing the use of receiver operating characteristic (ROC) curves. Many aspects of data analysis are classified and explained, and a critical account of methods of quantifying radionuclide uptake is given. There is a good discussion on the evaluation of clinical effectiveness, in which problems of trial design, analysis of results and comparison of techniques are carefully considered. Finally, a thoughtful chapter on "The Future" echoes and amplifies the useful concluding remarks to previous chapters.

The authors have achieved consistent clarity of style, and succeed in presenting an up to date and well referenced review of the subject. It should be read by every physicist entering this field and will be useful to many (of whatever discipline) as a source of information, explanation and stimulation.

R. A. SHIELDS

1987, *The British Journal of Radiology*, 60, 423–427

VOLUME 60 NUMBER 713 MAY 1987

The British Journal of Radiology

Demonstration of pulsatile cerebrospinal-fluid flow using magnetic resonance phase imaging

By J. P. Ridgway, B.Sc., M.Sc., L. W. Turnbull, B.Sc., M.B.Ch.B., F.R.C.R. and M. A. Smith, B.Sc., M.Sc., Ph.D.

NMR Imaging Unit, Department of Medical Radiology and Department of Medical Physics & Medical Engineering, University of Edinburgh, Royal Infirmary, Edinburgh

(*Received March 1986 and in revised form November 1986*)

ABSTRACT

The study of pulsatile cerebrospinal-fluid (CSF) flow may be useful in diagnosis of certain forms of intracranial disease. Previous techniques used to study CSF flow either are invasive or do not allow accurate measurement. Magnetic resonance imaging (MRI) offers a non-invasive method of studying the CSF pathways. Our technique uses MR phase images and allows quantitative measurement of flow velocities and volume-flow rates. Four volunteers were studied at the level of the second cervical vertebra (C2). The MRI pulse sequence was gated from the R-wave of the subject's electrocardiogram and 12 scans were taken corresponding to different times in the cardiac cycle. The variation in flow velocity throughout the cycle was plotted, and maximum caudad and cephalad flow velocities and flow rates were calculated. Good agreement was found between three of the four volunteers. The mean maximum caudad velocity was 2.91 cm s^{-1} occurring at a mean time of 190 ms after the R-wave. This corresponds to a mean maximum flow rate of 4.13 ml s^{-1}. The total imaging time for each study was about 1 h. Technical developments, allowing simultaneous acquisition of several images throughout the cardiac cycle, will reduce this time significantly.

The cerebrospinal-fluid (CSF) pathways are particularly difficult to study, and to obtain reliable information the haemodynamic conditions must not be altered, for example, by surgical intervention. Radiologists have, for a long time, been aware of the pulsatile nature of CSF flow at fluoroscopy during Pantopaque myelography and in cineradiology of myelography and encephalography (du Boulay, 1966; du Boulay et al, 1972). Estimations of CSF flow using these techniques, which were derived from observation of a television monitor, were inevitably imprecise.

The appearance of flowing fluid using magnetic resonance imaging (MRI) has been the subject of much research, and various techniques have been developed to demonstrate the velocity of blood flow. The effects of blood flow on magnetic resonance (MR) images are dependent on the pulse sequence used, and on the velocity profile of the flow. They can be interpreted as either an increase or decrease in signal compared with stationary material (Axel, 1984; George et al, 1984). The precise variation in signal intensity as a function of velocity is dependent on many factors and is thus difficult to predict.

The nuclear magnetic resonance signal has two components which are referred to as the real and imaginary parts of the signal. These two components can be used to calculate both the modulus and the phase of the signal for each pixel. It is the modulus value that is normally used to obtain the standard clinical MR images. It has been shown, however, that phase images can also be used to quantify flow velocities (Moran et al, 1985). Whereas the modulus MR image contains information on proton density, relaxation time parameters (T_1 or T_2) and flow effects, the phase image contains information on the velocity and direction of flow, as well as phase shifts due to magnetic-field inhomogeneity, chemical shifts, and changes in magnetic susceptibility. The velocity information is usually encoded by adding extra gradient pulses into the pulse sequence (Bryant et al, 1984; Van Dijk, 1984). Alternatively, the bipolar form of gradient pulses which are part of the standard imaging sequence, such as those used for slice selection, can be exploited to provide velocity encoding (Ridgway & Smith, 1986). The range of velocities to be measured can be altered by changing the temporal separation of the two components of the bipolar pulse. Thus, peak velocities in the ascending aorta, and slower venous flow, can both be imaged using the same technique.

Pulsatile CSF flow has been demonstrated in the cerebral aqueduct and pontine cistern using MRI by showing a variation in signal intensity over the cardiac cycle (Bergstrand et al, 1985). An inversion–recovery pulse sequence was used in this study and though a cyclical variation in intensity was shown, no direct quantification of velocity or direction of flow was possible. Phase imaging has not previously been used to image pulsatile CSF flow.

The study describes the extension of a phase imaging technique which was originally developed to measure arterial flow in the body. The technique was modified to measure slow flow in the head and neck.

METHOD

This study was performed using a 0.08 T resistive MRI system manufactured by M&D Technology Ltd.

The imaging technique acquires two phase images, each having different velocity encoding, achieved by varying the temporal separation of the dephase and rephase components of the slice selection gradient (Ridgway & Smith, 1986). The final velocity image is obtained by subtracting these two images, thus eliminating any phase shifts due to field inhomogeneity, chemical shifts or changes in magnetic susceptibility. The technique was modified to image at lower velocity ranges by extending the separation of the bipolar slice selection gradients in one of the velocity-encoding pulse sequences. The difference in separation for the two pulse sequences was thus extended from 2 ms to 12 ms. The maximum measurable velocity, corresponding to a phase shift range of $\pm 180°$, was thus decreased from 120 cm s^{-1} to 20 cm s^{-1} making finer velocity resolution possible. Further modifications involved the inclusion of stronger gradients and the use of a smaller-diameter RF coil, used routinely for head imaging.

The flow measurement was calibrated for mean flow velocities in the range 1–11 cm s^{-1}. A simple continuous-flow phantom was used, incorporating a tube of inside diameter 10 mm, containing copper sulphate solution with $T_1 = 250$ ms. The phantom was fed from a constant head tank and mean flow rates were calculated by finding the time taken for a known volume to pass through the phantom. The MRI pulse sequence was triggered from an external source at a repetition rate corresponding to a heart rate of 75 beats min^{-1}. Each scan was repeated three times and the flow rate recorded before and after each scan.

Four volunteers were imaged, gating the pulse sequence with the subject's electrocardiogram (ECG) (Smith et al, 1986). Heart rates were monitored and images were obtained with delays of 110, 140, 165, 190, 215, 240, 290, 390, 490, 590, 690 and 790 ms after the subject's R-wave. More images were obtained during the systolic period where the velocity variation appeared to be more rapid. The total imaging time for each subject was about one hour.

Prior to this study, one volunteer was imaged at 12 levels in the head and neck at the time during the cardiac cycle when the peak velocity was attained. The resultant images suggested that the peak velocity was higher in the neck than in the head. Imaging too low in the neck resulted in increasing loss of sensitivity with distance from the head coil. As a compromise the level chosen for the four volunteers was at the level of the second cervical vertebra (C2).

The mean phase shift within the ring-shaped subarachnoid space was calculated using two regions of interest; the outer represented the boundaries of the spinal canal and the inner, the spinal cord. From these two regions the mean phase shift within the subarachnoid space and its area were determined. The calibration curve was used to determine the velocity from the phase shift, and the area of the subarachnoid space was used to calculate flow.

In order to assess the reproducibility of the technique, expressed as a coefficient of variation, one volunteer was scanned six times at the same level at the time of peak velocity.

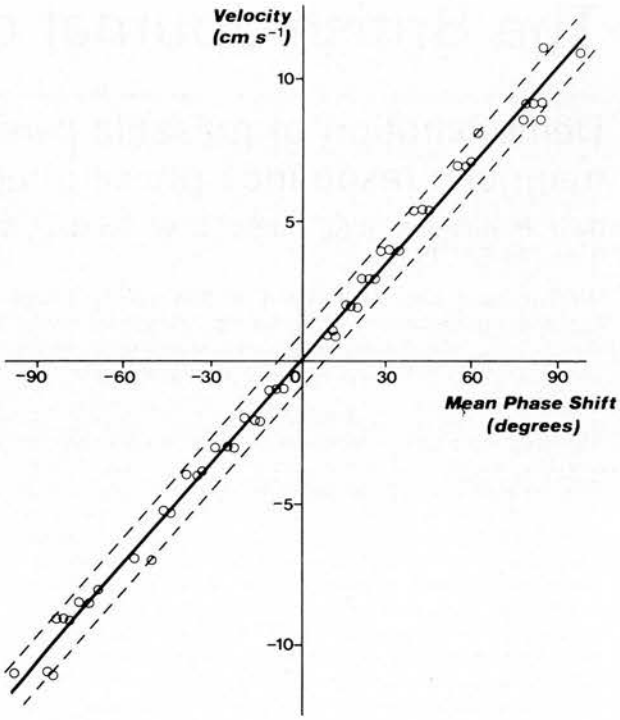

FIG. 1.

Calibration curve showing calculated mean velocity versus the mean phase shift. The 95% confidence limits with which velocity can be predicted from phase shift are also shown.

RESULTS

The results of the velocity calibration are plotted in Fig. 1, showing 95% confidence limits at ± 0.92 cm s^{-1}. There was a significant correlation ($r = 0.998$, $p < 0.001$) between the phase shift (degrees) and the flow velocity (cm s^{-1}).

A representative transverse section from one of the normal volunteers is illustrated in Fig. 2, showing both the modulus and the phase images. The CSF flow in the subarachnoid space can be seen on the phase image as a ring-shaped area. The displayed intensity of the phase image is related to velocity. Velocity in the caudad direction is represented by lighter shades of grey which correspond to a positive phase shift (Fig. 3A). Similarly, velocity in the cephalad direction is represented by darker shades of grey which correspond to a negative phase shift (Fig. 3B). Mid-grey represents zero velocity, corresponding to zero phase shift.

All volunteers demonstrated pulsatile flow within the subarachnoid space during the cardiac cycle and a representative flow-velocity curve is shown in Fig. 4.

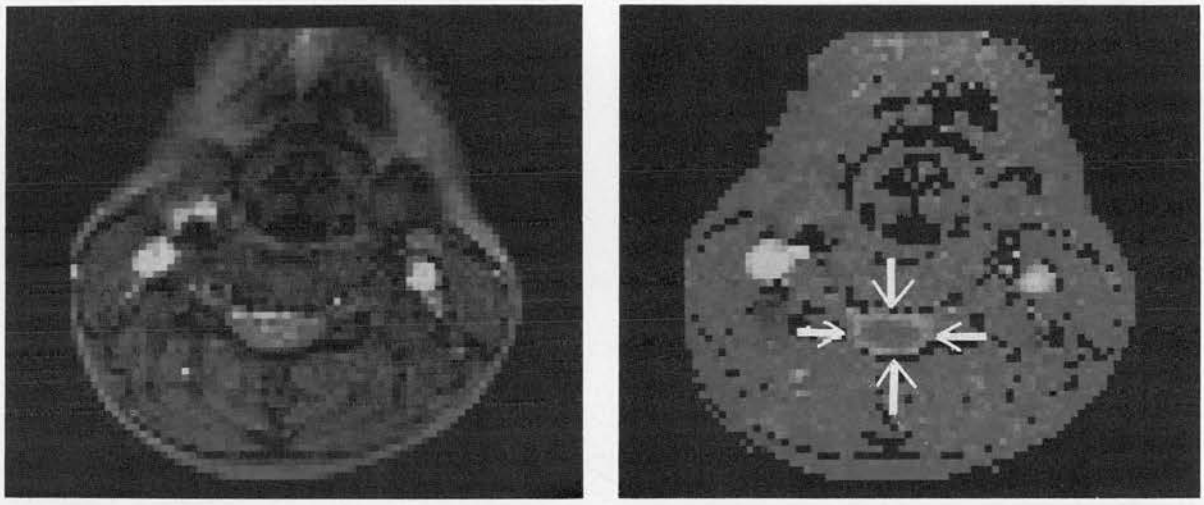

A B

FIG. 2.

Representative section of those used in the volunteer study showing (A) the modulus image and (B) the phase image. The CSF flow is seen on the phase image as a ring of increased intensity (arrows). Also seen are left and right internal jugular veins.

Maximum flow rates, maximum flow velocities and time to peak flow for all subjects are listed in Table I. At intervening times during the cardiac cycle, flow velocities were relatively small and their corresponding phase shifts were not significantly different from phase shifts measured in adjacent soft tissue. The maximum variation in heart rate in any one volunteer was from 65 to 83 beats min^{-1}.

The reproducibility of the repeated scan, analysed once, was 14.4%. However, this figure includes the error associated with the estimation of phase information from a single image which was found to be 8.7%. The reproducibility of the technique itself is therefore 11.5%.

DISCUSSION

This study not only confirms the ability of MRI to demonstrate pulsatile CSF flow, but also demonstrates

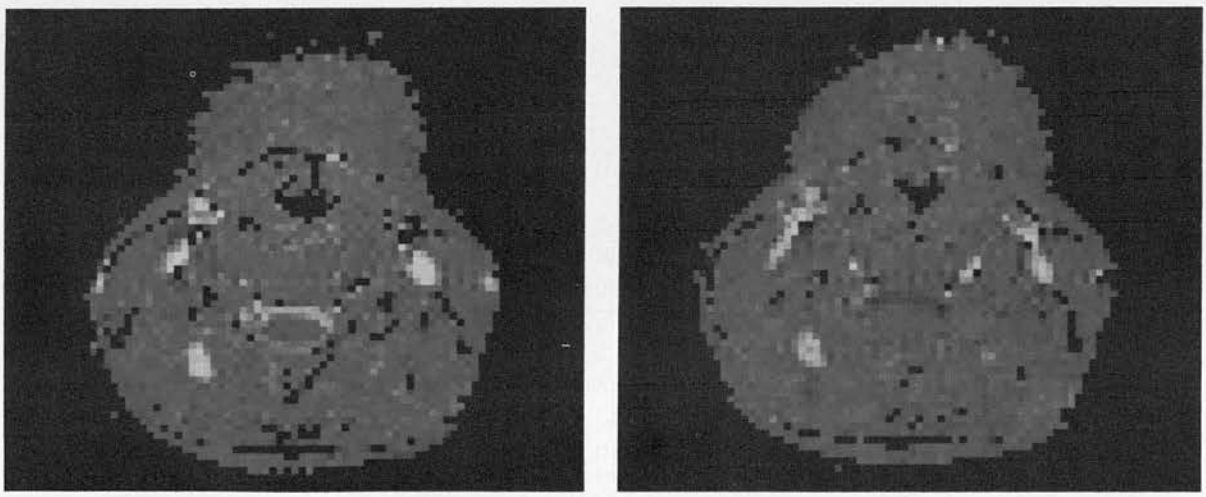

A B

FIG. 3.

Two representative phase images demonstrating the pulsatile nature of the CSF flow: (A) shows caudad flow (positive phase shift); (B) shows cephalad flow (negative phase shift).

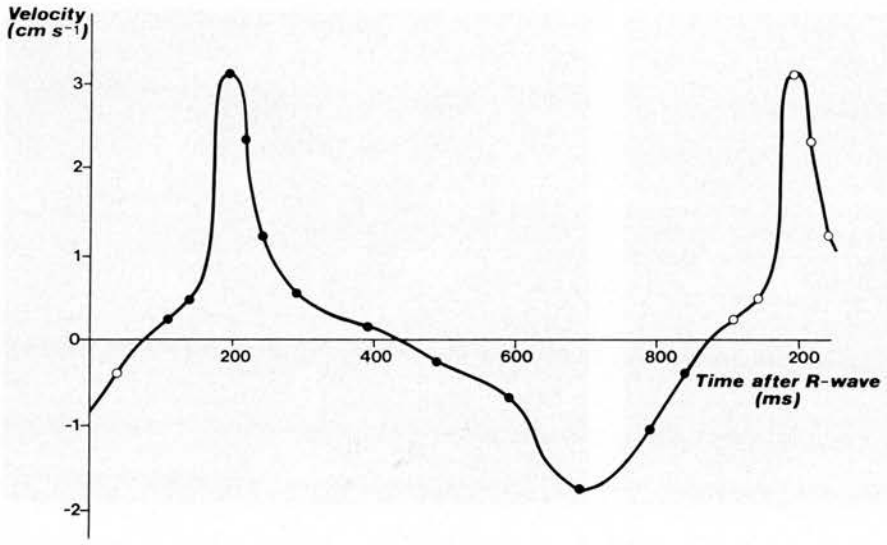

FIG. 4.

Variation of CSF flow velocity (cm s^{-1}) plotted against time after the R-wave (ms). The set of measured points are shown as filled circles. The same set of points was plotted (open circles) in adjacent ECG cycles to show the continuity of the curve. In this case the average R–R interval was 800 ms (corresponding to a heart rate of 75 beats min^{-1}).

that phase imaging enables quantitative measurement of flow velocity to be obtained with reasonable accuracy. In addition, the direction of flow can be assessed. The technique therefore has advantages over methods which rely on signal intensity (Bergstrand et al, 1985). However, unlike Bergstrand, we have been unable to demonstrate flow within the cerebral aqueduct, though this may be due, in part, to the lower signal-to-noise ratio that is obtained with the lower-field system used in this study.

There is good agreement between the flow rates and velocities obtained in three out of our four normal subjects. Shorter sampling intervals would enable these values to be established more accurately; currently the "peak" caudad and cephalad velocities could be underestimated. The variation in the time to peak CSF flow velocity may be due to many factors including the sampling time, *i.e.* time after R-wave, respiratory rate or variation in heart rate.

At present, the total imaging time for each subject is probably too long for routine clinical use. Simultaneous multislice acquisition would substantially reduce total imaging time but the spatial location of each section would be different. Alternatively, the acquisition of multiple images of a single section throughout the cardiac cycle, as has been done in cardiac imaging (Waterton et al, 1985) would also reduce imaging time.

This technique offers potential for the investigation of disorders involving the CSF circulation. In the case of complete obstruction, for example, pulsation distal to the obstructing lesion will stop, but it will persist on the cranial side. In addition, du Boulay (1966), using myelographic techniques, observed that when the subarachnoid space was narrowed but not obliterated the amplitude of movement could be considerably exaggerated. Magnetic resonance imaging offers a non-invasive method of studying the direction and velocity of CSF flow in such patients.

ACKNOWLEDGMENTS

This research is generously funded by a grant from the Scottish Home and Health Department. We would like to

TABLE I

MAXIMUM CSF FLOW VELOCITIES AND FLOW RATES

Subject	Max. caudad flow velocity (cm s^{-1})	Max. caudad flow rate (ml s^{-1})	Time of max. caudad flow after R-wave (ms)	Max. cephalad flow velocity (cm s^{-1})	Max. cephalad flow rate (ml s^{-1})	Time of max. cephalad flow after R-wave (ms)	Approximate mean R–R interval (ms)
1	3.17	4.41	190	1.33	1.89	690	750
2	1.78	2.44	215	1.10	1.78	110	750
3	3.57	4.71	165	1.70	2.28	690	800
4	3.12	4.96	190	1.74	2.99	690	800
Mean	2.91	4.13	190	1.47	2.24	—	775
SD	0.78	1.15	20	0.31	0.55	—	29

thank Mrs C. N. Rowan for secretarial services and Mr I. Lennox of the Department of Medical Illustration. We would also like to thank Professor J. J. K. Best and Dr D. M. Kean for their helpful comments and support.

REFERENCES

AXEL, L., 1984. Blood flow effects in magnetic resonance imaging. *American Journal of Roentgenology, 143,* 1157–1166.

BERGSTRAND, G., BERGSTROM, M., NORDELL, B., STAHLBERG, F., ERICSSON, A., HEMMINGSON, A., SPERBER, G., THOMAS, K. & JUNG, B., 1985. Cardiac gated MR imaging of cerebrospinal fluid flow. *Journal of Computer Assisted Tomography, 9,* 1003–1006.

BRYANT, D. J., PAYNE, J. A., FIRMIN, D. N. & LONGMORE, D. B., 1984. Measurement of flow with NMR using a gradient pulse and phase difference technique. *Journal of Computer Assisted Tomography, 8,* 588–593.

DU BOULAY, G. H., 1966. Pulsatile movements in the CSF pathways. *British Journal of Radiology, 39,* 255–262.

DU BOULAY, G., O'CONNELL, J., CURRIE, J., BOSTICK, T. & VERITY, P., 1972. Further investigations on pulsatile movements in the cerebrospinal fluid pathways. *Acta Radiologica Diagnostica, 13,* 496–523.

GEORGE, C. R., JACOBS, G., MACINTYRE, W. J., LORIG, R. J., RAYMUNDO, T. G., YUKIHIKO, N. & MEANEY, T. F., 1984. Magnetic resonance signal intensity patterns obtained from continuous and pulsatile flow models. *Radiology, 151,* 421–428.

MORAN, P. R., MORAN, R. A. & KARSTAEDT, N., 1985. Verification and evaluation of internal flow and motion. *Radiology, 154,* 433–441.

RIDGWAY, J. P. & SMITH, M. A., 1986. A technique for velocity imaging using MRI. *British Journal of Radiology, 59,* 603–607.

SMITH, M. A., RIDGWAY, J. P., BRYDON, J. W. E., BEEN, M., DOUGLAS, R. H. B., KEAN, D. M., MUIR, A. L. & BEST, J. J. K., 1986. ECG-gated T_1 images of the heart. *Physics in Medicine and Biology, 31,* 771–778.

VAN DIJK, P., 1984. Direct cardiac NMR imaging of heart wall and blood flow velocity. *Journal of Computer Assisted Tomography, 8,* 429–436.

WATERTON, J. C., JENKINS, J. P. R., ZHU, X. P., LOVE, H. G., ISHERWOOD, I. & ROWLANDS, D. J., 1985. Magnetic resonance (MR) cine imaging of the human heart. *British Journal of Radiology, 58,* 711–716.

Book reviews

Basic Doppler Echocardiography. Clinics in Diagnostic Ultrasound 17. Ed. by J. Kisslo, D. Adams and D. B. Mark, pp. xiii+215, 1986 (Churchill Livingstone, New York), £28.00.
ISBN 0–443–08431–9

The fundamental developments of cardiac blood flow analysis by Doppler ultrasound have paralleled those of imaging, but Doppler has been slower to enter general clinical use. However, the introduction of on-line spectral analysers and demonstration of the ability to measure transvalvar pressure gradients with accuracy equal to that of cardiac catheterisation, have stimulated enormous interest in the method and most machines currently purchased for cardiac applications are now of the "duplex" type, with facilities for pulsed-wave (PW) and continuous-wave (CW) Doppler. There is, thus, an undoubted demand for a book which, as its Preface states, aims to provide a simple and straightforward introduction for beginners to Doppler echocardiography.

The opening chapters explain the physical principles of PW and CW Doppler and the methods used to record flow data. Use of the machine controls is covered in detail, but with reference to only one particular machine and nothing, for example, about high-pass filters, mean or modal velocity estimators or high PRF systems. The examination technique is comprehensive, but assumes a firm background in two-dimensional cardiac imaging.

The second half deals with clinical applications. Valve stenosis and regurgitation are treated well. The chapter on ventricular function is short on practical advice needed by a beginner, for example how to trace the ejection velocity contour. Paediatric applications are poorly covered. The need for a chapter on fetal blood flow in a book for beginners is questionable.

Most of the illustrations and explanatory diagrams are helpful, but some photographs are out of focus. My major criticism is the prose style which, even allowing for trans-Atlantic differences, is long-winded and replete with jargon, something to be avoided in a book for newcomers. Firm editing could reduce the text by 30% and make the arguments much easier to follow.

The authors have wide experience of this new and exciting field and their effort to disseminate it is laudable. A little more self-discipline would have satisfied much better the need they have rightly perceived.

GRAHAM J. LEECH

Digital Subtraction Angiography: Practical Aspects. By A. van Breda and B. T. Katzen, pp. 230, 1986 (John Wiley and Sons Ltd, Chichester), £34.95.
ISBN 0–943432–60–X

As indicated by its title, this book is essentially a practical account of the capabilities and techniques of digital subtraction angiography (DSA). In addition to the chapters by the main authors there are contributions from a cardiologist, a radiographic technician and a nursing supervisor. Discussion covers the practical aspects of both intravenous and intra-arterial DSA of the various regions, including its value in interventional angiography. Consideration is also given to the implications that the mixed outpatient and day-patient population may have on the department, particularly with regard to patient preparation and after care. Emphasis is placed on the quality and value of "day case" intra-arterial studies, a technique considerably enhanced by the advent of high-flow, small-diameter catheters.

Each chapter is followed by references, mostly drawn from the American literature. Illustrations throughout the book are quite clear, although two illustrations have been incorrectly orientated. There are a number of minor and a couple of major printing errors which should have been avoided. Because this is a practical account of techniques, there is little critical analysis in a scientific form of the usefulness and the limitations of DSA: this would have enhanced the usefulness of the book.

Having accepted the drawbacks of the book, however, it would make useful reading for all members of a department which is envisaging the installation of a DSA unit.

R. A. FAWCITT

Clin. Phys. Physiol. Meas., 1989, Vol. 10, No. 3, 283–286. Printed in UK

Technical note

A system for cardiac and respiratory gating of a magnetic resonance imager*

John N Amoore and John P Ridgway

Department of Medical Physics and Medical Engineering, Royal Infirmary, Edinburgh EH3 9YW, UK

Received 30 September 1988, in final form 14 June 1989

Abstract. A cardiac and respiratory gating system is described which minimises MRI distortion by using a commercially available pneumatic capsule for respiration sensing, and by isolating the ECG and respiration detector circuitry with a fibre-optic link. Operator use is facilitated by displaying, on the ECG trace, the time during the cardiac cycle when images are acquired, and by displaying the respiratory signal. The system is presently in use with a MD 800 MRI system (M&D Technology Ltd, Aberdeen) operating at 0.08 tesla.

1. Introduction

The quality of magnetic resonance images of the thorax and upper abdomen is degraded by cardiac and respiratory movements to an extent that it is often not possible to obtain useful diagnostic information from them. The image quality can be improved by synchronising data acquisition with the cardiac cycle, allowing cardiac anatomy to be clearly resolved (Lanzer *et al* 1985), and with the respiratory cycle, providing clearer definition of structures within the upper abdomen (Runge *et al* 1984, Lewis *et al* 1986). A stand-alone system is described which detects the cardiac and respiratory signals and generates suitable logic pulses to synchronise data acquisition. Whilst such hardware is supplied with most of the present commercially available MRI systems, the system described combines a number of special features. The ECG and respiratory signals are detected using a battery powered signal acquisition system linked with a fibre-optic cable to a separate gating logic unit which generates the gating signals (figure 1). A commercially available pneumatic capsule and capacitive transducer system records the respiratory movements of the abdomen. The respiratory signal is displayed, enabling the operator to set the inspiration/expiration threshold. The time during the cardiac cycle at which cardiac images are acquired can be readily selected both prior to and during imaging, and can be displayed on an ECG monitor. The system is in regular use with an MD 800 MRI system (M&D Technology Ltd, Aberdeen) operating at 0.08 T.

2. System description

2.1. ECG and respiration detector

The ECG was amplified using three low power operational amplifiers in a standard instrumentation amplifier configuration and filtered to a bandwidth of 0.5 Hz to 20 Hz.

*Presented in part at the IPSM conference in Canterbury, Kent, in September 1988.

0143-0815/89/030283 + 04 $02.50 © 1989 Institute of Physical Sciences in Medicine

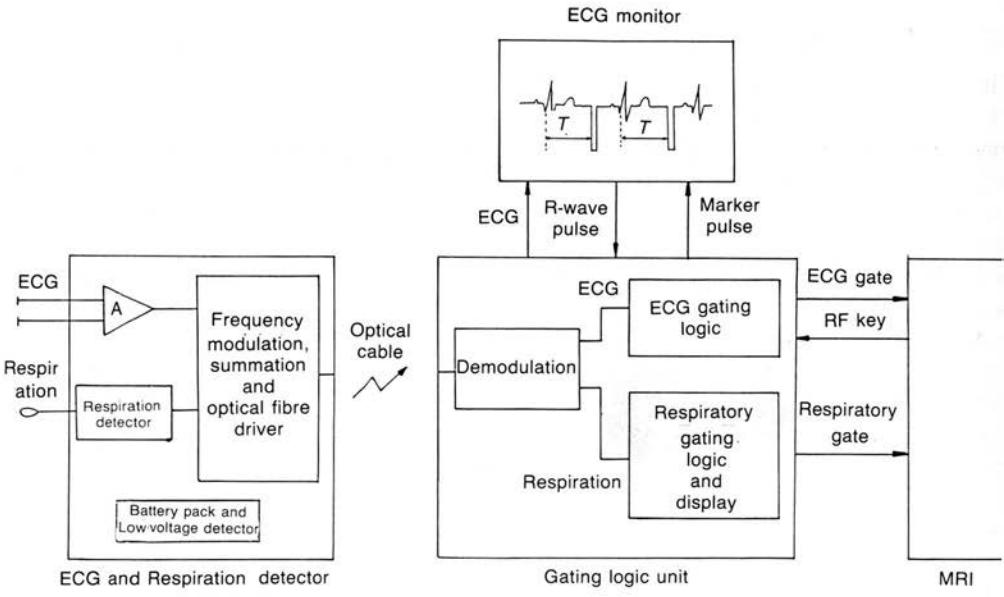

Figure 1. A block diagram of the MRI gating system showing the ECG and respiration detector, the optical pathway, gating logic unit, ECG monitor and imager.

The respiration detection circuitry was based on sub- modules of the commercially available MR10 apnoea monitor (Graseby Medical Ltd, Colonial Way, Watford, Herts WD2 4LG, UK). This uses a 15 mm diameter pneumatic capsule, which can be held in place either by surgical tape or by a belt surrounding the upper abdomen, to sense respiratory motion of the abdomen. Its ability to detect abdominal respiratory movements has been favourably reviewed (Munley *et al* 1985). Individual components of the MR10 can be separately ordered, enabling it to be easily incorporated into our data acquisition unit. The capsule is connected to a capacitive transducer by a one metre long small diameter plastic tube. The capacitive transducer forms part of an RC network, and the change in time constant is detected to generate an analogue respiration signal. The filter/amplifier is fabricated in a hybrid circuit which was modified to change the high pass filter from 0.5 Hz to 0.05 Hz to enable the low frequency respiratory waveform to be recorded. The high pass filter consists of a CR network; the capacitor was identified and an appropriate value of capacitor was connected in parallel with it to lower the high pass filter cut-off frequency.

A low battery detector and alarm circuit was included to alert the operator of the need to replace the batteries.

2.2. Optical fibre link

The ECG and respiratory signals frequency modulate 10 kHz and 540 Hz carrier waves respectively. The high frequency components of the square wave carriers were filtered and the carriers added together and transmitted over a fibre-optic cable. A set of active filters (high pass for the ECG carrier channel and low pass for the respiration carrier channel) and phase-locked loops extracted the ECG and respiratory signals from the received signal with less than 1% inter-channel cross- talk. The optical fibre link electrically isolates the detector circuitry from the gating logic unit, helping to ensure patient safety and to minimise the introduction of external electrical interference into the MRI detection system (Smith *et al* 1986).

2.3. ECG gating logic circuitry

The received ECG waveform was attenuated (1 mV per mV) and displayed on an ECG monitor which was also used to detect the R wave. The ECG monitor should make available the R-wave detection pulse, and should also have a marker pulse input such as used for defibrillator synchronisation. The train of R-wave pulses may be divided by 2 or 4 to allow the operator to acquire data each, or every 2nd or 4th heart cycle. The pulses trigger a monostable whose pulse width can be varied to enable the operator to select a delay of up to 2 s between the ECG R wave and the MRI system synchronisation pulse. The RF key logic pulse from the MRI system is used in conjunction with the ECG monitor's marker pulse input to display, superimposed on the ECG trace, the point during the cardiac cycle when image data is acquired. The time between the R wave and image data acquisition was measured and displayed, as was the R-R interval. The delay between triggering the magnetic resonance imager and the first imaging RF pulse was simulated by a monostable to enable the operator to set a desired point in the cardiac cycle for acquiring the cardiac image prior to data acquisition. The delay is varied by the operator selecting the appropriate pulse sequence being used.

2.4. Respiratory gating logic

The respiratory gating logic produces a rectangular wave which is low during inspiration. The operator can adjust a threshold level on the respiratory signal to select the onset of inspiration. The respiratory signal is displayed on a 20 segment bar-graph, and the threshold setting is displayed on a 20 element dot-graph positioned next to it. The rectangular wave output can be used either to acquire data during, say, expiration, or only at transitions from, say, inspiration to expiration. For a detailed explanation of respiratory gating methods see Ehman *et al* (1984), and Lewis *et al* (1986). Whilst the simple rectangular wave output is sufficient for respiratory gating and synchronisation, it does not allow the more sophisticated technique of respiratory motion artefact reduction known as Respiratory Ordered Phase Encoding (ROPE) to be carried out (Bailes *et al* 1985). Minor modifications to the respiratory gating logic can allow this technique to be implemented.

3. Discussion

The system enables magnetic resonance images to be gated with either cardiac or respiratory activity. Operator control of the time in the cardiac cycle when image data is recorded, is provided using low-cost digital logic circuitry.

Components from the commercially available MR10 apnoea monitor provided a low-cost and convenient solution to the design of the respiration detector circuitry. The pneumatic capsule and thin walled tube is made of plastic and so no ferromagnetic material, which may distort the uniform magnetic field of the imager, is introduced into the imager. Nor is respiration monitoring affected by the imager's pulsed RF field.

Several methods of detecting respiration for respiratory gating of magnetic resonance imagers have been described. Methods which monitor the temperature of respiratory air were found to be both uncomfortable over long periods of time, and to produce unreliable results (Ehman *et al* 1984). The more successful techniques were those which reflected respiratory motion more directly, and involved encircling the upper abdomen with a belt or pressure cuff. These include sensing the change in a length of a short elastic segment connected to a non-elastic cord circling the upper abdomen (Ehman *et al* 1984), or using the change in pressure in plastic, accordian-like bellows held in place with a non-elastic cord

(Runge *et al* 1984), or measuring the pressure in a pneumatic cuff surrounding the abdomen (Lewis *et al* 1986).

For some applications of gated MRI a high variability of R-R interval is undesirable (Smith *et al* 1986). In such cases ECG synchronisation pulses which occur outwith a specified R-R interval range should be ignored. This facility was incorporated into the imager software rather than the gating logic unit.

The system used to acquire the ECG from a MRI should not distort the imager's magnetic field, and nor should the imager's RF field interfere with the ECG. To reduce distortion of the magnetic field, electrodes and electrode connectors made from non-ferromagnetic material should be used. Careful electrode - skin preparation to reduce the electrode - skin impedance and minimising the loop area of the lead can reduce the RF field noise on the ECG. A full discussion on these topics is beyond the scope of this article, but is discussed by Wendt *et al* (1988).

References

Bailes D R, Gilderdale D J, Bydder G M, Collins A G and Firmin D N 1985 Respiratory ordered phase encoding (ROPE): a method for reducing respiratory motion artefacts in MR imaging *J. Comput. Assist. Tomogr.* **9** 835-8

Ehman R L, McNamara M T, Pallack M, Hricak H and Higgins C B 1984 Magnetic resonance imaging with respiratory gating: techniques and advantages *Am. J. Roentgenol.* **143** 1175- 82

Lanzer P, Barta C, Botvinick E H, Wiesendanger H U D, Moden G and Higgins C B 1985 ECG-synchronised cardiac MR imaging: Method and evaluation *Radiology* **155** 681-6

Lewis C E, Prato F S, Drost D J and Nicholson R L 1986 Comparison of respiratory triggering and gating techniques for the removal of respiratory artifacts in MR imaging *Radiology* **160** 803-10

Munley A J, Railton R, Fisher J and Barclay R P C 1985 Infant respiration monitoring – evaluation of a simple home monitor *J. Med. Eng. Technol.* **6** 261-5

Runge V M, Clanton J A, Partain C L and James A E 1984 Respiratory gating in magnetic resonance at 0.5 tesla *Radiology* **151** 521-3

Smith M A, Ridgway J P, Bryden J W E, Been M, Douglas R H B, Kean D M, Muir A L and Best J J K 1986 ECG-gated T_1 images of the heart *Phys. Med. Biol.* **31** 771-8

Wendt R E, Rokey R, Vick G W and Johnston D L 1988 Electrocardiographic gating and monitoring in NMR imaging *Magn. Resonance Imaging* **6** 89-95

Phys. Med. Biol., 1986, Vol. 3, No 7, 771-778. Printed in Great Britain

Technical note

ECG-gated T_1 images of the heart

M A Smith†‡§, J P Ridgway‡, J W E Brydon‡, M Been‖, R H B Douglas†, D M Kean†§, A L Muir‖ and J J K Best†§

† NMR Imaging Unit, ‡ Department of Medical Physics and Medical Engineering, § Department of Medical Radiology and ‖ Department of Medicine, University of Edinburgh, Royal Infirmary, Edinburgh, Scotland

Received 3 July 1985, in final form 15 November 1985

1. Introduction

Magnetic resonance imaging (MRI) has been used to investigate heart disease, either studying abnormal anatomy or attempting to identify pathological alterations of myocardial tissue. The anatomical studies have used cardiac-gated saturation recovery or spin-echo pulse sequences with short time to echo (TE), which produce reasonably high spatial resolution images containing mainly proton density information (Longmore *et al* 1985) or real-time echo planar imaging (Rzedzian *et al* 1983). For information concerning tissue, particularly important for the investigation of myocardial infarction (MI), it may be possible to identify abnormal pathology within the cardiac tissue using the relaxation times T_1 or T_2.

In vitro measurements of excised dog hearts have shown that both T_1 and T_2 increase following recent myocardial infarction (Williams *et al* 1980, Higgins *et al* 1983). The changes in T_1 correlate with changes in the water content of the tissue (Higgins *et al* 1983, Brown *et al* 1984, 1985) demonstrating that the initial increase in T_1 and T_2 is due to tissue oedema. The increase in T_1 is then reversed as the region of the heart wall is replaced by fibrous tissue (Brown *et al* 1984). Increases in T_2 *in vivo* following MI have been demonstrated in dogs (Wesbey *et al* 1984, Pflugfelder *et al* 1985) and in man (Higgins *et al* 1984, McNamara *et al* 1985). In one of these studies T_1 weighted images were also investigated but no increases in signal were detected (Pflugfelder *et al* 1985).

There is a wide variation in the results of the magnitude of the changes in T_1 and T_2 following infarction and also some disagreement concerning the relative merits of T_1 or T_2 in the assessment of MI. We feel that the suggested superiority of T_2 over T_1 is likely to be influenced by the fact that the MRI systems used were not designed to give accurate or precise T_1 values (Pflugfelder *et al* 1985) or that the pulse sequence combination used was more appropriate for T_2 measurements than for T_1 (Higgins *et al* 1983). In order to assess the true value of *in vivo* T_1 measurements of MI in man a pulse sequence specifically designed for T_1 measurement with high precision has been gated with the cardiac cycle to produce gated T_1 images.

2. Methods

A commercial 0.08 T resistive system, installed in a hospital environment for clinical studies (Smith *et al* 1984), has been modified to produce cardiac gated T_1 images. The

0031-9155/86/070771+08$02.50 © 1986 The Institute of Physics

imager generally uses a fixed pulse sequence which produces a saturation recovery image, an inversion recovery image and a calculated T_1 image for each section in a 4 min 16 s acquisition time. The imager uses an interlaced saturation recovery and inversion recovery pulse sequence with TR = 1000 ms for both and TI = 200 ms for the latter. One novel feature of the system, which makes it particularly suited to gated cardiac imaging, is the use of an adiabatic fast passage (AFP) pulse to invert the nuclei in the inversion recovery sequence (Hutchinson and Smith 1983). This pulse is very efficient at inverting the nuclei throughout the section imaged and it also has the advantage that it is not slice-selective in the inversion part of the sequence. This latter feature of the inverting AFP pulse is important because of the necessarily long delay between it and the subsequent 90° pulse, which is slice-selective, and which therefore must be synchronised with the cardiac cycle.

The timing of the pulse sequence is controlled by two timing integrated circuits, each with ten channels. In the normal mode of operation one of the timing channels controls the TR interval, which can be fixed at a preset value. This counter works in a free running mode and is automatically re-armed. For the gating sequence, this channel is changed to one shot mode. A single pulse sequence can then be started under direct software control by re-arming the appropriate channels. The computer used in the MRI system is a Digital PDP 11/23+. The software was programmed to respond to a pulse occurring on one of the status lines and a socket was fitted so that the system could be triggered externally from either a cardiac or respiratory gating pulse.

To obtain an ECG pulse from a subject inside the NMR imager, care was taken to reduce interference on the ECG signal from the RF pulses and also to minimise the noise introduced into the system from any patient connections. It was decided to monitor the ECG and use the R wave to determine the position of systole and diastole in the cardiac cycle rather than the less precise method of using a peripheral pulse from a region such as the finger. It was found that two electrodes placed one on either wrist produced severe interference on the ECG signal from the RF pulse. ECG detection in a perpendicular direction, with one electrode placed on the right shoulder and the other electrode just above the right hip produced no measureable interference from the RF pulses on the ECG signal. Conventional ECG electrodes were used in this position as illustrated in figure 1, the leads being taped to the patient with Micropore to ensure that there were no loops to pick up RF interference. The cables from the two electrodes were twisted together and connected to a rechargeable battery-powered unit 1.2 m from the centre of the magnet which converted the ECG to optical pulses so that it could be transmitted along a 12 m optical fibre. The distance of the battery-powered optical fibre unit from the central region of the magnet was found to be important. If the unit were nearer the centre of the magnet the ferromagnetic material within the unit would degrade the image; if the unit were further away then the electrode leads would act as an aerial for the external RF interference. The optical fibre is connected to a unit to convert the ECG signal into a form that can be fed into a conventional ECG monitor (Kontron Micromon 7141), both of which are sited 4 m from the magnet. The monitor has been modified to produce a pulse immediately after the detection of the QRS complex.

The trigger pulse from the modified ECG monitor is fed into a microcomputer (BBC model B) which in turn produces a pulse which is fed into the MRI system computer to trigger a single NMR signal acquisition. The microcomputer controls the delay between the patient's R wave and the part of the cardiac cycle to be imaged. A window setting can be used such that only R–R intervals within a certain range produce a

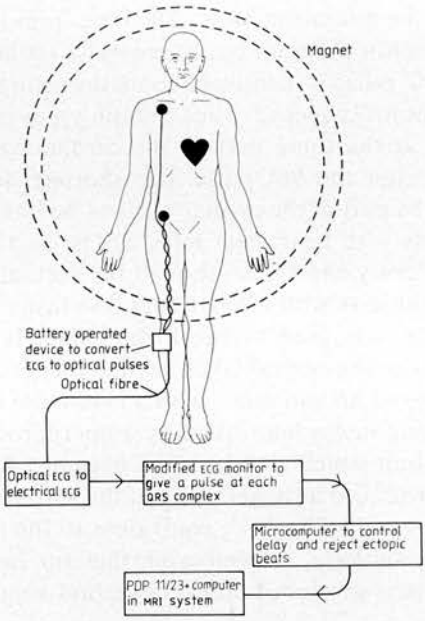

Figure 1. Schematic plan view of subject in MRI system. The positions of the ECG electrodes and leads and the battery powered box, converting the ECG to optical pulses, are shown in relation to the subject and the largest ring magnet.

signal for the MR system: thus ectopic beats are excluded. This is particularly important for end diastolic images as the section is not imaged immediately after the R wave, as is usually the case, but immediately before the succeeding R wave.

The timing of the T_1 gating sequence is illustrated in figure 2. There is a delay of 20 ms between the patient's R wave and the trigger from the ECG monitor due to the QRS complex detection. The delay from this pulse to the start of the AFP inverting

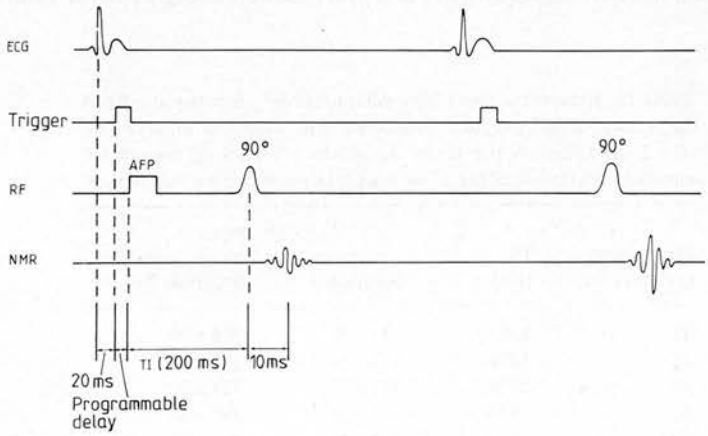

Figure 2. Timing diagram for a gated T_1 image showing inversion recovery and saturation recovery pulses during the interleaved sequence. The trigger from the ECG monitor occurs 20 ms after the upstroke of the R wave. The delay between the trigger pulse and the AFP is controlled by the microprocessor and will be different for each subject. A time from inversion (TI) of 200 ms is shown. The NMR signal is a field echo occurring 10 ms after the 90° pulse.

pulse is controlled by the microcomputer. The time from inversion (TI) can be altered in the main MR acquisition program but is generally set at 200 ms. The time from the trigger pulse and the 90° pulse is identical in both the saturation recovery and inversion recovery parts of the pulse sequence. Thus in both types of pulse sequence resonance occurs in the section at the same part of the cardiac cycle. The field echo occurs approximately 10 ms after the 90° pulse. The shortest delay available between the patient's R wave and the part of the cardiac cycle to be imaged is 230 ms, falling within systole even in patients with heart beat rates as fast as 120 min^{-1}. Signal acquisition can be triggered from every heart beat, though for accurate T_1 estimation every other heart beat is used in subjects with a heart beat rate faster than 70 min^{-1}.

A Perspex phantom was used to check the gated T_1 images. It contained three layers of $CuSO_4$ solution, the central layer having a T_1 of 330 ms and the outer layers a T_1 of 528 ms, and moved up and down with a maximum distance of travel of 5 cm. It was driven by a stepping motor controlled by a microprocessor which enabled either regular motion or motion which simulated an irregular R-R interval to be used. The microprocessor also produced a trigger pulse at the start of each cycle. The frequency of movement studied was 38–70 min^{-1}, equivalent to the frequency of trigger pulses obtained from human subjects, remembering that for heart beat rates greater than 70 min^{-1} a trigger pulse is produced on every second beat.

3. Results

Results obtained from the moving phantom are given in table 1. It can be seen that the precision of the calculated T_1, as demonstrated by the standard deviation of pixel values within the region of interest used, is not degraded by movement. There is a slight variation in T_1 value with TR, as would be expected. However the variation is within the long-term reproducibility (coefficient of variation) of T_1 measurement which is 2.9 and 6.5% for T_1 values 330 and 528 ms respectively.

An example of a cardiac-gated T_1 image of a normal subject at end systole is illustrated in figure 3 with an ungated image of the identical section for comparison. The time to end-systole from the R wave was determined using echocardiography. The

Table 1. Results obtained from phantom when moving at a fixed frequency, at an irregular frequency and when stationary. The $T_1 \pm 2$ SD refers to the mean T_1 within a region of interest ± 2 standard deviations of the T_1 values of the pixels within that region.

Frequency (cycles/min)	TR (ms)	$T_1 + 2$SD (ms)	
		Solution 1	Solution 2
38	1580	337 ± 32	566 ± 90
47	1280	333 ± 34	552 ± 66
56	1070	325 ± 26	524 ± 92
65	920	321 ± 28	497 ± 84
70	860	315 ± 24	493 ± 84
55-67	900-1100	329 ± 24	530 ± 64
50-75	800-1200	326 ± 32	532 ± 94
Static Phantom	1000	330 ± 30	528 ± 90

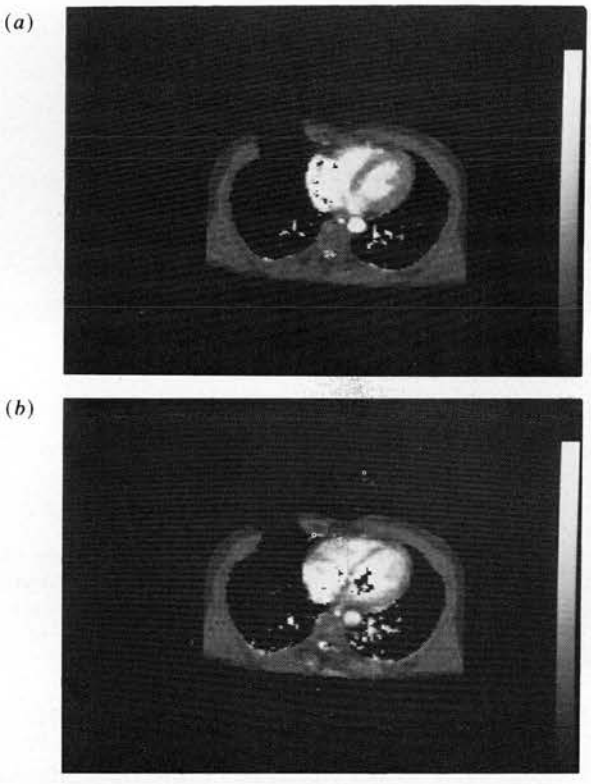

Figure 3. (*a*) Gated and (*b*) ungated transverse T_1 images of a normal human subject. The linear grey scale covers the range 50 to 650 ms.

section thickness used was 16 mm and the acquisition time for the gated image just under 4 min. The absence of signal from the anterior chest wall on the right-hand side is caused by the ferromagnetic material in the screening of the cable of the ECG connection. In the gated T_1 image the region of the left ventricular wall can be seen quite clearly with a uniform T_1 value. In the ungated image there is no such region of uniform T_1 corresponding to the ventricular wall; the T_1 value steadily increases from the outer edge of the heart to the centre. Eight small regions of interest were drawn encompassing the whole of the left ventricular free wall and the coefficient of variation of the T_1 values was found to be 3% in the gated image and 10% in the ungated image.

At end-systole the T_1 of the blood is fairly uniform. This is not the case in images later in the cardiac cycle, particularly during early diastole, where the T_1 of blood varies considerably. The cause of this is illustrated in figure 4 which shows the saturation recovery image at different stages during the heart cycle. It can be seen that the image acquired at the beginning of diastole contains a region of very low signal, caused presumably by the turbulence of the blood flowing into the ventricles. As the signal level from this image is the denominator in the equation to calculate T_1, this results in indeterminate values of T_1.

To date the technique has been used on 12 normal volunteers, many of these on more than one occasion, 13 patients with hypertrophic cardiomyopathy and 32 patients with MI, 7 within 4 days and the rest within 12 days of infarction. Occasionally the

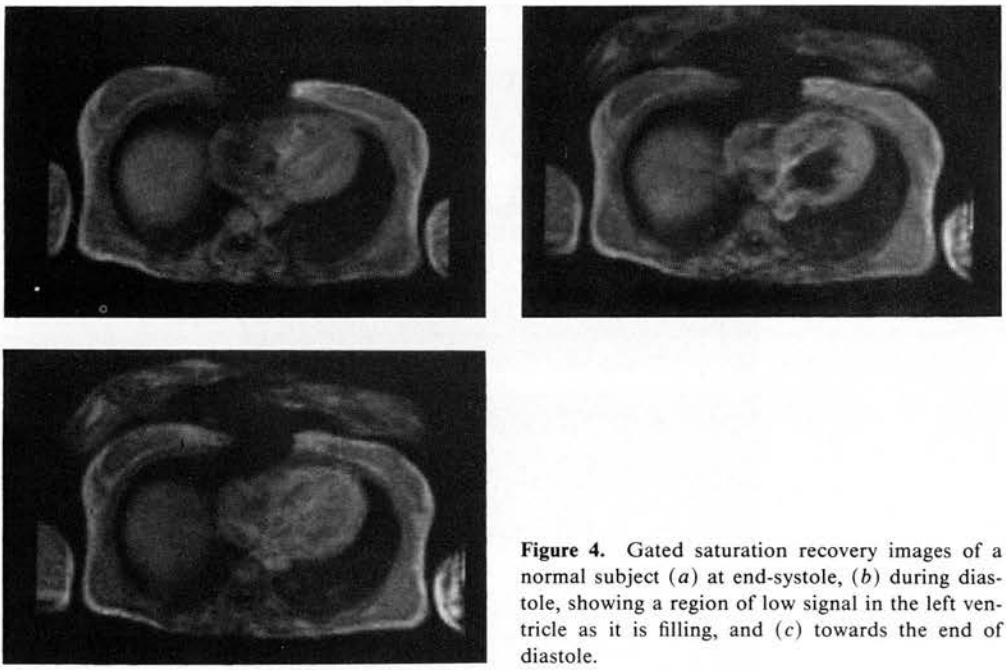

Figure 4. Gated saturation recovery images of a normal subject (*a*) at end-systole, (*b*) during diastole, showing a region of low signal in the left ventricle as it is filling, and (*c*) towards the end of diastole.

position of the two electrodes makes it impossible to produce a trigger pulse from the cardiac monitor. On such occasions the electrode on the right hip is moved to the left side of the patient and the cable to the electrode on the right shoulder is supported away from the chest wall by foam pads so that no signal loss occurs in the region of the heart. The use of this arrangement has improved the ECG signal sufficiently to allow a trigger pulse to be produced in all but one patient. However, the position of the electrode on the left-hand side of the patient causes interference on the ECG from the RF or gradient pulses, depending on the size of the patient and consequent proximity to the gradient windings or RF coil, which can cause unwanted trigger pulses. This can be overcome by gating the signal acquisition on every second, third or fourth pulse, depending on the type of interference. In some instances this can result in a lengthening of the time for an acquisition of a single section.

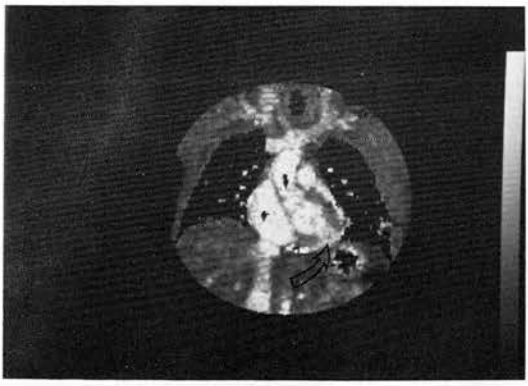

Figure 5. Gated coronal T_1 image of a patient with recent MI. The region of increased T_1, corresponding to infarcted tissue, is indicated.

Patients with recent infarction find the procedure acceptable, a complete investigation of four transverse and one coronal section taking between 20 and 30 min. Regions of increased T_1 have been found in the ventricular wall in patients with a recent infarct (Been *et al* 1985) and an example is shown in figure 5.

4. Discussion

The ability to obtain ECG-gated T_1 images of sufficient quality and in a sufficiently short time for clinical use has been demonstrated. The commercial system which has been modified has been shown to be particularly suitable for obtaining such images. This technique will be of value in assessing the use of *in vivo* T_1 measurement to identify abnormal pathology within the ventricular wall, particularly in patients with recent infarction. Most other MRI methods of investigating cardiac disease rely on the identification of wall thinning or abnormal motion using gated spin-echo images, often presented in cine mode. Such techniques can take a long time, particularly if the complete left ventricle is to be studied, which may prove unacceptable for patients with recent infarction. Moreover, echocardiography is already a well established and readily available technique producing similar information.

Many patients with cardiac disease will have an irregular heart beat; even if ectopic beats are not present then the R-R interval will vary during an investigation. Such a variation can produce a significant error in the T_1 estimation when a gated spin-echo sequence with short TR is used. In contrast, our use of a gated inversion recovery sequence with an inverting pulse that is not slice-selective ensures that the typical R-R variations obtained from patients have little effect on the T_1 values obtained.

It would be possible to obtain better linear spatial resolution by increasing the section width, thereby increasing the signal size, or by signal averaging, which would result in a considerably longer acquisition time. However, thicker sections have not been used as these would increase the partial volume effect, which increases with section thickness, as the heart is imaged in the transverse plane which itself is not perpendicular to the ventricular wall. To minimise the time that the patient is inside the MRI system signal averaging is not performed.

Future improvements to the system will be the availability of oblique sections so that the left ventricle can be imaged in a more appropriate plane, either perpendicular to the ventricular wall or along the length of the ventricle through the apex.

Acknowledgments

We are grateful to Mr Robert Chesser of M&D Technology Ltd and Mr David Norris of the Department of Biomedical Physics and Bioengineering, Aberdeen University, for valuable discussion. We would also like to thank Mrs C N Rowan for secretarial services. Financial support is acknowledged from the Lothian Health Board, Medical Research Council, Melville Trust, Scottish Home and Health Department, University of Edinburgh and Wellcome Trust.

References

Been M, Smith M A, Ridgway J P, Brydon J W E, Douglas R H B, Kean D M, Best J J K and Muir A L 1985 *Lancet* **ii** 348-50

Brown J J, Strich G, Higgins C B, Gerber K H and Slotsky R A 1985 *Am. Heart J.* **109** 486-90

Brown J J, Wallace W P, Gerber K H, Higgins C B, Strich G and Slotsky R A 1984 *Am. Heart J.* **108** 1292–7

Higgins C B, Herfkens R, Lipton M J, Sievers R, Sheldon P, Kaufman L and Crooks L E 1983 *Am. J. Cardiol.* **52** 184–8

Higgins C B, Lanzer P, Stark D, Botvinick E, Schiller N B, Crooks L, Kaufman L and Lipton M 1984 *Circulation* **69** 523–31

Hutchinson J M S and Smith F W 1983 *Nuclear Magnetic Resonance (NMR) Imaging* ed C L Partain, A E James, F D Rollo and R R Price (Philadelphia: Saunders) pp 231–49

Longmore D B, Klipstein R H, Underwood S R, Firmin D N, Hounsfield G N, Watanabe M, Bland C, Fox K, Poole-Wilson P A, Rees R S O, Denison D, McNeilly A M and Burman E D 1985 *Lancet* **i** 1360–2

McNamara MT, Higgins C B, Schechtmann N, Botvinick E, Lipton M J, Chatterjee K and Amparo E G 1985 *Circulation* **71** 717–24

Pflugfelder P W, Wisenberg G, Prato F S, Carroll S E and Turner K L 1985 *Circulation* **71** 587–94

Rzedzian R, Chapman B, Mansfield P, Coupland R E, Doyle M, Chrispin A, Guifoyle D and Small P 1983 *Lancet* **ii** 1281–2

Smith M A, Best J J K, Douglas R H B and Kean D M 1984 *Br. J. Radiol.* **57** 1145–8

Wesbey G, Higgins C B, Lanzer P, Botvinick E and Lipton M 1984 *Circulation* **69** 125–30

Williams E S, Kaplan J I, Thatcher F, Zimmerman G and Knoebel S B 1980 *J. Nucl. Med.* **21** 449–53